Optoelectronic study of InGaN/GaN LEDs

Michael Wallace

A thesis submitted to
the Department of Physics
University of Strathclyde
for the degree of
Doctor of Philosophy

27th September, 2016

Declaration of author's right

This thesis is the result of the author's original research. It has been composed by the author and has not been previously submitted for examination which has lead to the award of a degree.

Signed: Date:

Abstract

The quality of light emitting diodes (LEDs) has increased to a point where solid state lighting is becoming fairly common. Despite this, greater understanding of the effect of the device structure and the electric fields within them is helpful to continue improving device efficiency and uniformity and in reducing costs. In this thesis the optical and electronic properties of InGaN/GaN LEDs have been studied with a combination of luminescence spectroscopy, microscopy, conductivity mapping and efficiency measurements.

A study was made of the effects of the various electric fields, and the interplay between them, on LED luminescence and conductivity. Cathodoluminescence (CL) mapping shows die to die variation across large wafers revealing the powerful effects of a induced electric field on spectral intensity/position/width, in uncontacted devices. Micron scale spots in the LED material, lower in luminescence intensity and which trap charge, were revealed by CL/EBIC mapping with the origin attributed to cluster point defects in the active region. Depth resolved CL and CL under bias reveal the extent of asymmetry in carrier transport in the *p/n* type GaN around the active region.

LEDs grown with different active region temperature profiles were studied. Devices exposed to high temperature after quantum well growth (2T) were found to have a uniform spatial luminescence and a peak efficiency that is higher and occurs at a lower current density (0.1 W/A @ 1 Acm^{-2}). By contrast those with a low temperature cap (Q2T) exhibit dark spots in the luminescence, and a lower peak efficiency at a higher current density (0.04 W/A @ 10 Acm^{-2}).

The effect of improvement in LED design and material quality on the device efficiency, uniformity and spectral characteristics was studied. The addition of an $Al_{0.23}Ga_{0.77}N$ electron blocking layer (EBL) was found to reduce the size and strength of the dark spots by about a factor of 2, while an additional $In_{0.05}Ga_{0.95}N$

underlayer (UL) removed the dark spots entirely and shifted the luminescence peak by around 100 meV. The effect on the electroluminescence efficiency of the reduction in template dislocation density was found to depend strongly on the drive current density, with defect non-radiative recombination more important at low currents. Overall device efficiency was shown to be improved with an EBL and UL. The most efficient devices were those with the 2T type growth but the relative improvements are larger in LEDs grown with the Q2T method.

Together, the results present a number of factors limiting the performance of current LEDs and suggest potential routes for improvement and optimisation.

Acknowledgments

Firstly I would like to thank my supervisor, Professor Robert Martin, for his knowledge, patience and support throughout my thesis. His direction and ability to focus my mind was invaluable. I thank him both for giving me the opportunity to work in the group and for guidance through the good and bad times.

I am also very grateful for the input from my second supervisor, Professor Kevin O'Donnell. Our sojourn to Didcot was an educational and entertaining time. I even managed to contribute to the trip; getting a cryptic crossword clue!

Speaking of cryptic crossword experts, I am indebted to the understated expertise of Dr Paul Edwards, whose most welcome pedantry was more that matched by his willingness to impart his knowledge of optics, electron microscopy and the secrets of computer/device interfacing.

I wish to also extend my gratitude to my collaborators at the Universities of Bath and Cambridge, in particular Dr Margaret Hopkins, Dr Menno Kappers, Dr Duncan Allsopp and Dr Rachel Oliver. Not only did they provide all my materials but were extremely helpful and forthcoming with information and advice. Also those in the Institute of Photonics at Strathclyde were a very welcome and important part of the success of my studies, especially Dr Enyuan Xie and Pengfei Tian.

My time at Strathclyde has given me a great education but also a great friend in the form of my colleague, Dr Jochen Bruckbauer. Our long chats about science, science fiction, boardgames and many others topics, often in concert with Nikhil Ratajane, were a defining part of my time at Strathclyde and hopefully beyond.

I would also like to thank Martin and Elaine whose Scottish banter was always fun, especially when spoken broadly enough to be another language in the group! I am also very grateful for the company of the rest of my colleagues and friends at Strathclyde; Carol, Naresh, Ina, Ben, Nouf, Stefano, Catherine, Gunnar, Elena

and David as well as those who have moved on to other things; Simon, Jenny and Fransiska.

I, and many others, are deeply indebted to the help and assistance of the irreplaceable David Clark and Jed Drinkwater without whom most experiments would never have gotten off the ground.

I am very thankful to my old friends (and fellow doctors); David Mahon, Neil Hassall and Jamie Robinson, both for our weekly badminton sessions and the weekly gentle ribbing about me being the only non doctor in the group. The former is a great tension reliever and the latter was ideal inspiration to get the thing finished.

It's been a great help to have my other best friend, Jamie Connolly, always available throughout the entire thesis. Without his down to earth advice and fun company I would have been even more stressed!

I need to also thank my family as I am close to them and they have been a continued, extremely important, part of my life. My brother, Daniel, who is more like me than anyone, my sister Becci and little baby Daniel and my youngest sister Judy, the greatest card poet in all Scotland. I would not have got to where I am without the support and love from them or from my mum and dad. My mother has never stopped giving me the encouragement that I needed, especially in that difficult first year, and my father who, even after meeting so many eminent professors and doctors, is still the most intelligent and interesting person I know. This thesis is, more than nearly anyone else, dedicated to him.

Last, but certainly not least, I want to thank my wonderful wife, Ashley. I probably wouldn't have met her if it weren't for my thesis (and Jochen) but I would happily trade it in exchange for her. Luckily I don't have to, and if my family, friends and colleagues got me through the start and middle of it, she is responsible for me getting me to the end. I am thankful always for her sense of humour and silliness and for her love, support and kindness.

Michael Wallace Glasgow, 27th September, 2016

Publications

- **Wallace, M. J.** and Edwards, P. R. and Kappers, M. J. and Hopkins, M. A. and Oehler, F. and Sivaraya, S. and Allsopp, D. W. E. and Oliver, R. A. and Humphreys, C. J. and Martin, R. W. *Bias dependence and correlation of the cathodoluminescence and electron beam induced current from an InGaN/GaN light emitting diode* Journal of Applied Physics **116**, 033105 (2014)

- **Wallace, M. J.** and Edwards, P. R. and Kappers, M. J. and Hopkins, M. A. and Oehler, F. and Sivaraya, S. and Oliver, R. A. and Humphreys, C. J. and Allsopp, D. W. E. and Martin, R. W. *Effect of the barrier growth mode on the luminescence and conductivity micron scale uniformity of InGaN light emitting diodes* Journal of Applied Physics **117**, 115705 (2015)

- Kachkanov, V. and **Wallace, M. J.** and van der Laan, G. and Dhesi, S. S. and Cavill, S. A. and Fujiwara, Y. and O'Donnell, K. P. *Induced magnetic moment of Eu^{3+} ions in GaN* Scientific Reports **2**, 969 (2015)

- Ren, C. X. and Rouet-Leduc, B and Griffiths, J. T. and Bohacek, E. and **Wallace, M. J.** and Edwards, P. R. and Hopkins, M. A. and Allsopp, D. W. E. and Kappers, M. J. and Martin, R. W. and Oliver, R. A. *Analysis of Defect-Related Inhomogeneous Electroluminescence in InGaN/GaN QW LEDs* Superlattices and Microstructures In press.

Contents

List of abbreviations

1T	One temperature
2T	Two temperature
AFM	Atomic force microscope
AlGaN	Aluminium galliun nitride
BSE	Backscattered electron
CL	Cathodoluminescence
EBIC	Electron beam induced current
EBIV	Electron beam induced voltage
EBL	Electron blocking layer
EL	Electroluminescence
EPMA	Electron probe micro-analyser
EQE	External quantum efficiency
FWHM	Full width at half maximum
GaN	Gallium nitride
InGaN	Indium gallium nitride
InN	Indium nitride
IQE	Internal quantum efficiency
LED	Light-emitting diode
MBE	Molecular beam epitaxy
MOCVD	Metal-organic chemical vapour deposition
MOVPE	Metal-organic vapour phase epitaxy
MQW	Multiple quantum well
PL	Photoluminescence
Q2T	Quasi two temperature
QCSE	Quantum confined Stark effect

QB	Quantum Barrier
QW	Quantum well
SE	Secondary electron
SEM	Scanning electron microscope
SRH	Shockley-Read Hall
SSL	Solid-state lighting
SQW	Single quantum well
TB	Temperature bounce
TDD	Threading dislocation density
TEM	Transmission electron microscope
UL	Underlayer

Chapter 1

Introduction

When the 2014 Nobel prize for physics was announced it recognized the pivotal contribution of three men; Shuji Nakamura, Hiroshi Amano and Isamu Akasaki which led to the realisation of the high efficiency white light-emitting diode [1]. Many others were also involved in the story, including the early growers of violet emitting GaN in the 70's (Maruska and Tietjen [2]), of InGaN layers by MOCVD (Nagatomo [3] and Yoshimoto [4]) and many more, but the three awarded the prize were those who made the biggest breakthroughs.

The global drive to reduce greenhouse gas emissions is split into two equally important but separate strands - development and implementation of low carbon energy generation and attempts to reduce overall energy consumption. Lighting accounts for around 20% of all electricity usage worldwide and the wide-scale adoption of low energy lighting is predicted by the American Department of Energy to cut electricity use for lighting by half and save 620 TWh/year [5] ($\sim$ 5 kWh/person/day [6]).

Electric lighting originated with the invention of the filament bulb in the 1880s by Joseph Swan [7] and Thomas Edison[8]. In these devices, light is produced by passing a current through a tungsten filament and emitted via incandescence. However the majority of the energy (95%) is lost as heat and so such bulbs are very inefficient. The development of the fluorescent and compact fluorescent bulb in the 1950s [9] led to a large improvement in the efficiency of general lighting. The luminous efficiency can be as high as 80 lumens/W [10] but since such bulbs rely on a mercury containing gas to excite phosphors they pose an environmental

hazard upon disposal, and they also have (an admittedly improving) record of unpleasant flickering and poor colour rendering [9]. The unit of lumens/Watt is a measure of how much light, corrected for the spectral sensitivity of human vision, a source outputs per Watt of input power.

Light emitting diodes are considered to be the ideal light source as they can, in principle [11], convert electrical energy into radiation with 100% efficiency. In practice, this will never be realised, but even now the best external quantum efficiency (EQE) is reported to be up to 80% at operating currents of 100 Acm^{-2} [12]. The earliest report of electroluminescence from a semiconductor is from 1907, by Henry Joseph Round who observed the emission of yellow light from silicon carbide when contacted with a thin whisker of metal while working on rectifiers [13, 14].

The III-Nitride material system, most importantly the nitrides of indium, gallium and aluminium, can be alloyed to create ternary and quaternary compound semiconductors which emit across the entire visible spectrum (InGaN) and well into the UV (AlGaN), while retaining a direct bandgap and hence high efficiency. This property makes III-N immensely useful for LEDs and laser diodes [15, 16] These devices have many uses, besides general lighting, including blu-ray data storage [17], bio-sensors [18] UV water purification devices[19], visible light communication [20] and flat screen displays [21]. The plot in figure 1.1 charts the continuing improvement of LED luminous efficacy from the 70's to the present, along with comparison to the filament and fluorescent bulbs. The emergence and rapid improvement of blue/green and the advent of white LEDs, after 1990 is clear.

The barriers to creating a p-n junction based LED with GaN were difficulties in growing layers of reasonable quality on available substrates and making efficient p-type material. These were the issues solved by the Nobel prize winners; the former problem was largely solved by the discovery that a low temperature AlN layer grown on the substrate acts as a nucleation layer to allow high quality GaN growth [23, 24, 25, 26]. The issue of p-doping was solved partly by accident when it was found that irradiation by an electron beam activated the dopant [27] and subsequently that a high temperature anneal had a similar effect [28]. Both developments led to Nakamura's creation of the first "high brightness" InGaN/GaN double heterostructure LED [29]. Despite these successes, the optimisation of the

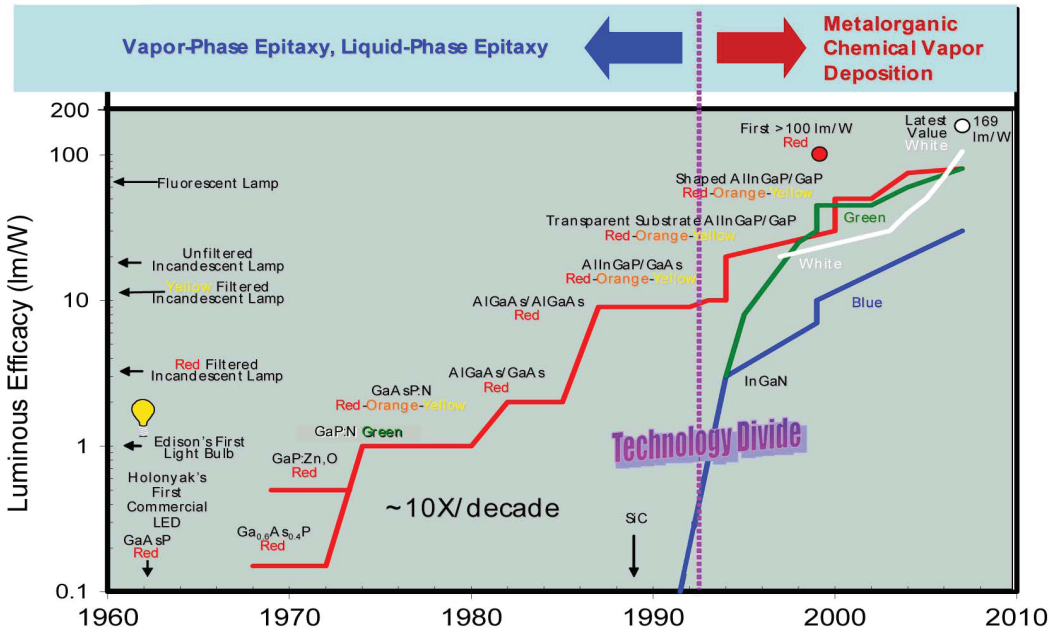

Figure 1.1: *Plot charting the development of LEDs and a comparison with the luminous efficacy of earlier light sources. From Crawford [22]. Note that the y axis is efficacy, not efficiency - the raw radiant efficiency (W_γ/W_{input}) of blue LEDs is far greater than green, but since human visual response is centered at 555 nm, green has the higher efficacy.*

growth of LED structures remains important in reduction of the cost of LEDs and in understanding fundamental physical problems, including the efficiency droop of devices at high currents. The manifestation of defects and inhomogeneities in both luminescence and conductivity mapping can be a useful tool in understanding the effects of LED growth [30, 31]. The control of the electric fields in such devices is also important for understanding the contributions and effects of such fields during operation [32, 33]

In this thesis the luminescence and conductivity properties of a number of series of LEDs are studied using a combination of spectroscopy and mapping of various forms of LED luminescence, conductivity mapping and bias dependent spectroscopy and electron beam induced current.

Chapter 2 covers the basics of LEDs, the III-Nitride material systems and electric fields in devices. This is followed in chapter 3 by a description of the experimental apparatus and methods used in the thesis, including electron microscopy

and electron beam induced current. Chapter 4 presents results of a study of the effect of applied bias on the luminescence and transport in an InGaN/GaN LED. This chapter characterizes a single die in detail using bias dependent cathodoluminescence and EBIC mapping and bias dependent photoluminescence and CL spectroscopy. It also demonstrates the power of several techniques, which are then used in chapter 5, which studies the effect of growing the active region using different temperature profiles on LED uniformity and efficiency. This is extended into chapter 6, where the effect of either adding or altering layers to a standard LED design are compared. The effect of including underlayers, electron blocking layers or changing the thickness of the quantum wells or template dislocation density are presented. Finally a summary of the work coupled with a discussion of possible other experiments to extend the thesis are covered in the conclusion.

Chapter 2

Theory

2.1 Introduction

This first chapter introduces the basic principles of the topics covered in the thesis. The principle of radiative and non-radiative recombination in semiconductors is introduced in both general terms and relating specifically to the III-Nitrides. These are the family of compound semiconductors comprising AlN, GaN and InN, of which GaN is the most technologically important. The material properties of the III-Nitrides are then covered, including uses, growth issues and with particular emphasis on the crystal structure and resultant polarity of *c*-plane material. This leads to a discussion of the spontaneous and piezoelectric induced fields in InGaN heterostructures and the quantum confined Stark effect (QCSE). The final section covers the principles and operation of light-emitting diodes (LED) and extends the discussion on the interaction of the quantum wells and applied electric fields to include tunnelling and carrier transport. The design of InGaN LEDs including their optimisation by the alteration or addition of different layers, is covered in the context of improving performance and efficiency. The concept of LED efficiency and the so called efficiency droop completes the chapter.

2.2 Light Emission from Semiconductors

Throughout the work in this thesis, luminescence is excited from the LEDs by several different mechanisms but regardless of the nature of the excitation, lumi-

nescence in semiconductors occurs via the recombination of excess electrons and holes.

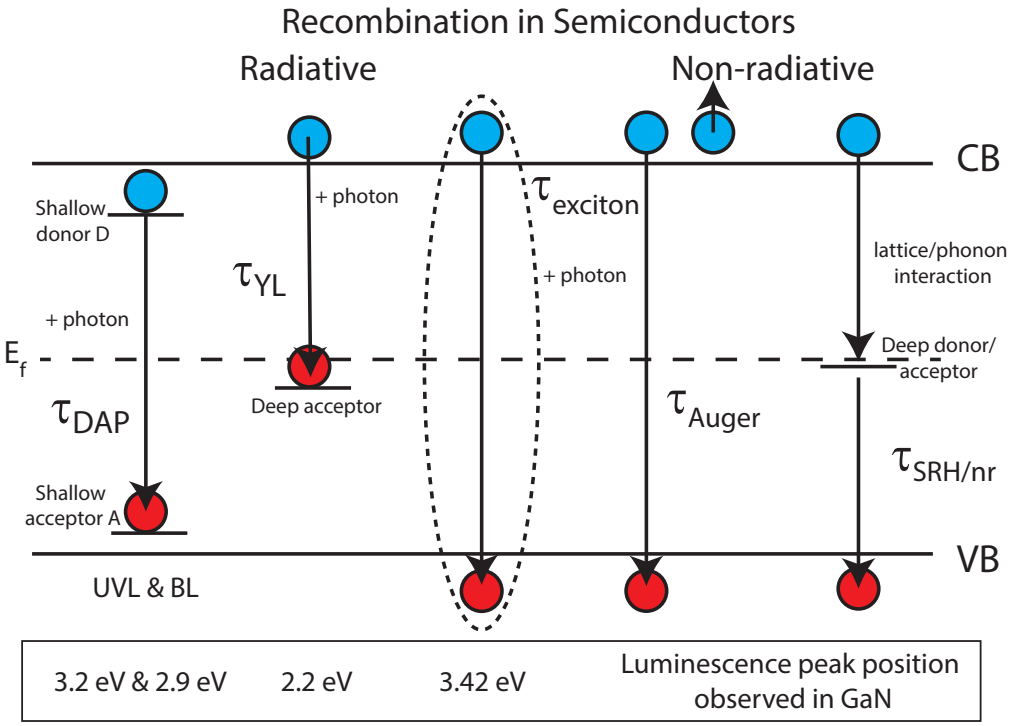

Figure 2.1: *Diagram indicating several important recombination channels in GaN. Underneath the radiative processes are shown the luminescence peak energies in GaN resulting from the transitions. Two non-radiative channels are shown - the SRH process via trap states in the bandgap and the Auger process. The different channels are discussed in the text. The τ are recombination lifetimes*

Recombination channels for electrons and holes in semiconductors consist of both radiative and non-radiative processes and several of the main routes are sketched in figure 2.1. Processes which involve transfer of energy from the excess carriers to the crystal are termed *non-radiative* recombination routes. The simplest, involving a single charge carrier was originally formalised by Shockley and Read [34] and by Hall [35] in 1952 in the context of recombination in Germanium through defect centres. Defects can include foreign atoms, lattice vacancies, dislocations, and native defects such as interstitials (where an atom is sitting in between lattice sites). Defects can be point like (such as interstitials or vacancies) or extended dislocations which run through large parts of the entire structure (such as edge/screw dislocations or stacking faults). Regardless of their

form these defects can create energy levels in the forbidden gap of the semiconductor (known as a deep level or trap). Energy is transferred to the lattice in the form of vibrational energy, known as phonons. In honour of it's originators, this process is referred to as Shockley-Read-Hall (SRH) non-radiative recombination. The recombination rate for this process, U_{SRH}, is related to the inverse of the non-radiative lifetime, τ_{nr} and the density, n, of the excess charge carriers as:

$$U_{SRH} = n/2\tau_{nr} = An \tag{2.1}$$

where A is the SRH non radiative recombination rate.

A second channel of non-radiative recombinations comes via the Auger process (Fig 2.1), which can be considered as the inverse of impact carrier generation.[36, 37] If an electron and hole recombine across the band gap, the energy can promote a third carrier (either an e or h) to a higher energy state in it's respective band. Since this is possible with either an electron and hole as the third carrier there are two possible "band to band" Auger recombination (AR) processes, termed *eeh* and *hhe*. The Auger interaction is a function of both temperature and the bandgap. The lifetime, τ_{Auger} is proportional to the bandgap and the temperature in the following manner [36, 38]:

$$\tau_{Auger} \propto \left[\frac{E_g(T)}{kT}\right]^{3/2} exp\left[\frac{E_g(T)}{kT}\right] \tag{2.2}$$

where $E_g(T)$ is the temperature dependent bandgap, and the other symbols have their usual meanings. With a larger bandgap the coupling between electron and hole is weakened and so the strength of the effect is reduced. Auger processes can occur intraband and interband. The former refers to a case where the second electron is promoted to a free state in the same band. Interband occurs when the second electron is promoted out of the conduction band to the next band. Delaney et al [39] showed that while intraband Auger is weak with large E_g, as in GaN, interband Auger has a resonance when the energy between the conduction band and the next band up is the same as the fundamental bandgap E_g. This resonance can be large for GaN and hence has the potential to increase the effective Auger recombination co-efficient.

The Auger process can also be mediated via alloy and phonon scattering [40].

Since it is necessary that momentum be conserved, the addition of scattering process provides a broader range of final states. When considering only the *eeh* process, which is dominant in GaN, the Auger recombination rate, U_{Auger} can be expressed as:

$$U_{Auger} = Cn^3 \tag{2.3}$$

where C is the Auger recombination coefficient and has units of cm^6/s. The value of C in GaN is widely disputed and it depends on whether one considers direct or phonon/defect assisted channels. Typically values of between 10^{-29} to 10^{-32} cm^6/s are found by experiment [41, 42, 43] and modelling [39, 40, 44]. There is a great deal of controversy about the importance of Auger recombination in the performance of III-Nitride LEDs and this is discussed in the section dealing with the so called "Efficiency droop".

The most important channel for light emitters, is that of radiative recombination. Three of the many possible light emitting interactions are shown on the left side of figure of 2.1. Band to band recombination is the fundamental interaction and is the only process in an ideal semiconductor, where no states exist in the forbidden gap. Since this process involves two carriers, the recombination rate, R, is proportional the density of both types of carriers, p and n via:

$$R = Bnp \tag{2.4}$$

where n and p are measured in cm^{-3} and B is the so called bimolecular recombination coefficient. The spontaneous radiative recombination rate can be determined using the van Roosbroeck-Shockley equation [45], which is an expression for the absorption rate per unit volume. In equilibrium, the recombination and absorption rate will be identical and so, assuming that $n{=}p$ (which may not be valid, as discussed in the subsequent page) a value of B can be found by:

$$B = R_0/n^2 \quad \text{where } R_0 \text{ is the absorption rate and assuming } n{=}p \tag{2.5}$$

R_0 is simply the photon density per unit volume, $N(\nu)$ divided by the photon

lifetime, $\tau(\nu)$.

$$R_0 = \frac{N_\nu}{\tau(\nu)} = \Big[\frac{8\pi\nu^2\bar{n}^2}{c^3}\frac{d(\bar{n}\nu)}{d\nu}\frac{1}{e^{h\nu/kT}-1}\Big]\Big[\alpha(\nu)c\frac{d\nu}{d(\bar{n}\nu)}\Big] \tag{2.6}$$

where, ν is photon frequency, $\bar{n}$ is the refractive index at ν, α is the semiconductor absorption coefficient at ν and the other symbols (c, h, k and T) have their usual meanings. The first square bracket is the Planck black body photon distribution in frequency and the second square bracket is the inverse photon lifetime. Integration of 2.6 over all ν yields R and via equation 2.5, a value for B in units of $\mathrm{cm}^{-3}\mathrm{s}^{-1}$ and $\mathrm{cm}^{3}\mathrm{s}^{-1}$, respectively.

Radiative Efficiency

Before discussing the radiative efficiency, it is important to note that the model commonly used, the ABC model, is overly simplistic in the III-Nitrides [38]. First, the assumption that $n = p$ is unsound in InGaN, either broadly or locally. InGaN, like GaN, has a high background electron concentration (10^{17} cm^{-2}) and so, unless at very high carrier concentrations, $n{>}p$. More pertinently, any potential fluctuations caused by inhomogeneities in material composition or layer thicknesses will proportionately affect holes more than electrons, due to their much larger effective mass. Also, carrier distribution in the quantum wells is well known to be unbalanced between electrons and holes, again due to the different mobilities. These effects mean that in any given spatial position in the device, it is unlikely to be the case that the local electron concentration is the same as the local hole concentration.

Furthermore, the assumption that the non-radiative A coefficient is constant with respect to carrier density is undermined by processes sensitive to carrier density. Principally, this can take the form of density activated defect recombination (DADA), and is a result of the saturation of local potential energy minima (caused by the variations described above) at high current/carrier densities. At low n, carriers are captured by the potential minima and hence are prevented from diffusing to non-radiative defect centres in the plane of the QW. As n increases, the available quantum states in the minima are saturated and new carriers spill-over or otherwise migrate to the defects, thereby increasing the effective value of

A. Continuous DC current flow or a high current density can also potentially generate new defects in the material either via heating damage or defect propagation [46] and this will increase the value of "A".

Despite this, the ABC model is a useful tool to appreciate the evolution of efficiency with carrier density. The ABC model is an empirical model which describes the recombination rates of the three processes described above. At steady state, the generation rate of carriers, G, is equal to the recombination rate, R and hence dn/dt = 0 where n is the carrier density. The ABC model expresses R as a simple 3rd order polynomial in n where:

$$R = -\frac{dn}{dt} = An + Bn^2 + Cn^3 \tag{2.7}$$

Where A is the coefficient associated with the Shockley-Read-Hall process, B is the bimolecular recombination coefficient as discussed previously and C is the rate associated with Auger recombination. The three recombination processes, SRH, radiative and Auger are dependent, respectively, on the first, second and third order power of the carrier density since they require one, two, and three charge carriers. As a result the units of the recombination coefficients are $1/s$, cm^3s^{-1} and cm^6s^{-1} respectively.

The quantum efficiency is then defined as the ratio of the radiative recombination rate to the total recombination rate:

$$\eta_{QE} = \frac{Bn^2}{An + Bn^2 + Cn^3} \tag{2.8}$$

The efficiency is a strong function of the carrier density, n, and hence the drive current density, J, (where $J = I/A$) of LEDs. The efficiency of light emitting diodes is discussed in more depth toward the end of the chapter in the context of both LED design and the so called "efficiency droop".

Defect luminescence

A large number of native and added impurities exist in the III-Nitrides, many of which act as luminescence centres. Since LEDs are doped both n-type and p-type, recombination to and from both acceptor and donor levels can occur. A comprehensive review of point defect related luminescence in GaN can by found in

[47] by Reshchikov and Morkoc and so a few of the most important luminescence bands and their origin are discussed now. A typical spectrum from Si doped GaN is shown in figure 2.2 which highlights several luminescence bands. The largest is the band edge peak at around 3.42 eV caused by exciton recombination across the fundamental bandgap.

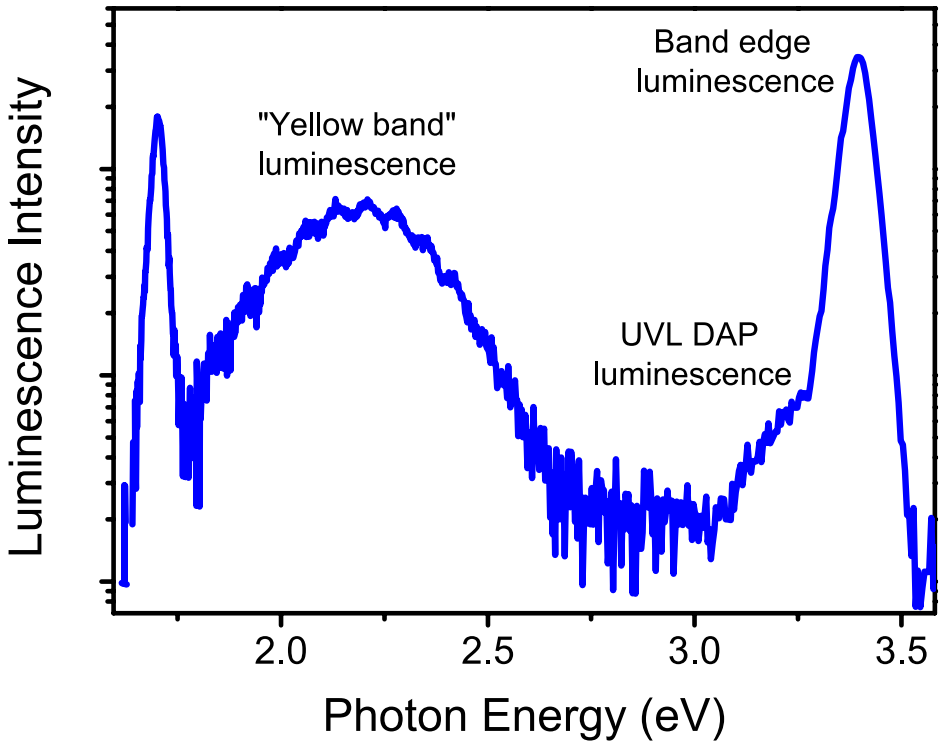

Figure 2.2: *Luminescence spectrum, at 295 K, of GaN showing the near band-edge at around 3.45 eV and the so called "yellow band" defect luminescence between 1.7 eV and 2.7 eV. The additional peak at 1.5 eV is the optical second order peak of 3.45 eV.*

Silicon and magnesium are used as the n-type and p-type dopants in GaN based devices. Silicon, in the concentrations used ($10^{19} cm^{-3}$) creates a level in the gap with an activation energy of around 30 meV [48], making it a very shallow donor. Magnesium has a significantly larger activation energy of about 200 meV [49], as evidenced by the difficulty in creating p-type GaN with low resistivity. Donor/acceptor pair (DAP) recombination is shown on the far left of figure 2.1. In GaN a so called blue peak at around 2.9 eV to 3.2 eV is attributed to shallow

DAP luminescence and is shown in figure 2.2. The most commonly observed defect related luminescence is the so called yellow band luminescence (YL) (the large broad peak seen in fig 2.2 at around 2.2 eV). It is typically observed in GaN:Si and is attributed to recombination between a shallow donor and a deep acceptor with an activation energy of around 0.8 eV [47]. The nature of the peak is still debated and while such a debate is not of great significance in this thesis it is important to mention that an increase in a variety of defect centres will increase the intensity of the YL.

A crucially important influence upon the recombination rate is the whether or not the semiconductor has a direct or indirect bandgap at the Brillouin zone centre. Momentum must be conserved, as always, in the electron/hole interaction, so recombination which produces a photon (which has negligible momentum) requires that the electron/hole pair must have the same wavenumber, k. Figure 2.3 demonstrates the case of a direct (a) and indirect (b) bandgap semiconductor. In (b) momentum must be exchanged with the crystal in order for the recombination to occur, this is mediated by phonons (vibrations of the bonds in the lattice) and consequently the process is less likely than in direct bandgap semiconductors.

Table 2.2 lists the absorption coefficients, bimolecular recombination coefficients and spontaneous lifetimes for several direct and indirect semiconductors. A difference of 3-4 orders of magnitude for B demonstrates the importance of the light emitter being a direct material at the bandgap. The $Ga_xIn_yAl_{1-x-y}N$ material system, regardless of alloy composition (and hence bandgap) is a direct material across the entire visible spectral range.

Material	α (cm^-1)	$\tau(s)$	B (cm^3s^-1)
GaAs (direct)	2×10^4	5.1×10^{-9}	2.0×10^{-10}
GaN (direct)	2×10^5	4.5×10^{-9}	2.2×10^{-10}
Si (Indirect)	1×10^3	3.0×10^{-5}	3.2×10^{-14}
Ge (Indirect)	1×10^3	3.5×10^{-6}	2.8×10^{-13}

Table 2.1: *Table of the spontaneous lifetime, bimolecular recombination coefficient and absorption at the band gap energy for two direct and two indirect semiconductors. Adapted from [50]*

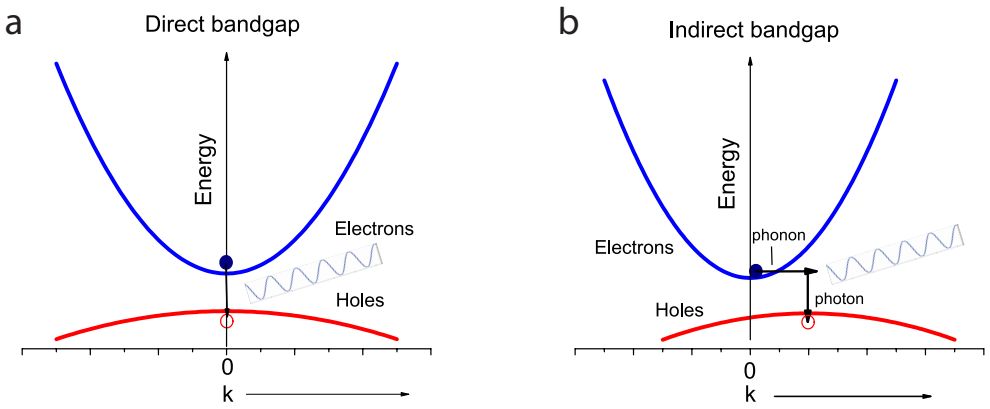

Figure 2.3: *E vs. k dispersion relation for direct (a) and indirect (b) bandgap semiconductors.*

2.3 The III-Nitrides

The III-Nitride material system is ideal for the creation of optoelectronic devices intended to operate across the visible spectrum and into the infra-red and ultra-violet. This is due to the wide band gap tunability made possible by alloying GaN, InN and AlN. The bandgaps and lattice constants are shown in the table below and in figure 2.4

Material	E_g (eV)	in plane lattice constant($\AA$)	lattice mismatch to GaN
InN	0.7	3.54	+10.6%
GaN	3.42	3.189	–
AlN	6.2	3.112	-2.4%
Al_2O_3		4.758	-16 %

Table 2.2: *Band gap, in-plane, a, lattice constant for the three III-N binaries and sapphire along with the relative lattice mismatch to GaN. Values are taken from Ambacher [51]*

Gallium nitride, aluminium nitride and indium nitride have principal band gaps of, respectively, 3.42 eV, 6.2 eV [51] and 0.7 eV [52]. Alloying GaN with InN or AlN produces ternary materials with an intermediate bandgap which is found by a linear interpolation between the bandgaps of the two binaries [53]. This is somewhat complicated by the effect of the change in strain state of the material from binary to ternary. This is reflected in the so-called bowing parameter b

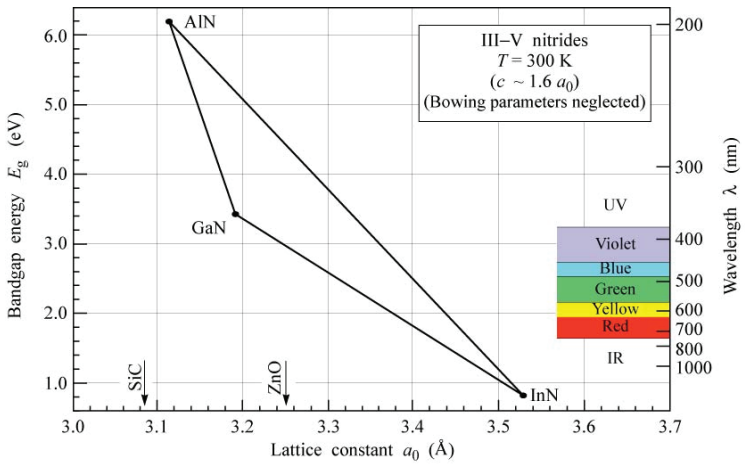

Figure 2.4: *Bandgap energy vs. the in-plane lattice constant (a) for the Al/Ga/In-N material system. From Schubert, chapter 12 [50]*

which appears in the quadratic in the below equation.

$$E_{g(In_xGa_{1-x}N)} = xE_{InN} + (1-x)E_{GaN} - b.x(1-x) \tag{2.9}$$

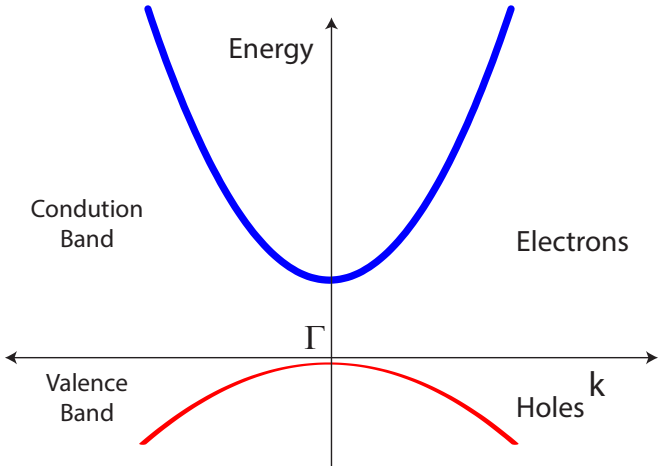

Figure 2.5: *Simplified dispersion relation for GaN at the Γ point showing the splitting of the valence band into the 3 hole effective masses. Adapted from Morkoc [38]*

.

where E_{InN} and E_{GaN} are the bandgap of InN and GaN, "x" is the relative composition of InN in the alloy (between 0 and 1) and, in the quadratic part,

b is the bowing parameter. Due to the difference in bandgaps, it is possible to manufacture potential dips or wells in the band structure of semiconductor devices by growing, for example, a layer of InGaN between two layers of GaN. If the InGaN layer is thin enough (<10 nm) it is possible to realise a physical version of the classic quantum mechanical problem of the particle in a well. In these quantum wells (QW), the electrons/holes are confined spatially and their energies are quantized. Quantum wells have dual uses in the design of LEDs and other optoelectronic devices; by phonon scattering carriers in the depletion region drop into the well and are no longer free to diffuse along the growth axis. This prevents carrier escape from the active region. Once captured the electron and hole wavefunctions will have an increased spatial overlap and so the recombination lifetime decreases. This greatly improves the luminescence efficiency of the LED. Quantum wells are typically used in multiples (MQW) in order to increase the overall volume of the desired optically active material. Commercial LEDs commonly use 5-10 period MQW structures. It should be noted that earlier devices used the so called double heterostructure (DH) design, which is essentially a single well of a size large enough where quantization is not a factor. This structure contains the carriers within the depletion region, but does not provide the greatly increased wavefunction overlap of the quantum well. However, the DH design has been argued to mitigate some of the problems of the high carrier densities caused by QWs, mainly non-radiative Auger recombination [54]. Despite this MQW based devices are now almost universally the choice of academia and industry alike.

A large issue with the III-Nitride system is the lack of availability of suitable substrates on which to grow the bulk material. A discussion on the growth methods of GaN is left to the next chapter, but suffice to say that native substrates - those with similar lattice parameters and crystal structure are not readily available. GaN melts at over 2,400°C and >6 GPa [55] and so growth from a stoichiometric melt (like silicon) is not feasible. The growth of GaN for LEDs takes place predominately on sapphire (Al_2O_3) and to an increasing extent silicon. As shown in table 2.2 there is an approximate 16% mismatch between GaN and sapphire. This results in the generation of a large density of crystal defects in the GaN, which are the result the GaN lattice attempted to match that of the sapphire. Many techniques have been developed to suppress the generation of

dislocations and defects within the GaN films during growth. These include the use of nucleation layers of low temperature AlN or GaN [24, 25, 26] (which is now the industry and academic standard), epitaxial lateral overgrowth (ELOG) [56] or other 3 dimensional growth modes of GaN. More details are can be found in [57] and the above references, but the salient point is that, despite these attempts, GaN based templates used for light emitting diode growth, typically have a large threading defect density of around 10^8 cm^{-2} to 10^9 cm^{-2} . Gallium nitride LEDs are remarkably tolerant of such high defect densities. In "conventional" III-V material (based on GaAs or GaP for example) such densities would render devices inefficient [58, 59]. Some of the reasons for this are discussed in the section at the end of the chapter on LED efficiency.

As stated previously, GaN is a direct bandgap semiconductor, but the diagram in figure 2.3 (a) is a simplistic picture. The effects of the crystal field and spin-orbit coupling in the wurtzite structure results in splitting of the valance band into 3 distinct bands - heavy hole (HH), light hole (LH) and split-off band. This is shown in figure 2.5. With the parabolic approximation, the dispersion relation is described by:

$$E_e(k) = E_C + \frac{p^2}{2m_e} = E_C + \frac{\hbar^2\mathbf{k}^2}{2m_e} \tag{2.10}$$

$$E_h(k) = E_V - \frac{p^2}{2m_h} = E_V - \frac{\hbar^2\mathbf{k}^2}{2m_h} \tag{2.11}$$

$$\tag{2.12}$$

where $\mathbf{k}$ is the wave-number, $E_{C/V}$ the conduction band and valence band energies and $m_{e/h}$ is the effective mass of the electrons in the conduction band and holes in the valence band. The curvature of the dispersion describes the size of the carrier mass; lower curvature is a higher effective mass. At 300 K, the masses of the carriers are m_e=0.2m_0, m_{HH}=1.4m_0, m_{LH}=0.3m_0 and m_{SH}=0.6m_0, where m_0 is the free electron mass. These values are taken from Morkoc [38]. Since the light hole and heavy hole bands are nearly degenerate an average for the hole effective mass is often quoted as 0.8m_0.

The group III-Nitride system differs from the other III-Vs (like GaAs, GaP) principally by virtue of its different crystal structure. The coordination geometry

of both GaAs and GaN is tetragonal, meaning that each cation has 4 anions as nearest neighbours and vice versa. The principal difference is that the III-Nitrides have a hexagonal symmetry and crystallize in the Wurtzite structure, as shown in figure 2.6 (a).

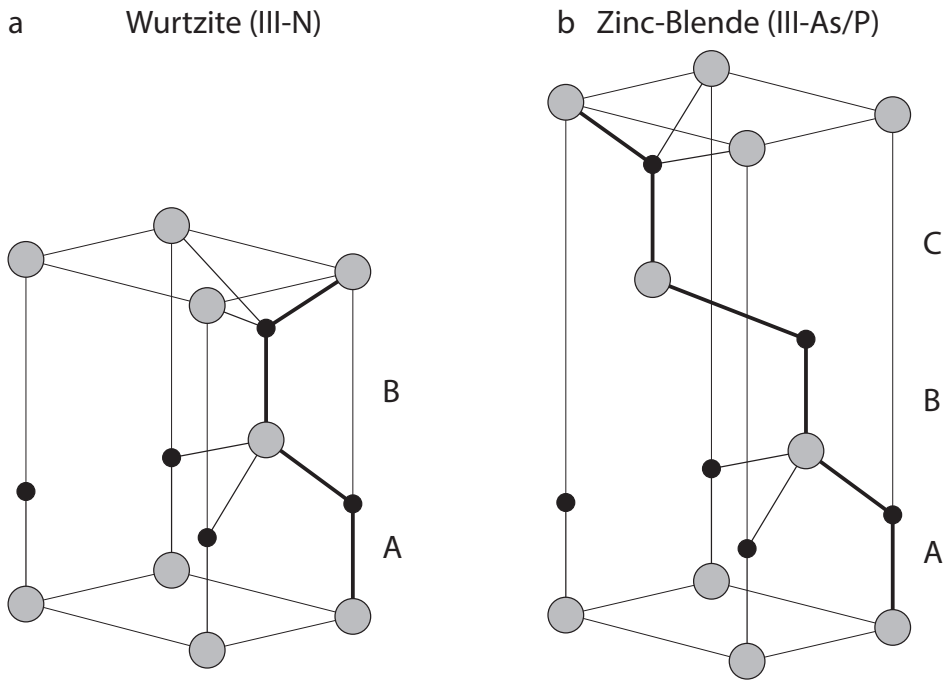

Figure 2.6: *Unit cell of a binary compound crystallized in the Wurtzite (a) and Zinc-Blende (b) configurations. Adapted from Morkoc [38]*

Most other III-Vs crystallize, however, with cubic symmetry, in the Zinc-Blende conformation as shown in fig 2.6 (b). The stacking sequence for Wurtzite is ABABAB, whereas Cubic is ABCABCABC, as annotated on the diagrams. The defining difference in the case of the Wurtzite structure is the lack of inversion symmetry - that is the unit cell cannot be reflected onto itself along the *c*-plane. Figure 2.7 shows the conventional hexagonal cell of the binary Wurtzite structure, indicating the two lattice constants (a and c), the cation/anion distance, u, and the most important polar (c) and non-polar (m) planes. The a and c parameters are, respectively, the basal and axial lattice parameter. In an ideal Wurtzite structure, where the atoms are considered as solid, touching spheres, the ratio of the two, $c/a = \sqrt{8/3} = 1.633$ and the shortest distance along one anion/cation

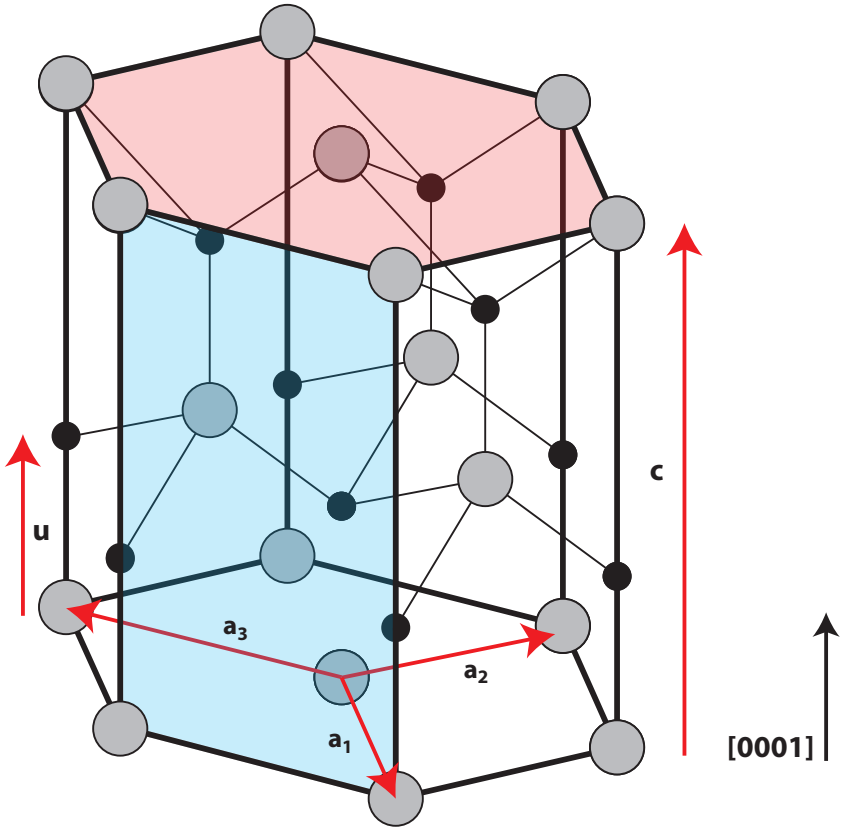

Figure 2.7: *The conventional cell of the Wurtzite crystal structure showing the hexagonal symmetry, the polar basal, c, plane (0001), the non-polar, m, plane (1$\bar{1}$00) and the a and c lattice parameter definitions. The conventional cell is extrapolated from the unit cell in figure 2.6 (a).*

bond in the c direction, u, is 0.375. When c/a and u are not equal to the ideal values, it leads to the creation of a non-zero polarization in the crystal. This can exist both spontaneously, i.e. in the crystal in its natural unperturbed states, and as a result of strain induced changes in the bond length. In GaN, InN and AlN, both these effects exist and they are now discussed. The u and c/a values for unperturbed Al/Ga/InN are given in table 2.3.

Binary	a	c/a	u
InN	3.54	1.612	0.377
GaN	3.189	1.627	0.376
AlN	3.112	1.601	0.38

Table 2.3: *Tabulation of the lattice parameters for the III-N wurtzite crystals. Values taken from Ambacher[60]. In an ideal wurtzite structure the c/a ratio and u are* $\sqrt{8/3}$*=1.633 and 0.375*

2.3.1 Polarization

Spontaneous polarization

The principal effect of the inversion asymmetry for devices is the occurrence of spontaneous polarisation in the crystal. Two effects are required in order that spontaneous polarisation occurs. Firstly, there must exist some non vanishing dipole with the tetrahedral basis of the crystal, and secondly that this dipole is not cancelled out via symmetry in the crystal. The first is demonstrated in figure 2.8 (a) which shows the tetragonal basis unit of GaN (or in principle AlN, InN or any of the ternary and quaternary III-N compounds). The dipole between the central metal atom and each Nitrogen occurs due to the difference in electronegativity. The electron field is in the direction of the positive ion (metal) to the negative (nitrogen) and, by convention the polarisation vector, $\mathbf{P}$ is in the opposite direction. The basal plane contributions of the polarisation $\mathbf{P}_{ax}$, $\mathbf{P}_{bx}$ and $\mathbf{P}_{cx}$ cancel. However the bond length in the c direction is elongated, with respect to an ideal tetrahedral structure [61] and so the parallel contribution does not vanish leaving a net polarisation from the nitrogen to the metal ion. The noncentrosymmetric nature of the Wurzite structure is demonstrated by considering the common view of the crystal as being composed of stacks of hexagonal bilayers. This is shown in 2.8 (b). The charge distribution in each metal/nitrogen bilayer is not compensated by any symmetry and this results in an overall polarisation in the $(000\bar{1})$ direction.

Piezoelectric polarization

Spontaneously polarisable crystals are known as pyroelectric (changes in temperature causes shifts in polarisation). They are a sub class of the piezoelectric

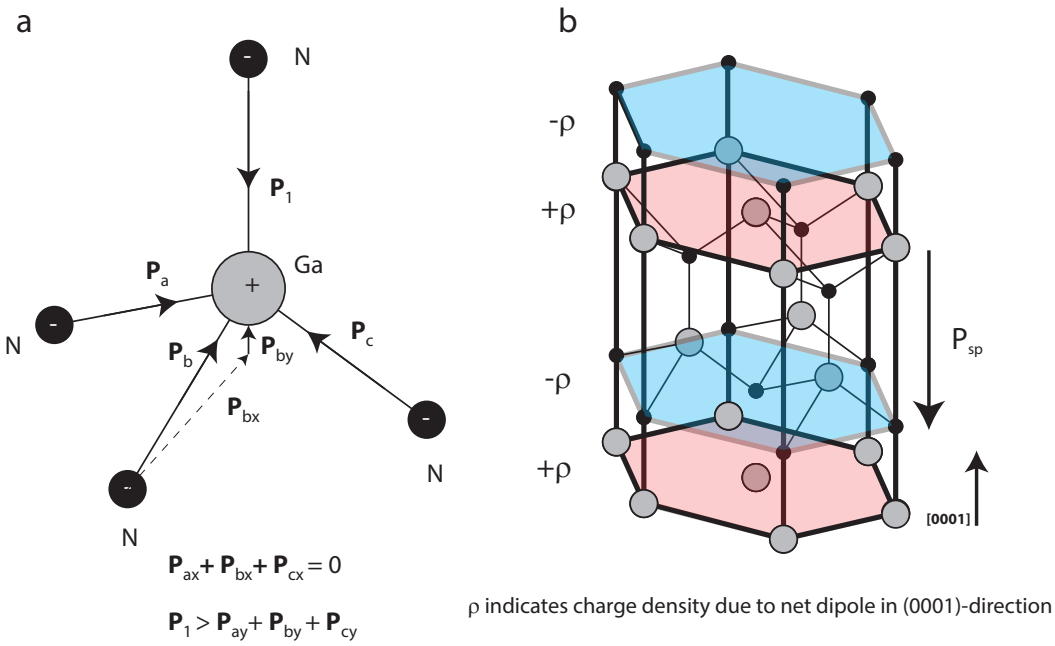

Figure 2.8: *(a) The tetragonal basis of the GaN and (b) the bilayer structure of the Wurtzite indicating the origin of the spontaneous polarisation present in the III-Nitrides*

crystal. In general, under external strain the crystal will deform, bond lengths and angles will be altered and the resultant change in the dipole configurations and sizes changes the polarisation state. Sources of strain in semiconductor crystals can come in several forms. The most intrinsic is thermally induced strain, whereby if the material is heated isotropically it will attempt to expand along each axis. Temperature is introduced during material growth, and it is also the case that the crystal is rarely free to move in any direction, typically just in the growth direction. In GaN LEDs, strain can occur at interfaces where a material with one lattice constant is grown pseudomorphically on another, whereby the second material adopts the "a" lattice constant of the material upon which it is grown. In quantum well growth, the InGaN which is grown on top of the GaN is under compressive strain, since the "a" lattice constant of InGaN (of any composition) is larger than GaN and the crystal is forced to contract in the basal plane to align with the GaN spacing.

Binary	P_{sp}	e_{33}	e_{13}	a	c/a	u
InN	-0.032	0.97	-0.57	3.54	1.612	0.377
GaN	-0.029	0.73	-0.49	3.189	1.627	0.376
AlN	-0.081	1.46	-0.60	3.112	1.601	0.38

Table 2.4: *Tabulation of the key physical and electrostatic parameters of the main III-Nitride binaries. From Bernardini and Fiorentini [62] and [60] In an ideal wurtzite structure the c/a ratio and u are* $\sqrt{8/3}$*=1.633 and 0.375*

The piezoelectric polarisation is related to the change in a and c lattice constants via the components of the strain tensor (e_{ij}) as [62]:

$$P_{PZ} = e_{13}(\epsilon_x + \epsilon_y) + e_{33}\epsilon_z \tag{2.13}$$

$$= 2e_{13}\frac{a_s - a_l}{a_l} + e_{33}\frac{c_s - c_l}{c_l} \tag{2.14}$$

where e_{13} and e_{13} are the in plane and c-axis piezoelectric constants, respectively, and $\epsilon_{x,y,z}$ is the strain in the x, y and z directions where, due to symmetry, $\epsilon_x = \epsilon_y$. a_s/a_l and c_s/c_l are the lattice parameters of the substrate (GaN) and the strained layer (in this case InGaN).

Due to the geometry of the growth, the crystal is free to deform in the c-axis. The strain in the c-axis can be related to the strain in the in-plane axes via the in plane and axial elastic constants, C_{13} and C_{33}, via:

$$\epsilon_z = -\frac{C_{13}}{C_{33}}(\epsilon_x + \epsilon_y) \tag{2.15}$$

By substitution of equation 2.15 into 2.13, the piezoelectric polarization can then be rewritten in terms of the a lattice constant as:

$$P_{PZ} = 2\frac{a_s - a_l}{a_l}(e_{13} - e_{33}\frac{C_{13}}{C_{33}}) \tag{2.16}$$

When InGaN is grown on GaN the strain is compressive, so the first term (including the e_{13} in the bracket), is negative. As a result, P_{PZ} is negative and so, as in the convention referred to in figure 2.8, the piezoelectric polarization points toward the surface - which is opposite to the spontaneous polarization vector, P_{sp}

2.3.2 The Quantum Confined Stark Effect

The polarisation induced in InGaN films when grown on relaxed GaN layers is of obvious significance to light emitting diodes.

The effect of the combination of the spontaneous and piezoelectric polarization in an InGaN quantum well, grown on GaN barriers is shown in figure 2.9(a). In the relaxed GaN layers, only the spontaneous polarization is present, while in the InGaN the far larger piezoelectric polarisation dominates. As a result there is an abrupt electrostatic difference at the interface of the two layers. In general a polarization gradient will produce a charge density described by:

$$\sigma = \frac{dP_T}{dz} \tag{2.17}$$

where P_T is the total polarisation, composed of the piezoelectric and spontaneous contributions. In this case, due to the abrupt interface a sheet charge will be produced, with a density described by the difference in polarisation at both sides of the interface:

$$\sigma = \Delta P_T = P_T(InGaN) - P_T(GaN) \tag{2.18}$$

$$= P_{SP}(InGaN) + P_{PZ}(InGaN) - P_{SP}(GaN) \tag{2.19}$$

The spontaneous polarization is similar in the GaN and InGaN, as shown in table 2.4, and they are both significantly smaller than the P_{PZ}. As a result the electric sheet charge is predominantly caused by the piezoelectric polarisation alone.

For $In_xGa_{1-x}N$ the size of P_{PZ} has been found, for an Indium content of 15%, to be from 1 MeV [63] to 2.5 MeV[64] and typically accepted to be around 2 MeV [65, 66, 67]. These results are well predicted by the linear model of Hangleiter et al [68], where the field is calculated based on a Vegard-like interpolation. The field, F, is related to the piezoelectric coefficients and elastic constants of InN and GaN, σ_{InN} and σ_{GaN} and to the composition dependent strain, $\epsilon(x_{In})$:

$$F(In_x) = [\sigma_{GaN}(1-x) + \sigma_{InN}x]\epsilon(x_{In}) \tag{2.20}$$

The effect of the induced electric field across the quantum well is shown in

figure 2.9(b). The electron and hole wavefunctions separate across the width of the quantum well and due to the triangular shaped potential they occupy lower energy states. The effect is to reduce both the wavefunction overlap and the optical transition energy which redshifts any emission.

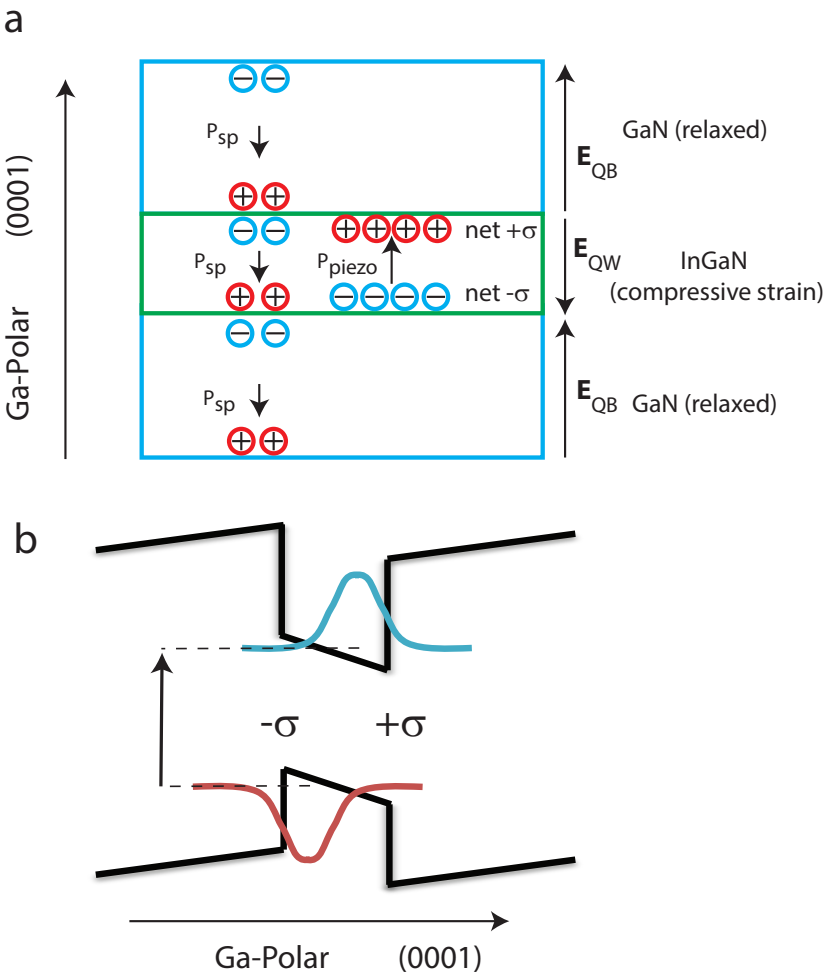

Figure 2.9: *(a) Schematic of the spontaneous and piezoelectric induced polarization directions, and resultant electric field in a single InGaN quantum well between two GaN barriers. The InGaN is compressively strained and the GaN layers are taken to be relaxed. The effect of the field upon the electron and hole wavefunctions in the quantum well is shown in (b). Adapted from [60]*

The effect is shown in more detail in figure 2.10 which shows a finite quantum well both without (a) and with (b) the influence of the QCSE.

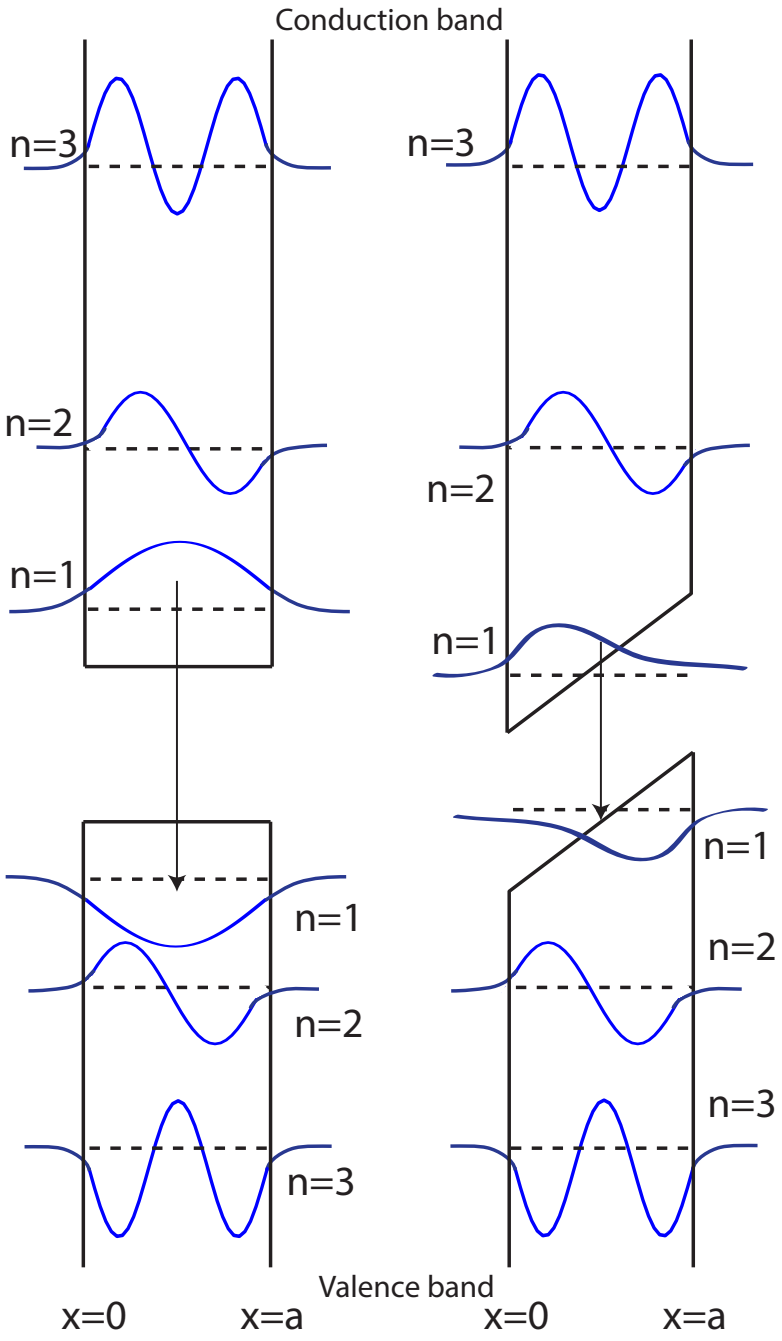

Figure 2.10: *Energy levels in the conduction band and valence band for finite quantum wells without (a) and with (b) the impact of the QCSE. Note that energy levels in the valence band are closer together due to the larger hole effective mass. Adapted from Ryou et al [69]*

Confinement of the carriers on the scale of the InGaN layers (typically 2-4 nm) leads to quantisation of the electron/hole wavefunctions. The wavefunction in one dimension, ψ(x) is described by the time independent Schroedinger equation:

$$\frac{\partial^2\psi(x)}{\partial x^2} + \frac{2m_{e/h}}{\hbar^2}(E - eFx)\psi(x) = 0 \tag{2.21}$$

where E is the particle energy, $\hbar$ is the reduced Planck constant, $m_{e/h}$ the electron or hole effective mass and eFx describes the presence of a uniform static field, such as the piezoelectric induced charge produces. With an infinite flat well, the solution produces the well known eigenstates and associated energy eigenvalues:

$$\psi(x) = A_n sin\left(\frac{n\pi x}{a}\right) \quad \text{and} \quad E = \frac{\hbar^2 n^2 \pi^2}{2m_e a^2} \tag{2.22}$$

The case of a finite well without an applied field is shown in figure 2.10 (a). In this case the boundary conditions result in the wavefunction decaying exponentially outside the wells.

The effect of the polarization induced electric field is considered acting upon an infinite quantum well. The sketch in figure 2.10 (b) is shown with a finite well to give a more realistic picture. The following argument is based on that found on pages 114-116 of [70]. Equation 2.21 can be expressed in the form:

$$\frac{\partial^2\psi(x)}{\partial x^2} - \psi(x) = 0 \tag{2.23}$$

Using Airy functions and a variational or perturbation method [70] leads to the following expression for the energy of the ground state:

$$E(F) = E(0) - 2 \times 10^{-3}\frac{m_{e/h}e^2F^2a^4}{\hbar^2}(eV) \tag{2.24}$$

where E(0) is the zero field energy (eqn 2.22). The induced piezoelectric field reduces the transition energy between the 1st energy levels in the conduction and valence band. It is of note that higher excited states (n=2 etc.) are less effected by the electric field [70, 71]. The overlap reduction can be seen in the diagram in figure 2.10. The wavefuction in the ground state is compressed into the triangular part of the well and as a result the electron/hole overlap integral is reduced. The QCSE is detrimental to LED efficiency because the reduction

in wavefunction overlap results in a lower radiative recombination rate. Since the effect is caused by the electric field across the well, any change in the overall electronic state of the device can mitigate or exacerbate the effect. The operation of light-emitting diodes necessitates the addition of an external electric field. LEDs are now discussed, including the basic operation, the effect of the electric fields and some of the specifics of GaN based LED design.

2.4 Light-emitting diodes

The fundamental component of modern LEDs (and practically all solid state electronics) is the p/n junction - a structure which takes advantage of one of the unique characteristics of semiconductors (as opposed to metals): current can be mediated by both electrons and holes.

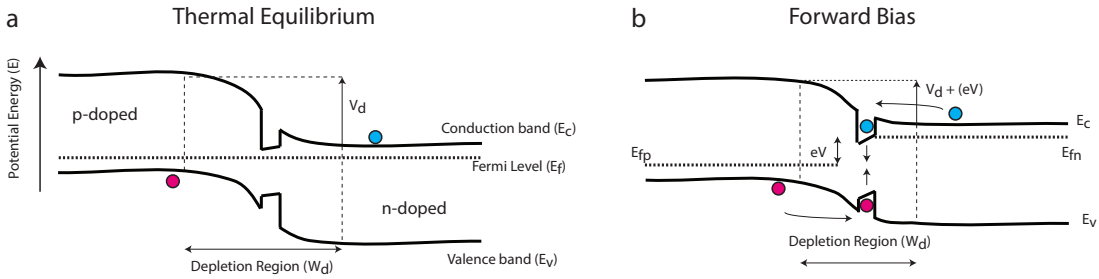

Figure 2.11: *Schematic of the band structure of a p/n heterojunction or SQW LED at thermal equilibrium (a) and under forward bias (b). In (a) diffusion from the p and n type GaN is retarded due to the potential barrier. In (b) carriers diffuse into the depletion region, are captured by the well and recombine.*

Figure 2.11 demonstrates the electronic band structure of symmetrical *p/n* heterojunction. This is similar to the band structure of an LED with a single quantum well (SQW) LED. In a homojunction, where only one semiconductor material is present, an interface exists in the material where on one side the semiconductor is *p*-doped and the other side it is *n*-doped. Diffusion of electrons/holes to the *p/n*-type sides exposes charged ions on each side, acting to counter further diffusion and creating the depletion region, with width (W_d). The diffusion potential created, V_d is proportional to the concentration of donors and accep-

tors dopants, N_D and N_A, the intrinsic carrier concentration, n_i and the junction temperature:

$$V_d = \frac{kT}{e}\left(\frac{N_A N_D}{n_i^2}\right) \tag{2.25}$$

The width of the depletion region is related to the diffusion potential and the dopant concentrations by:

$$W_d = \sqrt{\frac{2\epsilon}{e}(V_d - V)\left(\frac{1}{N_A} + \frac{1}{N_D}\right)} \tag{2.26}$$

where V is the bias applied to the diode, and ϵ the dielectric permittivity. When a forward bias is applied across the LED (fig 2.11 (b)) the depletion region shrinks, carriers are injected into the active region and can recombine. The relationship between diode applied voltage and current is an exponential and is given by the Shockley equation:

$$I = eA(\sqrt{\frac{D_p}{\tau_p}}N_A + \sqrt{\frac{D_n}{\tau_n}}N_D)(e^{e(V-V_D)/kT} - 1) \tag{2.27}$$

where A is the cross sectional area of the device and $D_{p/n}$ and $\tau_{p/n}$ are the diffusion constants and minority carrier lifetimes of the holes and electrons respectively. The diode current will be equal to the so called saturation current when the exponential term approaches zero i.e. under a large reverse bias.

The I-V relation is shown graphically in figure 2.12 in which (a) is a linear plot and (b) a semi-log (y-axis) plot.

Electroluminescence

If a sufficient forward bias is applied to overcome the diffusion potential, the Fermi levels on either side of the interface will split and electrons and holes will diffuse into the depletion region (which, as a result will decrease in size), as shown in figure 2.11 (b). Recombination between carriers can then occur via emission of a photon; electroluminescence. However carriers recombining in this fashion are affected by their characteristic diffusions lengths, L_n and L_p. In GaN the electron diffusion length in the bulk is >100 nm and this is larger than the typical size of the depletion region in an InGaN LED. The existence of the

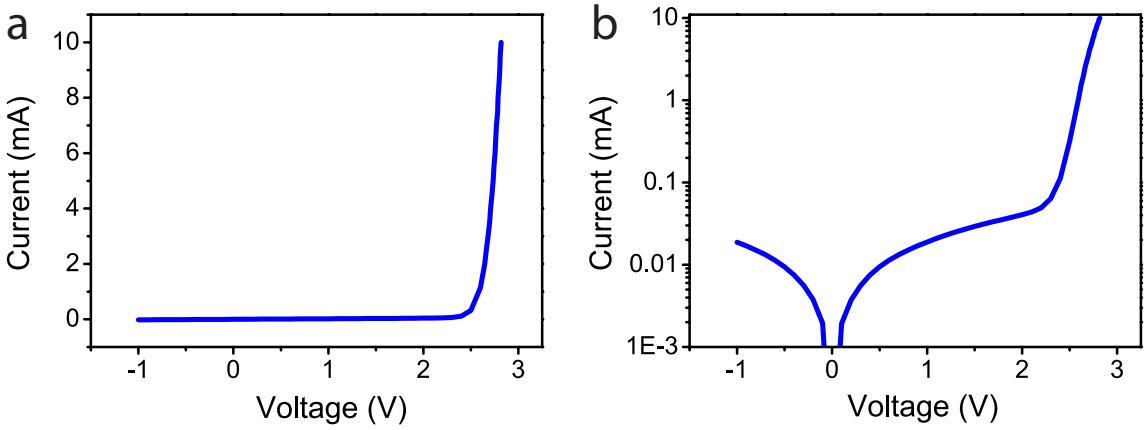

Figure 2.12: *Typical I-V curve for a blue InGaN LED (a) is a linear and (b) is a semi-log plot.*

quantum wells confines the carrier and, as described above, increases the overlap of the electron/hole wavefunctions, thereby increasing the recombination rate.

2.4.1 LED design

A description of the actual means and methods of LED growth and processing is contained within the subsequent chapter, so this section is intended to cover the physical properties of the particular layers which are often grown in InGaN LEDs for the purposes of optimising device performance.

Electron Blocking layers

Poor electron capture caused by overshoot or escape from the active region has been postulated as a cause for reduced device efficiency [72, 73, 74]. Electrons enter the active region with kinetic energy due to the applied bias and potential energy due to any energy discontinuity in the bandgaps of the n-type conduction band and quantum wells. This must be lost via phonon interactions in order to be captured by the wells. If the transit time across the depletion region is shorter than the recombination time, the electron may escape into the *p*-GaN where it is lost for the purposes of useful light emission. AlGaN electron blocking layers (EBL) are commonly grown above the last quantum barrier so to prevent this.

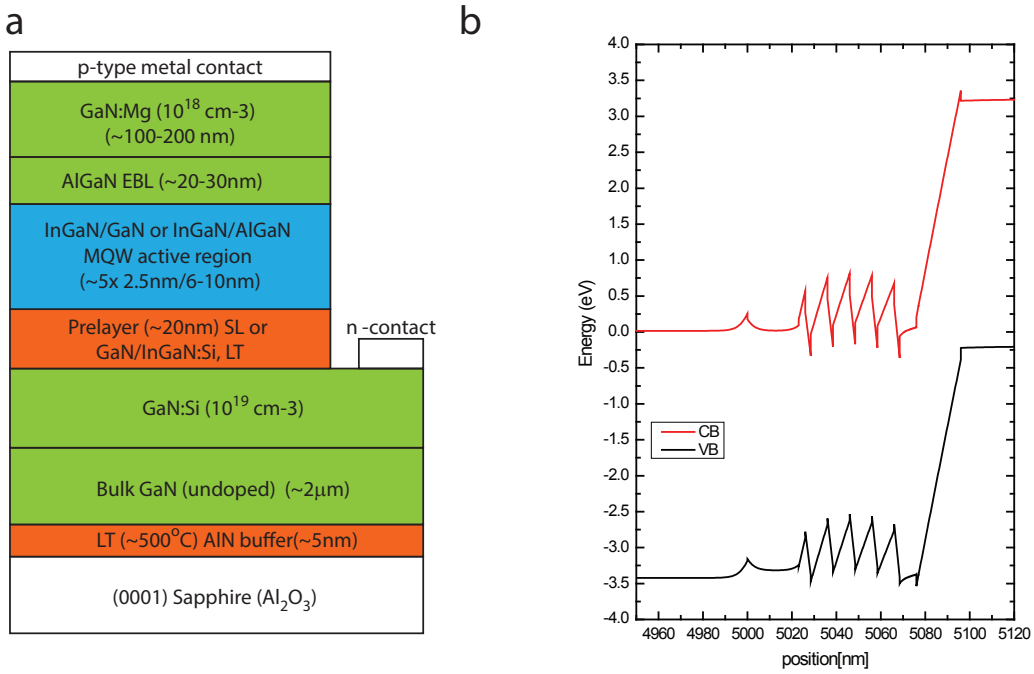

Figure 2.13: *(a) A simple physical schematic of a mesa etched LED, with both an underlayer and electron blocking layer. The plot in (b) displays the band structure (E vs. growth direction) for a similar LED.*

AlGaN has a wider bandgap, which provides a potential barrier to both electrons and hole. Undoped, this results in an unwanted barrier to holes which already have poorer injection due to their higher effective mass. As a result the AlGaN EBLs are doped *p*-type which raises the barrier height into the conduction band relative to the active region conduction band. Polar devices, where the piezoelectric induced fields exist, may present a problem for the effective operation of EBL. It has been reported that the interface between the GaN barriers/AlGaN/p-GaN results in both a reduced barrier for electrons at high carrier density [75, 76] and creates notches in the valence band around the EBL which traps holes and prevents their distribution in the quantum wells [77, 72]. Using quaternary alloys (AlInGaN) as EBLs to replace the conventional AlGaN has been suggested to eliminate this effect due to the possibility to polarization match using composition control [78]. The difficulty of epitaxy for such a layer however, means that AlGaN layers, around 25 nm, are still industry standard.

Underlayers

The role of underlayers, or pre-layers, is both broader and somewhat more disputed than that of electron blocking layers. Underlayers are those grown before the active region (as shown in figure 2.13 (a)) and can take the form of single layers, typically doped, or super-lattices (SL). Those underlayers which appear in devices studied in this thesis consist of single layers of Si doped GaN or InGaN. It has been reported by several groups [79, 80, 81, 82] that the band structure and electric field in the active region is significantly altered by the presence of another interface where polarization mismatch causes charge accumulation. Doped underlayers will be discussed in more detail in the chapter which contains a study of devices containing an underlayer.

LED efficiency

.

The usefulness of light emitting devices is primarily characterised via their radiant efficiency. A key measure of this is called the external quantum efficiency (EQE) and measures the ratio of the number of photons which emerge from the LED to the number of electrons which are pumped into the device. The wall plug efficiency include all stages of the conversion of electricity from the mains socket to photons emitting into free space. State of the art devices are reported to have EQEs and full wall plug efficiencies of up to 80 % and 65% respectively [83]. The EQE ($\eta_{external}$) is broken down into the injection efficiency ($\eta_{injection}$), internal quantum efficiency ($\eta_{internal}$), and the light extraction efficiency ($\eta_{extraction}$) as in equation 2.28.

$$\eta_{external} = \eta_{injection}\eta_{internal}\eta_{extraction} \tag{2.28}$$

The extraction efficiency is the ratio of the number of MQW generated photons which escape to free space to the total number of photons generated within the active region. Losses come from a combination of absorption by the various layers in the LED structure and by re-absorption of the photons, due to total internal reflection at the air/semiconductor or other interfaces. Various methods are used to improve the latter; surface roughening of the top layer which randomises the

incidence angle of escaping light [84, 85, 86, 87]. Photonic crystal structures are also grown both on the surface [88, 89, 90] or embedded within the LED structure below the active region [91, 92] to increase the coupling of the emitted photons to light emitting modes. This can either be done by reducing propagation in transverse modes (in the plane of the quantum wells), by controlling the photonic density of states to favour modes which escape or via diffraction. Improving the light extraction from processed and packaged dies is an area of significant study, as the extraction efficiency in a completely unoptimised LED wafer (smooth surfaces, planar geometry, no photonic structure or anti reflection coatings) can be as low as 4% [85]. A study of the effects of encapsulation of an LED die with a hemispherical epoxy is presented in the final section of chapter 5.

The injection efficiency can be defined as the ratio of those excess carriers which recombine in the active region (whether radiatively or non-radiatively) to the total which recombine anywhere in the material [93]. For example, if an electron overshoots the active region, as discussed above, and recombines in the p-GaN, that would be considered as reducing the injection efficiency.

Referring back the discussion at the start of the chapter, the internal quantum efficiency of the optically active region can be described (with the aforementioned provisos about simplicity) by the ABC model. It is sometimes the case that the internal quantum efficiency is treated as containing the injection efficiency, and an extra term is added to the ABC to account for losses due to carrier escape, as in Piprek [94]

$$\eta_{IQE} = \eta_{inj}\eta_{int} = \frac{\eta_{inj}Bn^2}{An + Bn^2 + Cn^3} \tag{2.29}$$

where η_{int} is the internal efficiency of the quantum wells and η_{IQE} describes the net internal quantum efficiency of the whole LED, minus extraction components.

To a first approximation, both the extraction and injection efficiencies are not direct functions of current density and so a common way to measure the performance of LEDs is to plot the light output/current vs. current density. This can be done on absolute scale, where one measures the total radiant output power in Watts (usually via an integrating sphere - see Chapter 3) or simply in relative terms, where the emitted light is measured in arbitrary units. As long as the collection efficiency of the optical system does not vary as a function of drive

current, both methods will yield similar information, namely the effect of carrier density on efficiency.

2.5 Efficiency droop

An unwanted characteristic of LEDs based on the III-N material system is that of the "efficiency droop"[94]. At higher drive current densities (typically 10—50 Acm^{-2}[41], although it can be as low as 1—10 Acm^{-2}) the efficiency of the devices reaches a maximum and starts to drop. This behaviour is independent of heating effects [95] and is not observed in LEDs based on the other III-V material systems (GaAs, InP etc.). A great deal of work has been done in the field to explain the root cause of the effect and although much progress has been made the question is still open. Excellent reviews of the fundamentals have been written Ozgur [96] and Piprek [94] Regardless of the cause, the effect which leads to the efficiency droop is a drop in the radiative recombination rate relative to the total non-radiative recombination rate with an increase in carrier density.

Currently the leading candidate for efficiency droop is Auger recombination, which is considered an intrinsic material property. As discussed in previous sections, the Auger process is inversely proportional to the bandgap and so direct band to band Auger is a small effect in wide band gap semiconductors like GaN [97, 39, 44]. However, studies of the processes involving phonon and impurity mediated Auger by the group of Chris Van De Walle [40] and earlier that of Hader and Moloney [44] showed that such interactions are able to produce "C" coefficients large enough to account for those observed experimentally in droop measurements. Direct observation of Auger electron emission, scaling with efficiency droop was first observed in 2013 [98]. This, and the observation of Auger induced hot carriers [99], have greatly supported the hypothesis that the Auger process is crucial in the efficiency droop. The most important device design related explanations are those of polarization field induced carrier loss or poor capture in the quantum wells [100, 78, 72].

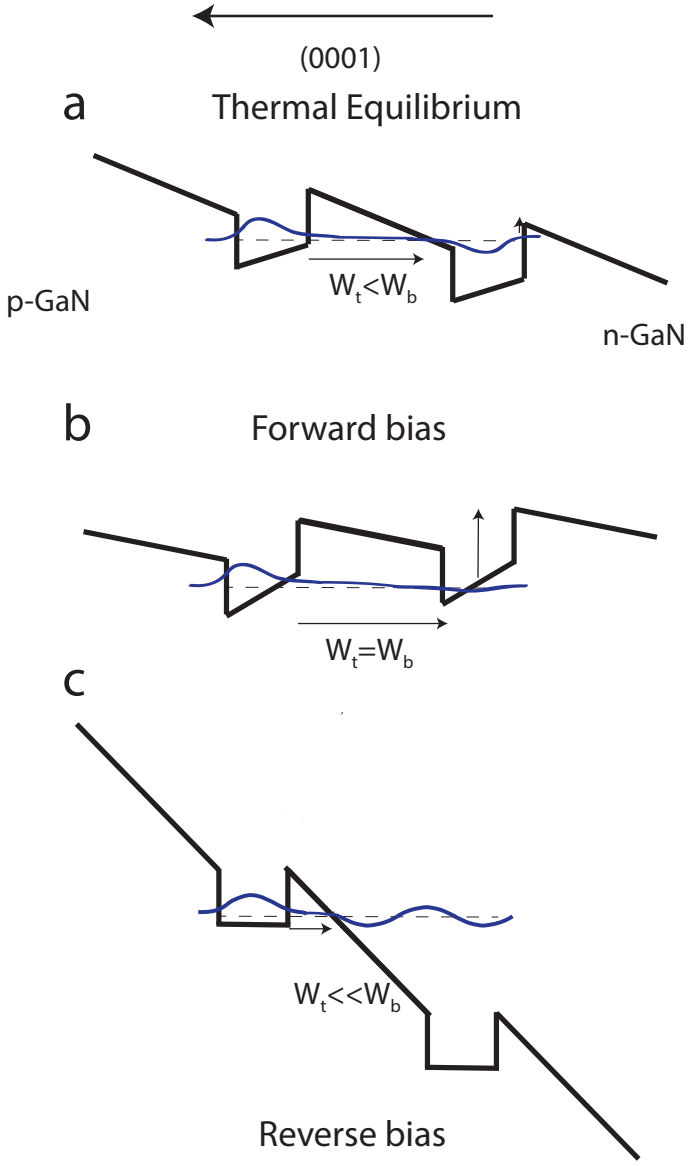

Figure 2.14: *Diagram of the carrier tunnelling through the QWs in the conduction band of an InGaN LED with 2 quantum wells. (a) Thermal equilibrium, (b) forward bias - QCSE increased and (c) reverse bias - QCSE compensated. W_b is the actual material barrier width and W_t is the effective barrier width for tunnelling. In the reverse bias case the electron wavefunction becomes a travelling wave in the quasi-free space above the QW.*

2.5.1 Electric field effects

The interaction of the applied electric field with the polarisation induced field has significance for both device operation and characteristics. To a great extent the effects on the LED behaviour and performance due to the interplay of the electric fields are left to the results chapters but a short introduction is presented here.

Strictly, is in inaccurate to talk about different electric fields in the device. Physically they are not distinct; at any given point in the structure the potential has a singular value which results from the net effect of any separately generated fields. However, due to the separate origins it is helpful to refer to them individually.

LEDs are typically grown by MOCVD in the Ga-polar orientation as the film quality is greater than N-polar surfaces. Furthermore, the devices are also grown p-type up to aid the annealing step of the magnesium dopant. As a result the in-built p/n junction field and piezoelectric induced field are in opposite directions. An applied forward bias opposes the built in field and is, therefore, in sympathy with the piezoelectric induced field. The field in the wells increases and the QCSE will be exacerbated. In contrast, an applied reverse bias will act to flatten the band at the bottom of the quantum wells.

However, this is not observed due to the most common mitigating effect upon the QCSE in devices, that of free charge screening [101]. As the forward bias increases, so does the current density, and large sheet carrier densities build up which have the opposing polarity of the induced field and hence tend to cancel it out. Experimentally, it is common to observe a blue shift of the emission line in polar InGaN/GaN LEDs, with increasing current due to this compensation of the piezoelectric induced fields as well a band filling of quantum states with higher energies.

The relationship between the externally applied bias and the piezoelectric field is shown in the diagrams in figure 2.14 which show the conduction of a 2 period MQW LED, with band bending incorporated, at thermal equilibrium (a), forward bias (b) and reverse bias (c).

Tunnelling

Electrons (or holes) confined within the quantum wells may be able to penetrate through the quantum barrier, if sufficiently thin, to an adjacent quantum well or to the quasi free space above the wells. The probability of this occurring is affected by the total electric field in the active region, which generates a triangular potential in the GaN reducing the effective barrier to tunnelling. This process is known as Fowler-Nordheim or field assisted tunnelling. The probability, T, through the barrier can be described using the Wentzel-Kramers-Brillouin (WKB) approximation [67]

$$T = exp\Big[-2\int_0^{W_t} k(z)\mathrm{d}z\Big] \tag{2.30}$$

where W_t is the effective width of the barrier, and $k(z)$ is the wavenumber. Within the barrier k is defined by:

$$k(z) = \sqrt{2m(V(z) - E)/\hbar} \tag{2.31}$$

where E is the energy of the bound state, m is the effective mass and $V(z)$ is the barrier potential which, in the case of triangular barriers is simply:

$$V(z) = V_b - eFz \tag{2.32}$$

where V_b is the potential of the barrier at z=0 and F is the applied electric field. Substituting equations 2.32 and 2.31 back into 2.30 yields the probability as:

$$T = exp\Big[\int_0^{W_t} \sqrt{\frac{2m}{\hbar^2}(V_b - eFz - E)}\mathrm{d}z\Big] \tag{2.33}$$

the width, W_t, is controlled by the size of the applied field, as can be seen in figure 2.14. With a large reverse bias, W is small, while under forward bias it is equal to the length of the barrier.

Finding the integral gives the expression for T as:

$$T = exp\Big[-\frac{4\sqrt{2m}}{3\hbar}\frac{(V_b - E)^{3/2}}{eF}\Big] \tag{2.34}$$

The tunnelling current J_T therefore relates to the barrier height and electric field in the depletion region as $J_T \propto exp(-E^{3/2}/F)$

The other route of electron/hole escape from the quantum wells is thermionic emission [102, 103, 104, 105]. At non-zero temperatures carriers can hop out of the quantum wells by semi-classical means. The thermionic current from well to barrier is governed by temperature and Boltzmann type distribution of carriers with energies up to the effective barrier height i.e.:

$$J_{Therm} \propto \frac{(kT)^2}{\hbar^3}.exp\left(-\frac{E_b - E_{QF}}{kT}\right) \tag{2.35}$$

Where E_b is the energy of a carrier at the barrier height, E_{QF} is the energy of the quasi-Fermi level and the other terms have their usual meanings. Although temperature and the density of available quantum states are the key factors in determining the importance of thermionic emission, the electric field also has an effect, by virtue of how it will affect the barrier height E_b.

Carriers above the quantum wells are subject to drift, which may cause them to leave the active region. The drift current is proportional to the drift velocity (v_d), and hence the field in the depletion region; $J_D \propto v_d \propto F$

The relative importance of tunnelling, thermionic emission and drift as carrier loss mechanism is governed to a large degree by the excitation method and this is discussed in the subsequent chapters which describe the means and characteristics of electron hole pair generation.

The following chapter covers the experimental equipment and methods used as well as the basics of LED growth, fabrication and preparation for use in the experiments.

Chapter 3

Experimental Details

This chapter describes the various experimental techniques which were used to study the light-emitting diodes as well as an overview of how they were grown, fabricated and prepared for use. The principles of electron microscopy, spectroscopy and electron beam induced current (EBIC) are covered.

3.1 LED growth, fabrication and preparation

3.1.1 Material Growth

MOVPE

Metal Organic Vapour Phase Epitaxy (MOVPE) (also known as Metal Organic Chemical Vapour Deposition - MOCVD) is the industry standard means of growing thin film GaN-based LEDs. All the devices studied in this work were grown by MOVPE and the vast majority were grown at the University of Cambridge in a Thomas Swan close-coupled showerhead reactor, an image of which is shown in figure 3.1. At the heart of the MOVPE system is the reaction chamber. At the bottom of the chamber, the substrate sits on a hot plate which is heated, in the case of GaN growth, to around 1050 °C. Precursor materials, for the group III elements, are housed outside the chamber in liquid form in bubblers, in the cases of gallium and aluminium precursors, and in solid form for the indium precursor. A carrier gas, typically hydrogen or nitrogen is passed through bubblers and the precursors are transported, in the gas phase, to the reaction chamber. On the

roof of the chamber multiple inlet valves, which are opened and closed depending on the elements needed, allow the gases to enter. To grow gallium nitride and the other III-nitride materials, trimethlygallium, trimethlyindium, trimethylaluminium and ammonia (NH_3) are used to provide, respectively, gallium, indium, aluminium and nitrogen. The gases meet at the heated substrate surface and the thermal energy enables a chemical reaction to occur, which frees the gallium and nitrogen, and allows a thin layer of the resultant compound to be deposited on the surface. The chemical equation is as follows:

$$(CH_3)_3Ga/In/Al + NH_3 = Ga/In/AlN + (CH_4)_3 \tag{3.1}$$

Figure 3.1: *Image of the Thomas Swan CCS MOCVD reactor used at the University of Cambridge. The vast majority of devices studied in this work were grown by Dr Menno Kappers using this machine.*

The pioneering work in the MOVPE growth of GaN on sapphire, was performed by the group led by Akasaki at Nagoya University, in the mid to late 1980s [23, 27, 26]. A thorough review of the development and current state of the MOVPE growth of III-nitrides can be found in *Coordination Chemistry Reviews* by Watson [106].

Amano and Akasaki demonstrated that high quality thin film growth requires that a low temperature AlN (or GaN) buffer layer be deposited on the sapphire substrate which acts a nucleation surface for further GaN growth and as a block to dislocation propagation. Subsequent growth of GaN happens 3-dimensionally: GaN islands form, which then lead to trapezoidal growth and eventual coalescence of the various trapezoids into a smooth film, with a relatively low defect

density, growing in the c-direction. Nominally undoped GaN can then grown on top of this nucleation layer. In this work the combination of sapphire substrate, low temperature GaN nucleation layer and subsequent non-intentionally doped GaN layer was treated as the template upon with the active device was grown. The dislocation density of the best GaN on sapphire templates were around 4x10^8 cm^{-2} and this is discussed in more detail in Chapter 6. Gallium nitride is intrinsically n-type and realising electrically active p-type material is notoriously difficult. The most important developments leading to the creation of blue LEDs, was the process of successful p-type activation by Amano and Akasaki in 1989 [27] and the subsequent work by Shuji Nakamura in 1992 [28]. The magnesium dopant used for GaN is known to be a deep centre, with its energy level sitting over 160 meV above the valence band [107, 108]. It was found that irradiation of the device with a low energy electron beam, after growth, yielded modest p-type conductivity. Nakamura developed this by realising that a thermal anneal at around 1100 °C could produce a similar effect. Crucially, such a thermal process is far more easy to incorporate into a simple manufacturing process, whereas it is not practical to irradiate every wafer with an electron beam scan. It was discovered that both processes liberate hydrogen from the material, leading to a model where hydrogen passivates the magnesium donor by bonding with the hole site in the crystal. It is important to note that despite this development, hole carrier concentrations in p-type GaN are still lower (1-2 orders of magnitude) than those of electrons in n-GaN. This is because the large activation energy is $5 \times kT$ (at room temperature), so only a small percentage of unpassivated acceptors will be occupied by valence band holes at room temperature. The following section addresses the variations in the type and composition of the layers in the electrically and optically active region of the devices.

LED structures

The great majority of the LED devices studied in this work were grown using the principle of iterative design. While the particular structure (number, type and thickness of various layers) varies from wafer to wafer, each growth run of the LEDs contains several similarities. All devices in this work were grown on a sapphire/GaN template, with a thick (2-3 μm) n-type GaN layer ($\sim 10^{19}$ cm^{-3}

electron concentration). The layers grown above the n-type GaN varied depending upon the particular design of the structure which was grown. Specific details of the growth for given LEDs are given in the appropriate sections of the results chapters but, as an introduction, the following list describes the typical layers and their variations. Note that the list is given in the growth order (i.e. the first item is closest to the n-GaN and therefore furthest from the surface)

- Underlayers (UL) - Thin ($\sim 25\ nm$) GaN or InGaN layers grown beneath the active region to improve device efficiency. Such layers have been reported to improve LED efficiency through several mechanisms; strain relaxation [109, 110], electron capture increase [111], defect reduction in the active region [112, 113] and recently through the reduction of the electric field in the first quantum well [79, 80]. Variation were made in: **material thickness of underlayer**, **doping of underlayer** and whether or not the layers were inserted at all.

- Active region/Multi-quantum well (MQW) - The light emitting region of the LED. Within the active region variations were made in: **No. of QWs**, **Thickness of QWs/QBs**, **indium content of the QWs**.

- Electron blocking layers (EBL) - Thin ($\sim 25\ nm$) AlGaN layers grown above the quantum wells to prevent electron overshoot from the active region. The main variation related to the EBL was whether or not it was inserted at all.

Above the EBL (or MQWs, where there was no EBL) a p-GaN layer, 120–200 nm thick, was grown with a typical activated hole concentration of 10^{17} cm^{-3}.

3.1.2 Fabrication

The LED structures were fabricated at the University of Bath into full devices using a combination of lithography and metal sputtering deposition. The wafer processing starts with the deposition of a patterned etch mask. The mask is chosen to be resistant to the later GaN etch. In this case the mask material used is hydrogen silsesquioxane (HSQ) as, unlike SiO_2 or SiN_x, it can be deposited by spin coating which reduced the overall processing time. Photolithography was

used to create the desired etch pattern and the wafer is then etched down to the n-GaN using a inductively coupled plasma (ICP) etch. This exposes the n-GaN and electrically isolates the separate devices. After removal of the photoresist and etch mask a thin $\sim$ 10 nm oxidized Ni/Au semi-transparent current spreading layer is deposited on to the p-layer. Non-alloyed Ti/Al contact stripes were formed on the n-layer (as an Ohmic contact) and over the Ni/Au in an interdigitated arrangement that minimizes current crowding. The device is annealed in oxygen for 5 minutes at around 500°C in a rapid thermal annealer. The annealing process is required to improve the Ohmic contact between the metal and the p-type GaN, which tends to be resistive [114]. The resultant dies have an effective area of 1×1 mm^2. Figure 3.2 shows an illustration of the resultant LED die.

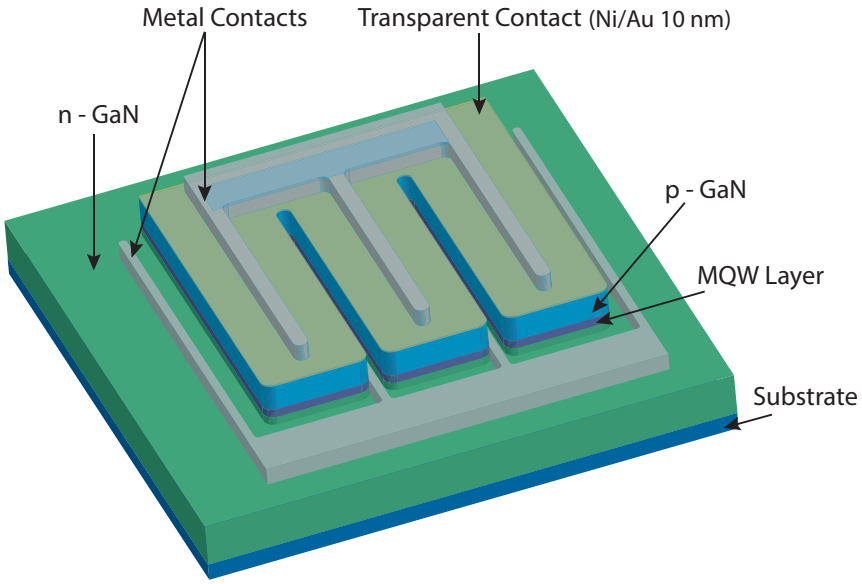

Figure 3.2: *Illustration of the structure of a single processed LED die of the type used primarily in this work. Illustration kindly provided by Katie Cavanagh at University of Bath*

3.1.3 Device preparation

All the full LED devices used in this work were received as sections of 2" processed wafers. For different experimental techniques, different preparation of the dies was required. The majority of the pieces used in the electron probe (see below)

were further cut, using a diamond pen, and mounted onto PCB boards using conductive silver paint as an adhesive on the back side of the wafer. The PCB boards were patterned beforehand (by the Electronics Workshop at Strathclyde) with sixteen copper pads - 4 along each edge - which act as bonding pads for the LEDs. The dies were wire bonded to the pads using a using a wedge bonder at the Institute of Photonics, with 25 μm Si doped Al wire. A photograph of the LED wafers mounted and bonded to a PCB is shown in figure 3.3(a). In this configuration the dies could be inserted into the vacuum chamber of the electron probe where the copper pads are addressed by spring loaded internal contacts, themselves attached to external sockets. In the photoluminescence experiments (below), the dies were mounted on the open top of transistor outline (TO-5) cans (figure 3.3(b)), as neither the size nor the thermal conductivity requirements of the cold finger on the cryostat system could accommodate the PCB boards.

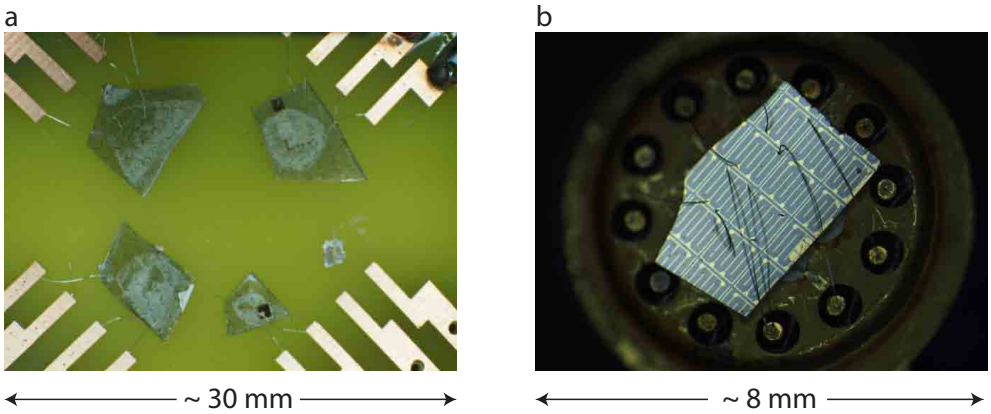

Figure 3.3: *Photograph of mounted and bonded LED wafers on the PCB (a) and TO-5 can (b) holders.*

3.2 Electron Beam Interactions and Measurements

High energy electrons (500 eV-300 keV) are used to probe crystalline materials because, in addition to the superior magnification in comparison to optical microscopes, multiple signals can be measured when the electron beam impinges upon

material. Figure 3.4 illustrates the various interactions between an incident high energy electron beam and a semiconductor sample. In general, incident electrons in the beam can undergo both **elastic** and **inelastic** collisions with the atoms and electrons in the crystal. Elastic scattering, or Rutherford scattering is responsible for the creation of **backscattered electrons**. Several inelastic interactions can occur and will produce a variety of possible signals; slow and fast **secondary electrons** via loosely bound electron collisions, **X-Rays** and **Auger electrons** emission via interaction with tightly bound inner core electrons and **cathodoluminescence** as well as bremsstrahlung radiation, and plasmon scattering. Each of these processes has a different associated scattering cross-section, Q, which described the strength to the interaction and in general Q is proportional to the atomic number (Z) or weight (A) and inversely proportional to the beam energy, E. Each of these highlighted processes are now discussed in turn.

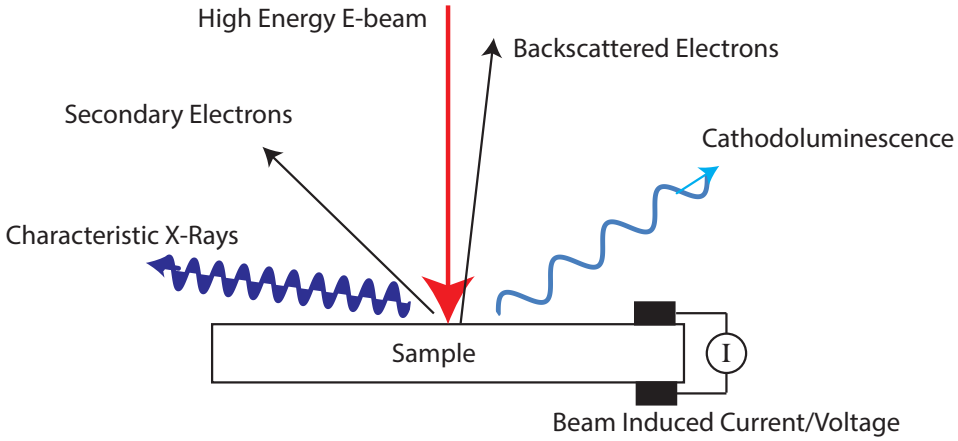

Figure 3.4: *Illustration of some of the outcomes of the interaction of the electron beam with a sample.*

Backscattered electrons

Electrons which meet the atomic nuclei will be deflected, as in the classic Rutherford gold film observation scattering [115]. The primary electrons can be reflected back at a narrow solid angle and with an energy up to that of the incident electrons. Variations in material composition can be probed, since the Rutherford

cross-section, Q_{bse1} goes as the square of the atomic number:

$$Q_{bse} \propto Z^2 \tag{3.2}$$

those atoms with large atomic number (Z) have heavier nuclei and will scatter more strongly than lighter elements. The BSE yield in a composite material will be proportional to the weighted average of the Z number of the constituent species. Due to this, chemical variations in a material can be seen and so BSE atomic contrast imaging is popular in many fields, especially geology. Electrons which are detected as backscattered electrons may have undergone one or more elastic scattering events and possibly inelastic scattering also. Due to the high energy of BSE, they can be detected from a depth of a few 10s of nanometres, in GaN.

Secondary Electrons

Secondary electrons (SE) are those which have been ejected from the outer shell of atoms due to inelastic collisions with the incident electrons, and typically have a far lower kinetic energy, around 1–50 eV [116]. As a result secondary electron signals come from the first few nanometers of the material since the energy of the secondary electrons is insufficient to allow them to travel further due to the likelihood of undergoing subsequent inelastic scattering events. Secondary electrons are used primarily to image the topography of a sample, as the yield is strongly dependent upon the local angle of incidence. The secondary electron yield is less affected by the atomic weight than in backscattered and is dependent upon the Fermi energy (E_F) in the sample:

$$Q_{se} \propto 1/(E_{SE} - E_F)^2 \tag{3.3}$$

As a result the SE yield will be effected strongly by any electronic variations in the material, for example an applied potential, which will alter the position of the Fermi level.

Characteristic X-Ray emission

If the incident electrons eject more tightly bound electrons, a vacancy will be produced in the inner shell of the target atoms. This results in the emission of a high energy photon, typically an **X-Ray** via the relaxation of a higher energy electron into the vacancy. These X-Rays are characteristic of the atom from which they are produced and so are used to identify elemental species within the material. Since X-Rays have a high energy and low interaction cross section, they can travel through the bulk of the material and so the detection of X-Rays produces a measurement characteristic of the entire sample. As a result, the volume from which the X-Rays originate is entirely dependent on the interaction volume of the incident electrons (see below and in figure 3.5)

3.2.1 Cathodoluminescence

In semiconductors, the incident electrons will generate electron hole pairs through the process of impact ionization, and the recombination of these can produce the phenomenon of **Cathodoluminescence** (CL). In semiconductors, the luminescence originates mostly from electrons which are promoted from the valence band to the conduction band which then relax back, either directly to produce *band edge emission* or through some intermediate energy level in the gap. Since the band gap energy is typically no more than a few electron volts and the beam energy is several thousand electron volts, many electron hole pairs can be produced by a single incident electron. The number of electron/hole pairs created by the beam, known as the generation factor (G) depends on the beam energy, E_b and the ionization energy of formation, e_i as in equation 3.4:

$$G = \frac{E_b(1-\gamma)}{e_i} \tag{3.4}$$

where γ is the fraction of the beam energy which is carrier out of the material by the backscatter electrons. This fraction increases monotonically and weakly with the atomic number [117, 118]. For GaN, where Z is considered as 19 ($(31+7)/2$) the backscattered coefficient is around 16%.

Two connected concepts are that of the "Depth-dose" function and the electron range, R. The electron range is a an empirical function of the beam energy and

the material density, ρ which was developed initially by Everhart and Hoff in 1971 [119]:

$$R_e = (0.0398/\rho)E_b^{1.75} \quad \text{in} \quad \mu m \tag{3.5}$$

The formula was generalized by Kanaya and Okayama in 1972 [120]:

$$R_e = \frac{0.0276A}{\rho Z^{0.889}}E_b^{1.67} \quad \text{in} \quad \mu m \tag{3.6}$$

Primary electrons with a large energy will, on average, travel further through the material before exhausting their energy through inelastic scattering, impact ionization events or being backscattered back out of the sample. At low acceleration voltages, those electrons which are not backscattered will deposit most of the energy near the surface.

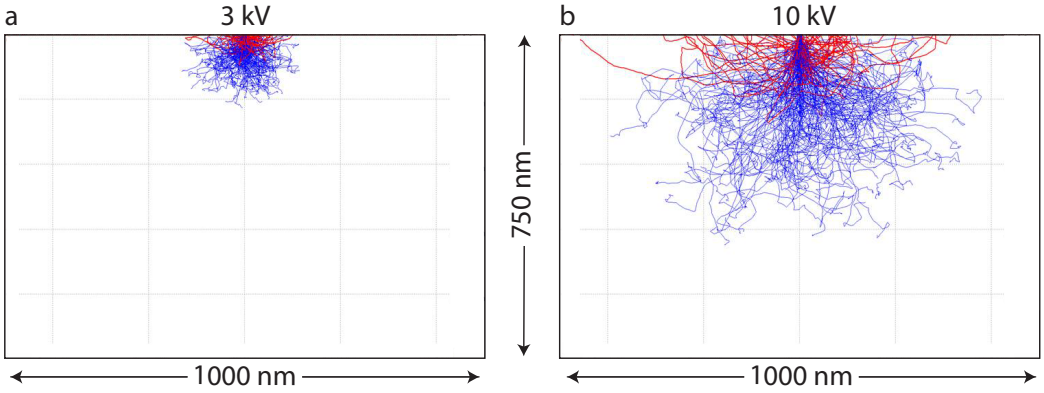

Figure 3.5: *Electron trajectories in GaN from a 3 kV (a) and 10 kV (b) electron beam. Modeled using CASINO. [121]*

The trajectory of electrons can be modelled via Monte Carlo simulations which is required when the electrons travel scatter further than a few mean free paths - where an analytical treatment becomes impossible. A commonly used used Monte Carlo simulation program for electron beam interactions is CASINO (monte CArlo SImulation of electroN trajectory in sOlids) [121] and CASINO v2.42 was used in this work to model the penetration of electron beams into the LEDs. Monte Carlo simulations in figure 3.5 demonstrate a sample of the electron trajectories in GaN from a 3 kV (a) and 10 kV (b) electron beam. The most obvious effect is the size of the volume into which the electrons penetrate - a

lower beam energy by a factor of 3 cuts the maximum electron depth by a similar value. However, these plots are of limited instructiveness because they represent only a sample of the electron paths and do not describe the deposited energy.

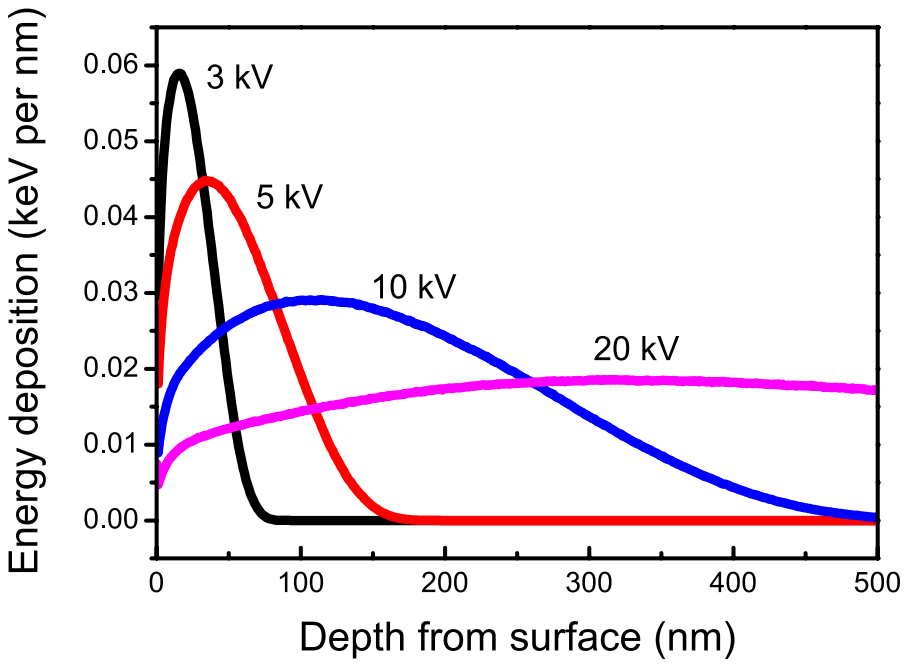

Figure 3.6: *Plots based on Monte Carlo simulations, using CASINO, demonstrating the deposition of energy in GaN of electron beams of various energies.*

The deposition of the beam energy as function of depth from the surface, from a CASINO simulation, is plotted in figure 3.6 for several acceleration voltages. A percentage of the input beam energy will be carried out by the backscattered electrons, the γ from equation 3.4. In each of the 4 curves in figure 3.6 the total energy deposited (i.e. the area under the curve) is normalized to the same value. This reflects the conditions of experiments described in later chapters where, in order to maintain a total deposited power, the beam current was adjusted such that kV $\times$ nA = constant. At 10 keV the depth of the maximum energy deposition is just over 100 nm, which is similar to the depth of the active region below the surface of the LEDs, and so for most of the electron beam experiments, acceleration voltages of around 10 kV were used.

3.2.2 Electron Microscopy

Electron microscopes represents a significant step up in resolution in comparison to light microscopes, and state of the art SEMs (scanning electron microscopes) can image features at a length scale of ≈ 1 nm. Before discussing electron microscopy, it is useful to make a note on errors in all subsequent measurements. The variation studied in the devices is much larger than any equipment uncertainties in the apparatus used. As such, the lack of error bars based on systemic or equipment error is because they would be dwarfed by variation in the material parameter variations. Where there are error bars, they typically are the result of averaging data sets. These are specified where they appear. All electron microscopes consist of three primary parts: the source, the detector(s) and the sample. The electron source, and its associated beam control/focusing components, comes in two main varieties - thermionic emission and field emission. Both typically use a tungsten or LaB_6 wire filament, due to the relatively low work function, Φ, and a high melting point (around 3,700 K for W). In a thermionic emitter, current is passed through the filament, increasing the temperature allowing electrons to exceed the work function and escape the material. Field emission occurs by the Fowler-Nordheim process as described in the previous chapter, whereby a large electric field is applied between the tip and anode to reduce the effective work function and allow escape via tunnelling. The filament in this case is refined to a very small needle to create a high field density at the tip. A variant is a called the Schottky gun, where the filament is heated, which prevents the build up of material which migrates in the vacuum to the tip. In either case the aim is to bring the emitted electron beam to the sample plane in a focused point. The beam ideally has a high brightness (current/solid angle), a low divergence, narrow spread of electron energies and stability.

Secondary electron detection is performed using a design pioneered by Everhart and Thornley in 1960 [122]. A scintillator plate sits off to one side of the sample surrounded by a permeable Faraday cage. A positive bias is applied (+200V) to the cage to attract the low energy secondary electrons. The far more energetic backscattered electrons will not be appreciably deflected by the relatively low voltage and, due to the geometry, they will not reach SE detector. Within the cage a much higher positive voltage is applied to the surface of

the scintillator (>+10kV) - this accelerates the secondary electrons to energies sufficient to excite many (10^6-10^7) photons in the detector to provide sufficient gain for an interpretable signal. Backscattered electrons can be detected by using a similar arrangement, but by applying a negative bias to the Faraday cage to deflect SEs away. This is typically not employed due to poor overlap between the emission angle and detector position. It is more common to use an annular Schottky or p/n junction solid state detector placed below the pole piece of the microscope. Since the response of the detector scales with electron energy and has a cut off above their typical energies (50-100 eV) secondary electrons are effectively screened out.

The most frequently used tool throughout the work was a Cameca SX100 Electron probe microanalyser (EPMA). The EPMA is a thermionic emission scanning electron microscope primarily designed around three wavelength dispersive X-Ray (WDX) spectrometers 3.7. The WDX detectors are used for both qualitative and quantitative elemental analysis and mapping but since the vast majority of the work involved studying fully processed LEDs where the composition of the top layers is well known, this feature was rarely used.

3.2.3 CL and EL Hyperspectral Imaging and mapping

In a conventional scanning electron microscope set-up, to record the generated cathodoluminescence signal the simplest method is to use a large area photodiode or photomultiplier tube (PMT). As in the case of secondary electron imaging, the output from the beam scan provides the indexing for the lateral source of the light and so the detector is designed to capture as much light as possible. This produces a panchromatic image, that is, with no selectivity of wavelength and is useful when there is only one luminescence band from a sample, or if only the total brightness is of interest. Spectral resolution can be achieved either by selecting one wavelength band at a time (monochromatic) or many (hyperspectral). In our EPMA (fig 3.7), we are able to collect a full spectrum at each point of a raster scan of the stage (or beam) by using the 1024 channels of an Andor CCD attached to the image plane of a spectrometer. The emitted light is captured by a reflecting objective and focused to the image plane of a 1/8 m Oriel spectrometer (f\3.7), through a 25 μm entrance slit. This produces a 3D datacube with

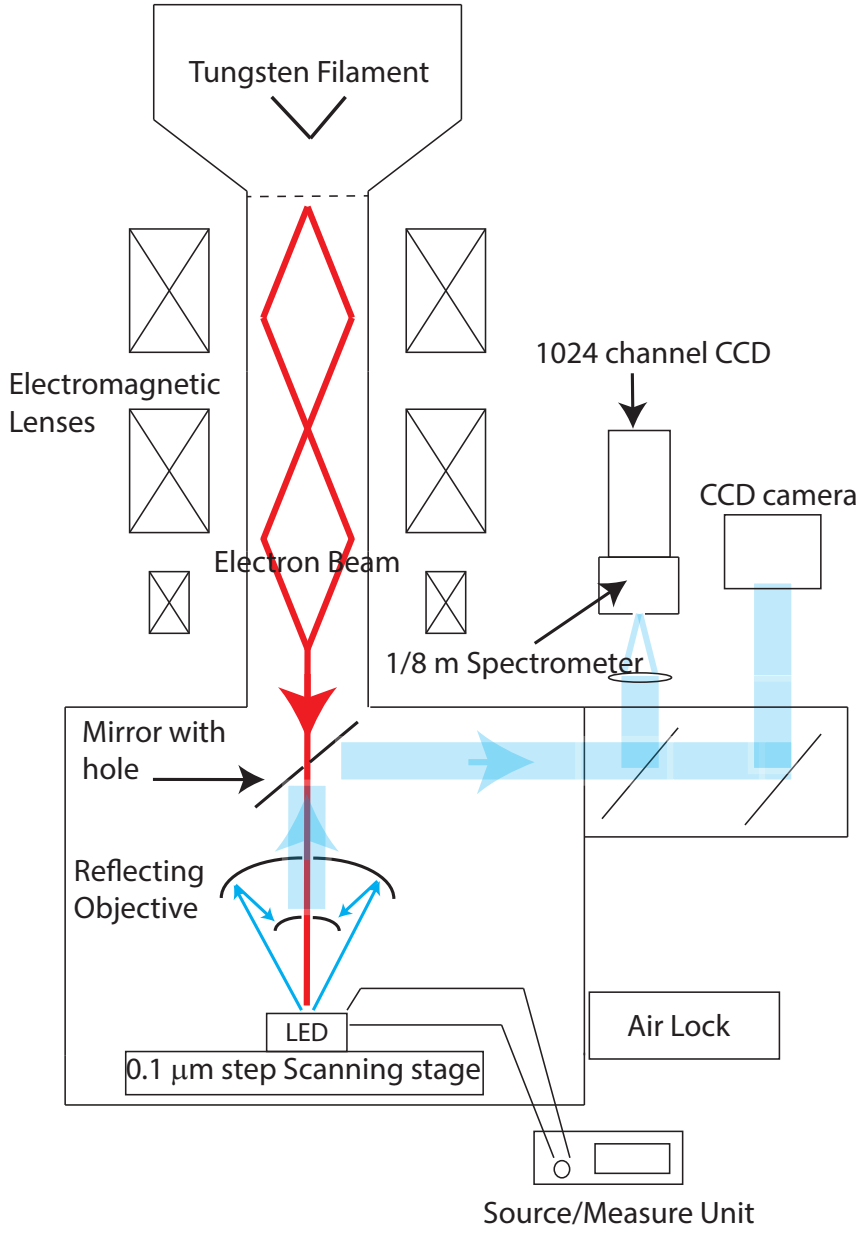

Figure 3.7: *Schematic diagram of the electron probe micro-analyser (EPMA). The three WDX detectors are omitted for clarity as they were not used to any significant extent. Both the reflecting objective lens and the mirror above the sample have holes to allow passage of the electron beam.*

both spatially and spectrally resolved information on the cathodoluminescence or electroluminescence. In the majority of the experiments described in the the-

sis, the system was used in stage scanning mode, as opposed to beam scanning. Cathodoluminescence and other maps of the devices under study were performed by scanning the mechanical stage under a fixed electron beam. The stage has a minimum step size of 100 nm and operates using a raster scan.

Mapping of the electroluminescence from contacted LED dies was performed in the EPMA due to the availability of the scanning stage and identical collection optics to that used for CL. The spectrometer entrance slit was replaced by an 8 μm pinhole which, given the approximate 3x magnification factor from the sample to the entrance plane, gives a spatial resolution of around 3 μm. Smaller pinholes, 5 and 2 μm, were used to try to increase resolution but test maps recorded showed undesirable optical effects which were likely due to imperfections either in the mounting of the smaller pinholes or the pinholes themselves. Furthermore it was found that the 3 μm steps were sufficient to resolve particular features of interest and make comparisons to corresponding CL/EBIC maps.

The relative collection efficiency for the CL and EL can be estimated by considering the aperture for light capture. The slit width for CL collection is 25 μm and EL collection uses a 8 μm diameter pinhole. The entirety of the pinhole is always filled under EL conditions. In CL, the spot size at the entrance slit is dependent on the size of the focused spot of the electron beam. When a spot size of 1 μm is used, this translates to 3μm size at the slit. The ratio of the captured area would then be: $Int_{EL/CL} = (8/3)^2 \approx 7$x. A full comparison requires estimating the relative power density of the EL and CL. The power contributing to the captured luminescence in the EL is simply:

$$P_{EL} = I_{diode} \times V_{diode} \times (A_{pin}/A_{diode}) \tag{3.7}$$

where I_{diode} and V_{diode} are the diode current and voltage and A_{pin}/A_{diode} is ratio of pinhole area projected onto the die surface to the total die area. In the CL, the power depends on the acceleration voltage and the beam current. Assuming that the slit width is greater than the lateral extent of the interaction volume the spot size does not matter and the power is then:

$$P_{CL} = (V_b \times I_b) \times \delta_{QW} \times \eta_{align} \tag{3.8}$$

where V_b is the beam acceleration voltage, I_b is the beam current and δ_{QW} is

the fraction of the beam power which is deposited into or diffuses to the active region and does not subsequently escape the depletion region. The η_{align} accounts for the possibility that the optics are not perfectly aligned, i.e. if the spot is not focussed properly on the slit some light is lost.

Assuming a 1 mm^2 die, an EL current and voltage of 10 mA and 3 V, electron beam parameters of 10 kV and 1 nA, with a δ_{QW} value of 0.2 (as estimated in chapter 4) and η_{align} taken as 0.5, the ratio of the CL to EL power which contributes to light generation is found by dividing equation 3.8 by 3.7:

$$\frac{P_{CL}}{P_{EL}} = \frac{(V_b \times I_b) \times \delta_{QW} \times \eta_{align}}{I_{diode} \times V_{diode} \times (A_{ppin}/A_{diode})} \approx 3.7 \tag{3.9}$$

The value is less than an order of magnitude and can easily change or become less than 1, by simply increasing the EL current to 100 mA, or by reducing the beam parameters or alignment efficiency. These parameters are changeable, particularly η_{align} which is somewhat variable in measurements. Other assumptions are that all of the injected EL current combines in the active region, which is unlikely due to losses to various processes like shunt and series resistances and carrier overflow among others. Due to these provisos it is not possible to compare the EL and CL measurements in a completely quantitative manner with great confidence as any difference could easily be down to the variable parameters. As such, only quasi-quantitative (relative intensity variations) and qualitative (mapping homogeneity etc.) comparisons are made between CL and EL intensities in the thesis.

All the hyperspectral datasets were analysed using a home built program, created by Dr Paul Edwards. Each pixel in the data array contains a spectrum and each of these are subsequently fitted to Gaussian, Lorentzian or Voigt curves, and the resultant parameters were plotted as 2-dimensional maps of the spectral characteristics (i.e. peak intensity, peak position and full width at half maximum). Subsequent mathematical operations could then be applied to the maps such as extracting statistics (mean, standard deviation, etc.) or performing a statistical correlation to investigate the relationship between two parameters.

3.2.4 Electron Beam-Induced Current

Electron beam-induced current (EBIC) is the process whereby high energy incident electrons generate, either directly or indirectly, a measurable current in a target material [116]. The signal can come directly from the primary electrons themselves or via a secondary process such as the generation and subsequent collection of electron/hole pairs created during inelastic collisions with the primary electrons. In the case of this work it is the latter process which was exploited and so the subsequent discussion pertains to the "indirect" EBIC (though much of the principle is the same in other forms of EBIC - for more detail see Joy chapter 6 [116]. In order to collect an EBIC signal the charge carriers (electron or hole) must find a way from the point of generation to whatever contacts are used to probe the material. The two primary modes of charge movement in semiconductors are diffusion and drift. Since the diffusion length for electrons in GaN at room temperature is less than 100 nm [123, 124] (and that of holes is even lower) diffusion alone is typically insufficient to generate a measurable EBIC. It should be noted, however, that since EBIC is sensitive to the diffusion process, it can be (and is) used to investigate phenomena which influence carrier diffusion, such as threading dislocations in GaN [123, 125], grain boundaries and other crystal imperfections. Drift under the influence of an electric field typically acts across a much larger distance (depending on the particular electronic state of the semiconductor). Since conducting probes are already being used to collect the EBIC signal, it is an easy matter to apply an external field across the semiconductor in order to provide a driving force for the EBIC. Since the vast majority of the samples studied in this work, and all those looked at in EBIC mode, were fully processed LEDs) there is a pre-existing driving force within the material - the built-in electric field at the p/n junction.

Electron holes pairs which are generated in, or diffuse to, the depletion region will undergo one of three processes:

- radiative recombination
- non–radiative recombination or
- separation by the built in field across the depletion region

The EBIC signal will originate from the latter of these three processes. The sum of the three process will equate to the excess carrier generation rate:

$$G = R_{\mathrm{NR}} + R_{\mathrm{R}} + I_{\mathrm{EBIC}}/q \tag{3.10}$$

where G is the generation rate, R_{NR} and R_{R} the non radiative and radiative recombination rates, respectively and I_{EBIC} the EBIC current. As discussed in the previous chapter, carrier escape from the active region comprises of both drift and tunnelling and so the EBIC signal will be affected by the rate of these processes. Due to the large energy of electron beam induced secondary charge pairs, the drift process is typically more significant than tunnelling due to the lower relative occupation of the quantum wells [32]. When the LED is contacted (i.e. in short circuit), this separation of charge creates an excess current which is measured as the EBIC. The phenomena of electron beam induced voltage (EBIV) is one related to EBIC and is analogous to the photo-voltaic effect in the way that EBIC is to a photo-current. When the device is uncontacted (i.e. in open circuit) the generated charge which drifts out of the depletion region has no circuit in which to flow and so builds up at the edge of the depletion region. Since holes will drift to the n-side and electrons to the p-side the effect is to act like a forward voltage and so narrow the depletion region, the size of the voltage is proportional to the density of charge generated in the depletion region.

The generation is shown diagrammatically in figure 3.8 (a) (EBIC) and (b) (EBIV).

In order to clarify what is actually meant by EBIC in this work, an important distinction has to be made between the different possible current measurements. These are displayed graphically in figure 3.9. Firstly there is the LED dark current (I_{drk}), which is simply the I-V characteristic when the device is under no excitation (either by light, electron beam or anything else which causes a non-zero generation rate of carriers in the active region). The total current when under illumination (I_{brt}) is the sum of the dark current and whatever extra current is induced by the excitation process. In this work the EBIC is defined as:

$$EBIC = I_{drk} - I_{brt} \tag{3.11}$$

A special case exists at 0 V where (with a die with a good I-V relation)

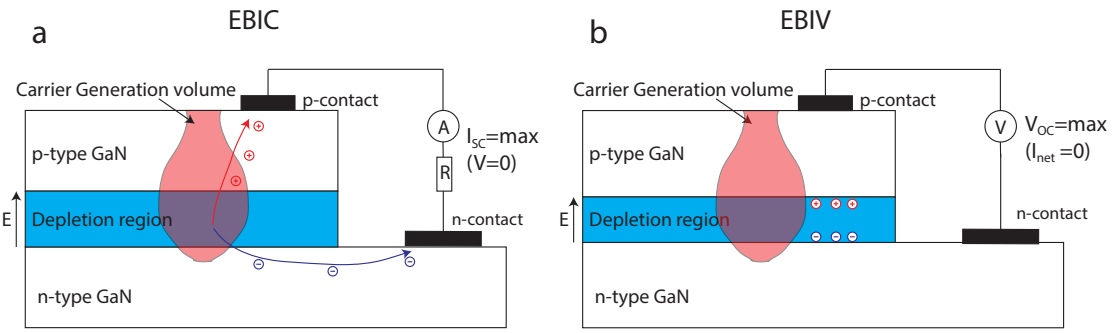

Figure 3.8: *Schematic of electron beam generation of an EBIC signal (a) and EBIV (b) signal. The two are shown at the extremes - I_{SC} with zero applied bias and V_{OC} where the net current is zero. Note that the depletion region is narrower in (b).*

$I_{drk} = 0$ and so $EBIC = I_{brt}$.

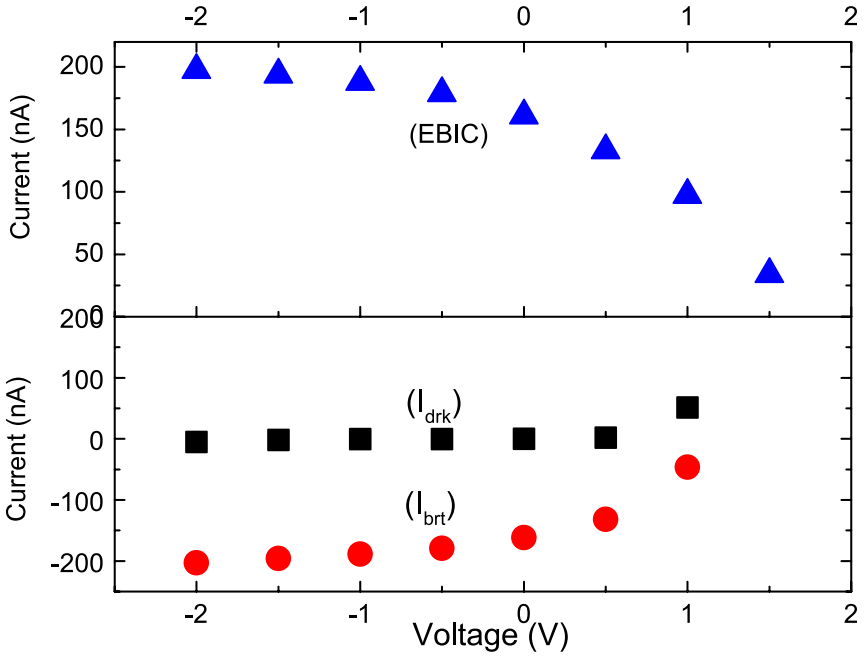

Figure 3.9: *Current-voltage curves for an LED in "dark" (black squares), under illumination (red circles) and the difference, defined as the EBIC (blue triangles)*

The EBIC mapping measurements were performed simultaneously with the

CL mapping as the combination of the two reveals significantly more information than either can separately. Also, since the EBIC already requires the electron beam, acquiring simultaneous CL was a trivial process. The I-V characteristics of the dies used are crucial - if the device possessed a large reverse bias leakage current or a forward shunt resistance, they were considered unsuitable for EBIC measurements. Typically, the dark current at $\pm$ 3 V was measured and if the reverse current was found to be $> \sim 500$ nA, the dies were considered too leaky to use.

During the progression of the project, the actual method of acquisition of the EBIC changed as the technique was refined to become more powerful. Throughout the experiments the LEDs used were those which were already bonded for the purposes of performing EL - the idea being that the same LEDs could be studied in EL, CL and EBIC modes. Initially the EBIC mapping was performed via the use of a Keithley series 2401 Source/Measure unit. This particular model has an addressable buffer capable of holding 2,500 16-bit floating point numbers, so with this capability EBIC maps with dimensions of 50×50 pixels were produced. The Keithley was attached to the electrical outputs from the EPMA, which in turn addressed the contact pads on the LED sample holder. By use of Visual Basic control software, the Keithley was set to apply a set bias voltage (typically 0 V) and then to record the value of the current through the LED at each pixel of the electron beam scan. The data were stored as a string in the buffer and, using the software, read out into a 50×50 array of values. This array could then be represented as image in the CHIMP software and analysis performed in the same manner as on the CL hyperspectral data.

Due to the 2,500 data point limit of the buffer, there was a limit on the size and resolution of EBIC maps which could be collected. Since the electron beam scans were frequently performed with 1 μm steps, the typical maximum field of view in the EBIC images, and any simultaneously collected CL data, was $50\times$ 50 μm^2. This proved a limitation since any EL scans of the same area were limited to approximately 17 by 17 pixels, due to 3 μm resolution of the EL. To get around this limit, multiple $50\times$ 50 μm^2 images could be taken and knitted together during data processing. This, however, was both time consuming and imprecise because of the difficulties of ensuring exact alignment of the scanning stage. The acquisition was improved by replacing the Keithley by a combination

of a Stanford Instruments pre-amplifier and an ADC-10 analog/digital converter. The pre-amp was set to apply a fixed bias and then connected to the LED output. The pre-amp was set to the appropriate sensitivity (based on a spot measurement of the EBIC using the Keithley) and it's output connected to the analog/digital converter. The converter was in turn attached to the computer and a digital, 8 bit value of the pre-amp voltage was read out in real time into an array with dimensions equal to that of the simultaneously collected CL hyperspectral data set. In this way EBIC (and simultaneous CL) maps of arbitrary size could be collected.

3.3 Photoluminescence

In photoluminescence (PL), light with a higher energy than the bandgap of the target material excites electrons from the valence band to the conduction band which then relax via thermal interactions with the lattice, radiative emission or a combination of the two. PL differs from CL in a significant manner because the excited electrons typically have energies less than twice that of the band gap, and hence significantly lower than those generated by electron beam excitation. In this sense it is closer to EL, where the carrier energy is also similar to the band gap. However the generation profile is more akin to CL than EL due to the fact that electron/holes pairs are generated together throughout the material (where the band gap is sufficiently low).

PL was performed purely as spot measurements and no mapping was involved. The PL was carried out in vacuum in a closed cycled Helium cryostat and a schematic of the setup is shown in figure 3.10. An inductive heater was coupled to the cold finger of the cryostat to enable temperature dependent measurements from 10 K - 300 K. Electrical contact wires were connected between the sample stage and the outside (using the same inlet as the heater) which could be attached to a bonded LED on the inside of the vacuum chamber and source/measure unit on the outside. This was initially done to allow EL measurements to be performed as a function of temperature but was later utilised to enable PL to be measured from a contacted LED, as a function of applied bias. The laser beam was passed through a Pellin-Broca prism which allows for filtering of a laser line, to select only the wavelength required [126]. Light hitting the front face, is refracted,

totally internally reflected and a single wavelength will emerge from the other face exactly 90^0 from the entry face. Neutral density filters of varying absorption were placed in the path of the beam to allow measurements to be performed as a function of laser power density.

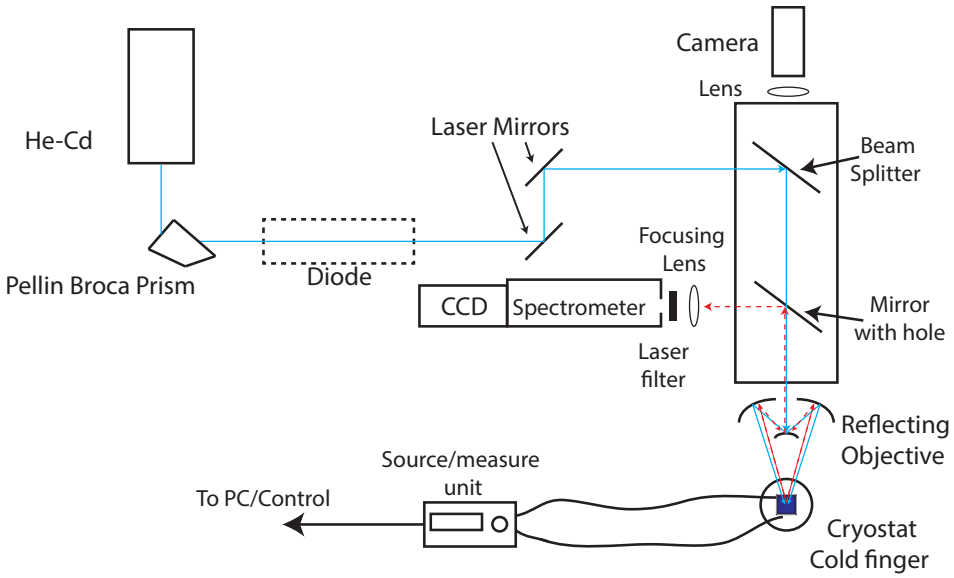

Figure 3.10: *Schematic of the PL system used. The laser diode was mounted on a removable magnetic stand to allow use of the He-Cd laser. Long pass laser line filters (for each laser) were required before the spectrometer entrance slit as the incident laser light is partly backscattered back through the optical system.*

The excitation was provided by either a 405 nm solid state laser diode or a 325 nm He-Cd gas laser. Photons with wavelength 405 nm have a lower energy that the bandgap of GaN (3.065 eV vs. 3.42 eV) whereas the 325 nm laser emits photons of a higher energy (3.82 eV). As a consequence of this, excitation with the 405 nm laser results in generation of charge carriers within the InGaN quantum wells only (resonant excitation), whereas 325 nm excitation generates carriers throughout the material, including the *p*-type GaN (off resonant). This leads to two different routes to recombination of carriers in the quantum wells. In the off resonant case, electron/holes pairs must diffuse to the active region to recombine, whereas in the resonant case the carriers are unlikely to escape the quantum wells before recombination and so no transport effects are included.

3.4 Integrating Sphere

An integrating sphere allows accurate, and calibrated, quantitative measurements of the emission properties of light sources [127]. Spheres come in various sizes in order to cater to sources of varying sizes, from a few tens of centimeters across to many tens of meters designed to measure large light commercial or industrial light fixtures. In this work a 25 cm diameter sphere was used to measure the calibrated radiant flux from the 1 mm LEDs. The sphere was supplied by Labsphere and, crucially, includes a NIST (National Institute of Science and Technology) traceable calibrated reference lamp.

A schematic of the sphere is shown in figure 3.11. The sphere is coated with a reflective, diffusing white coating. The emitting light from the test lamp quickly becomes homogeneous and a set fraction of the light is sampled by an optical fibre, which is protected from direct light from the source by a baffle. A small Ocean Optics spectrometer with a 1 nm spectral resolution is then connected the fibre. Software linked to the spectrometer automatically generates the spec-

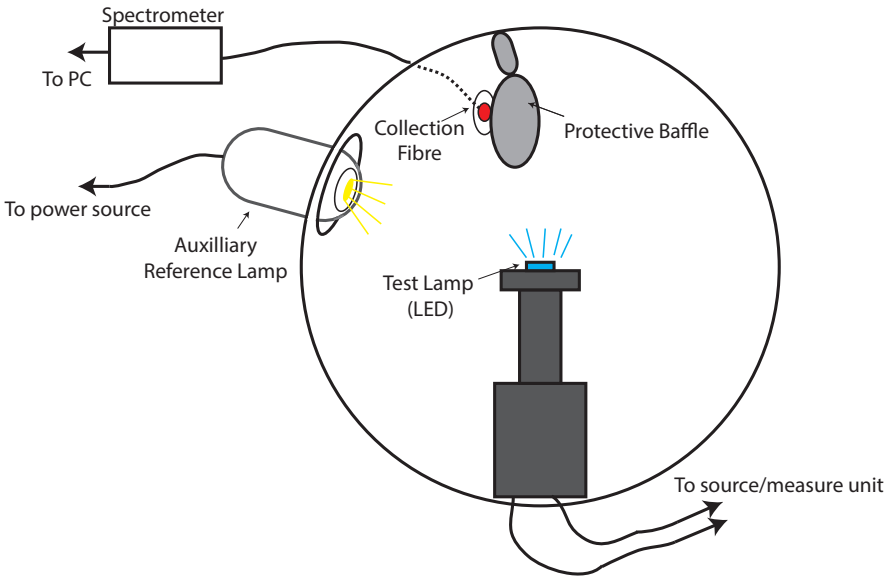

Figure 3.11: *Schematic showing the approximate layout of the integrating sphere. The position of the "test lamp (LED)" is also where the primary calibrated reference lamp sits. The collection fiber aperture sits behind the baffle to protect the spectrometer from direct light from the test lamp.*

tral parameters the most important of which are the radiant flux (W/nm) and the luminous flux (Lumens/nm). The colour rendering index, correlated colour temperature and chromaticity co-ordinates are also calculated but since these are only useful for white light LEDs, it was the purely the radiant flux output values that were of interest in the course of this work.

3.5 Summary

This chapter has described the principles, design and operating of the experimental apparatus used in the work presented subsequently. The methods of the growth, fabrication and preparation of the devices were explained. Electron microscopy and hyperspectral spectroscopy was then covered along with the origin and measurement of the electron beam induced current. Photoluminescence and the use of an integrating sphere were finally addressed. The next four chapters will cover the main bulk of the thesis, describing the experimental observations, analysis and results.

Chapter 4

Effect of the applied bias on the luminescence and carrier transport in InGaN LEDs

4.1 Introduction

This opening experimental results chapter is based on a single LED sample (though not a single die), the details of which are described below, and covers experiments using various techniques. This aims to serve two purposes; firstly to explore fully the properties of the particular LED by a combination of luminescence mapping and spectroscopy as a function of applied bias, excitation conditions and electronic states. Secondly it is a means to introduce, describe and show the power of the different techniques which are used in subsequent chapters to look at series of LEDs with different growth parameters and/or different layers.

The LED sample studied in the following section is one which was grown early in the project and, as such, might be considered as "'basic"' or as a template with respect to the layers it contains or, rather, omits. Like the majority of devices used it is *c*-plane III-N on sapphire grown by Metal Organic Chemical Vapour Deposition (MOCVD) as described in chapter 3. It consists of 2 μm *n*-type GaN doped with Si at 5×10^{18} cm^{-3}, a 135 nm *p*-type GaN doped with Mg to a carrier concentration of 3×10^{17} cm^{-3} and a 5 period multiple quantum well (MQW) active region. The wells were grown at 740°C while the barriers were grown

with a two step process; the first few nanometers were also grown at 740°C and the remainder at around 900°C. The MQW thicknesses and InN content of the wells were measured by X-Ray diffraction (XRD) at the University of Cambridge. The thicknesses of the quantum wells and GaN barriers were 2.4 ± 0.1 nm and 6.9 ± 0.1 nm, respectively and the InN content was measured to be 21 %. There was no electron blocking layer (EBL) or doped underlayer in the devices and the threading dislocation density of the template was estimated to be $4{\times}10^8$ cm^{-2}. The dies were processed and prepared into 1 mm^2 dies in the manner described in Chapter 3. For the CL/EBIC measurements, sections of wafer were mounted on the PCB boards and in the PL measurement they were mounted onto TO-5 cans as described in chapter 3.

4.2 LED wafer mapping

A noticeable variation in the LED dies, in terms of emission wavelength and intensity, is observed across the 2 inch wafer, likely caused by inhomogeneity in the substrate temperature during growth. Measurements of a quarter wafer of the LEDs was performed using cathodoluminescence hyperspectral imaging in the EPMA, as described in chapter 3. All the electron beam experiments were performed at room temperature using the EPMA. Due to the thickness of the *p*-type GaN layer on top of the active region, a beam voltage of 10 kV was used for all measurements, unless stated otherwise. As discussed in the previous chapter, at 10 kV the peak of the energy deposition profile occurs at around 110 nm, close to the top of the MQW stack in this sample.

Figure 4.1 shows false colour maps of the multi-quantum well CL spectral intensity (a), peak position (b) and peak full width at half maximum (FWHM) (c) with (d) a map of the secondary electron signal obtained during the CL mapping. Figure 4.2(a) shows an example CL spectrum taken from the hyperspectral data set - the images shown here are of parameters relating to the MQW peak at 2.5 eV. There is significant non-uniformity across the wafer, both a broad scale variation - particularly in the peak position (c) and also the intensity (a) - but also from die to die at random points across the wafer. The former variation can be attributed to variations in temperature across the growth substrate of the LED material. Figure 4.2(b) shows the result of PL mapping from the wafer

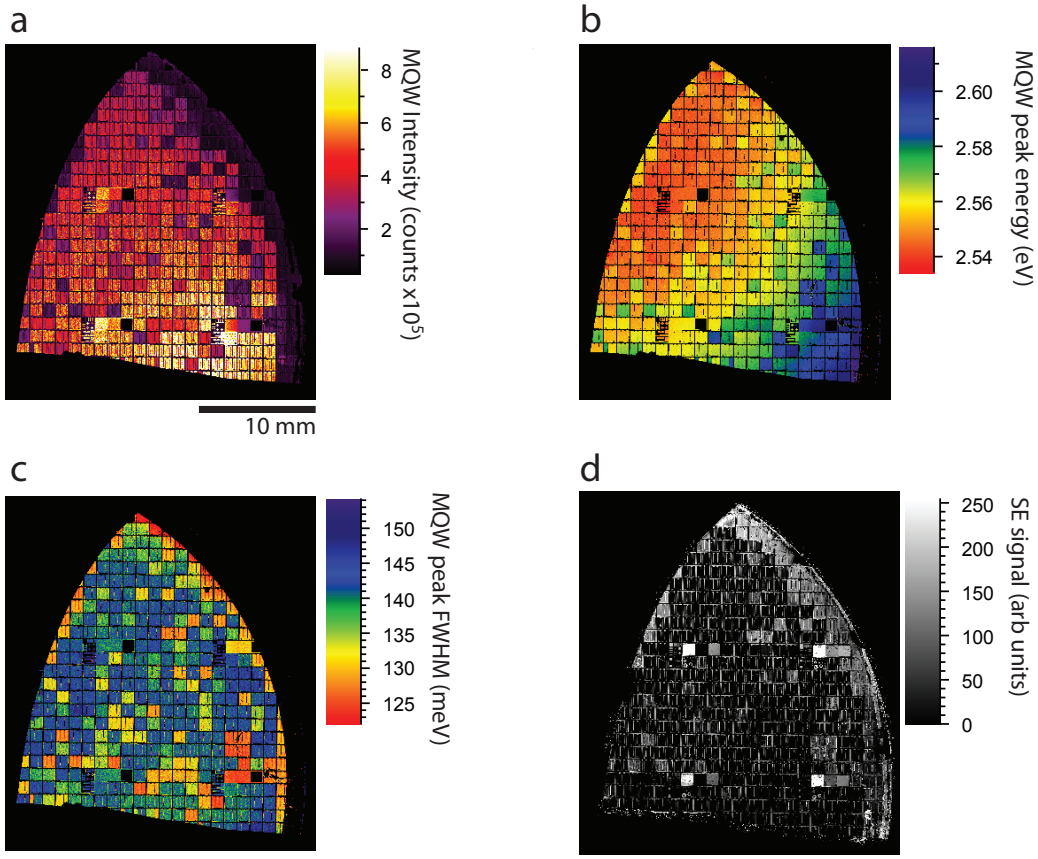

Figure 4.1: *Cathodoluminescence hyperspectral mapping and secondary electron imaging of an approximate quarter wafer. Each small square on the wafer is a* 1×1 mm^2 *individual LED die. (a), (b) and (c) are the MQW spectral integrated intensity, peak position and FWHM, respectively while (d) is the simultaneously collected SE signal. The spectral parameters were obtained from a fit of the entire CL spectrum - shown in figure 4.2 (a).*

before processing, i.e. before the individual dies were isolated or contact metal was deposited. The black line roughly defines the area of the sample studied by CL, and it is readily apparent that the broad redshift of the emission in CL (c) from bottom right to top left is matched by the same in the PL. Within the area the variation in peak wavelength runs from around 485 nm to 475 nm in bands. This is similar to the banded variation in CL wavelength running from 490 nm (2.53 eV) to 477 nm (2.6 eV) . The small difference is likely due to the differing excitation conditions, for example carrier density, between PL and CL measurements. Where the substrate temperature was lower during growth, a

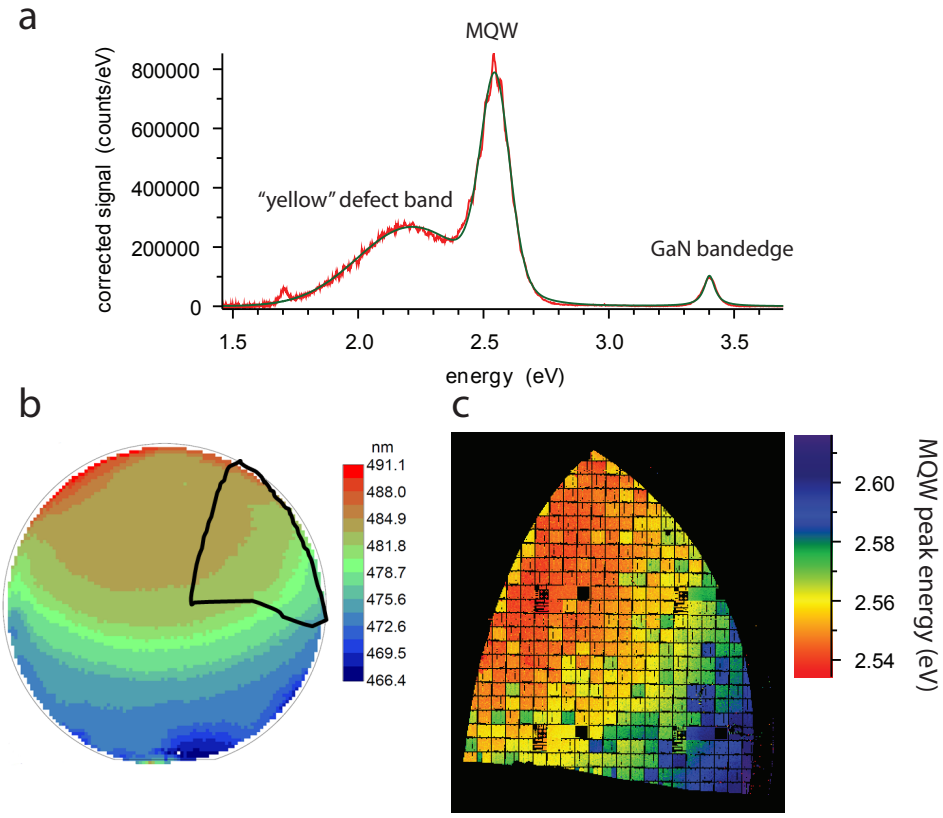

Figure 4.2: *(a) Example fitted spectrum from the LED wafer showing the three different luminescence bands, (b) photoluminescence wavelength mapping of the entire 2" wafer (performed by Dr Menno Kappers at University of Cambridge using Accent RPM wafer mapper) with an overlay of the section of the wafer mapped here by CL. (c) is a repeat of the figure 4.1(c) showing that, when compared to (b), the large scale peak position variation observed in CL is the same as seen in PL mapping.*

higher InN fraction was incorporated into the quantum wells. This results in a redshifted emission band and, due to lower material quality, a reduced emission intensity, and this correlation is observed in the data from the wafer.

The other variation - die to die - is due to electronic differences in the devices, as opposed to material differences. Particular dies are locally lower in luminescence intensity, are blueshifted, have narrower emission lines and an increased SE signal. The uncontacted LEDs can be thought of as being in open circuit, that is, unconnected to any external EMF/applied bias. The beam electrons create electron/hole pairs throughout the material and some of these carriers will re-

combine, radiatively or non-radiatively, either in the InGaN quantum wells, or in the GaN. Some of those generated in the depletion region will be separated by the in-built electric field. As there is no circuit for this charge to flow through, it builds up at the edges of the depletion region; electrons on the n-type side and the holes on the p-side. This acts as an effective forward voltage, analogous to the photo-voltage in a photovoltaic cell. Since the processing is never perfect, some of the dies may be in short circuit where separated charge carriers will flow around the circuit and have no influence on the p/n junction field (analogous to photo-current). These processes are shown diagrammatically in figures 4.3(a) and (b) which demonstrate the behaviour of charge carriers in an unconnected (open circuit, $I = 0$) and short circuit ($V = 0$) LED.

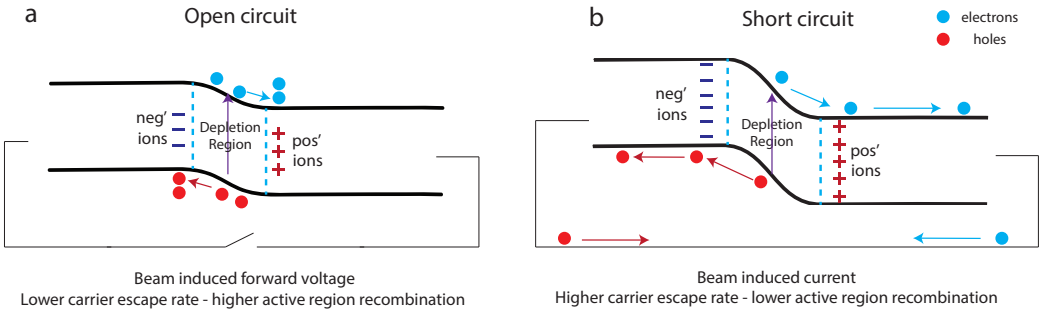

Figure 4.3: *Simplified band structure of the LED at the active region under open (a) and short (b) conditions. Due to the electron beam, generation of carriers occurs throughout the material, but only generation within the depletion region is shown to illustrate the effect.*

The LED's electronic state - whether in open or short circuit - affects the characteristics of the luminescence in three ways. These are shown in figure 4.4 and listed below:

- **Spectral intensity**: With an induced forward voltage (*open circuit*) the p/n junction field is lowered and the drift induced escape of charge from the depletion region is reduced. Therefore open circuit yields higher intensity and short circuit will result in a lower intensity.

- **Spectral peak position**: An induced forward voltage is in sympathy with the piezoelectric field in the QWs due to the well/barrier interface charge. This enhances the QCSE, redshifting the emission line. Therefore open

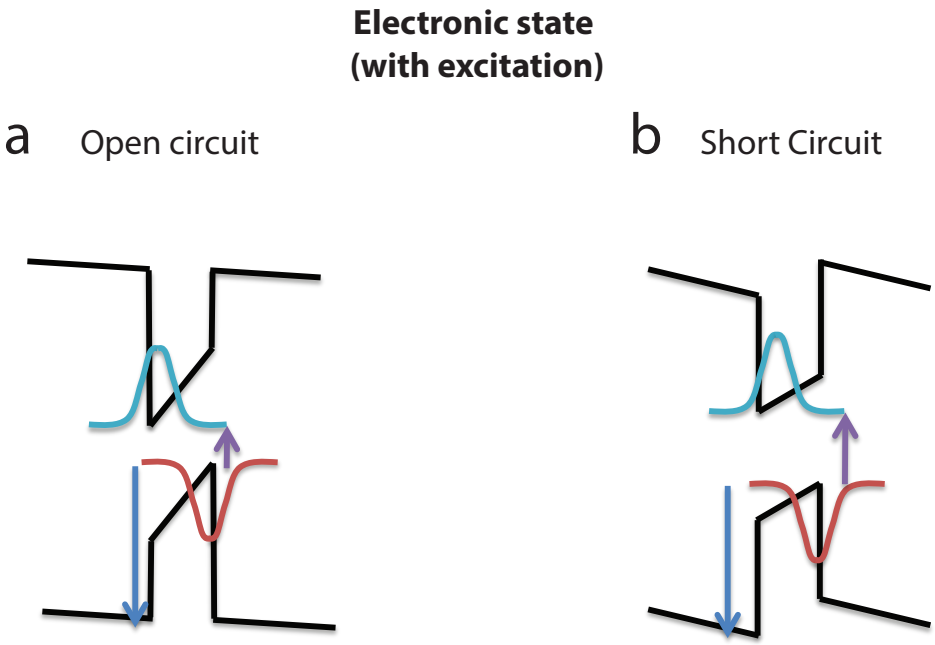

Spectral parameters

Increased	**Intensity**	Decreased
Redshift	**Peak Wavelenghth**	Blueshift
Broader	**Peak FWHM**	Narrower
Lower	**SE signal**	Higher

Figure 4.4: *The effect upon the spectral characteristics from recombination from a single InGaN quantum well within the depletion region of the LED. The device is in open or short circuit and under electron beam excitation.*

circuit will red shift the peak and short circuit will blue shift the peak position.

- **Spectral FWHM**: Increasing the QCSE leads to a spread in energy of the possible quantum states the electrons and holes can occupy - a broader emmision line. Therefore open circuit broadens the spectra and short circuit will narrow the spectra.

In the devices which are darker, bluer, and have narrowed emission lines, therefore, the electronic state will be closer to that figure 4.4(b) rather than (a). Devices with some leakage current, perhaps due to a misalignment of the mask during processing, approach the extreme version of figure 4.4(b), i.e. with no induced electro-voltage and the maximum possible induced current (without applying an external reverse bias). It was found during testing of LEDs, either using the probe station or upon wire bonding that around 10% of the total number of devices would exhibit a short circuit. A roughly equal amount showed large leakage currents ($\gg$100 μA) in reverse bias. This accounts for the fact that the LEDs on the wafer fall into more than just two categories (open circuit and closed circuit). If all the devices were either in short or open circuit, only two families of dies would be seen on the wafer plots. Those devices with intermediate intensities are likely those which have some leakage current but are not entirely short circuited.

4.3 Simultaneous CL and EBIC mapping under applied bias

The following section details a study of the sample using the CL, EBIC and EL mapping techniques described in the experimental section.

EBIC acts as a complementary technique to CL because it adds further information about the behaviour of generated charge carriers [128, 129, 32]. They will undergo one of three mutually exclusive processes: radiative recombination, non-radiative recombination or escape to the circuit. This is represented by the following equation:

$$G = R_{\mathrm{NR}} + R_{\mathrm{R}} + I_{\mathrm{EBIC}}/q \tag{4.1}$$

where G is the generation rate, R_{NR} and R_{R} the non radiative and radiative recombination rates, respectively and I_{EBIC} the EBIC current. Since CL gives a measure of R_{R}, EBIC directly measures I_{EBIC} and the size of G depends on the electron beam conditions, an indirect measure of relative non radiative recombination is made possible by simultaneous measurement of CL and EBIC.

Carrier recombination and transport in LEDs are also strongly influenced by

the applied electric field, both across the whole depletion region in the form of carrier overshoot and capture [130, 131, 132, 133], and also in the quantum wells themselves via tunnelling [65, 133] and the QCSE [101]. Consequently the applied voltage greatly affects the intensity and spectral characteristics of the CL spectrum as well as the EBIC. Both drift (equation 4.2), whereby excess electrons and holes are swept out of the depletion region by the net field, and tunnelling (equation 4.3) through the quantum barriers, act to remove carriers from the active region:

$$\mathbf{J}_{\text{drift}} \propto \mathbf{F} \tag{4.2}$$

$$\mathbf{J}_{\text{tunnel}} \propto \exp(-\Delta E/\mathbf{F}) \tag{4.3}$$

where $\mathbf{J}_{\text{drift}}$ and $\mathbf{J}_{\text{tunnel}}$ are the components of the current density due to drift and tunnelling, respectively, ΔE is the barrier height and $\mathbf{F}$ the electric field.

Above the LED turn-on voltage forward diffusion current dominates and electroluminescence (EL) occurs due to recombination of the injected carriers. Thus to avoid overlap of CL and EL signals all electron beam measurements were made below the turn-on voltage when the EL intensity is low. When a reverse bias is applied, the junction field strength and the width of the depletion region both increase. This has the effect of increasing the EBIC at the expense of the rates of both forms of recombination. Under forward bias, the field is compensated, reducing carrier loss mechanisms and leading to an increase in recombination in the active region.

To reduce any damage to the sample, which would have affected subsequent measurements of a given area, a low beam current of 1 nA was used and the spot was defocused to a diameter of 1 μm.

A DC source/measure unit (Keithley 2401) was used to drive the devices and also to record the beam induced current. The applied bias was varied from −2 V to +1.5 V in 0.5 V steps. The stage was scanned and at each point in the stage scan a full CL spectrum was collected by a CCD camera to build up a hyperspectral data-set. The CCD was set to trigger the source/measure unit to take readings of the beam induced current at each spectral acquisition, building up a beam induced current image simultaneously with the CL hyperspectral image.

The hyperspectral data sets were analysed using CHIMP, and each spectrum was fitted with a Voigt peak to extract 2D maps of peak intensity, position and width. The induced current maps were corrected for the diode "dark" current at each voltage by subtracting from every pixel a fixed value of the current, measured while the beam was switched off. As previously stated, all EBIC results presented are based on these corrected currents, i.e. only the extra current which the electron beam itself induces. Maps of the EBIC were plotted and analysed using the same software to compare the luminescence spectra to the induced current across the scanned area. Electroluminescence (EL) mapping (without the e-beam) was also performed by using the 8 μm pinhole as the entrance aperture of the spectrometer, producing maps with a spatial resolution of around 3 μm.

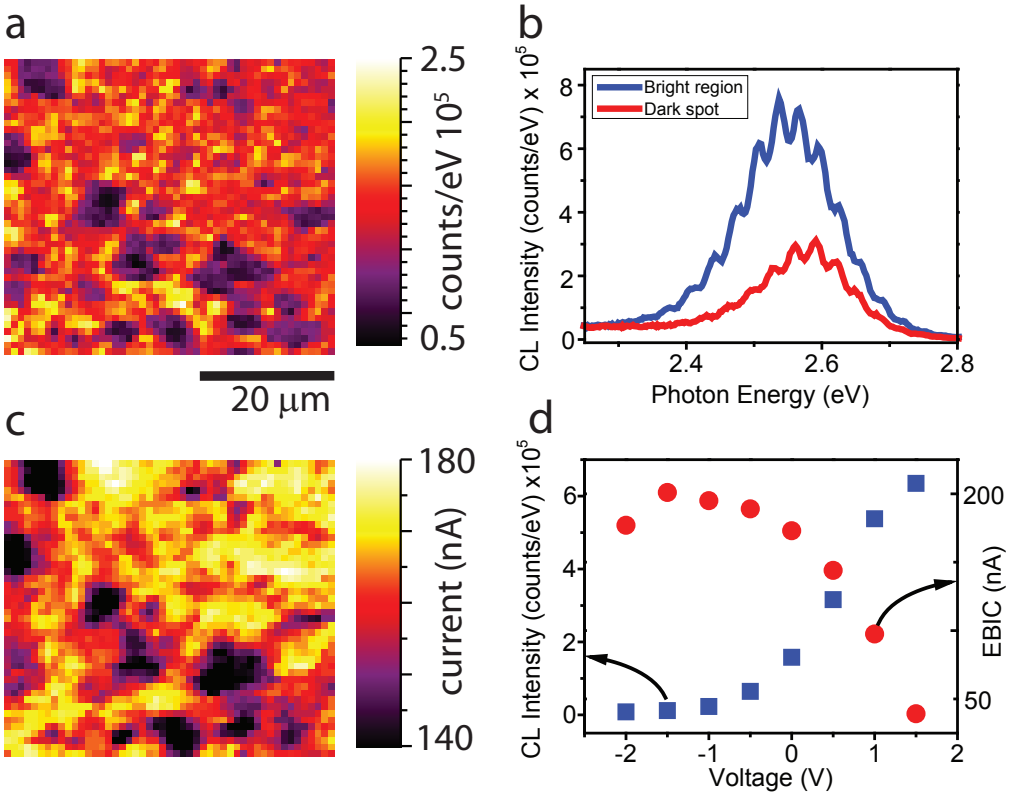

Figure 4.5: *CL (a) and EBIC (c) maps acquired from the LED at 0V . (b) typical CL spectra in the dark spots and background areas and (d) the mean CL intensity (squares) and mean EBIC (circles) vs. applied bias*

Figure 4.5 shows typical spectra (b) and maps of fitted CL intensity (a), and

EBIC (c) of a 49 × 44 μm^2 region of the LED from a device at short circuit (0 V). The dominant features in each map are patches around 5–10 μm in size which appear dark in both the CL and EBIC are also blue shifted. Given the independent nature of the three processes described in equation 4.1 these areas must have a higher rate of non radiative recombination. The background signal in both these maps appears non-uniform, but this is not unexpected since InGaN [134] material unlike binary GaN [125] is found to be generally non uniform in EBIC and CL. Fig 4.5 (d) plots the average MQW CL intensity and induced current for each map (averaged over all the pixels in the map) as a function of bias, and shows their reciprocal nature whereby the increase in electric field draws carriers away from the active region. The change in CL and EBIC are not linear and increase significantly at after the applied bias goes beyond −0.5 V, due to the flattening of the band structure around the p–n junction beyond this point.

A comparison of the electron beam measurements with the EL was made in order to investigate if the variations seen in the CL affect the luminescence uniformity of the device when under operation. Mapping of coincident CL, EBIC and EL is shown in figure 4.6. The area mapped is a different one to that from fig 4.5 but is from the same die. The dark spots are apparent in all three of the CL, EBIC and EL maps although with lower resolution in the EL due to the limiting size of the collection pinhole. However, additional features are visible in both the EL and EBIC. Large filament type structures with bright contrast run across the mapped area in the EBIC and EL data. These areas also correlate with a significant blueshift, of around 30 meV, in the EL emission peak. The EL was measured at 100 mA (∼3.2 V) (the CL/EBIC was collected, as before, at 0 V) where the dominant effect upon the emission wavelength is likely to be screening of the QCSE by the high free carrier density (heating effects were reduced by using a pulsed current source with 4% duty cycle). However the filament type contrast is not strong at all in the CL. A a higher radiative and lower non radiative recombination rates would be consistent with the increased EL and EBIC, but increased brightness in the CL would be expected if that were the cause. Only variations in and around quantum wells will contribute to the CL, and so the bright filament areas in the EL and EBIC could come from patches of increased conductivity in the p-type and/or n-type layer which do not directly effect CL intensity. Such areas would lead to higher carrier densities

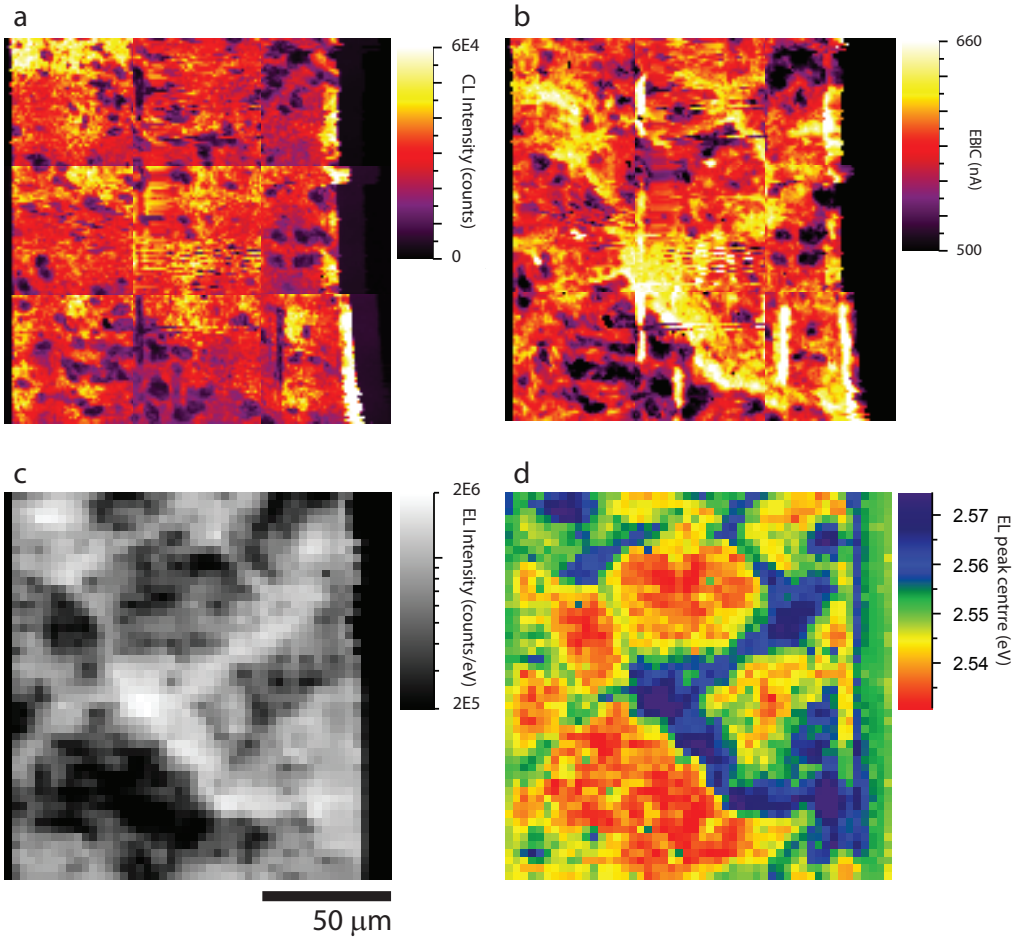

Figure 4.6: *Maps, from a different area showing the correlation between CL (a), EBIC (b) (both at 0 V), and EL intensity (c) and peak position (d) at 100 mA, 3.2 V*

in the MQW, giving brighter EL and allow a larger EBIC to escape from the depletion region. This would also explain the approximate 30–40 meV blue shift which is observed in these areas. Higher free carrier density would act to screen the in built piezoelectric fields, counteract the band bending in the quantum wells and so reduce the QCSE which would blueshift the emission peak.

A possible origin of these filament features is revealed in figure 4.7 (a) which compares an optical Nomarski image of the LED *template* with the EBIC map from figure 4.6. As stated in chapter 3, the template consists of the sapphire substrate, the nucleation layer and the nominally undoped 2 μm GaN layer. Striations similar to those seen in the EBIC and EL maps can be observed in the

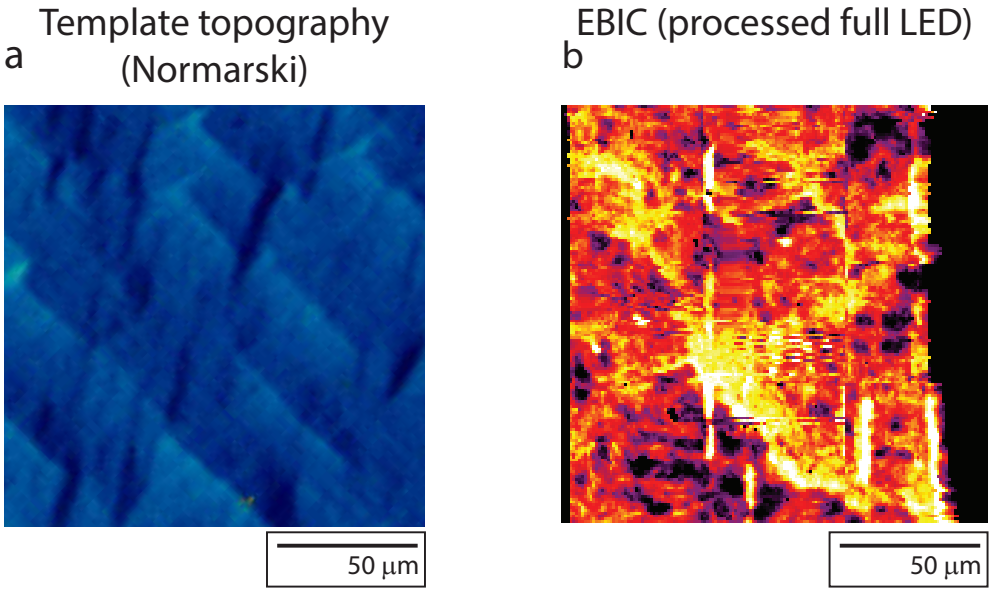

Figure 4.7: *Optical Nomarksi image of the LED template (before n-GaN growth) in (a) and EBIC map from figure 4.6*

Nomarski image in (a). It is important to note that this image is not from the same sample, but that the template used for the devices studied in this chapter is the same as the example in (a). The template has a threading dislocation density (TDD) of approximately 4×10^8 cm^{-2} and this is considered a low defect density (LDD) template in this work. A study of the effects of template TDD appears at the end of chapter 6. It is conceivable that variations in the thickness of the template are mirrored in similar thickness fluctuations in the active region. This presents another possible explanation for the blueshift and increased EL/EBIC. A local decrease in the thickness of the quantum wells would cause a blue shift in the emission peak due to increase quantum confinement and an increase in the probability of carriers tunnelling out of the wells [135, 32] increasing the EBIC signal and potentially lowering the CL signal. It is also possible that the variations in the template have affected the incorporation in InN in the corresponding areas of the active region. A lower InN percentage would blueshift the MQW emission line as well as increase the luminescence intensity and EBIC signal, due to an improvement in the local material quality. Further behaviour of the filaments is observed by studying the CL under an applied bias. Figure 4.8 shows sections of a

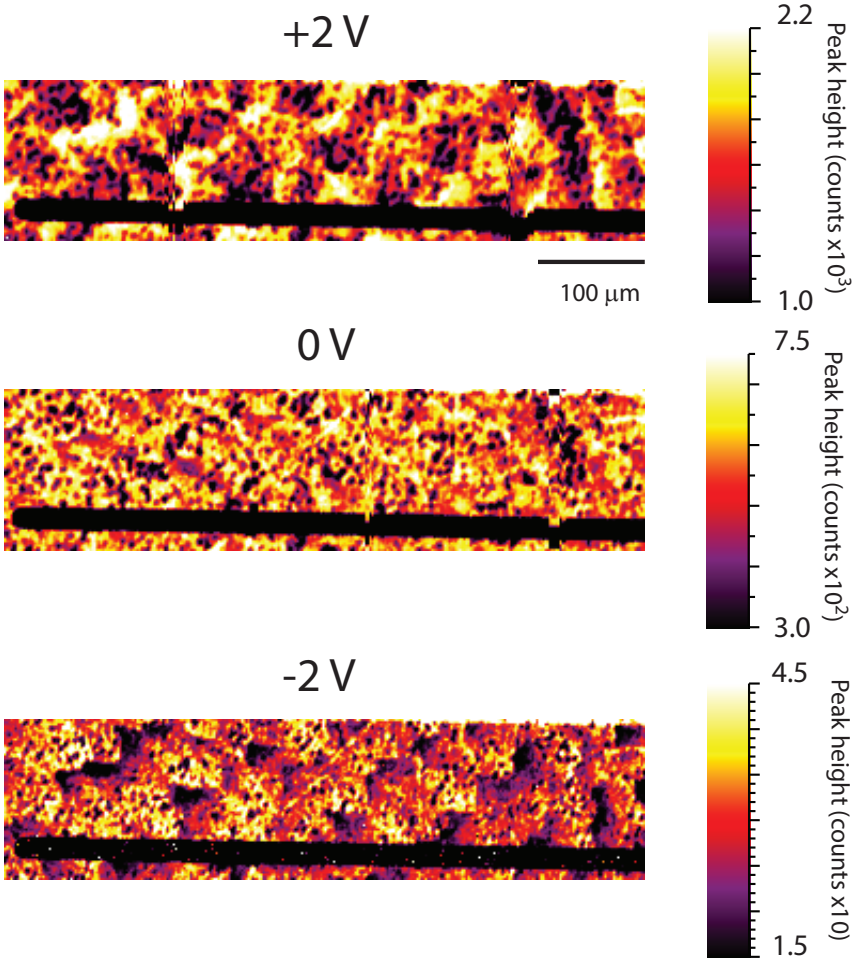

Figure 4.8: *MQW CL intensity maps of a segment of the same LED material at +2 V (a), 0 V (b) and -2 V (c) applied bias.*

MQW CL intensity map along the length of one of the *p*-type contact fingers. At 0 V (b) the uniformity is similar to the CL map in figure 4.6 (a) - the dark spots can be seen but the filament contrast is very low. However, at ± 2 V, the features are as clear as in the EBIC/EL maps. What is also conspicuous is the change in the contrast between +2 V and -2 V: in the former the filaments are brighter than the surroundings and in the latter they are darker. This suggests that the filaments are more sensitive to the change in electric field than the background. With a narrower quantum well, carriers can escape more easily as the electric field assisted tunnelling and drift escape probabilities are increased. At reverse bias, this is a strong effect due to the large electric field, and so those areas with

thinner quantum wells and/or barriers will exhibit lower radiative recombination. At +2 V where the junction field is nearly compensated, carrier escape is much lower, as discussed previously. In this case, decreased well thickness increases carrier density and results in an increased luminescence. If the effects were due to variation in InN content in the filament areas, one would not expect to have such a strong effect when changing in electric field in the active region. Therefore, while it is not possible to rule out changes in InN content, this suggests that material thickness variations are the primary source of the observed contrast.

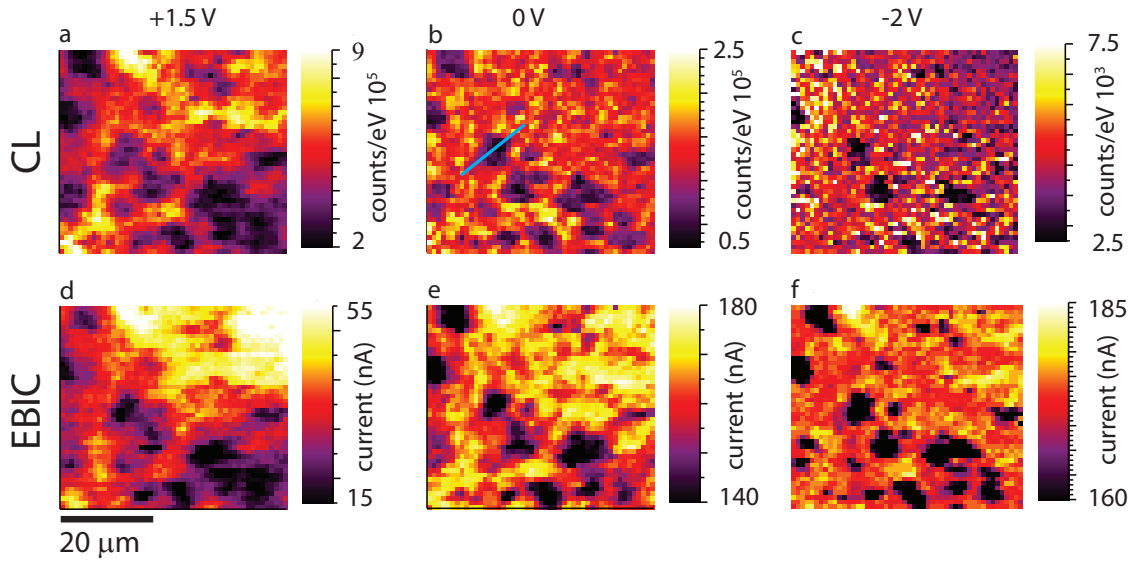

Figure 4.9: *Maps of the CL intensity (a,b,c) and EBIC (d,e,f) at +1.5, 0 and −2 V. The blue line in (b) shows the line scan which is presented in figure 4.10a*

The change in CL and EBIC as a function is bias is shown in figure 4.9 where maps collected with the device under biases of +1.5 V, 0 V and −2 V are shown. As shown in fig 4.5d, a drop in voltage from +1.5 V to −2 V causes the CL intensity to decrease and the induced current to increase, which fits the model of a larger electric field driving carriers out of the active region. It is evident from the CL maps that as the electric field in the junction is increased (i.e. a more negative applied bias) both the size and number of the dark features appears to decrease. To quantify the change, line scans were extracted from across several dark spots on the CL intensity and EBIC maps at each bias.

The scans from +1.5 V and −2 V in the CL are shown in fig 4.10a. The

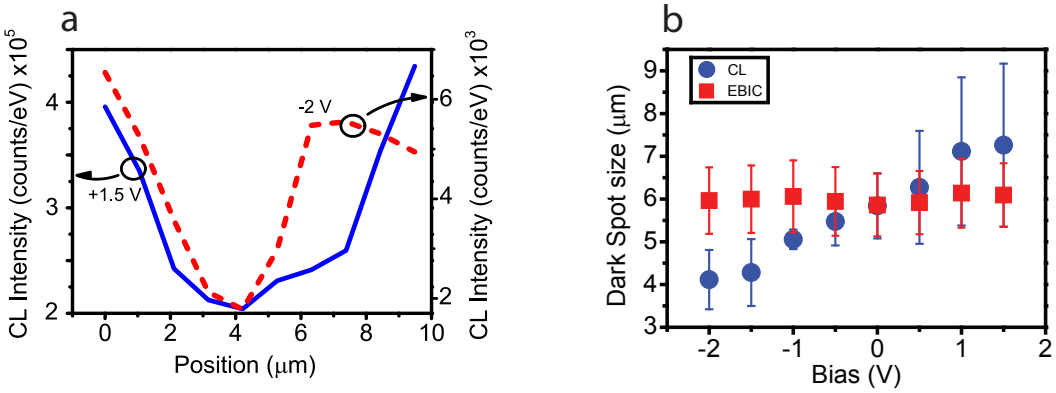

Figure 4.10: *(a) CL line scans taken from across the single dark spot, indicated by the blue line in figure 4.9, at +1.5 V (solid line) and −2 V (dashed line), and (b) estimated size of dark feature in CL (circles) and EBIC (squares) vs. bias. The error bars are due to averaging the size of several spots.*

traces show that the width of the dark areas is markedly reduced as the reverse bias increases. The size of the spots was estimated by measuring the FWHM of the central dips in the linescan and the results for all 8 maps in the bias series are shown in fig 4.10b. In the CL case, there is a linear increase in feature size from about 3 μm to 7 μm as the junction field is decreased. The EBIC data shows no clear change in spot size with bias. The error bars in the plots are due to the variation in the sizes of the dark spots across the sample. In the CL data the error bars seem to decrease closer to 0 V though it is not obvious why this would be the case. The spot size increase is within the plane of the quantum well, while the processes of carrier capture and escape are primarily in the growth direction, perpendicular to the plane of the wells. When the band structure in the *c*-direction (outside the quantum wells) is flatter (i.e. at forward bias) these processes are slower due to reduced drift velocity, giving the carriers longer to diffuse within the QW plane before recombining, thus explaining the increased feature sizes in CL. The invariance of the EBIC size is likely due to the fact that the EBIC current consists mostly of charge carriers which have drifted out of the active region, as opposed to tunnelling [32]. The carriers have a kinetic energy too large to be captured by the quantum wells, and therefore are not sensitive to diffusion in the quantum well plane. Since the CL comes *only* from the quantum

wells themselves we infer that EBIC contrast on this scale is affected by variation somewhere in the active region. However, since the majority of our EBIC current is due to carriers not captured by the quantum wells [32], we must conclude that whatever defect causes the decrease in CL intensity inside the quantum wells, must also affect the entire depletion region.

This implies that variation in the EBIC is observed on two levels: firstly in the large scale filament structures which, due to correlation with higher EL intensity and emission energy and lack of correlation with CL at 0 V, are possibly due to variations in quantum well thickness caused by the template, and possibly changes in the InN content. Secondly a spottiness in the optically active region which correlates with the dark spots in CL. AFM and electron channelling contrast imaging (ECCI) (not shown) estimated the threading dislocation density to be around 5x10^8 cm^{-2}. Given this we can conclude that these observed dark spots are not individual dislocation as, based on this density, the expected number of spots in our 2500 μm^{2}area would be over 10,000.

The dark spots are also found to be blueshifted, with respect to the background, by between 10–40 meV depending on applied bias. At 0 V the blue shift is approximately 20 meV, as seen in figure 4.11a. Fig 4.11b shows example spectra taken from a dark spot and a bright area at +1.5 V, 0 V and −1.5 V. Only the peak associated with the quantum well is shown. The rising background on the low energy side could be attributed to parasitic cyan emission [136] or the yellow defect band, excited in the *n*-GaN by the electron beam. In each of the series of spectra there is an approximately two orders of magnitude drop in intensity, accompanied by a blue shift. Fig 4.11c plots the peak position, as a function of bias, for an average of several dark spots and bright areas and the difference between these two values. The graph shows that, while the emission from the dark and bright areas both red shift with increasing bias, the peaks in the dark spot spectra only shift by around 30 meV with those from the brighter areas changing by almost twice as much. The voltage drop across the active region acts to change the potential inside the quantum wells. Assuming an abrupt *p*–*i*–*n* junction, the field in the depletion region can be expressed as [137]

$$E_{\mathrm{dp}} = \frac{2\sqrt{V_{\mathrm{bi}}(V_{\mathrm{bi}} - V_{\mathrm{a}})}}{W_0} \tag{4.4}$$

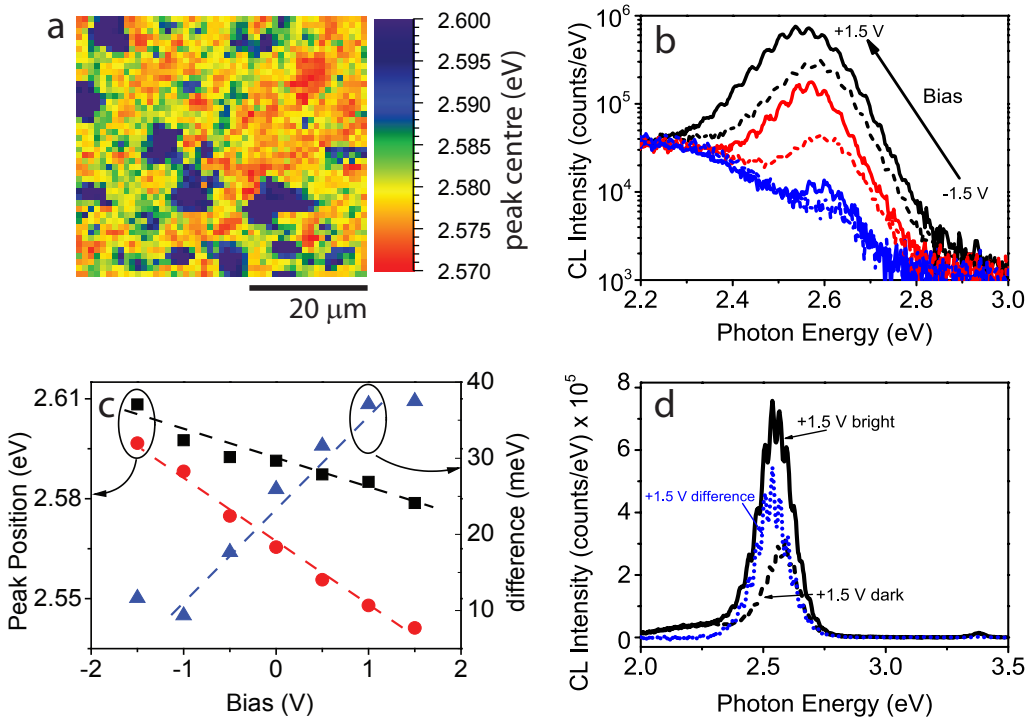

Figure 4.11: *(a) Map of the CL peak energy fit at 0 V; (b) Sample spectra, centred on the MQW emission band, from bright area (solid lines) and dark spot (dashed lines) at −1.5, 0 and +1.5 V; (c) peak position as a function of bias for bright area (circles), dark spots (squares) and the difference (triangles) (the dashed lines are guides to the eye); and (d) subtraction of dark area spectrum from bright area spectrum at +1.5 V highest peak in the from a bright area, lowest from a dark area and the dotted line is the difference*

where E_{dp} is the electric field across the depletion region, V_{bi} is the built-in voltage, V_{a} is the applied bias, and W_0 is the width of the depletion region in thermal equilibrium. Using the values of N_{d} and N_{a} quoted in the introduction along with literature values of the intrinsic carrier concentration of GaN, V_{bi} and W_0 were calculated, respectively, to be 3.3 V and ≈ 100 nm. Since our concern is the effect of the *change* in bias upon the *change* in transition energy it was sufficient to calculate the electric field, using eqn 4.4, between the two extremes of our applied biases (±1.5 V). The change in electric field was found to be 3.1×10^5 V/cm. Across each quantum well of 2.4 nm, the resultant change in potential energy of the charge carriers is 3.1×10^5V/cm × 2.4nm = 74mV, or 74 meV per charge carrier.

The experimentally observed blueshift in the bright region, when changing bias from +1.5 to -1.5 V, is ~ 61 meV. This is within 15% of the calculated effect of the change in bias (74 meV). The difference could be due to a number of factors. Firstly, the change in carrier energy is not trivially linked to the potential energy change in the well due to the offset added to the band structure by the QCSE. Secondly, based on previous arguments, the number of electron/hole pairs in and around the depletion region is not invariant with applied bias; at larger reverse biases more charge contributes to the EBIC. As a consequence the screening of the QCSE also diminishes, and this would reduce the observed blue-shift as the reverse bias increases: in effect adding a linear offset to the peak position plot. Given these additional effects, it is likely that the biggest contribution to the peak shift in the bright areas is the change in electric field caused by the applied bias. In the dark regions however, the shift is much smaller and this implies that something more complicated is going on here; in order for the 30 meV shift seen in these areas to be accounted for purely by the change in applied electric field would require either a lower electric field across the depletion region or a reduction in the thickness of the quantum wells. A more probable cause is related to the correlation of the peak position with the lower EBIC and CL intensity. An explanation for the dark spots based purely on areas of increased non radiative recombination cannot account for the large blue shift. The drop in EBIC could be due to increased trapping of carriers in these area by point defects. This extra charge would act to blue shift the spectra through screening of the QCSE. This explains both the difference in peak positions between the dark spots and bright areas and why the change in peak position occurs at a different rate, as a function of bias, in the two areas.

In conclusion, using a combination of CL and EBIC under varying bias, along with complementary EL mapping, it has been possible to investigate the luminescence and conductivity micron scale variations across a single LED as a function of the electric field across the active region. Large domains ($\sim$ 100 μm) of increased conductivity in either the p-type or n-type material were revealed by a correlation of bright contrast in EL and EBIC, and in the CL at forward or reverse bias. Correlation with Nomarski images indicates the origin comes from fluctuations in the template thickness. Small regions in the quantum wells, around 2–10 μm across, were found to yield lower signals for both cathodoluminescence

and beam induced current, indicating areas of increased non radiative recombination. The observed sizes of the dark spots in the CL maps change with applied bias, becoming larger as the field across the depletion region is reduced and the free carriers are able to diffuse further in the plane of the quantum well before recombining. The spectral emission was blue shifted within the dark regions. The origin of the dark spots was suggested to be due to clusters of non-radiative point defects which can cause in increase in carrier trapping in the depletion region and subsequent reduced radiative recombination and EBIC and increased screening of the QCSE leading to a large blueshift of the emission line.

4.4 Depth and bias dependent Cathodoluminescence

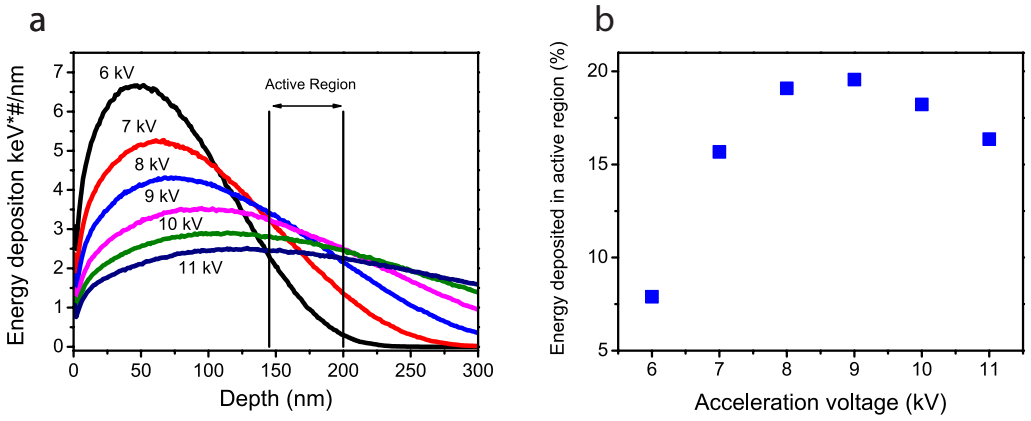

Figure 4.12: *(a) Monte Carlo simulation of the electron beam energy deposition in the sample. The two vertical dark lines mark the approximate extent of active region. The plots have been normalized such that the area under each curve (i.e. the total deposited energy) is the same. This has been done to reflect the conditions of the experiment. (b) shows the percentage of the total beam energy deposited in the QW region as a function of the acceleration voltage.*

In this section the effect of the applied bias on carrier transport into the active region is studied by using a varying electron beam acceleration voltage to control where the charge carriers are generated, with respect to the active region.

In the previous sections of this chapter, all of the CL and EBIC measurements were performed with a single, fixed, electron beam acceleration voltage of 10 kV. As discussed in chapter 2, the selection of the acceleration voltage is of crucial importance in determining the carrier generation profile as function of depth. This has consequences for LED analysis because the active region, which is to be probed, sits at a some depth below the surface of the structure ($>$ 100 nm) and extends for a finite depth ($\approx$ 50 nm). For a given total deposited beam power (i.e where keV $\times$ beam current = constant) very low and very large acceleration voltages will result in relatively little of the total energy being deposited in the active region. In the sample discussed here, the depth from the surface to the quantum wells is found by adding the thickness of the *p*-GaN to the thickness of the Ni/Au current spreading layer i.e.

$$z_1 = T_{p-\mathrm{GaN}} + T_{\mathrm{NiAu}} = 135\ nm + 10\ nm = \underline{145\ nm}$$
$$z_2 = z_1 + T_{\mathrm{MQW}} = 145\ nm + 55\ nm = \underline{200\ nm}$$

Where z_1 and z_2 are the start and end of the active region, T_{NiAu}, T_{p-GaN} and T_{MQW} are the thickness of the current spreading layer, *p*-GaN and multi-quantum well stack, respectively. The thickness of the active region itself is simply $(T_{well}+T_{barrier})\times\ 5\ +\ T_{barrier}$. Monte Carlo simulations using CASINO [121], similar to those shown as examples in chapter 3, were performed to relate the acceleration voltage to the deposition of energy in the active region in the LED. Figure 4.12(a) shows the energy deposition curves in the sample for electron beam energies from 6 keV to 11 keV. The curves are normalized so that the total energy deposited in the structure is the same for each acceleration voltage. The active region from 145 nm to 200 nm is marked by the vertical lines. Figure 4.12(b) shows the energy deposited in the active region as a function of acceleration voltage. As can be seen the peak is around 9 kV where just over 20% of the total energy is deposited within the QWs and this drops to less than 10% at 6 kV and around 15% at 11 kV. Simplistically, this would suggest that the CL signal at 6 kV and 11 kV would be expected to be, respectively, 50% and 75% of that seen at 9 kV. The simulation, however, does not account for the effects of the inbuilt junction field or of the quantum wells in the active region. In this section, the

effects of the electric field on the acceleration voltage dependent CL intensity are investigated.

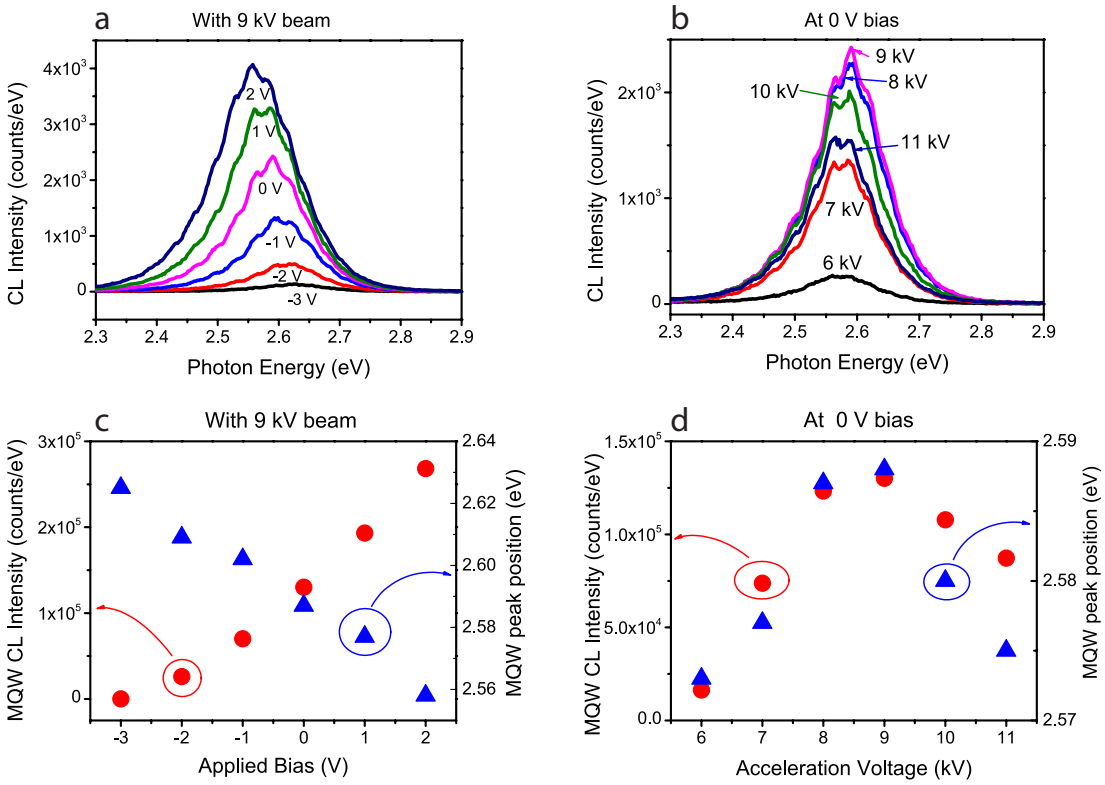

Figure 4.13: *Sample bias dependent, at 9 kV, (a) and acceleration voltage dependent, at 0 V, (b) CL spectra centred around the MQW peak. (c) and (d) are plots of the respective MQW intensity and peak positions as a function of applied bias (c) and beam voltage (d).*

CL spectra were obtained in the EPMA from an virgin LED die. The beam acceleration voltage was varied from 6 kV to 11 kV in 0.2 kV steps and at each voltage the beam current was adjusted in order that the product of the beam voltage and current (i.e the delivered power) was constant. In order to prevent each measurement affecting the subsequent one (by changing the sample) the beam was defocused to 1 μm and set to quickly raster scan over a 100×100 μm^2 area. The acquisition time assigned for the collection of each spectrum was chosen to be several orders of magnitude longer than the scan time. This was done to prevent the mean spectra oversampling the top part of the scan area, when the

acquisition stops during the middle of a scan. At each beam acceleration voltage the applied bias across the die was varied from -3 V to +2 V in 1 V steps and a spectrum was acquired for each bias. A sample of the spectra are shown in figure 4.13 (a) and (b) which are plots of, respectively, the CL spectra from -3 V to 2 V at a fixed beam voltage of 9 kV and the CL spectra from 6 kV to 11 kV at a fixed applied bias of 0 V. The spectra are centred around the MQW peak to emphasise the effects upon the active region. The plots in (c) and (d) show the peak intensities and positions from the spectra in (a) and (b), respectively. The applied bias in (c) causes a redshift with increasing forward bias, due to enhancement of the QCSE. This is accompanied by an increase in the luminescence intensity due to a reduction in the overall depletion region field which lowers carrier escape from the active region. The effect of increasing the acceleration voltage, in (d), is that both the peak intensity and position reach a maximum at around 9 kV, and the curve shapes are similar to those seen in the simulation of the energy deposition within the wells in figure 4.12(b). The increased carrier generation is trivially responsible for the increase in luminescence, and it is also the cause of the blueshift. The larger free carrier density screens the polarization fields at the quantum well/barrier interface and results in a reduction of the QCSE, increasing the QW transition energy.

In figure 4.14(a) the MQW CL intensity as function of beam voltage is plotted at a bias of +1V and -2 V along with the simulated energy deposition. The plots are normalised to their own maxima (at 9 kV). The CL intensity plot is most similar to the simulated energy deposition at a forward applied bias. At reverse bias, there is a larger relative decrease in intensity, from the 9 kV maximum, than would be expected based on the energy deposition alone. Figure 4.14 (b) plots the acceleration voltage dependent MQW CL for each applied bias, normalised to their own mean values. As can be seen, the beam voltage dependence of the CL is extremely sensitive to the applied bias across the LED. Below a bias of +1 V, either increasing or decreasing the beam voltage from 9 kV drops the luminescence intensity by a large degree, up to a factor of 5 $\times$ at -3 V.

The size of this decrease is plotted in (c) which shows the average drops in CL intensity either side of the 9 kV maximum. A clear trend shows that with increasing reverse bias the CL intensity becomes more sensitive to the acceleration voltage and the related deposition profile.

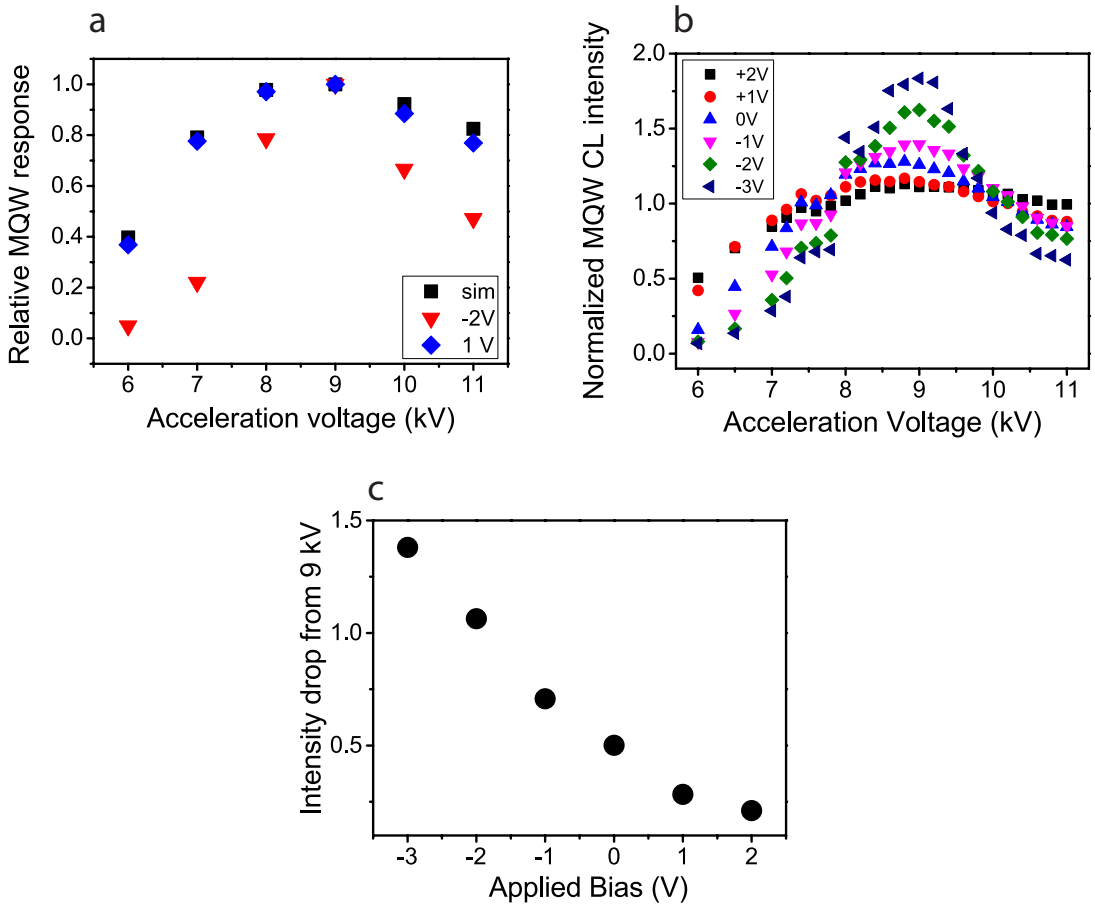

Figure 4.14: *Comparison of the relative MQW CL intensity at +1 V and -2 V with the simulated energy deposition (a). (b) is the acceleration voltage dependent CL for each bias, normalized to each bias series mean. (c) is a plot of the average drop in CL intensity on either side of the 9 kV maximum.*

The high sensitivity at reverse bias is due to the large electric field across the active region and the effect it has on carriers generated outside the region. Such electrons and holes must diffuse for some distance in order to be captured by a quantum well, and this is less likely when the depletion region is both wider and has a larger electric across it. At forward bias, when the band structure is flatter, carrier diffusion into the depletion region is not countered by a large electric field and so shifting the deposition energy to outside the MQW stack has proportionately less effect on the final luminescence intensity. Conversely at reverse bias, where there is a large electric field across the depletion region, diffusion toward

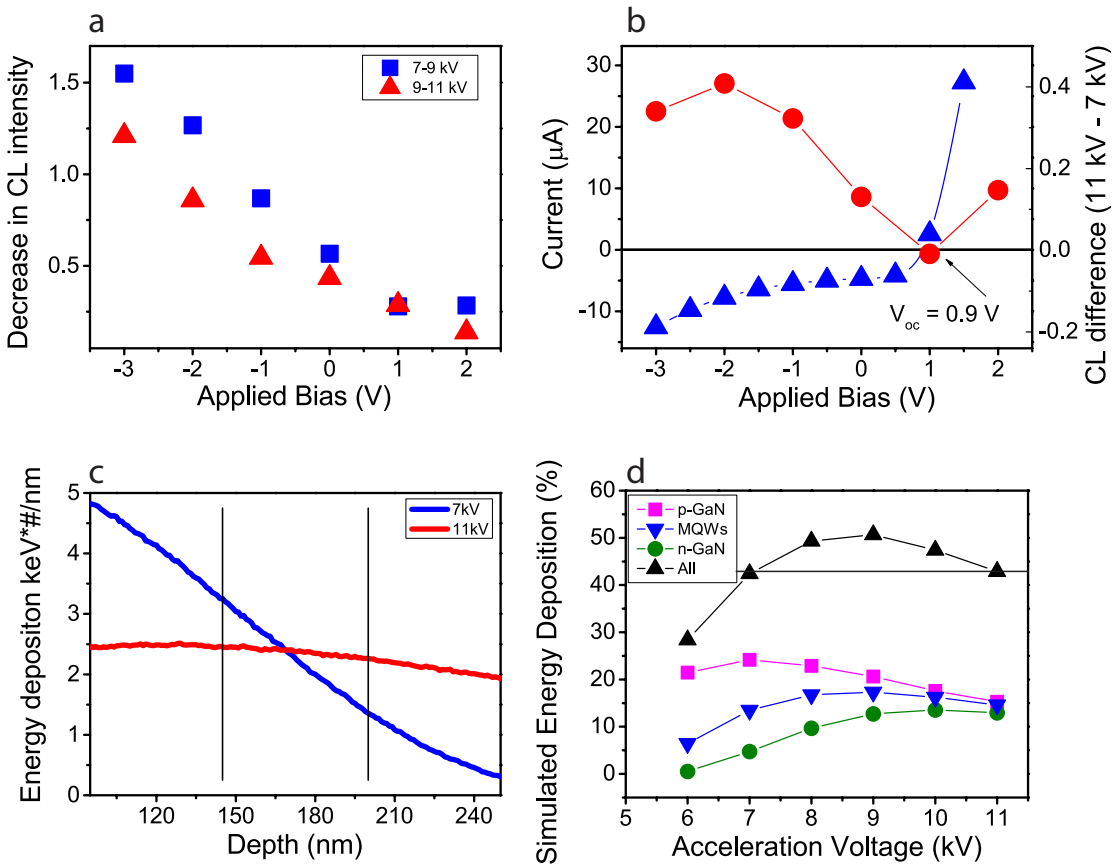

Figure 4.15: *Plot of the difference between the, normalised, MQW CL intensity at 9 kV and 7 kV (squares) and 11 kV (triangles) (a). (b) plots the difference between the CL intensity at 11 kV and 7 kV, along with the diode I-V relation under electron beam excitation. The plot in (c) shows the Monte Carlo energy deposition simulation at 7 kV and 11 kV, in the 50 nm either side of the active region and (d) plots the deposition of energy within the annotated regions of the LED.*

the MQWs is retarded by the field. As such there is less contribution from carriers not generated directly in the active region and so moving the energy deposition away from the MQWs results in a larger decrease in relative CL intensity.

The reduction in CL intensity caused by changing the beam voltage away from the 9 kV maximum is not symmetrical; decreasing to 7 kV reduces the intensity more than increasing to 11 kV. This is shown in figure 4.15 (a), which plots the drop in CL intensity in the range 9 - 7 kV (squares) and 11 - 9 kV (triangles).

The comparison between 7 kV and 11 kV is significant because the total energy deposition around the active region at these beam voltages is almost identical. However, at 7 kV the deposition is mostly in the *p*-GaN and at 11 kV, more is in the *n*-GaN. Figure 4.15 (a) is similar to the average decrease plotted in figure 4.14 (c), but draws out the difference in the MQW CL between deposition in the *p*-type GaN versus the *n*-type GaN.

The difference between the two curves in (a) is plotted in (b) along with the I-V characteristic of the die. The plot is just the difference in intensity between 7 kV and 11 kV. Note that the I-V curve is an average of the I-V curves at each acceleration voltage, which are nearly identical due to fixed power deposition. By extrapolating from the data points, the open circuit voltage (at which point no current flows) was found to be approximately 0.9 V. At +1 V, close to the open circuit point, the CL intensity at 7 kV and 11 kV is nearly identical. Away from this voltage, the CL is more intense at 11 kV.

The comparison between 7 kV and 11 kV is significant because the total energy deposition around the active region at these beam voltages is almost identical. This is demonstrated in figures 4.15 (c) and (d) which, respectively, highlight the energy deposition curves for 7 kV and 11 kV near the active region (c) and plot the energy deposition percentage for different regions of the LED (d). As can be seen in the plot in (d) and in table 4.1, the total energy deposition, at both 7 kV and 11 kV, into the MQW and into the 50 nm to either side of it (into the *p* and *n*-GaN) is approximately 43%. At 7 kV, about 5× as much energy goes into the *p*-GaN as the *n*-GaN, while at 11 kV the deposition is roughly evenly split across the ∼150 nm region.

Beam voltage (kV)	MQW	50 nm *p*-GaN	50 nm *n-GaN*	total
7	13.5%	24.1%	4.7%	42.4%
11	14.6%	15.2%	13.0%	42.9%

Table 4.1: *Tabulated beam energy deposition percentages at 7 kV and 11 kV.*

At open circuit, there is, by definition, no net carrier motion and so luminescence can only come from steady state carrier density generated directly in the active region. Figure 4.16 plots the CL spectra at 7 kV and 11 kV for both -1 V and +1 V (near the open circuit voltage). As shown in (a) the MQW CL is identical at 7 kV and 11 kV, near the open circuit. This suggests that the

contribution to the luminescence from carriers generated in the active region is the same at both acceleration voltages. Therefore, the increased luminescence at 11 kV away from open circuit, as shown in (b), must be due to the contribution from carriers diffusing to the MQWs from the p and n-GaN. Since the deposition at 11 kV, compared to that at 7 kV, is weighted to the n-GaN as opposed to the p-GaN, this could be accounted for by more efficient carrier transport through the n-GaN than the p-GaN. The diffusion length of minority carriers in p-type and n-type GaN has been reported in the literature at various values. For n-GaN, with a majority carrier density around 10^{18}cm^{-2}, the minority carrier (hole) diffusion length has been variously reported as between 70 nm [138], 200 nm [139], 300 nm [140, 141] and up to 400 nm [142]. For p-type, the reported values are similarly wide, and depend more on magnesium concentration that n-type does on silicon concentration. Values of 70 nm [138], 90 nm [140], 140 nm [139] have been reported. Given this, it is reasonable to conclude that the brighter luminescence at 11 kV (compared to 7 kV) is due to the difference between carrier generation in the p and n at these two voltages and the resultant improved net carrier transport into the MQWs at 11 kV.

In summary, the effect of interplay between the electric field and the generation profile to carrier motion in the LED has been explored via bias and depth dependent CL. It was found that the applied bias has a strong effect on the beam voltage dependence of the MQW CL. At reverse bias, a larger drop in intensity

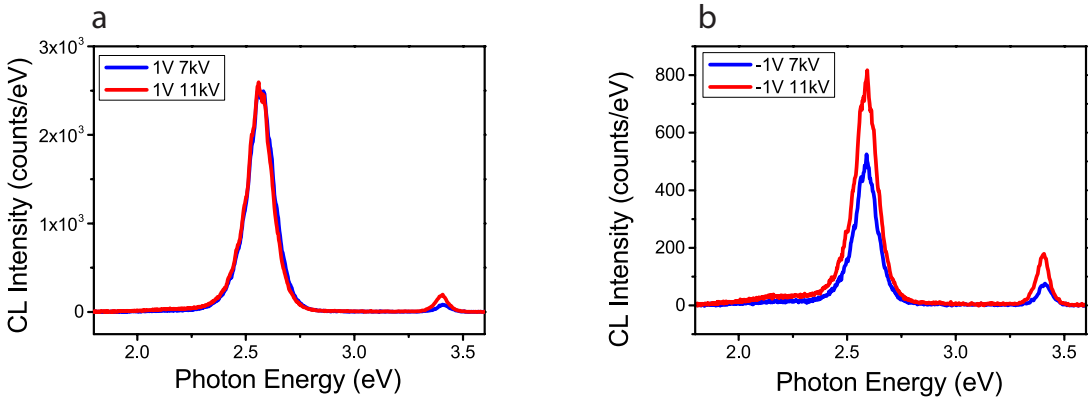

Figure 4.16: *CL spectra at 1 V (a) -1 V (b) at acceleration voltages of 7 kV and 11 kV.*

was seen when moving away from the beam voltage which gives the maximum signal. Stronger carrier diffusion in the n-GaN was revealed by comparing the MQW CL intensity at 7 kV and 11 kV, where the total energy deposition around the active region was the same. The increased intensity at 11 kV was due to the increased deposition of energy in the n-GaN, where carrier diffusion was found to be stronger. The only exception was at the open circuit voltage ($\sim$+1 V), where the intensity was the same. This is due to there being no diffusion contribution from outside the active region.

4.5 Bias and excitation dependent Photoluminescence

As seen in the previous sections, electron beam excitation results in carrier generation throughout the entirety of the LED structure, inside and outside the quantum wells. The depth resolved measurements demonstrated the importance of carrier transport to the active region. In this section the effect of direct carrier generation in the quantum wells is compared to indirect generation via the use of above and below bandgap excitation as a function of applied bias.

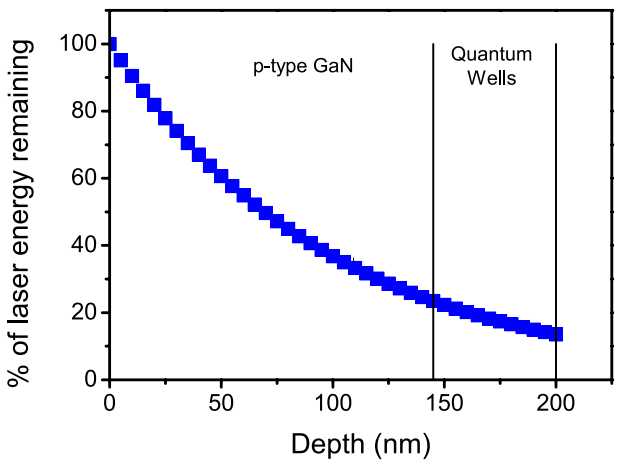

Figure 4.17: *Plot of the energy loss of the 325 nm laser as a function depth travelled through the LED*

Photoluminescence spot measurements were performed in the manner de-

scribed in chapter 3, using both the 405 nm diode laser and 325 nm He-Cd laser. With the 405 nm excitation, carrier generation occurs only within the InGaN as the photon energy is too low to promote electrons from the valence to the conduction band in GaN. Generation with the 325 nm beam is, in some ways, similar to the electron beam excitation in that carriers are created in the *p*-GaN and quantum barriers as well as in the quantum wells. After the various beam propagation and focusing steps the maximum power of the lasers on the sample surface was 4 mW and $\sim$ 32 mW for the He-Cd and diode, respectively. Neutral density filters were placed in the beam path to reduced the intensity to study the effect of a change in incident power. The absorption of the 325 nm laser in the GaN is a function of penetration depth though the material. This is expressed via the Beer-Lambert relation:

$$I_z = I_0 e^{-\alpha z} \tag{4.5}$$

where I_z is the radiance after a distance z, I_0 is the initial radiance, and z is the distance from the material surface. The absorption coefficient, α, is dependent upon both the material and the laser wavelength. In GaN at a photon energy of 3.815 eV (325 nm), α is around $1.2\times\ 10^{-5}$ cm^{-1} [143]. The function is plotted in figure 4.17 which shows the percentage of the incident laser energy remaining as a function of depth from the surface. As in figure 4.12(a), the approximate position of the optically active region is indicated by the black lines. At this point the laser energy has reduced to 20% of it's initial value, and the decay from 100 nm to 200 nm is similar to the profile of the CL energy deposition at around 6–7 kV shown in fig 4.12(a).

A bias of between -4 V and +2 V was applied across the LED and spectra recorded at each voltage.

Figures 4.18 shows a comparison of the results obtained with the He-Cd and diode lasers. The PL spectra as a function of bias, from the two lasers are shown in (a) and (b) respectively. The most obvious difference between the two is the presence of the yellow band emission and GaN bandedge peak at 3.4 eV in the He-Cd spectra. The former is result of defect related recombination in the *p*-type material, while the latter gives an indication that the laser energy reaches the *n*-GaN as bandedge emission is rarely seen in heavily doped *p*-GaN at room

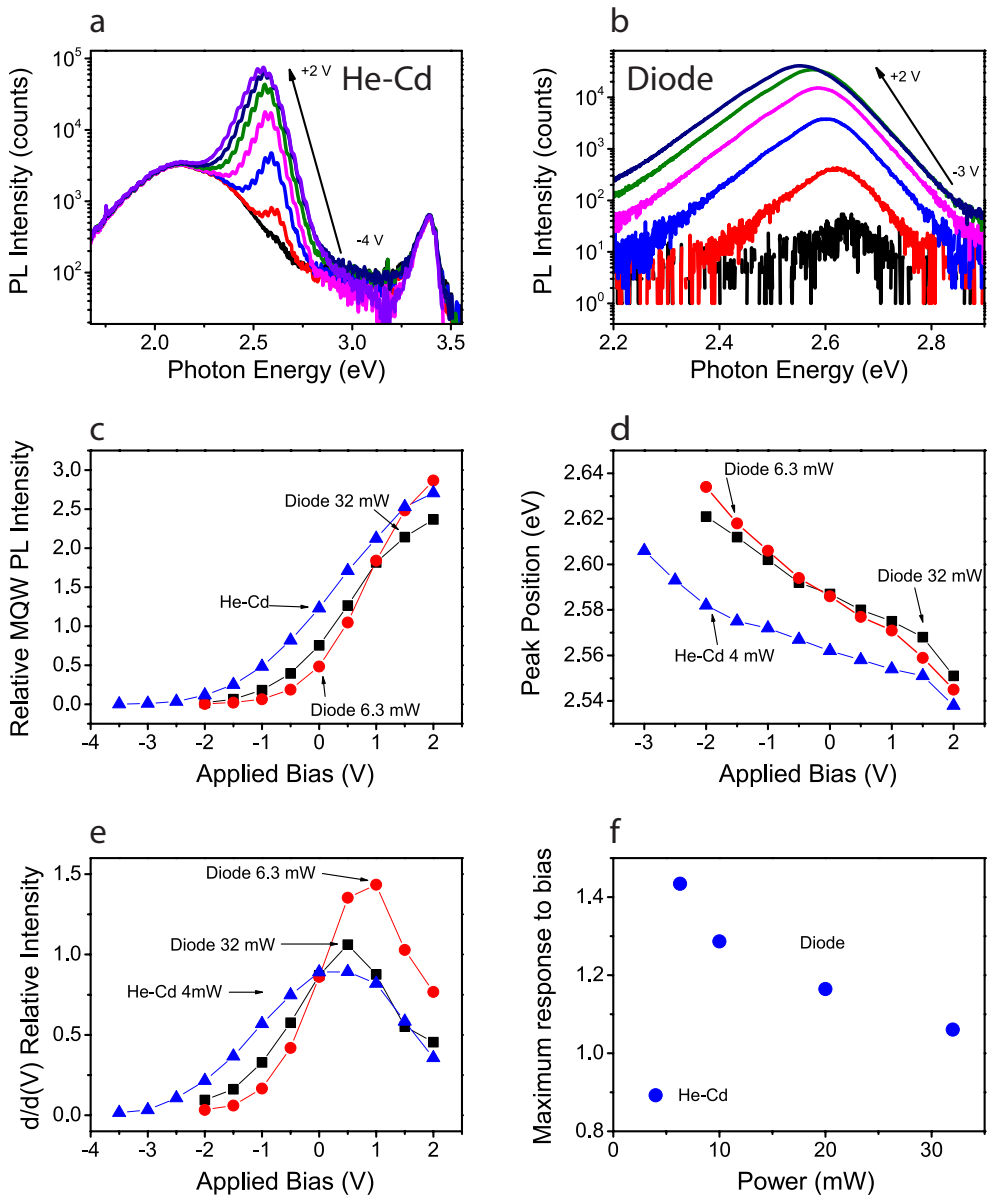

Figure 4.18: *Photoluminescence spectra of the LED and associated data acquired with indirect (325 nm He-Cd) and direct (405 nm diode) laser excitation. (a) and (b) are the bias dependent PL spectra at room temperature for the He-Cd and diode lasers, respectively. (c) and (d) plot, respectively, the normalised MQW intensity and peak position for the He-Cd at 4 mW and the diode at 6.3 mW and 32 mW. (e) is a graph of the 1st derivative of the plots in (b) (and two more diode laser powers) to show the response to the bias and (f) plots the maximum values from (e).*

temperature. The MQW luminescence peaks in both cases blue shift and decrease in intensity as the reverse bias is increased, as seen in the previous sections.

Neither the yellow band or bandedge luminescence are affected by the change in bias, which is expected as the electrons and holes which escape the active region due to the applied bias, exit at opposite sides of the depletion region.

The MQW PL intensity is plotted as a function of applied bias in (c) for the He-Cd and diode excitation at 6.3 and 32 mW. As in the depth resolved CL section, the intensity has been normalised to the mean of each series to show the relative variation with the change in the bias. There is a marked difference between the diode and He-Cd response to the applied bias, especially at reverse bias. Using 325 nm excitation the intensity increases quickly as the voltage is increased from -2 V. With the 405 nm, however there is a noticeably later "turn on" of the luminescence. This effect is demonstrated in (e) which plots the first derivative of the three series in (c).

Regardless of the laser power each of the series from the diode are very similar between -2 V and 0 V, with the major difference being that for lower laser powers the maximum gradient is larger and occurs at a slightly higher forward voltage. The He-Cd, however, responds more to the change in voltage at reverse bias but less at positive forward voltages.

In the 405 nm excitation, carriers are generated only within the quantum wells and carrier loss from the active region will be primarily through tunnelling processes. The increase in luminescence intensity in the 405 nm laser excited series is due to a reduction in tunnelling, as opposed to the He-Cd where the increase will be in part due to improved carrier transport into the active region. The result implies that, at reverse bias, when the bias is increased in the forward direction there is relatively little reduction in tunnelling meditated escape from the active region compared to the improvement of carrier capture by the active region through the reduction in drift mediated escape. At around 0.5 V the effect of flattening the overall band structure further, thereby reducing drift related escape effects is lower than the gains due to the reduction in tunnelling from the QWs. This effect is supported by both the difference in the He-Cd to diode response and by the plot in figure 4.18 (f) which shows the maximum values from (e) a function of laser power. For the diode, lower incident powers result in a larger response to the bias around 0.5 V - this is due to the relative

importance of tunnelling and drift with different carrier densities. At lower laser powers occupation of quantum wells will be less dense and there is a lower chance of thermionic escape from the wells. At higher powers, therefore, there is an increased likelihood of carrier escape from the active region due to drift.

This section follows on from the previous one in demonstrating the importance of the carrier generation profile in regards to the bias dependent luminescence. With direct excitation of the quantum wells it was found that there is a relatively weak response to increased forward voltage at reverse bias and a strong dependence closer to flat band conditions. The dependence was found to be stronger at lower carrier densities suggesting that the increase was due to a decrease in tunnelling. This was supported by the response to indirect excitation, where at reverse bias, an increase in bias has a stronger effect on intensity whereas near flat band conditions the response is weak. This is due to the increased importance of transport to the depletion region and reduction in drift mediated escape.

4.6 Summary

This chapter has demonstrated the strong effect of the inbuilt, piezoelectric and applied electric fields upon LED luminescence. The effect was first explored via the observation of die to die variations on a wafer, indicating the importance of appreciating the effects of the e-beam measurement upon the electronic state of the LEDs, as well as a potential check on the uniformity and success of processing. The combined CL-EBIC study of the LED revealed dark spots where non radiative recombination occurs and, via the effects on the peak position revealed through bias dependence, where charge may be trapped. The location of the defects was probed via the bias dependence size and intensity of the CL and EBIC signals from the spots, indicating that they exist not just in the QWs but through the active region. Based on this, the origin of the dark spots were suggested to be due ot clusters of point defects in the active region. Bias and depth dependent CL was used to compare minority carrier transport in the p-type and n-type GaN. At 7 kV and 11 kV, where the energy deposition around the active region is very similar, the CL intensity was found to be larger at 11 kV when generation is weighted to the n-GaN, suggested improved carrier transport from that side of the depletion region. Using power dependent PL, the effect of the applied bias

was found to be three fold - prevention of majority carrier escape from the active region, reduction in tunnelling through the QWs and greater ease of diffusion based transport to the QWs.

Chapter 5

Effect of the barrier growth mode on the luminescence and conductivity of InGaN LEDs

5.1 Introduction

The industry standard for high efficiency blue/white/green light emitting diodes (LEDs) involves the use of InGaN/GaN multi-quantum well (MQW) /quantum barrier (QB) active regions to increase carrier densities and radiative recombination efficiency and to increase the total light emitting volume. The high quality growth of these layers is of importance to both the optical and electrical characteristics of such devices. The optimum temperature for the growth of high quality GaN is around 1050 °C [24]. However, since indium nitride has a low dissociation temperature (550 °C), [144] GaN barriers have to be grown at lower temperatures to maintain high indium nitride content in the wells. Aside from growing the barriers and wells at a single temperature, optimal for InGaN deposition (around 700–800 °C [145] for InN % $\sim$ 10-20%) — which we define as the 1T method — there are several methods used by groups, including those at University of Cambridge, to balance indium desorption and barrier crystal quality. One is the so called two-temperature (2T), [145, 146, 147] approach where the temperature is ramped up and down between around 900 °C for the barrier and 750 °C for the wells. This is expected to improve the crystal quality of

the GaN, but results in an increased indium loss from the QW [148]. Another method, quasi two-temperature (Q2T) [144, 149, 150, 151], is to grow the first few nanometers of the GaN barriers at the InGaN growth temperature before growing the remainder at the higher temperature which serves to provide a protective cap on each quantum well. In this work a fourth method was also used where the temperature is ramped to around 800 °C after growth of the QWs before bringing it back down to grow the barriers at the low temperature. This is referred to as T-Bounce (T-B) [152] and it has been used to investigate the importance of annealing the InGaN layer and of the barrier quality on the LED performance. The different growth modes are indicated diagrammatically in figure 5.1.

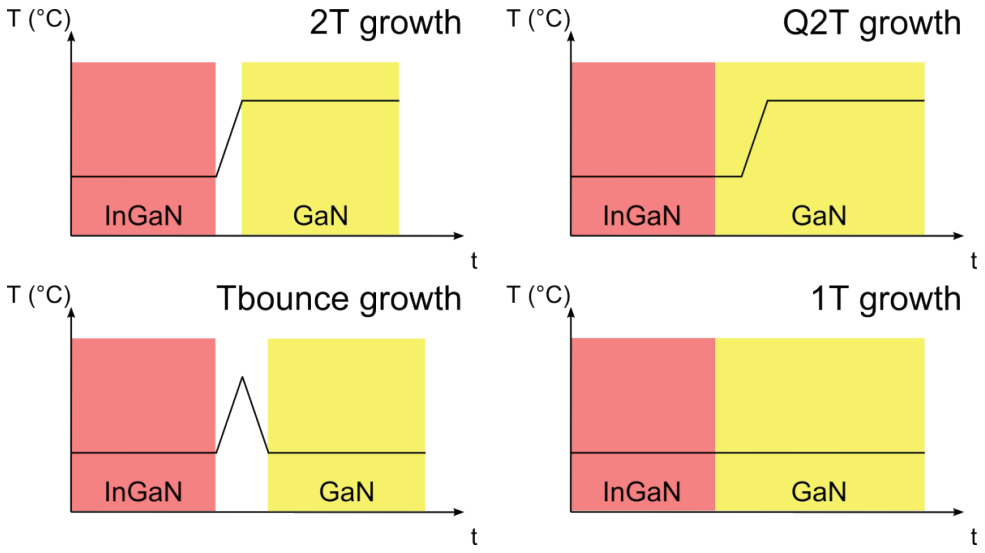

Figure 5.1: *Diagram describing the four different growth modes studied in this chapter. Image provided by Fabien Massabuau at University of Cambridge.*

5.2 EL and CL imaging

A set of four samples was grown by metal organic chemical vapour deposition (MOCVD) at the University of Cambridge by Dr Menno Kappers in the manner described in chapter 2. All the structures studied consist of 2 µm *n*-type GaN, a 5 period MQW active region and a 130 nm *p*-type GaN (inc p^+ contact layer). There was no electron blocking layer or underlayer in any of the devices. The grown wafers were processed at the University of Bath by Dr Margaret Hopkins

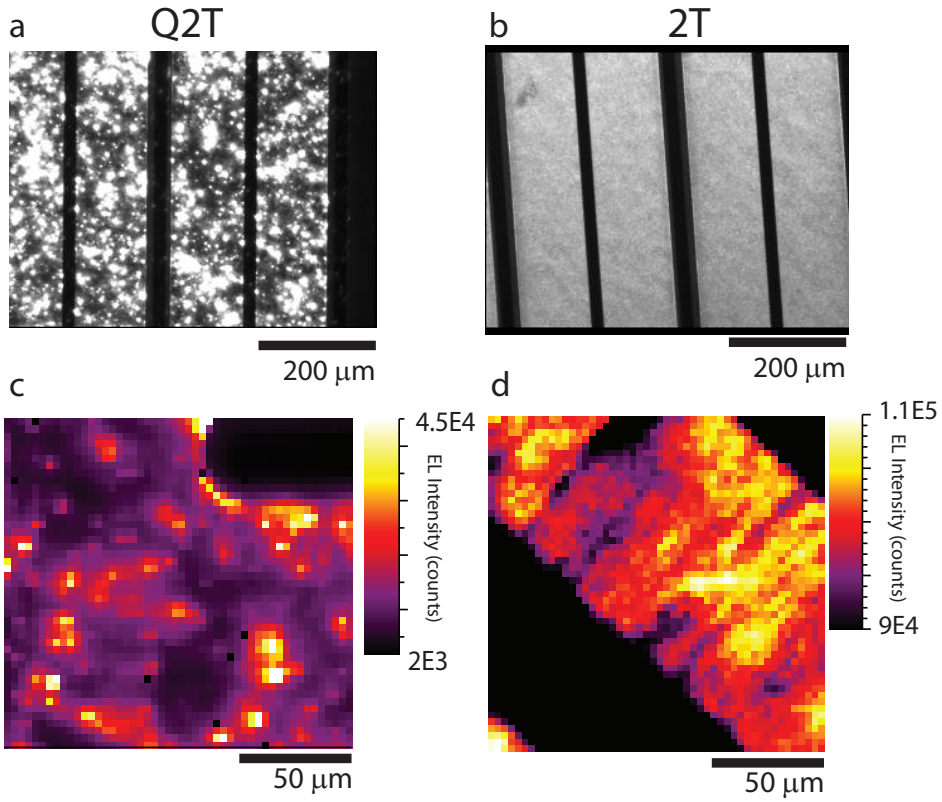

Figure 5.2: *Optical EL micrographs (a, b) and EL intensity maps (c, d) from a Q2T and 2T LED under 10 mA drive current.*

and Siva Sivaraya and then mounted on the PCB boards at Strathclyde as described in chapter 3. The samples are nominally identical apart from the active region which was grown using the 1T, 2T, Q2T and T-B methods. These were mapped by cathodoluminescence (CL) hyperspectral imaging using an electron beam acceleration voltage of 9 kV and beam current of 10 nA. This beam energy was used to position the peak of the energy deposition close to the active region. A subsequent pair of devices grown and processed identically, with the Q2T and 2T methods was studied by EL mapping and simultaneous CL and EBIC imaging to investigate both the luminescence and conductivity variations on a micron scale. An electron probe microanalyser (EPMA) was used to simultaneously perform the CL hyperspectral imaging and EBIC mapping of both devices with a spatial resolution of 1 µm. Electroluminescence measurements were carried out using the same EPMA scanning stage and optics. The electron beam was switched off

and an 8 μm pinhole replaced the spectrometer entrance slit to provide a lateral resolution of 3 μm [153].

Under a forward current, Q2T and 2T devices show markedly different patterns of emission. Figure 5.2 shows optical luminescence micrographs and EL integrated intensity maps taken of typical Q2T (a, c) and 2T (b, d) grown LEDs under a 10 mA drive current. The emission from Q2T is dominated by bright spots and patches between 5 and 10 μm in size with an intensity variation of more than one decade between dark and bright. 2T, in contrast, has a much more uniform appearance, with small variations, $\sim$ 20%, and over a broader scale ($\sim 30 - 50$ μm). As discussed in the previous chapter, the small intensity variations in the 2T sample are likely to be related to the morphology of the templates due to similarity with features in Nomarski images of the templates.

5.2.1 TEM imaging

Transmission electron microscopy (TEM) (performed at University of Cambridge) has revealed that those LEDs grown without an annealing step (Q2T and 1T) exhibit highly uniform quantum well thicknesses as shown in figure 5.3[152]. By

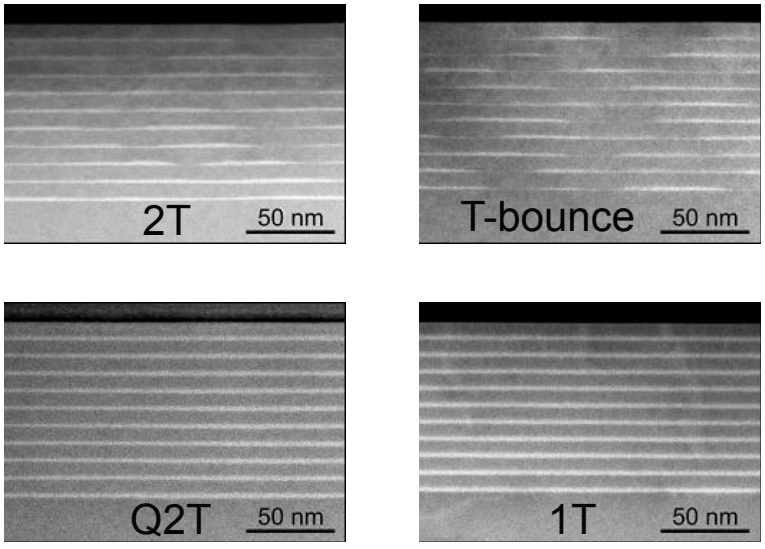

Figure 5.3: *Transmission electron microscope (TEM) images of the active region of the four samples grown with using different temperature profiles. These measurements were carried out at the University of Cambridge and the image is adapted from figure 1 from Oliver et al [152]*

contrast, the devices where an anneal step is present (2T, T-B) were shown to have significantly varying well thicknesses; in some the InGaN is present at all, resulting in gaps in the quantum wells on a length scale of several tens of nanometers.

5.2.2 Processing effects

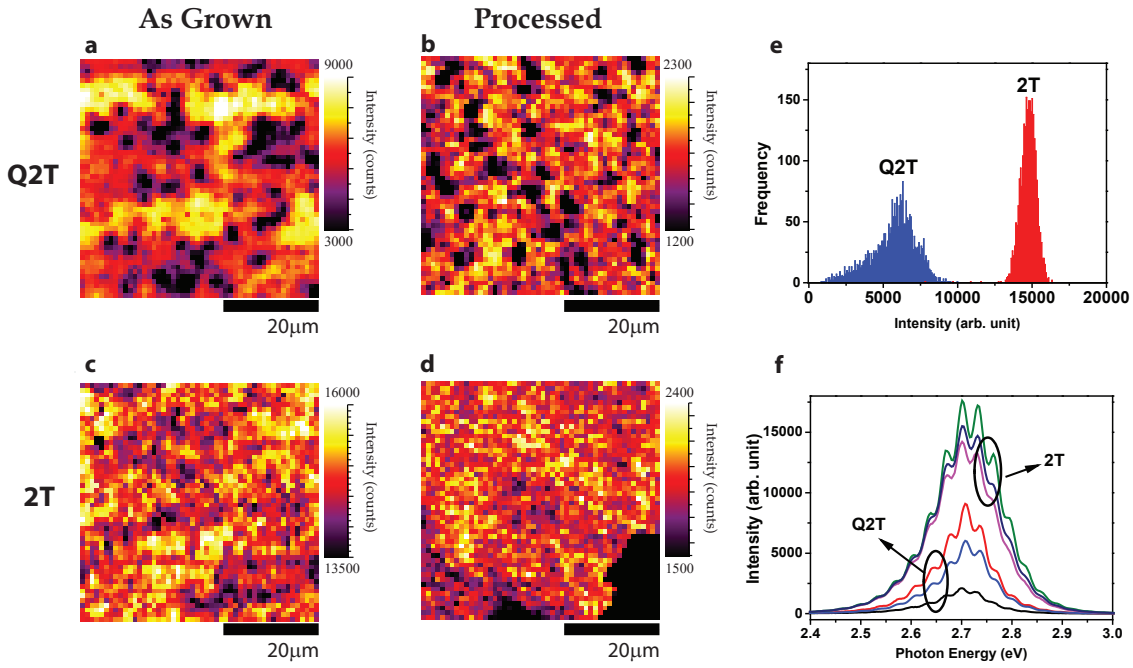

Figure 5.4: *MQW CL intensity maps of the Q2T (a, b) and 2T (c, d) in unprocessed and LED form, respectively. Histograms (e) and CL spectra (f) taken from the "As Grown" maps*

In order to ascertain if the difference in emission was due to effects caused by processing of the LED wafers, CL imaging was performed on 2T and Q2T grown LED structures in both "as grown" form (only the epitaxy) and processed form (after etching and metal contact deposition). Fig 5.4(a–d) show 50×50 μm^2 quantum well CL intensity maps from (Q2T and 2T) samples in uncontacted LED and as-grown wafer form. In both forms, Q2T shows a high degree of non-uniformity in emission intensity: small regions, measuring 2–10 μm in size show a decrease in CL intensity by approximately a factor of 5 compared to the brightest areas. This is emphasized in the histograms and spectra in figures 5.4(e) and (f).

The Q2T histogram has a tail on the low intensity side which corresponds to the presence of the dark spots. Since the dark spots appear on both the processed and unprocessed wafer and have a very similar size, we can conclude that the cause is not due to the deposition of the current spreading layer or any other post-growth fabrication steps.

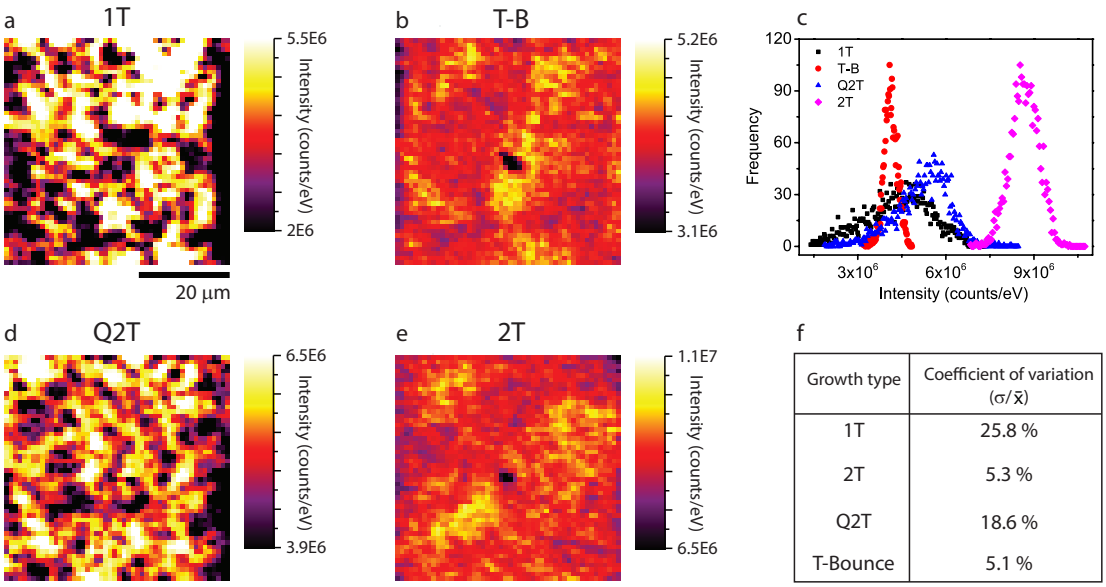

Growth type	Coefficient of variation ($\sigma/\bar{x}$)
1T	25.8 %
2T	5.3 %
Q2T	18.6 %
T-Bounce	5.1 %

Figure 5.5: *CL MQW intensity maps from the set of four as grown (uncontacted) LEDs; 1T (a), T-B (b), Q2T (d), and 2T (e). The maps are plotted on the same relative intensity scales. Histograms (c) and the calculated coefficients of variation (f) extracted from the four maps. The dark spots in the centres of (b) and (e) are due to electron beam damage during calibration*

Figure 5.5 (a, b, d and e) is a set of CL MQW intensity maps, taken under the same conditions, from the set of 4 *unprocessed* LED samples grown with the different active region temperature profiles. The intensity maps are plotted on the same relative scales and, as can be seen, the 1T and Q2T samples have a similar spotty emission pattern to that of the Q2T LED from the first set, while T-B and 2T are similarly comparable. This is demonstrated in figures 5.5 (c) and (f), which show the histograms and the coefficients of variation from the four maps, respectively. The coefficient of variation, COV, is defined by: COV $= \sigma/\bar{x}$, where σ is the standard deviation of the data set and $\bar{x}$ is the mean. The

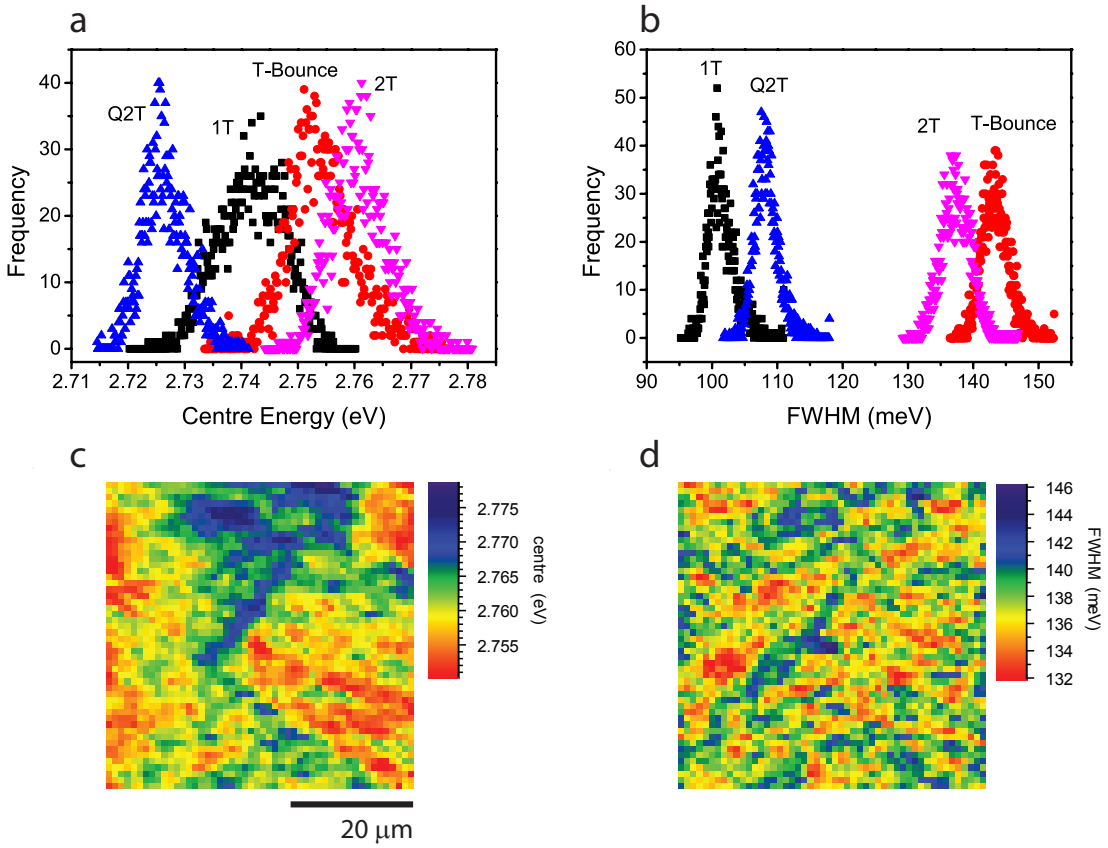

Figure 5.6: *Histograms extracted from CL maps of the fitted centre energy (a) and FWHM (b) from the set of four unprocessed samples. (c) and (d) are examples of the centre energy and FWHM maps from the 2T sample.*

distributions from the 1T and Q2T in (c) clearly show an asymmetric tail on the low intensity side, which is directly attributable to the dark spots. The 2T device has the highest average intensity and around twice that of the T-B sample. In the previous study [152], the EL efficiency from a large number of dies was studied and it was found that T-B device had the highest internal quantum efficiency (IQE) in EL mode. The observation in the CL would appear to be slightly at odds with the EL findings in [152], however in that paper they found that the 2T devices had the highest IQE when measured by photoluminescence. Differences between CL and EL could be due to the different way carriers are generated in CL compared to EL. In CL, carriers generated in and around the active region have, on average, a much higher energy than those which diffuse to the active

region in EL [32]. In the latter case the energy is only a few eV, around the energy of the bandgap, and can easily be captured by the quantum wells. For MQW luminescence, charge pairs generated by a high energy electron beam are required to lose significant energy before being captured by the QWs and so, in this time, there is an increased probability of non radiative recombination, mediated by barrier defects. Since the T-B sample would be expected to have lower quality GaN barriers due to the lower growth temperature, it likely results in more non-radiative recombination and lower CL than would be expected in the 2T material. It is also possible that the particular area of the T-B material observed here is of poorer quality that those used in the EL measurements, however the results presented in figure 5.6 do not suggest that the area is in any other way anomalous, as described subsequently. It is worth noting that EL efficiency measurement in this work (in a later section of this chapter) also found that the 2T device was slightly more efficient that the T-Bounce.

Figures 5.6 (a) and (b) show, respectively, the histograms extracted from maps of the centre energy and FWHM from the four as grown samples (examples of the respective maps are shown in figure 5.6 (c) and (d)). The emission energy is larger in the material which has undergone the high temperature ramp and this is consistent with a reduction in the InN composition of the QWs. Since each sample was grown with the same nominal trimethylindium flux, the blue shift in the annealed samples is likely due to decreased indium incorporation in the quantum wells caused by the higher temperature to which the InGaN is exposed before barrier growth. The full width at half maximum shows an even more marked difference between the annealed and protected samples - the Q2T and 1T material have significantly narrower emission lines, around 105 meV, than the 2T and T-B with line widths of about 140 meV. This indicates that the former have a more uniform nanoscale environment. This is backed up by the TEM imaging of the quantum wells in figure 6.17 where the T-B and 2T have broken non-uniform wells resulting in the carriers seeing a more varied potential environment.

These plots indicate that the four samples fall into two “families”: those where there is no temperature ramp between quantum well and quantum barrier growth (1T, Q2T) and those where there is a temperature ramp immediately after well growth (2T, T-B). The highest temperature to which the quantum wells are

exposed is the same for all 4 devices, as it comes during the 950 °C anneal of the *p*-GaN performed to activate the acceptors. This suggests that the cause of the dark spots is related to whether or not the quantum wells are capped by a low temperature GaN layer ***before*** the ramp to high temperature. The previous study on these samples [152] also showed that the devices fall into these two families, with the capped samples having smooth wells and the uncapped having gappy wells.

5.3 Uncapped material

In order to further investigate the origin and nature of the dark spots, MQW samples where the growth was terminated after the deposition of the active region, were studied. In these materials there is no *p*-type GaN layer and the GaN below the quantum wells is not intentionally doped *n*-type. Consequently no *p/n* junction exists in the material and no high temperature activation step occurs either. Two samples were studied, one grown with the Q2T method and one with the 2T system, each with 5QWs.

The quantum wells and barriers are around 2.5 nm and 7.5 nm thick, respectively, giving a period of 10 nm. The lack of the approximately 150 nm of GaN between the surface and the quantum wells necessitates using a lower acceleration voltage to ensure that the maximum of the energy deposition occurs within the active region.

Figure 5.7 shows a comparison between the uncapped Q2T (a) and 2T (b) 5 QWs structures, in the form of MQW CL intensity maps taken with a beam voltage of 3 kV. Since the lateral extent of the interaction volume at 3 kV is significantly smaller than at 10 kV, a step size of 500 nm as opposed to 1 μm was used. The dark spots which are characteristic of the low temperature cap devices are present in the Q2T material and not in the 2T material. Since these samples do not undergo an *p*-GaN activation step we can conclude that the existence of the spots in the full LED structures is neither dependent on nor affected by the high temperature anneal step made at the end of the growth. As in figure 5.5 the maps are plotted on the same relative scale to emphasise the large variation in the Q2T structure.

A comparison of the appearance of the dark spots in the Q2T sample using

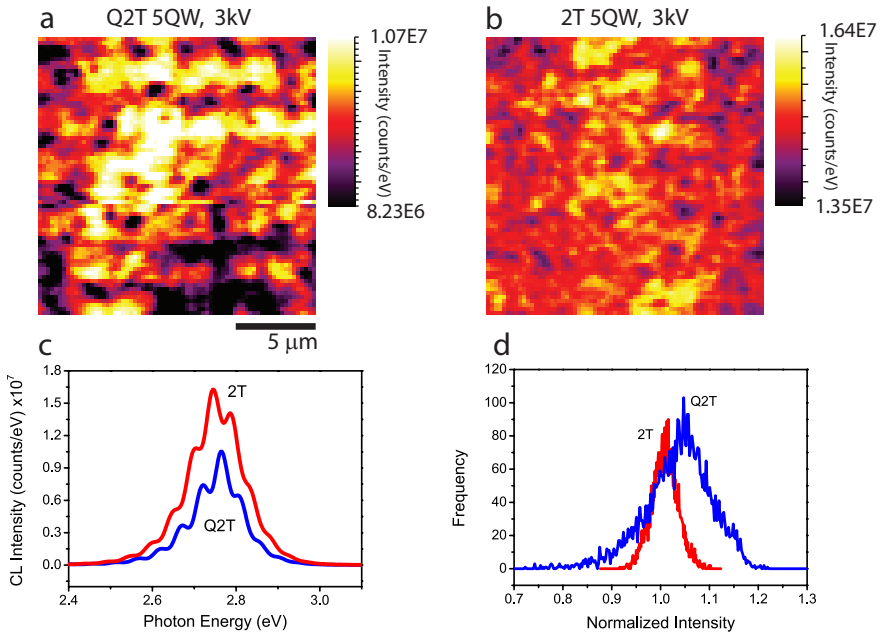

Figure 5.7: *MQW CL intensity maps of the 5QW Q2T (a) and 2T (b) thin cap material using a 3 kV electron beam. The maps are plotted with a range equal to ± 10% of its own mean in order to demonstrate the different scales of intensity variation in the sample. (c) and (d) plot the mean spectra and intensity histograms for the two maps.*

a beam voltage of 3 kV and 6 kV is shown in figure 5.8. The mean intensity of the map at 3 kV is more that six times larger than in the map at 6 kV. The coefficients of variation are comparable with the value at 6 kV being slightly larger. Furthermore the appearance of the maps are somewhat different. The dark spots are less clear in the 6 kV map, which it also has a slightly more granulated appearance.

Figure 5.9 (a) shows the results of two Monte Carlo simulations in the sample using beam energies of 3 kV and 6 kV. The line denoted "End QWs" shows the end of the quantum well stack - based on the dimensions given in the previous paragraph. As in the simulations in chapter 4 the total energy deposited in the sample (in the simulation) is the same - achieved by normalising the two curves.

Fig 5.9 (b) shows CL spectra from the thin Q2T material with beam voltages of 3 kV and 6 kV. Note that the total deposited power was the same at 3 and 6 kV, achieved by altering the beam current - in this way the simulation in (a) mirrors

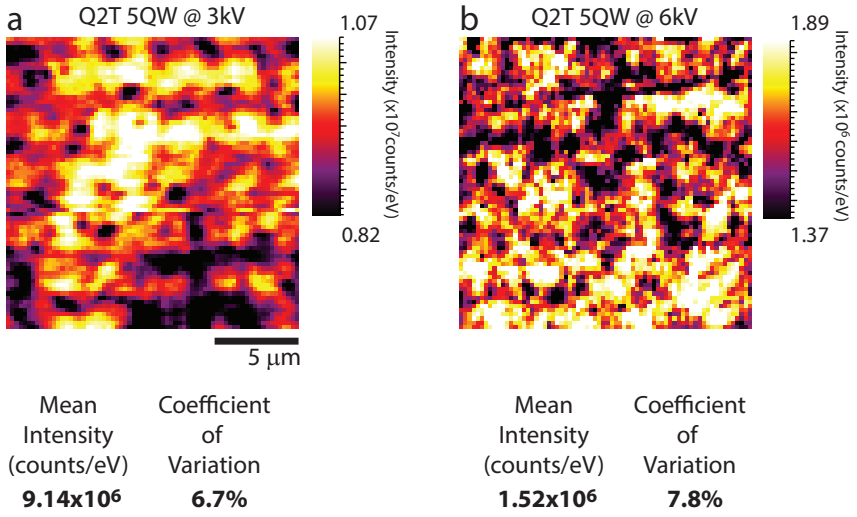

Figure 5.8: *Maps of the fitted MQW CL intensity Q2T thin cap sample at 3 kV (a) and 6 kV (b). The mean and calculated coefficient of variation for each are shown below the maps.*

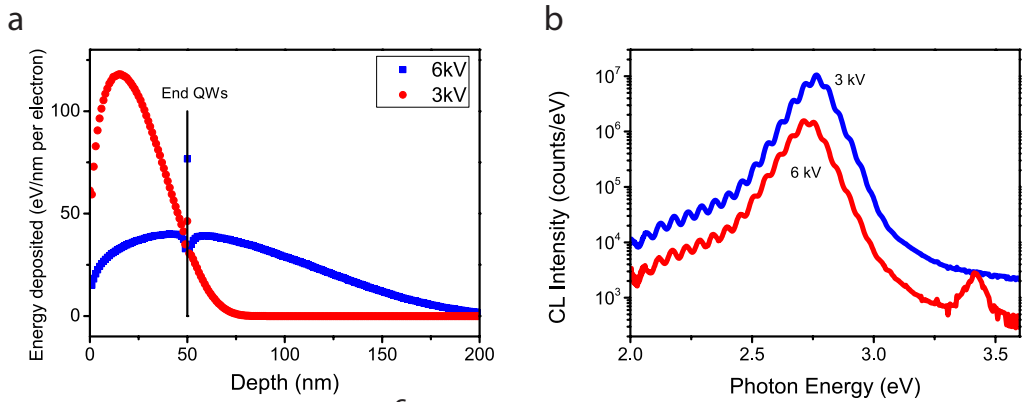

c

Beam Voltage	Total % of beam energy deposited in QWs	MQW CL intensity (10^8 counts)
3 kV	91	4.42
6 kV	37	0.72

Figure 5.9: *(a) Plot of the e-beam energy deposition as function of depth in the uncapped MQW samples, for 3 kV and 6 kV. Mean spectra from the Q2T thin cap sample (b) based on the maps in figure 5.8. The table (c) compares the energy deposited in the QW stack (based on the simulations) with the experimentally measured CL MQW intensities.*

the conditions of the experiment in (b). At 3 kV, the total MQW intensity is around 5 times greater than at 6 kV, and this is not unexpected given the curves in (a) - only 37% of the energy in the 6 kV beam is deposited directly in the wells, as opposed to 91% using the 3 kV beam. These numbers are summarised in the table in (c).

The size of the effect varies between simulation and experiment. The 6 kV beam deposits only 2.5 times less energy in the wells than the 3 kV beam but results in a 5 fold decrease in intensity. This may be because, at 3 kV the deposition is largely in the top of the QW stack whereas at 6 kV the carriers generated near the bottom of the stack may diffuse into the GaN layer below before recombination in the quantum wells. The GaN band-edge peak can be seen clearly in the 6 kV trace in (b) but is absent in the 3 kV curve indicating that, in the latter case, very few carriers diffuse to the GaN.

5.4 Cathodoluminescence/EBIC (CLEBIC) mapping

Based on this data, the EBIC/CL studies were performed on one type of LED from each "family"; a 2T and Q2T device which, based on the CL, are the brightest from each set. LEDs possessing a good I-V characteristic (i.e. with a low reverse leakage current) were chosen for EBIC measurements. The devices were held at 0 V to measure the short circuit current. Figure 5.10 compares the CL data with the simultaneously collected EBIC signal for the Q2T and 2T grown LEDs. (a), (c) and (e) show the fitted CL intensity and peak position, and EBIC maps of 2T, while (b), (d) and (f) are the equivalent maps for Q2T.

In the 2T sample, an anti-correlation exists between the CL intensity and EBIC signal. Areas higher in luminescence intensity contribute less current to the external circuit when excited by the electron beam. There is also an anti-correlation between the intensity and fitted peak position, with areas of lower intensity also slightly blue-shifted by around 10 meV. These correlations are shown in the plot in figure 5.11 (c and d).

Both these relationships are consistent with a variation in the effective electric field across the p/n junction and the resultant competition between recombination

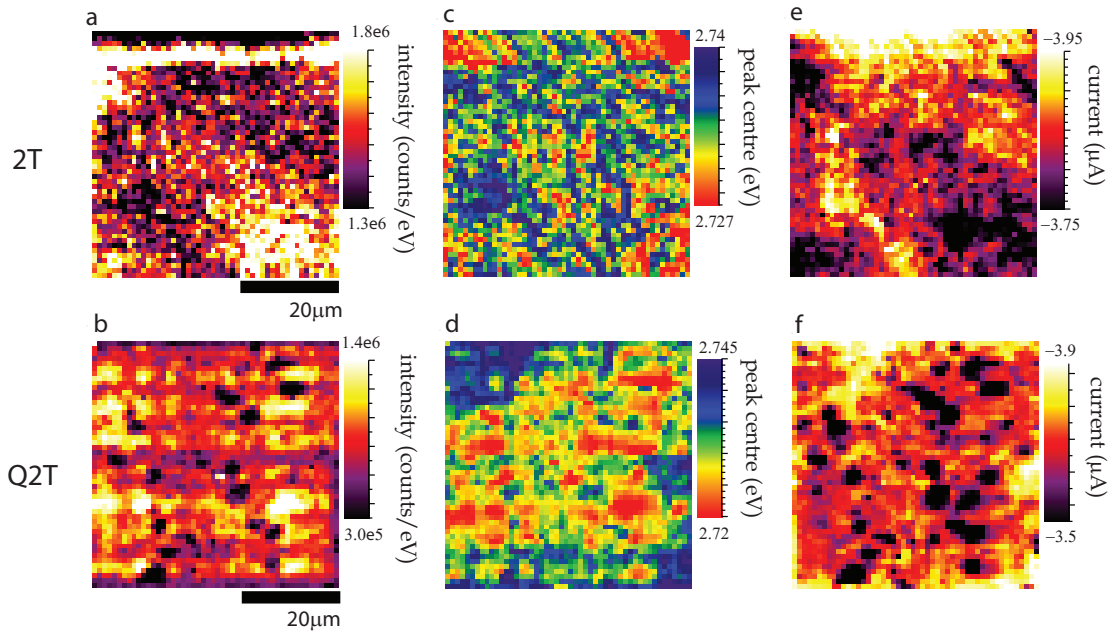

Figure 5.10: *2T/Q2T CL intensity (a)/(b), CL peak centre (c)/(d) and EBIC (e)/(f) maps*

and carrier escape. In areas where the electron beam induces a forward bias the depletion field contribution to the total electric field is reduced altering the occupancy of the QWs and the balance between carrier capture into the wells and re-emission changes, with the latter favoured. As such, more carriers escape to the external circuit before being able to recombine in the active region (either radiatively or non-radiatively), lowering the intensity and increasing the measured EBIC. Furthermore, with a larger junction field a blue shift in the emission energy is expected due to compensation of the quantum confined Stark effect (QCSE). The polarization induced field is *opposed* to the inbuilt *p/n* junction field and so an increase of the junction field partly compensates the field due to the QCSE, blueshifting the emission.

The CL and EBIC maps and their correlations are quite different in the Q2T grown device. The most obvious feature from the EBIC map (fig 5.10(f) is the presence of dark spots which coincide precisely with the dark features in the CL intensity map. These areas exhibit a lower radiative recombination rate that is not accounted for by an increase in carrier escape from the depletion region; in

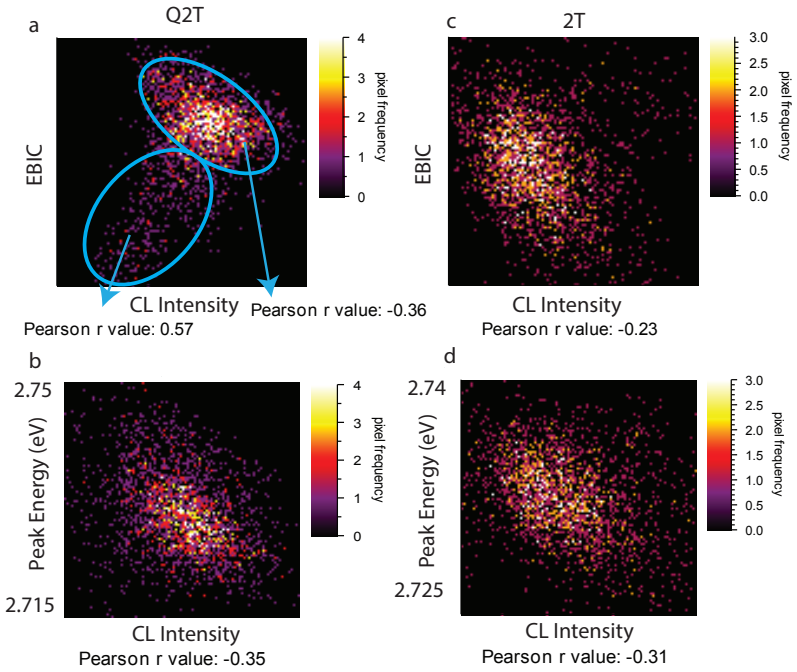

Figure 5.11: *Statistical correlation plots between CL MQW intensity and EBIC/CL peak centre for the Q2T (a, b) and the 2T (c, d) LEDs. The Pearson r value is a measure of the strength of the correlation; a value of 1 denotes a perfect linear correlation: −1 denotes a perfect anti-correlation*

fact the carrier escape is significantly lower also. This indicates unambiguously an increase in the non-radiative recombination rate. The correlation plot in figure 5.11 (b) demonstrates that the relationship between the CL intensity and EBIC is not as simple as in the 2T material. Two sections of the plot exist; a positive correlation which corresponds to the areas encompassing the dark spots, and an anti-correlation which at higher intensities has a Pearson r value very similar to that of the 2T device. The relationship between the intensity and peak position is also similar to that of the 2T material, in that the brighter areas are redshifted. This indicates that outside the dark spots the material is similar to that found in the 2T device.

The Q2T (and also the 1T) material are host to significant regions of carrier trapping and non-radiative recombination on the micron scale. This is belied by the observation on the nanoscale of smooth, uniform active regions. It is indisputable that the effect observed in this work originates from the active region -

the CL peak is from the InGaN MQWs and the driving force for the EBIC in these structures is from the depletion region. It is not a coincidence that the precise opposite effect is seen in the 2T (and T-B) material; broken, irregular quantum wells in the active region exist with uniform light emission and EBIC signal on the micron scale. The gaps in the QWs can account for an improved macroscopic efficiency of the entire die but the absence of such gaps cannot account for micron scale dark spots - the model of increased efficiency relies on isolating charge carriers from defects on a nanoscale - far below the resolving power of the method used here. A conceivable explanation which bridges the two length scales might be the formation of clusters of point defects [135], which without the high temperature step are not annealed out. Based on the maps here, they would be of sufficient size that they could be easily missed by an arbitrary TEM slice. The relationship between these spots in CL to actual operating of the Q2T/1T devices has been considered, and the results are presented in the subsequent section.

5.5 Electroluminescence mapping and efficiency

5.5.1 Integrating sphere measurements

The four LED samples, 1T, 2T, T-B and Q2T were measured in the integrating sphere, as a described in chapter 3, in order to obtain quantitative values of their efficiency as a function of drive current. It is important to note that a degree of variation exists between different dies from the same wafer and the data presented represents only single dies from each sample. As such the purpose is to study both the shape of the efficiency curves and the absolute efficiencies of the devices. It should also be noted, however, that a greater number of dies were studied by University of Cambridge in order to obtain average statistics and the results obtained here do not deviate to any significant extent from those produced by a larger scale sampling of typical dies. Figure 5.12 (a) and (b) show plots of, respectively, the external quantum efficiency to 10 Acm^2 (100 mA) and the L-I curves up to 100 Acm^2 (1000 mA) for the four devices. As stated in chapter 3, the EQE is only available up to 100 mA because, for currents above this, the pulsed source is used which measures only the applied drive current and not the applied voltage.

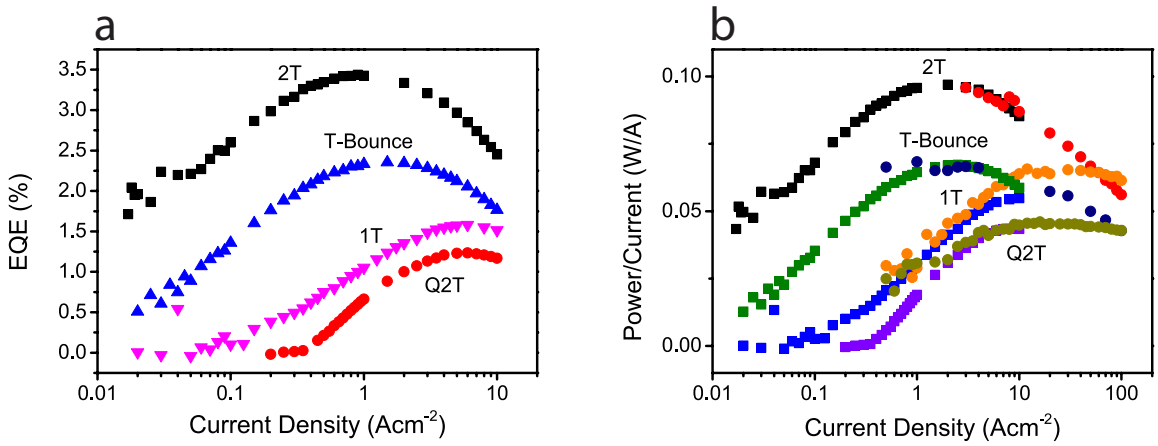

Figure 5.12: *Semi-log plot of the external quantum efficiency (a) and L-I curves (b) for LEDs grown with the four different active region growth profiles. In (b) the "squares" are from CW measurements made up to 100 mA and the "circles" originate from measurements taken using pulsed electroluminescence.*

The devices with the high temperature ramp immediately after well growth (2T and T-B) have both the highest peak efficiency and the lowest drive current at which the efficiency droop occurs. At higher currents (>50 Acm^{-2}) the efficiency curves of the 2T/T-B and Q2T/1T come together and, in the case of the this set of samples the 1T device is more efficient at 100 Acm^{-2} than the 2T. The reason for these different behaviours is linked to the competing components of the coefficients in the ABC recombination model. At low current densities, the dominant process suppressing radiative efficiency is the non-radiative Shockley-Read-Hall recombination (see section 6 of chapter 2). The shape of the 2T/T-B curves with respect to the 1T/Q2T is consistent with the former devices having a lower "A" co-efficient, i.e. a lower contribution to recombination from the SRH process. In figure 5.13(b) efficiency curves derived from the ABC model are plotted using fixed values of B ($5\times10^{-10}cm^3s^{-1}$) and C ($4\times10^{-29}cm^6s^{-1}$) [154] coefficients and four values of the SRH "A" coefficient. As can be seen, an increase in A by an order of magnitude results in both a lower peak efficiency and a shifting of the droop onset to higher carrier densities (and hence current densities). In fig 5.13(c) the efficiency curves from the 2T and 1T devices are shown with the calculated efficiency curves with two of the different A values.

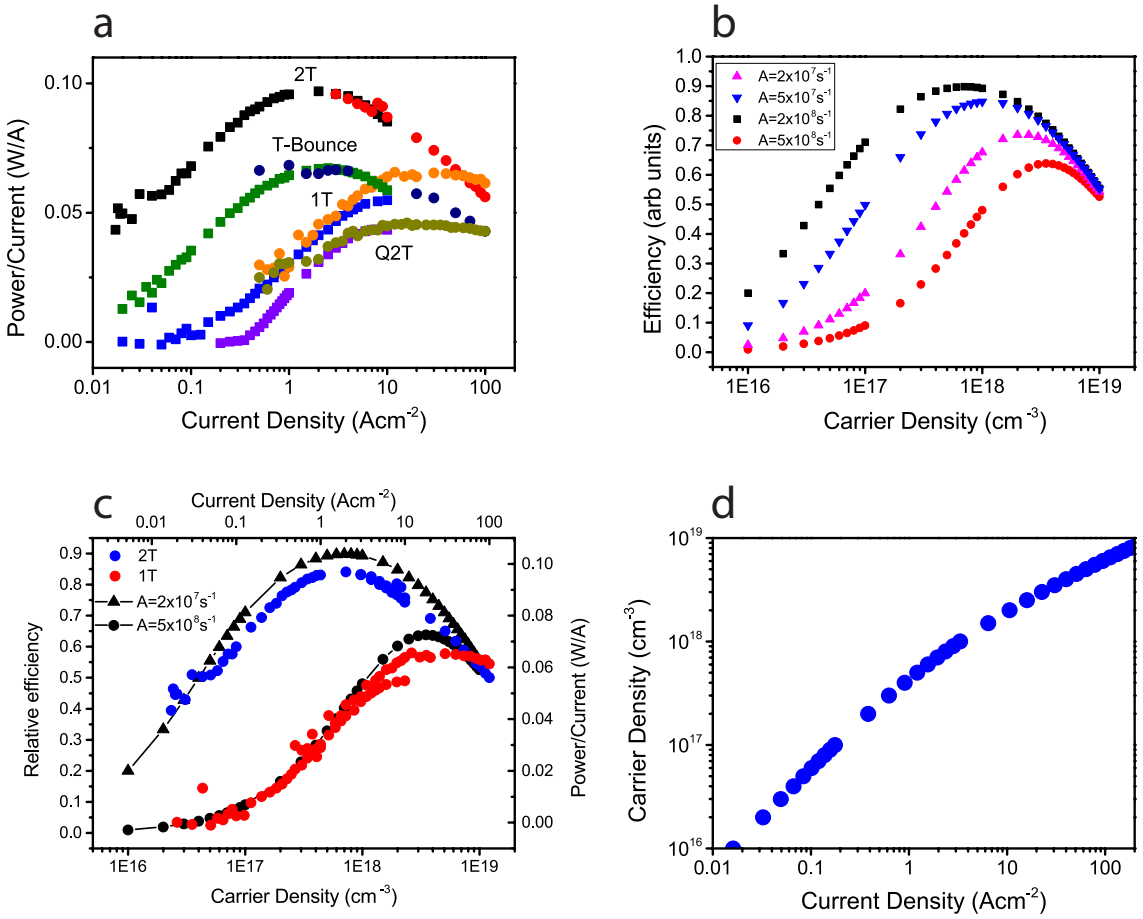

Figure 5.13: *(a) Replicates the efficiency curves from 5.12(a). (b) plots efficiency curves using the ABC model showing the effect of a change in the non radiative SRH "A" coefficient.* $B = 5{\times}10^{-10}cm^3s^{-1}$ *and* $C = 4{\times}10^{-29}cm^6s^{-1}$ *(c) shows the efficiency curves for the 2T and 1T devices overlayed (on a separate axis) onto two of the calculated efficiency curves - note that these are not fits. (d) plots carrier density as a function of current density.*

This is a simplified model since it is not fitted to the data and the B and C values will vary between the devices, but it is sufficient to demonstrate the effect of increased first order non-radiative recombination on the shape of the efficiency curves. The two x-axes used; carrier density for the calculated curves and current density for measured data are not independent. With a given carrier density, n,

the resultant current density, J can be found by [155]:

$$J = qd_{eff}(An + Bn^2 + Cn^3) \tag{5.1}$$

where d_{eff} is the effective thickness of the active region. In fig 5.13 (d) a plot of J vs. n using a typical value of 1 nm for d_{eff}. This has been plotted to show that the two overlapping x-axes in (c) are consistent with the plot in (d) and hence are reasonable.

Observations on the nanoscale by TEM (fig 6.17), and the micron scale by the CL/EBIC/EL mapping can help account for the increased non-radiative recombination rate in the Q2T/1T material with respect to the 2T/T-B material. The non-uniformity of the quantum wells on the nanoscale will localise carriers in potential wells caused by the fluctuating InN concentration and so prevent carrier diffusion to non-radiative defects, in the 2T family.

The dark spots in the CL, EBIC and EL on the micron scale are clear sources of non-radiative recombination. The effect of these regions extends to the macroscopic L-I curve shape which is governed by the shape of the L-I curve for dark spots as shown in the next section.

5.5.2 Spatially resolved EL

In order to determine what effect the dark areas have on the emission efficiency of the LEDs EL mapping was used to spatially resolve the efficiency curves. Figure 5.14 (a)-(c) shows EL maps at 10 mA, 100 mA and 500 mA from a different area of the Q2T LED, where both the dark and bright spots can be resolved. At 10 mA the emission is dominated by many small bright spots, around 3–10 μm in size (similar to fig.5.2 (c)). As the current increases the contrast from the bright spots drops and some of the dark spots become more apparent; at 500 mA the luminescence is significantly more uniform, the COV having dropped from around 50% to 20%. Using these maps we are able to spatially resolve the luminescence efficiency across the region and figure 5.14 (d) plots *L-I* curves (intensity/current vs. current) for the average of several bright spots, dark spots and the overall map average for several different currents. In the bright areas, efficiency droop occurs at or just below 100 mA, but in the dark areas the onset of droop does not appear until several hundred milliamperes, a further indication that non-radiative

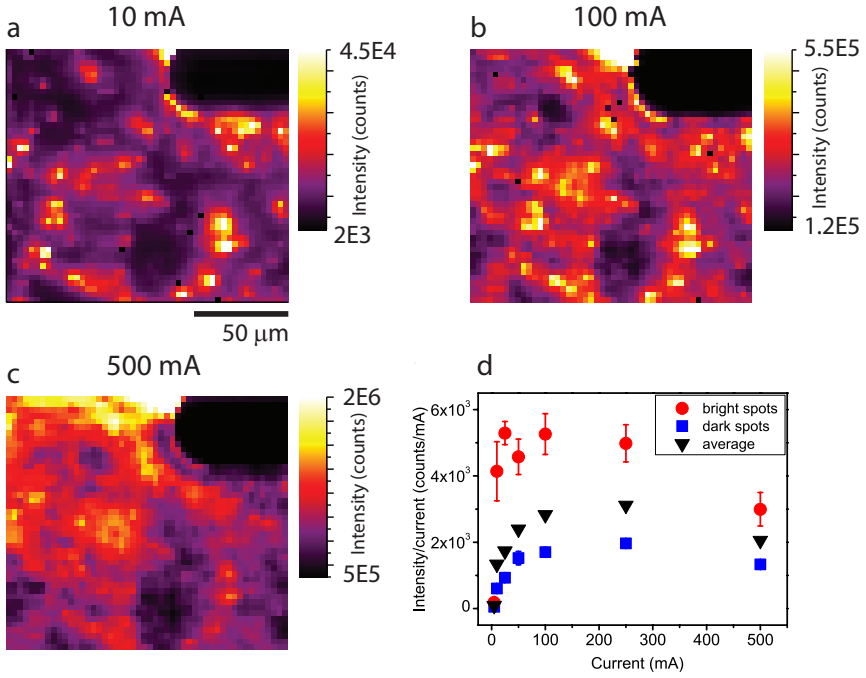

Figure 5.14: *EL intensity maps, from the Q2T LED, at 10 (a), 100 (b) and 500 mA (c). The current was pulsed at a 4% to mininse heating effects. L-I curves taken from several dark spots and bright regions (d)*

recombination is more prevalent in the latter. More remarkable is the fact the curve for the average intensity is almost identical to that of the dark spots. This would strongly suggest that the overall efficiency curve shape observed for the Q2T (and likely 1T) devices is dominated by the dark spots, and that the areas outside the dark spots are similar in drive current response to the 2T, T-B devices.

5.6 The effects of encapsulation

The maximum EQE values produced through the use of the integrating sphere and shown in figure 5.12 are around 3.5% for the 2T device. These numbers are low in comparison to the best blue LEDs, which can be as high as 50–80% [83, 156, 157] Part of the reason is that these devices are not packaged in any way to enhance the light extraction from the chip. Many methods exist to increase the *extraction efficiency* such as using a flip chip design to extract through the sapphire and avoid reflection losses [63] surface roughening [85] and photonic

crystal patterning[89, 158]. A crucial and almost universally implemented step, however, is the encapsulation of the device with an epoxy dome which acts not only to protect the device but to increase the extraction efficiency by providing a secondary interface to reduce internal reflection losses. Chips based on the 2T growth method were provided by University of Cambridge and processed and packaged with a polymer dome at UC-ITRI in Italy. Two devices were returned to Strathclyde - with and without encapsulation - and these were measured using the integrating sphere to obtain the efficiency curve. The results of the measurement are shown in figure 5.15 (a). The black dots are the result of dividing the curve for the encapsulated die by the non encapsulated one. Two effects were considered in the model: the change in critical angle going from a GaN/air interface to GaN/epoxy interface and the subsequent effect upon the escape cone and Fresnel losses at the interfaces of the various media. The critical angle at any interface is derived from Snell's law of refraction:

$$sin\theta_{\text{crit}} = \frac{n_2}{n_1} \tag{5.2}$$

where θ_{crit} is the critical angle (beyond which total internal reflection occurs within media 1), and n_1/n_2 are the refractive indices of the two media. The refractive index is a function of wavelength and with a peak photon energy of $\sim$ 2.75 eV, n_{GaN} is around 2.5 - which is taken as a fixed value. The index of the epoxy is estimated to be around 1.6. With these values the critical angles are:

$$\theta_{\text{air,crit}} = sin^{-1}(\frac{1}{2.5}) = 23.6^\circ \qquad \theta_{\text{epoxy,crit}} = sin^{-1}(\frac{1.6}{2.5}) = 39.8^\circ \tag{5.3}$$

and this is shown in figure 5.15 (c). In general the fraction of the generated light which will be coupled into the escape cone is described by:

$$\frac{P_{out}}{P_{total}} = \frac{\text{Area defined by} \quad \theta_{crit}}{\text{Area of sphere}} \tag{5.4}$$

The area on the sphere defined by the solid angle is shown in figure 5.15(b) and is defined by the integral from $\theta = 0$ to $\theta = \theta_{crit}$ of small area element A. It

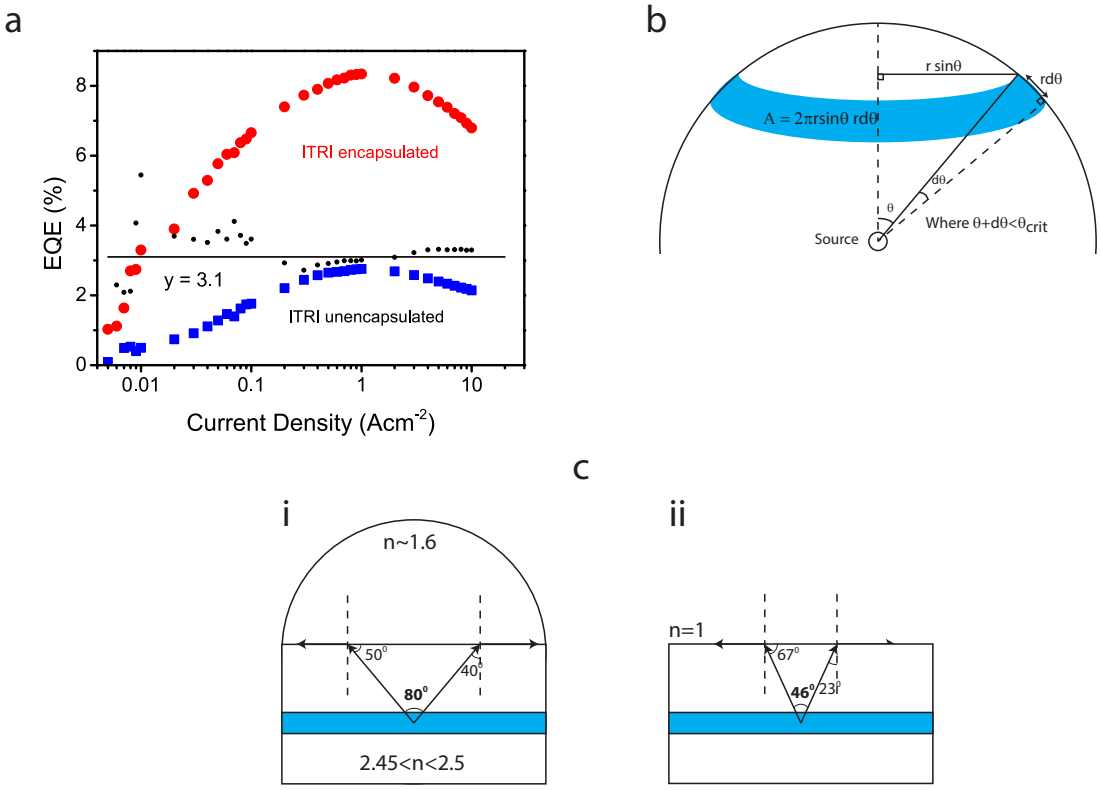

Figure 5.15: *(a) EQE curves for the encapsulated and unencapsulated dies processed at UCITRI, of the 2T LED "as is" and with the 2.7x correction due to encapsulation as described in the text. (b) Shows the definition of the area element "A" (adapted from [50]), (c) (i) and (ii) are sketches of the effect of the change in critical angle with and without an epoxy encapsulate.*

follows that the power which escapes is given by:

$$P_{out} = P_{total}\frac{2\pi r^2(1 - cos\theta_{crit})}{4\pi r^2} \tag{5.5}$$

The improvement in the escape of light from GaN between air encapsulate and the epoxy encapsulate is given by:

$$\frac{P_{epoxy}}{P_{air}} = \frac{1 - cos(\theta_{epoxy,crit})}{1 - cos(\theta_{air,crit})} = \frac{0.232}{0.084} = \mathbf{2.8} \tag{5.6}$$

The geometry of the dome is such that the light which escapes the GaN is incident on the air/epoxy interface approximately normal, and so no further losses

occur due to total internal reflection.

A second source of loss is via Fresnel (reflective) losses which occur at the interfaces due to the differences in refractive indices. The transmission, T, at each interface, is given by:

$$T = 1 - R = 1 - (\tfrac{n_2 - n_1}{n_2 + n_1})^2$$

when there is no encapsulation

$$T_{GaN/air} = 1 - (\tfrac{2.5-1}{2.5+1})^2 = \mathbf{81.6}\%$$

when encapsulation is added, there are two interfaces

$$\rightarrow T_{GaN/epoxy} = 1 - (\tfrac{2.5-1.6}{2.5+1.6})^2 = 95.2\% \quad \text{and} \quad T_{epoxy/air} = 1 - (\tfrac{1.6-1}{1.6+1})^2 = 94.7\%$$

$$\text{so} \quad T_{total} = \mathbf{90.2\%}$$

The addition of the encapsulate reduces the Frensel losses by a factor of $0.9/0.82 = 1.1$. As a result there is a total intensity increase of $1.1 \times 2.8 = 3.1$. This is consistent with the increase observed between the two dies in figure 5.15(a); a line has been plotted at y = 3.1 and clearly falls in line with the ratio of the two LI curves (the black dots). The peak EQE jumps from around 3% to nearly 9% and this indicates that optimizing the extraction efficiency is extremely important as any small increases in IQE due to quantum well design can be lost if effective packaging does not exist.

5.7 Summary

In summary, this chapter has demonstrated the effect of the manner in which the active region is grown upon LED uniformity, luminescence, conductivity and efficiency.

The use of a simultaneous combination of cathodoluminescence hyperspectral imaging and electron beam induced current mapping to study the variations in luminescence and conductivity of InGaN/GaN LEDs grown with different barrier temperature profiles. Those devices where the quantum wells are uncapped prior to being exposed to a high temperature (2T, T-B) were found to have uniform

luminescence intensity and an anti-correlation between CL and EBIC, on a micron scale, due to competition between carrier recombination and escape from the active region. Where the devices are grown with a protective GaN low temperature cap (Q2T, 1T) the luminescence in both CL and EL is dominated by dark spots 2—10 μm in size despite having uniform quantum well thicknesses on a nanoscale. These dark spots are found to have a lower EBIC signal also, indicating regions of non-radiative recombination and possible carrier trapping. Studies of both unprocessed and incomplete LED structures support the theory that the variation is not caused by either processing or post growth *p*-GaN annealing steps. The peak electroluminescence efficiency of those samples without the high temperature ramp was shown to be both lower and occur at a higher drive current density than in the 2T/T-Bounce family - an observation consistent with increased SRH non radiate recombination caused by the dark spots and easier access to defects due to the QW nanoscale uniformity. The mapping of the variation in EL efficiency curves from the non-uniform samples showed that while the bright regions are similar to the high temperature cap devices the dark spots appear to dominate the overall LED efficiency curve and have lower droop. The effect of encapsulation on the more efficient 2T sample was shown to increase the external quantum efficiency by between a factor of 2.5-3.

Chapter 6

Effects of the variation of LED layers on LED performance

6.1 Introduction

Following on from the previous two chapters, which looked at the techniques through the lens of a single sample and then subsequently at a particular series of samples, this chapter aims to study the effect of progressive adaptation and improvement of the LEDs through the addition of extra layers, and changes in the active region and substrate. The chapter is broken down into four sections; the first looks at the effect of the addition of a layer of silicon doped InGaN *under* the active region. This section also includes a discussion of the effects of electron blocking layers in the material. The second section deals with changing the thickness of the quantum wells, and the third the effect of changes in the substrate dislocation density. The final section compares the efficiency of devices with these layers, along with those devices from the previous chapter.

6.2 Si doped underlayers

Layers inserted before the active region (i.e. grown after the n-type GaN) are employed for a variety of reasons. Such pre-layers or underlayers can take the form of simple single material layers (e.g. InGaN) of varying thickness [159, 160] or so called superlattices [161, 162], alternating very thin (∼1–2 nm) layers of

different III-nitride alloys, somewhat like a MQW with a large number of closely spaced wells. As discussed in chapter 2 a doped pre-layer before the active region has been found to reduce the internal electric fields within the subsequent wells by pinning the Fermi level to the donor energy level in the Si doped layer and bending the field in the active region [79, 80, 81]. The effect is greater on the quantum well immediately next to the underlayer when the layer contains a % of InN, which acts to compensate charge at the first well/barrier interface. Simulations of the conduction band, performed at the University of Manchester by Matthew Davies, showed that, in quantum well samples (i.e. not LEDs, with no n/p region,) the addition of a doped InGaN UL has a large effect on the band structure, particularly on the quantum wells closest to the underlayer [81].

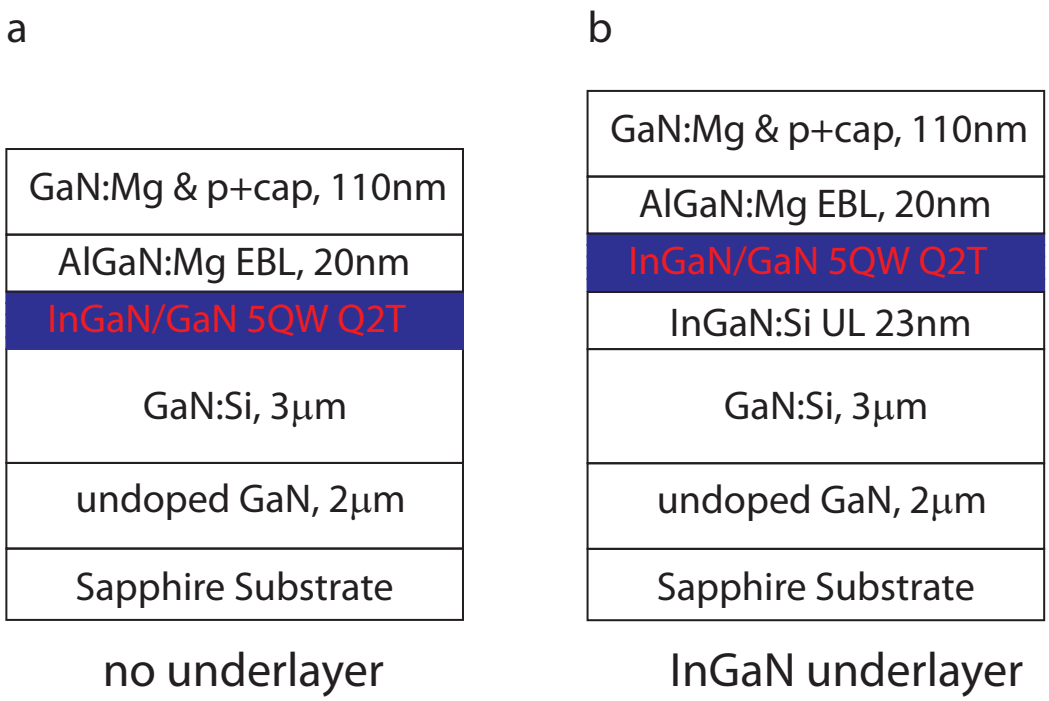

Figure 6.1: *Schematics (not to scale) of the 2 samples with varying underlayers. (a) is the baseline without an extra layer and (b) is the structure with a Si doped InGaN layer.*

The improvement of LED quality and performance with the addition of InGaN underlayers has also been reported. Akasaki et al. in 2004 and in 2006 [163, 112]

found that the addition of a 50 nm $In_{0.04}Ga_{0.96}N$ layer increased the PL and EL efficiency due to a reduction in non-radiative centres via the introduction of In atoms in the underlayer. A micro-PL study by Son et al. in 2006 [164] also found an improved efficiency with the use of a low InN InGaN UL, and they also observed improved spatially homogeneity in the PL mapping. Torma et al. in 2008 [113], observed a large reduction in threading dislocation and V-pit density, and a subsequent increase in EL intensity.

The effect of the underlayers on the EBIC and the luminescence uniformity is investigated in this section. Two LED structures were studied, one with no underlayer and one with a doped $In_xGaN_{1-x}N$ layer (x=0.05). The optically active region in both samples was grown using the Q2T growth method described previously and consists of a 5 period InGaN/GaN well/barrier structure. A 23 nm AlGaN electron blocking layer was grown on top of the MQW stack in each device. Schematic diagrams of the LED structures are shown in 6.1.

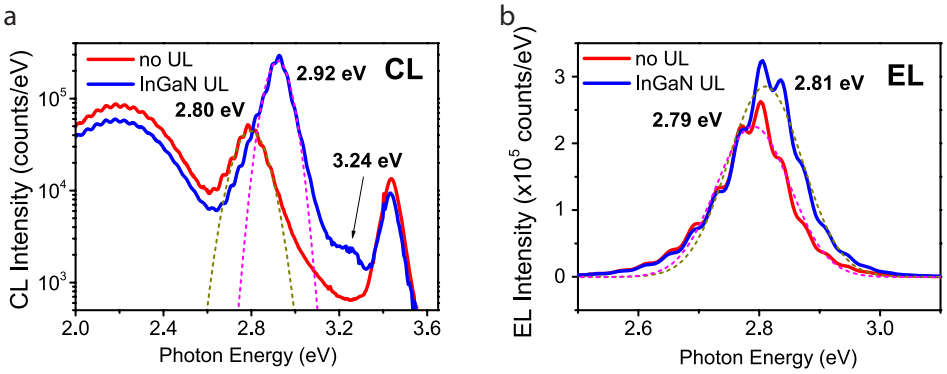

Figure 6.2: *(a) Mean CL (a) and EL (b) spectra from a 50×50 μm^2 area in the UL and no-UL LEDs. The CL is plotted on a semi-logarithmic scale in order see the various luminescence bands. The energies given are the fitted peak positions of the MQW emission and the approximate position of the small peak in the InGaN UL CL spectrum.*

Hyperspectral EL mapping was performed at 5 mA followed by simultaneously acquired CL and EBIC over the same area. The CL was performed with a beam voltage of 10 kV, beam current of 4.5 nA and spot diameter of 1 µm. The effects of the underlayer on the spectra can be seen in fig 6.2 (a) and (b), which show the mean CL and EL spectra from 50×50 μm^2 maps of luminescence intensity. Gaussian fits to the MQW peaks have been performed and the resultant peak

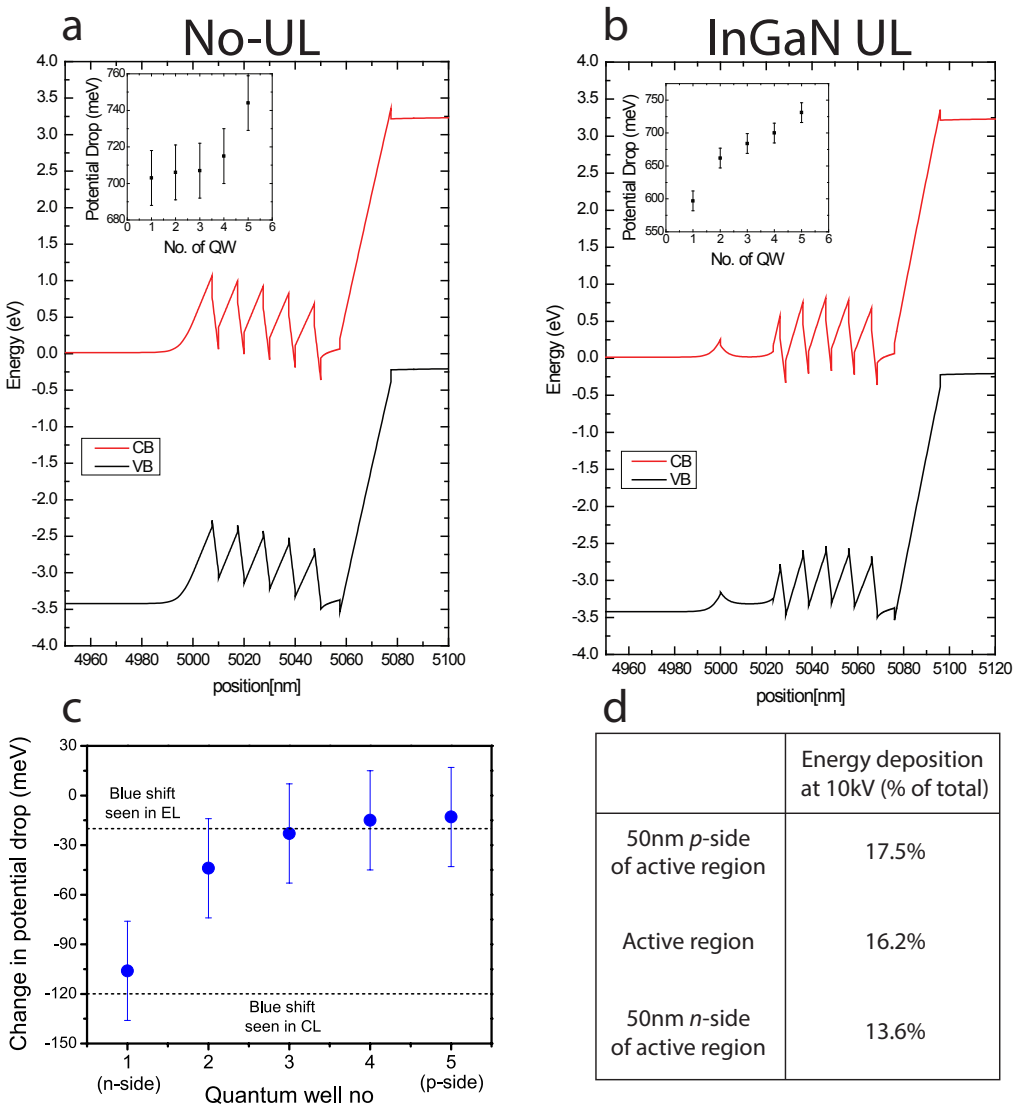

Figure 6.3: *Nextnano simulations of the band-structure around the quantum wells in the no-UL (a) and InGaN UL (b) LEDs. The change in the potential drop with the addition of the underlayer is shown in (c), and (d), which shows e-beam energy deposition uniformity around the QWs. The simulations were performed by Matthew Davies at the University of Manchester. Labels in (d) refer to percentage of total deposited e-beam energy which is deposited in the 50 nm above or below the quantum wells or within the approx 50 nm encompassed by the wells.*

positions are annotated on the plots. The fits reveal a spectral shift to higher energy emission, in both CL and EL, with the addition of the underlayer. In

the electroluminescence, the change is entirely due to increased recombination in states on the high energy side of the distribution. Recombination in states below about 2.8 eV is largely unaffected. In the cathodoluminescence, however, the change occurs on both sides of the MQW peak and the peak blue shift is significantly larger, around 120 meV in comparison with only 20 meV in the EL.

The change in the electric field across the quantum wells caused by the underlayer compensates to some degree the piezoelectric induced electric field in the quantum wells and so decreases the QCSE. Simulations of the band-structure in an InGaN UL and a no-UL device were performed by Matt Davies at University of Manchester using the Nextnano software. The results of these are shown in figure 6.3 (a) and (b). The size of the potential drop across each quantum well is shown in the insets. Essentially these are the bandgap discontinuities between the InGaN wells and GaN barriers, modified by the QCSE. The size of this potential drop is changed by the addition of the underlayer due to the additional interface charge between the UL and the first GaN barrier.

The graph in figure 6.3 (c) shows the numerical difference between the potential drops in the wells, with and without the underlayer (i.e. subtraction of data in inset (a) from inset (b)). The plot is against "well number" where well 1 is that which is closest to the underlayer. The zero point on the y-axis would indicate no change in the potential due to the addition of the InGaN underlayer. As indicated, the largest effect, of the addition of the UL, is on the well closest to the underlayer itself (well 1). The dotted lines indicate the size of the blue shifts from the, no-UL to UL LED, observed in the CL and EL spectra in fig 6.2. As can be seen, the 20 meV shift seen in the EL is similar to the potential change in those wells closest to the *p*-type side, while the large 120 meV shift in the CL can only be accounted for by recombination in the greatly altered well next to the underlayer. This suggests that in EL, the carriers are not finding their way to the bottom of the QW stack as, if this were the case, one would expect a much larger peak shift. It is important to note that the drive current is only 5 mA and this could partly be the reason for this observation.

The assertion that the CL probes the bottom QW to the same degree as the top well, is supported by the table in fig 6.3 (d) which tabulates the percentage energy deposition in the active region and the 50 nm to either side of it. As shown, the energy deposition at the bottom of the quantum wells is within a few

% of that deposited at the top.

This model is also supported by the increase in intensity with the addition of the UL. In CL, the integrated intensity increases by over 4×, while in EL it is a more modest 30%. An increase in intensity can come from a increase in the non-radiative lifetime, or a reduction in the radiative lifetime. The former will be discussed in the next section, but the reduction in the QCSE will reduce the radiative lifetime by increasing the carrier overlap. Since the CL probes the well where the compensation is largest, this may, in part, account for the much larger increase in CL intensity compared to EL, with the addition of the underlayer.

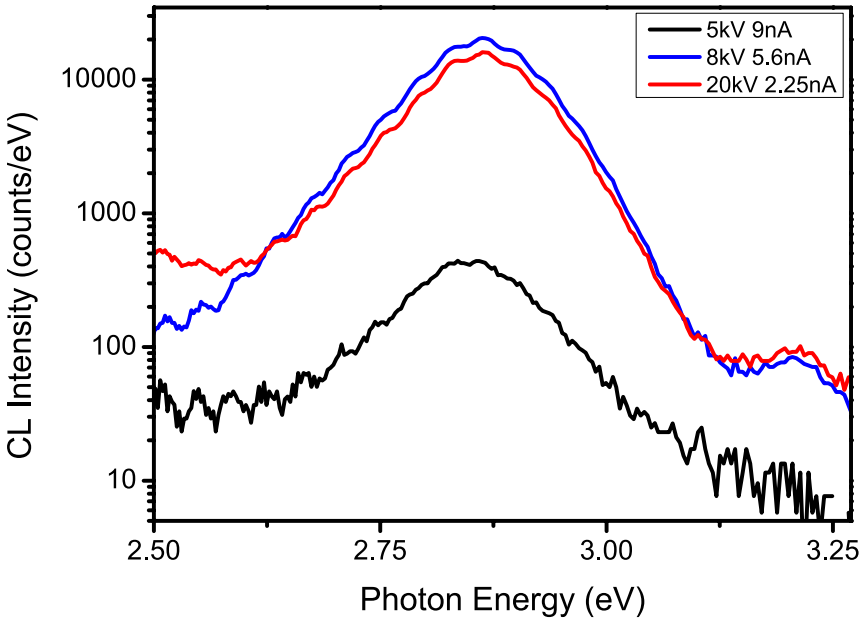

Figure 6.4: *CL spectra from the UL sample at 5 kV, 8 kV and 20 kV. (note the beam current was adjusted to maintain total power deposition)*

In addition to the change in the MQW peak, the inclusion of the underlayer creates an additional, small, shoulder peak on the high energy side of the MQW emission, centred at around 3.24 eV. Since no such peak is observed in the sample with no UL, this is likely caused by the presence of the underlayer and potentially to direct band to band recombination within the underlayer itself. With an InN

content of 5% and assuming a bowing parameter of 1.5 eV [165] the bandgap can be estimated as:

$$\begin{aligned} E_{g(In_xGa_{1-x}N)} &= xE_{\mathrm{InN}} + (1-x)E_{GaN} - b.x(1-x) \\ E_{g(In_{0.05}Ga_{0.95}N)} &= (0.05 \times 0.7) + (0.95 \times 3.42) - (1.5)(0.05)(0.95) \\ &= 3.21\ eV \end{aligned}$$

This value is very close to the position of the observed peak, indicating that the origin is very likely to be the InGaN layer. This was confirmed by depth dependent CL. CL spectra from the UL device, at 5, 8 and 20 kV, are plotted in figure 6.4. At 5 kV, the peak does not appear despite the voltage being sufficient to excite the active region. This confirms that the origin is not *above* the MQWs. At 8 kV the MQW peak is larger than at 20 kV, due to the expected effect of reduced deposition in the active region. However, the 3.24 eV peak has increased at 20 kV indicating that it lies beyond the MQWs. If the peak originated inside the quantum well stack, the intensity would increase and decrease in line with the main MQW emission. Given this observation and that the transition energy is consistent with an InGaN layer of 5% InN it is reasonable to conclude that band-to-band recombination in the underlayer is the origin of the peak.

6.2.1 Luminescence/EBIC mapping

Turning now to spatial mapping of the UL samples, figure 6.5 displays the MQW CL intensity (a&d), EBIC (b&e) and EL intensity (c&f) from the no-UL and UL devices, respectively. The CL mapping reveals a significant difference between the two devices; dark spots, as seen in the previous Q2T (and 1T) LEDs, appear in the no-UL map but are notably absent in the UL device. This is confirmed in figure 6.6 (a), which plots histograms extracted from the two MQW CL maps. The dotted lines through the plots are Gaussian fits to the plots and show that, while the InGaN UL map has a normal distribution, there is a tail on the low intensity side of the no-UL histogram. This is due to the dark spots from figure 6.5 a and is highlighted in (b) which shows only pixels which contribute to the tail (defined by the black lines in fig 6.6 (a).

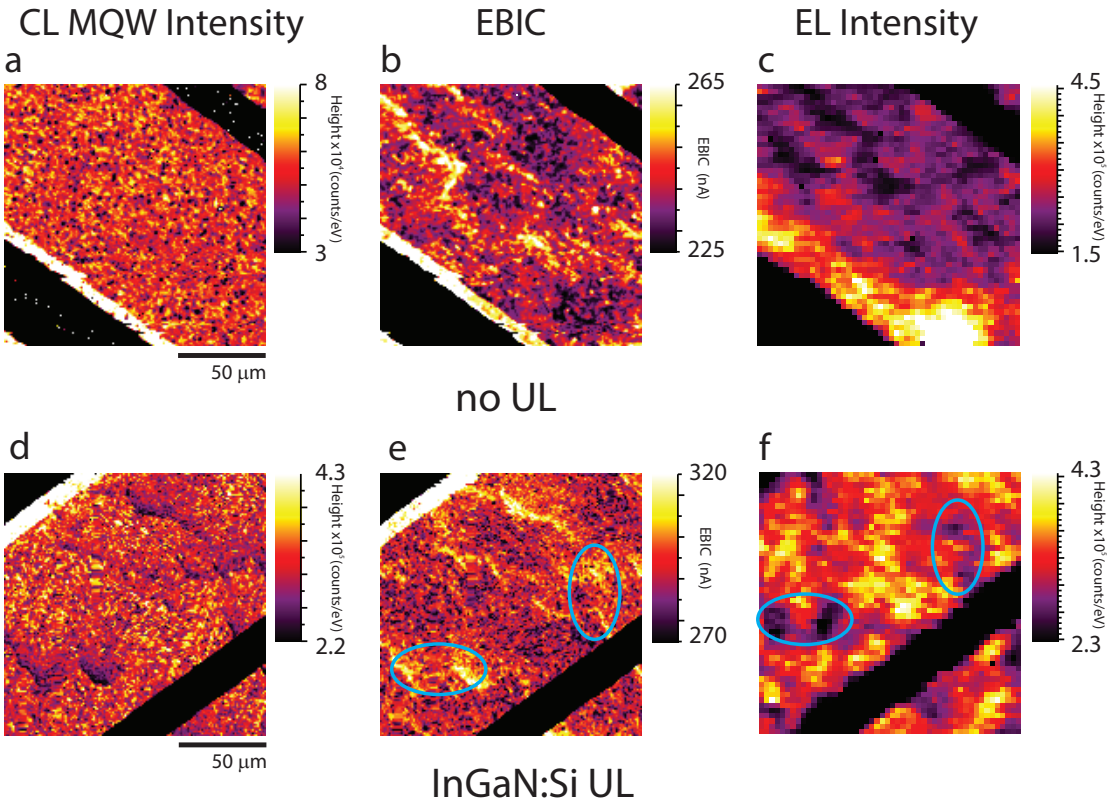

Figure 6.5: *Luminescence and conductivity mapping of two of the underlayer samples. (a, d) are the MQW CL intensity, (b, e) the simultaneously collected EBIC and (c, f) are EL maps of the same area from the no UL and the InGaN UL devices, respectively. The CL/EBIC was obtained at 10 kV, 1 nA with the bias held at 0 V. The EL maps were taken at 5 mA CW.*

The most apparent difference in the mapping, between the UL and no-UL material is the removal of the dark spots entirely with the addition the 23 nm InGaN layer. The dominant spatial inhomogeneity in the UL CL map are the filament features, which have an anti-correlation with the EBIC signal. The effect of the UL on the electric field and the resultant change of the CL spectra and intensity have been discussed previously, but the change in the spatial characteristics may be explained by the effect the underlayer has on dislocations in the active region. A study by Armstrong and Crawford's group at Sandia, published in 2015 [159], looked at the effect of a 3% InGaN layer on a SQW LED. By performing deep level optical spectroscopy to look directly at defect contri-

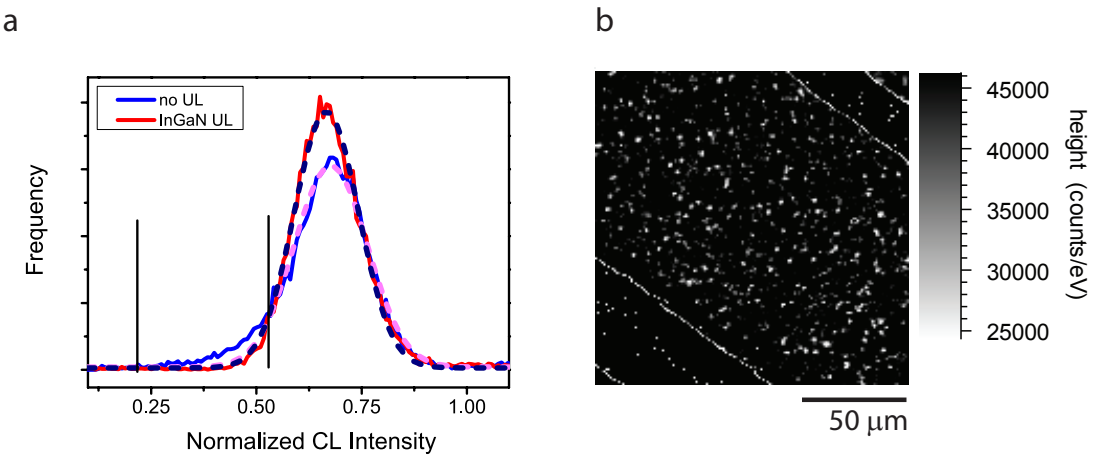

Figure 6.6: *(a) Histograms taken from the CL MQW intensity maps of the no UL and InGaN UL sample from figure 6.5(a) and (b) is the CL intensity map of the no UL device showing only those areas which contribute to the low intensity part of the histogram (between the black lines in (a)). The dotted lines in (a) are Gaussian (normal distribution) fits to the histograms.*

bution in the wells, they concluded that the improvement was due to reduction in deep level states caused by point defects in the quantum wells. This work agreed with a similar report in 2006 [112] that their observed EL increase was due to a reduction in non-radiative centres (NRC). Armstrong suggested that the reduction in generation of such defects was due to the longer gap between the growth of the high temperature GaN:Si and the lower temperature active region. The low temperature InGaN layer acts as a buffer between the defects in the GaN and allows stabilisation before growth of the low temperature QWs/QBs, and so reduces defect propagation.

It was concluded in chapter 5 that the presence of the dark spots in the Q2T material was due to the existence of clusters of point defects which were not "annealed out" due the low temperature growth of the first part of the quantum barrier. It is reasonable to conclude, therefore, that the disappearance of the spots with the addition of the underlayer is due to the partial elimination of these point defects because of the retardation of defect generation caused by the presence of the LT-InGaN UL.

The mapping also shows that the UL device generates a larger EBIC signal,

around 20% greater than the no-UL LED. This may, in part, be due to the change in the electric field (as shown in figure 6.3 (a) and (b)) where carriers not captured by the quantum wells can more easily escape the active region and contribute to the EBIC. A second possibility could be due to the reduction in point defects. It is likely that, due to the 1 μm step size, many small "dark spots" below this scale are averaged into the background in the no-UL sample. As such they are not explicitly seen, but likely contribute the lower EBIC in the dark parts of the background EBIC map. The reduction of the defects with the UL will increase the background EBIC signal as well as remove the larger spots.

6.2.2 Filament spectral characteristics

Due to the lack of the dark spots in the UL sample, the variations in the CL are reminiscent of the filament structures seen in the 2T devices. Such structures were discussed in previous chapters, and attributed to inhomogeneity in the template, as seen by Nomarski imaging. In this section, the effects on the spectral characteristic caused by the filaments are looked at in a little more detail. Maps of the GaN "yellow band" and GaN band-edge luminescence intensity are plotted in figure 6.7 (a) and (b). MQW peak spectral position width maps are plotted (c) and (d). Two CL spectra, one from "on" the filament (in the white circle in (a)) and "off" the filament (the black circle in (d)) are plotted in (g) and the similar EL spectra plotted in (h). The MQW CL intensity and EBIC have also been plotted in (c) and (f) to avoid reference to the figure 6.5 a few pages back. It is immediately apparent that a strong anti-correlation exists between the YB and band-edge signal. This is not unexpected; good band-edge luminescence is indicative of high material quality, and consequently the amount of defect related luminescence would be reduced. This is consistent with the correlation with the higher EBIC signal on the filament, which would also increase with a higher quality n-type GaN. In the previous chapter, the increase in EBIC, along with a decrease in CL intensity and a blue shift was accounted for by narrower quantum wells. While the observations here show a similar relationship, the appearance of the yellow and band-edge bands cannot simply be explained by changes in the active region. It suggests that the thickness variations in the template, which give rise to the filaments and possibly thinner wells, are less defective than the

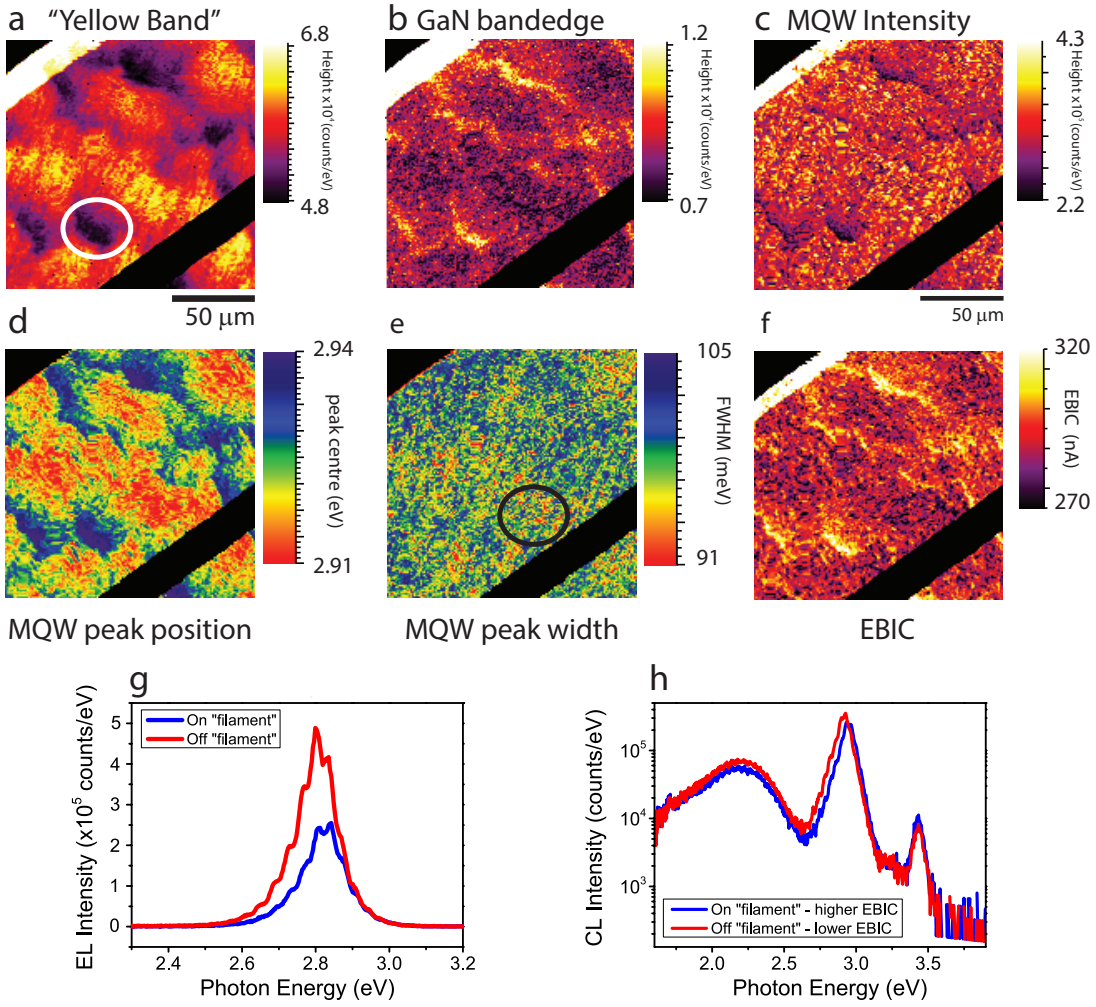

Figure 6.7: *Maps of the yellow defect band intensity (a) GaN band-edge intensity (b), MQW peak position (d) and MQW FWHM (e). The EL (g) and (h) CL spectra are from the highlighted areas on a filament (white) and off a filament (black). For comparison the MQW intensity and EBIC maps are shown in (c) and (f).*

surrounding areas - at least in the *n*-GaN.

6.2.3 Effect of electron blocking layer on Q2T grown LED

Although no specific series of LEDs with different electron blocking layers (EBLs) was available to study, it was possible to assess the effect of the inclusion of the

AlGaN EBL by comparing the "no-UL" device from the previous section with the Q2T devices studied in the first two chapters (which do not contain EBLs). Figure 6.8 displays the MQW CL parameters (intensity (a), peak position (c) and peak width (d)) and the EBIC (b) from the no-UL device.

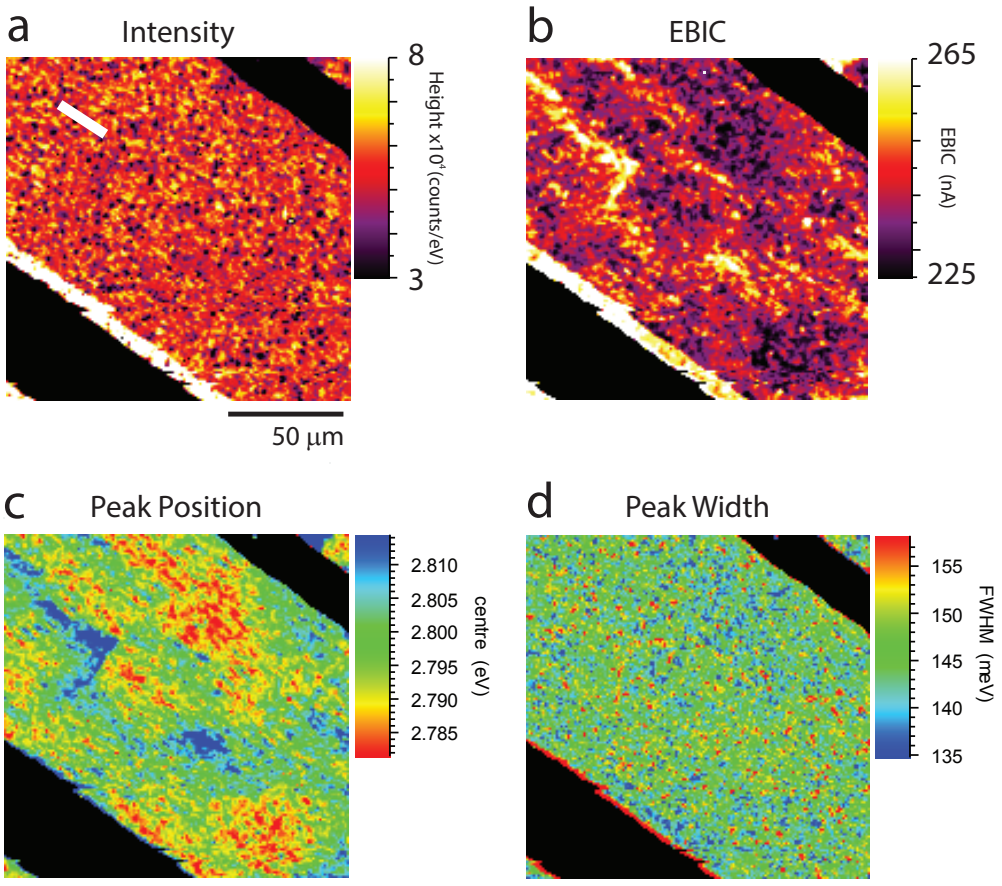

Figure 6.8: *MQW CL intensity (a), EBIC (b), fitted peak position (c) and fitted FWHM (d) from the no-UL sample. The white line in (a) indicates the position of the linescan displayed in fig 6.9.*

At first inspection, the dark spots do not appear in either the EBIC or EL maps, which would be different to the observations in previous Q2T devices. However, by taking linescans across the dark spots which are visible in the MQW CL intensity, the correlations are made evident. Several linescans were taken across the dark spots visible in the intensity map and in the same location in maps of peak position, FWHM and EBIC. One of the resultant sets of traces is presented

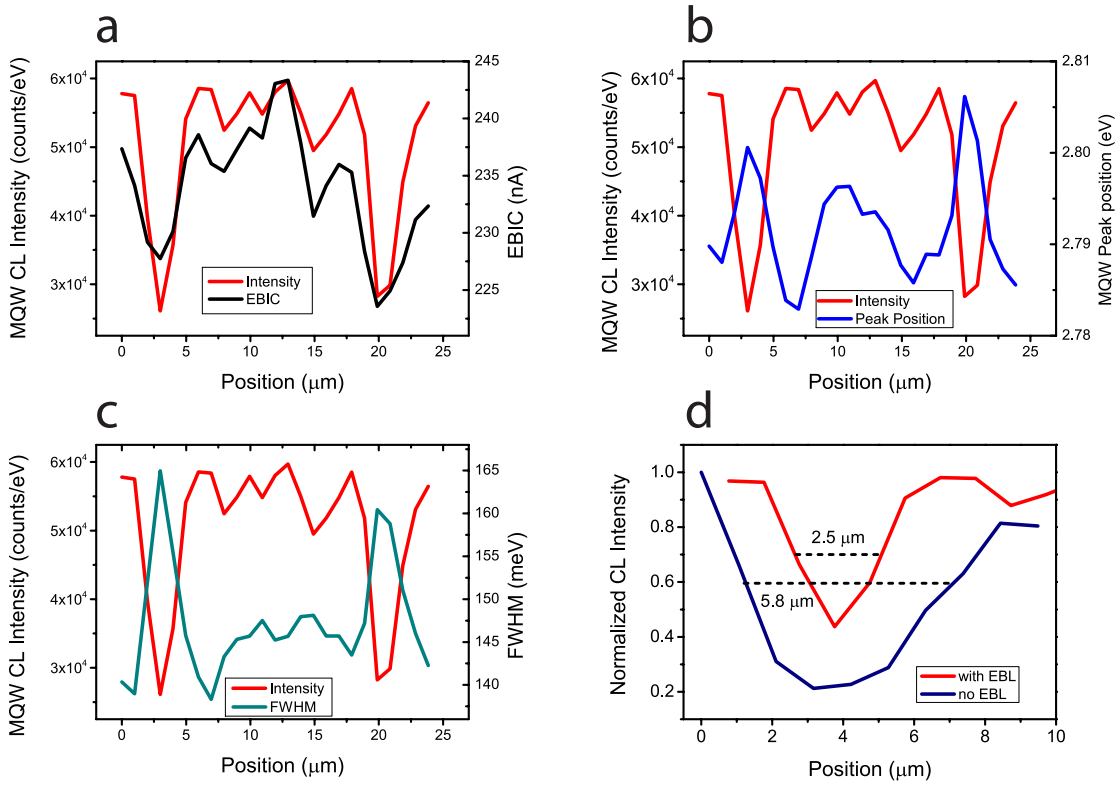

Figure 6.9: *Linescans originating from the no-UL device, MQW CL parameters maps in figure 6.8 and the EBIC map (a, b, c & d). (d) shows a comparison between the linescan for the no-UL device and from the Q2T sample studied in chapter 4.*

in figure 6.9 (a), (b) and (c). As can be seen there is a direct correlation between the intensity and EBIC on the spots and the previously observed anti-correlation with the peak position and width is also present. To make the comparison with the device with no EBL, the scan in (d) compares the scan across one spot with a scan from the device studied in chapter 4. As a reminder, in that study, the width of the spots in CL were studied as a function of applied bias. Since the bias in the no-UL data set was fixed at 0 V, the 0 V scan from the previous device has been plotted. Two differences can be readily seen; the spot width (as defined by the FWHM of the dip) is less than half of that in the earlier device. This may partly explain why the dark spots are not resolved in the EL map; the resolution of that technique is around 3 μm, larger than the feature

size. Second, the "darkness" of the spots is greatly reduced - the traces have been normalised to their own background level and while the chapter 4 spot is only 20% as bright as the background, the spots in the no-UL device only reduce the CL intensity from the background by about half. The significant difference between the no-UL sample here and that in chapter 4 is that the latter did not possess an electron blocking layer. Since it is grown after the active region, the blocking layer would be expected to have no direct effect on the nature of the defects within the quantum well/barrier stack. However, AlGaN on GaN is typically grown at around 900–1000°C [166] (these EBLs were grown at 960°C) and it is known that growth at these high temperatures can cause dissociation or damage of the MQW stack [166, 167]. Given this interference with the active region, it is conceivable that growing the EBL has had a positive effect on the intensity by annealing out the point defects which are responsible for the dark spots in the Q2T devices.

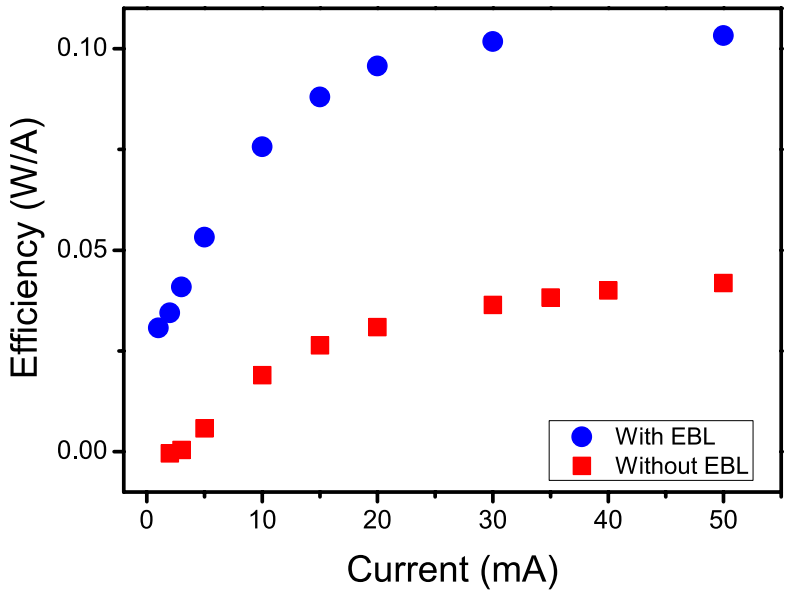

Figure 6.10: *Efficiency curves of the Q2T and the no-UL devices (nominally the same except an EBL in latter)*

There is a large increase in the radiant intensity of the no-UL sample in comparison to the Q2T LEDs without an EBL. This is shown in figure 6.10 which compares the efficiency curves, to 50 mA for the no-UL and "Q2T" device.

The increase in intensity can be attributed to two factors. The first would be the intended effect of the electron blocking layer; namely preventing overshoot and escape of injected electrons from the active region. The second contribution is the reduction in size and strength (i.e. the % drop in intensity w.r.t. background) of the dark spots.

6.2.4 Summary

In this section the effects of adding an InGaN underlayer and an AlGaN blocking layer have been studied. The addition of the underlayer affected the spectral position, intensity and width due to the change in electric field across the quantum wells. The bottom-most well, is particularly affected, due to the additional polarization interface between the UL and first barrier. By comparison with modelling performed at University of Manchester it was possible to show that, at 5 mA in EL mode, carriers do not recombine in the first well to a great degree, whereas in CL, a larger blueshift is seen due to recombination in that well. The InGaN underlayer removes the dark spots from the Q2T device and this is related to a reduction of non-radiative point defects in the active region, caused by the growth of low temperature layer between the high temperature GaN:Si and the quantum wells/barriers. Only spatial variations relating to the effects of template inhomogeneities remain, and an anti-correlation between GaN band-edge and yellow band luminescence suggest that, on top of the effect on the MQW parameters, there is a lower instance of defects around the filaments in the GaN. The addition of an AlGaN blocking layer to the previously studied Q2T devices (without an underlayer) showed that the growth of the high temperature AlGaN layer on top the active region reduced the size and strength of the dark spot point defect clusters. This was borne out in a comparison of the EL efficiency, which showed a significant increase in intensity with the addition of the EBL.

6.3 Quantum well width

The size of the quantum wells has a fundamental effect on the emission characteristics and efficiency of LEDs. Indeed, the existence of quantum wells at all is not strictly necessary for light emission. Early and experimental devices use so-called double heterostructures (DHs) [168, 54] which consist of a single layer of InGaN between the p-GaN and n-GaN layers. The advantages of this design are the relatively large optically active volume as well as a more uniform injection of electrons and holes in comparison to a MQW structure. In quantum well stacks, it has been reported that the light emission is not uniform and it is comes mostly from the first wells on the p-side [169]. In a DH, the carrier density is significantly lower however, and while this is useful in that it mitigates to some extent Auger non radiative recombination [54], the wavefunction overlap is also lower, resulting in lower radiative recombination rates. Despite the issues related to non-uniform injection [169] and deleteriously high carrier densities at high current density [160], quantum wells are the most efficient structures for conversion of current to photons. Unlike in a double heterostructure the well width has effects beyond the simple increase of optically active volume. As described in chapter 2, quantum confinement is a significant issue and a change in well width leads to a shift in the energy of the minimum (and subsequent) energy levels. The relation between energy and quantum well width, using the square infinite well approximation is given by equation 6.1

$$E_n = \frac{\hbar^2 n^2 \pi^2}{2ma^2} \tag{6.1}$$

where n is an integer, $\hbar$ the reduced Planck constant, m the particle mass and a the quantum well width.

As also described in chapter 2, in a real device the well is neither infinite nor square, owing to the finite quantum well/barrier bandgap offset and to the polarization induced, built-in or applied electric fields. However the principle is the same; for practical considerations a change in well width primarily effects the active region volume, carrier density and the wavelength of the light emitted from the device.

All the devices looked at so far have quantum wells around 2.5 nm in width. In this section, devices grown with 2.5, 3.5 and 4.5 nm wide wells are compared

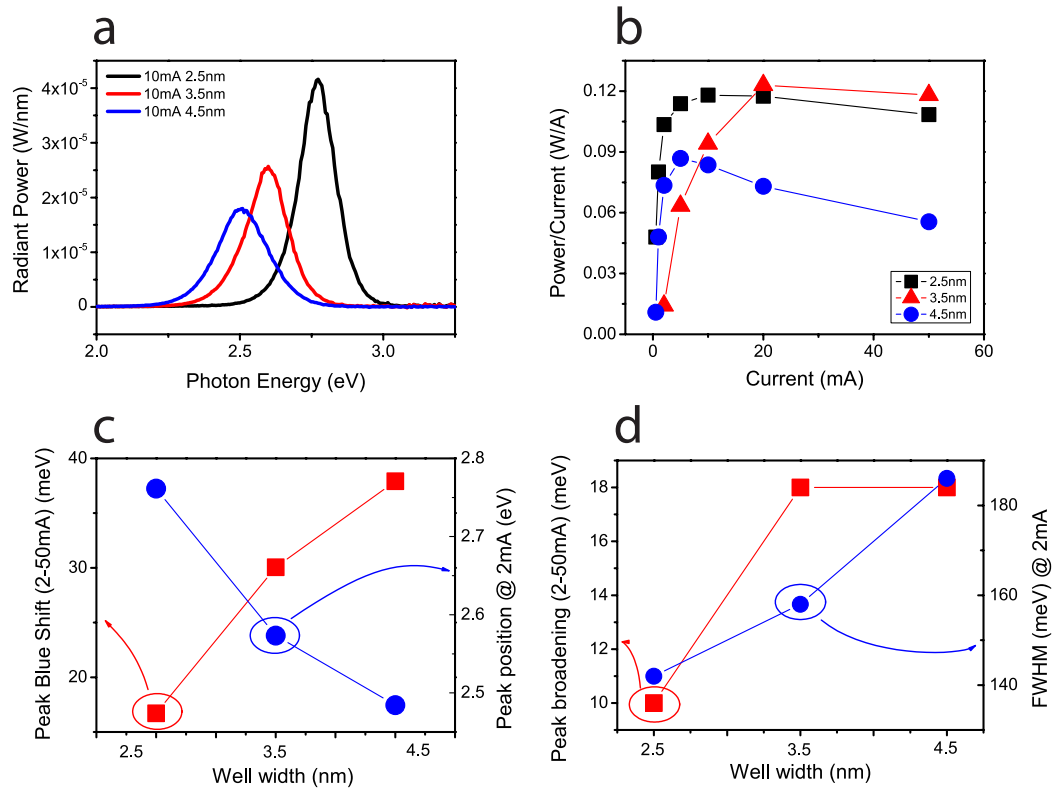

Figure 6.11: *Data extracted from EL measurements of the 3 well width devices in the integrating sphere. EL spectra at 10 mA (a), L-I curves up to 50 mA for each device (b). (c) and (d) are plots of the the peak position and FWHM at 2 mA and the blueshifts/line broadening between 2 and 50 mA, respectively.*

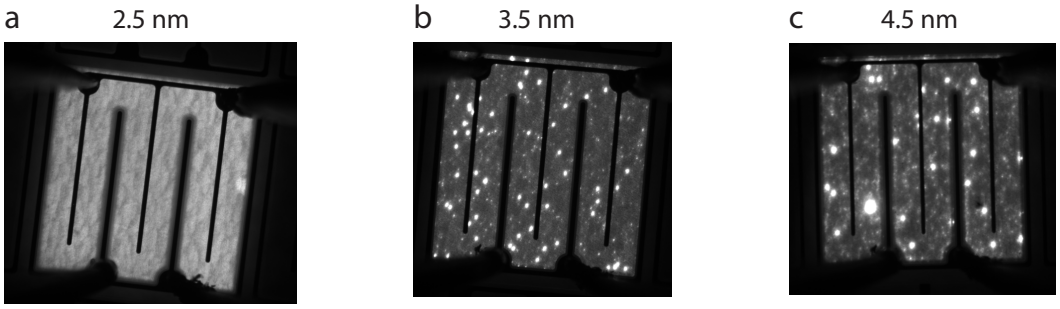

Figure 6.12: *Optical micrographs encompassing a single die of the 2.5 nm (a), 3.5 nm (b) and 4.5 nm (c) quantum well devices. The drive current was 10 mA and the images were provided by Dr Margaret Hopkins of University of Bath.*

through EL, EBIC and CL mapping as well as by measurements in the integrating sphere.

The electroluminescence spectra at 10 mA (cw) measured in the integrating sphere are shown in figure 6.11(a) along with the L-I curves for each device up to 50 mA (b). The device with the narrowest quantum wells is the brightest at low currents but is eventually overtaken by the 3.5 nm QW LED at 50 mA. The 4.5 nm QW device is less intense than the other two, particularly, at high currents. This is likely to be a consequence of the effect which the active region volume has upon the carrier density. The relative volumes are 1:1.4:1.8, so in the case of the 4.5 nm wells the carrier density is, all other variables excluded, around half of that in the 2.5 nm device. As a result, the wavefunction overlap in the "4.5 nm" device is reduced and this results in a reduced recombination rate. In the 2.5 nm wells, the carrier density is larger than either of the other well widths and so, at low drive currents, the radiative recombination is also increased. At higher drive currents, however, the Auger process becomes important and hence the 2.5 nm well devices suffers from more non-radiative recombination than the 3.5 nm QW LED. Figure 6.11(c) plots the peak position of the EL spectra at 2 mA. As would be expected based on the reduction of quantum confinement there is large redshift of around 188 meV from the "2.5 nm" to "3.5 nm" device and a further 90 meV redshift to the "4.5 nm" die. As the current increases the EL spectra from each device blueshifts due to the screening of the QCSE by the increasing free carrier density and/or phase space filling. The size of this shift (between 2 mA and 50 mA) is also plotted in figure 6.11(c), and it shows that as the well width increases the size of the peak shift increases also. In the devices with wider wells the QCSE is larger [170] and so the effect of carrier screening is increased as there is more field to compensate. The width of the luminescence peaks is also affected, as demonstrated in figure 6.11(d) where the FWHM of the peaks are plotted against well width. The increase is about 16 meV from 2.5 nm to 3.5 nm and a further 28 meV to the 4.5 nm device. The increase is likely due to the larger volume of InGaN which the carriers in the thick wells are sampling; the inherent non uniformity of the material results in a larger spread, in energy, of states which are able to be occupied.

The lateral variations in the luminescence intensity from the devices with the larger quantum wells are shown in figure 6.12. The emission from the 2.5 nm quantum well device is fairly uniform - similar to previous devices. The EL in the other two LEDs, however, is dominated by large bright spots measuring tens

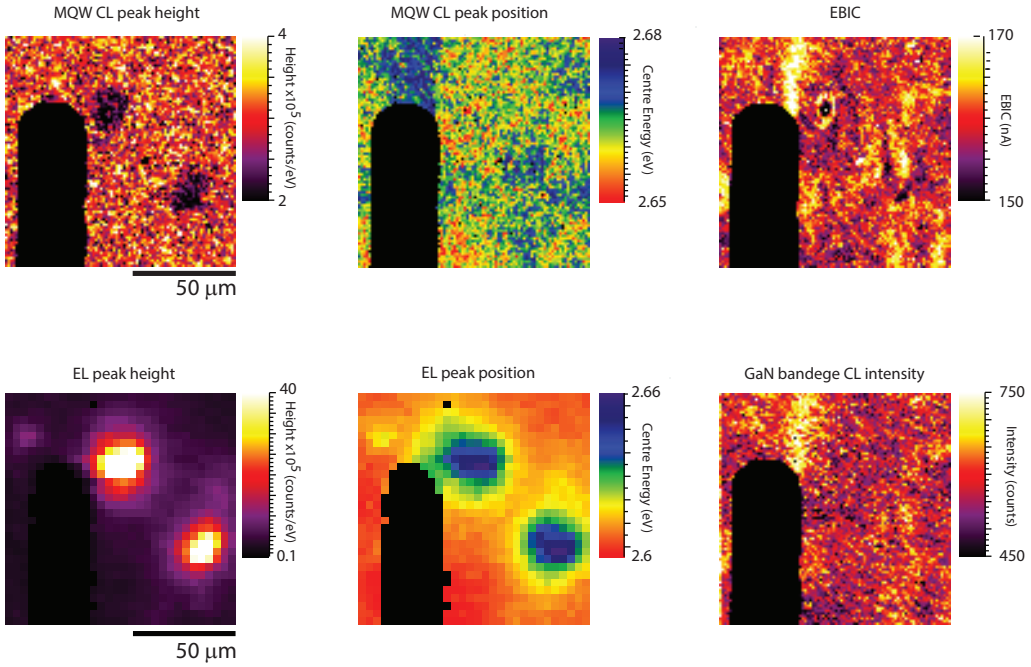

Figure 6.13: *Luminescence and EBIC maps from a 90×90 µm² area of the 3.5 nm quantum well device. The MQW CL peak height and centre as shown in (a) and (b), respectively. The equivalent EL is shown in (d) and (e). (c) is the simultaneously collected EBIC and (f) the GaN band-edge intensity.*

of microns across. The micrographs in figure 6.12 appear to indicate the size of the spots is greater in the 4.5 nm LED but that the prevalence is lower than in the 3.5 nm device. However, the relatively small number of the spots within the 1×1 mm² area means that this cannot be said with great certainty.

CL, EBIC and EL mapping were performed on the two thicker QW samples to investigate the nature of the bright spots. At this point it is important to mention that the hyperspectral mapping from which the data shown in figures 6.13, 6.14, 6.15 and 6.16 was extracted was performed jointly with Christopher Ren, from University of Cambridge, at the University of Strathclyde [171]. The maps, spectra and linescans shown were all produced independently after the collection of data, and the majority of the analysis was performed separately. Figures 6.13 and 6.14 display maps which encompass several bright spots from the 3.5 nm and 4.5 nm LEDs, respectively. In both devices the EL peak intensity at the centre of the bright spots is around 2 orders of magnitude greater than the

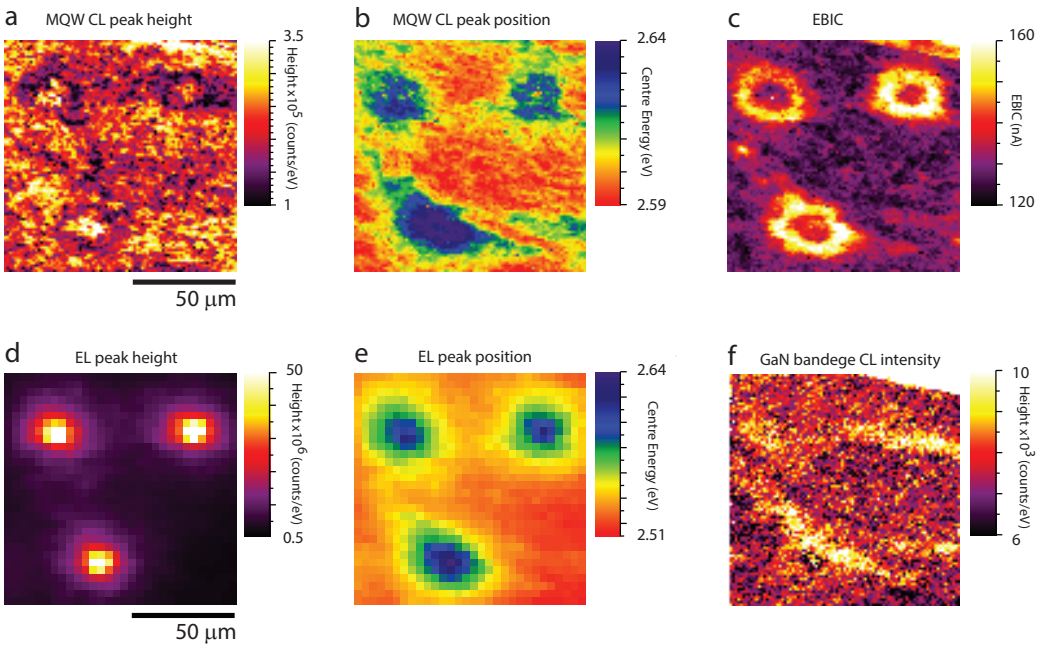

Figure 6.14: *Luminescence and EBIC maps from a 90×90 µm² area of the 4.5 nm quantum well device. The MQW CL peak height and centre are shown in (a) and (b), respectively. The equivalent EL is shown in (d) and (e). (c) is the simultaneously collected EBIC and (f) the GaN band-edge intensity.*

surrounding background, and the peak position is greatly blue shifted - around 60 meV in the 3.5 nm device and more that 100 meV in the 4.5 nm LED. The CL on the other hand displays dark contrast, which suggests that the increase in EL intensity is not due to an increased radiative recombination rate in these areas. The explanation may come from the striking nature of the EBIC map in the 4.5 nm device, where bright rings are observed around a darker centre. This observation, coupled with the large blueshift in the EL suggests that these are areas with a higher conductivity in the growth direction. Charge carriers are transported easily out of the active region resulting in an increased EBIC signal and reducing recombination in the quantum wells. Under forward bias the increased conductivity creates a higher carrier density which increases the EL intensity and, due to screening of the QCSE, blueshifts the emission line. The effect is much more pronounced in the 4.5 nm QW device and a single ring was mapped using a step size of 500 nm to investigate the centre of the spots more closely. The resulting CL and EBIC images are shown in figure 6.15 where (a),

(b) and (c) are maps of different CL bands, (d) is an example spectrum and (e) the EBIC signal.

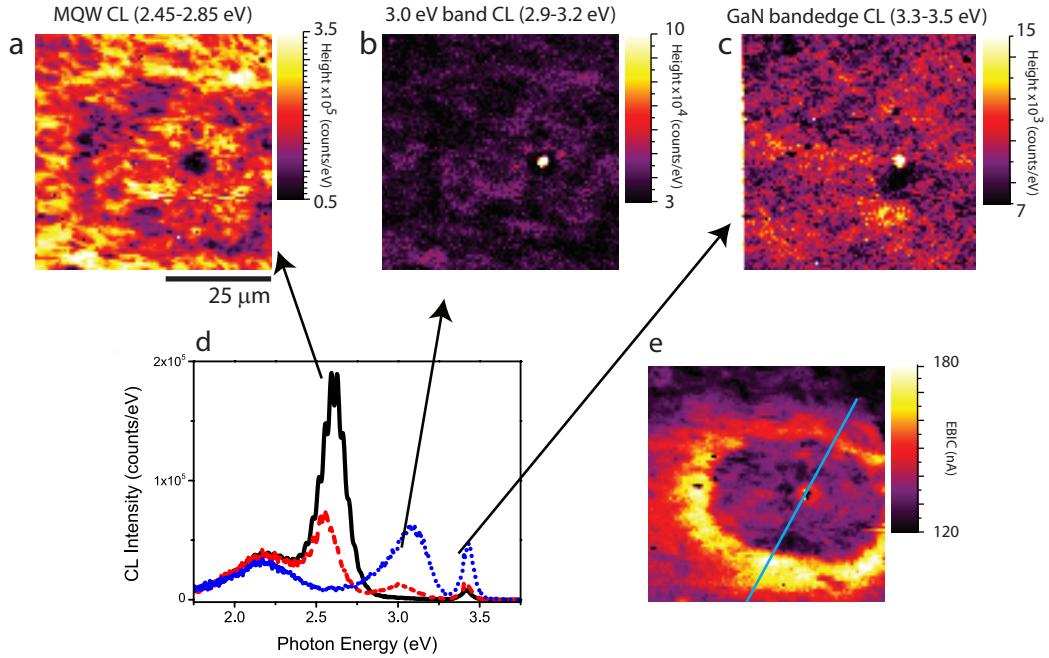

Figure 6.15: *CL and EBIC maps extracted from a dataset taken across one the large rings. (a), (b) and (c) show the MQW, 3.0 eV and GaN band-edge emission intensities. (d) shows spectra from within the centre of the inner ring (dotted blue line), just off centre (red dash line) and the map average spectrum (black solid line). (e) is the simultaneously collected EBIC.*

The structure appears to made up of two separate parts. Firstly there is the outer ring, measuring about 40 µm across, which is bright in EBIC and dark in MQW CL. This is the area which appears to possess a larger conductivity, in the *c*-direction. In CL mode, carriers escape from the active region before being allowed to recombine and hence the EBIC signal is increased. In EL mode carriers are conducted into the active region more readily in the region of this ring and so the radiative recombination rate increases and, due to free carrier screening of the QCSE and phase space filling, the peak shifts to higher energy. Secondly, at the centre of the spot there is significant change in the emission spectrum along with a large decrease in the EBIC signal. At the centre, the

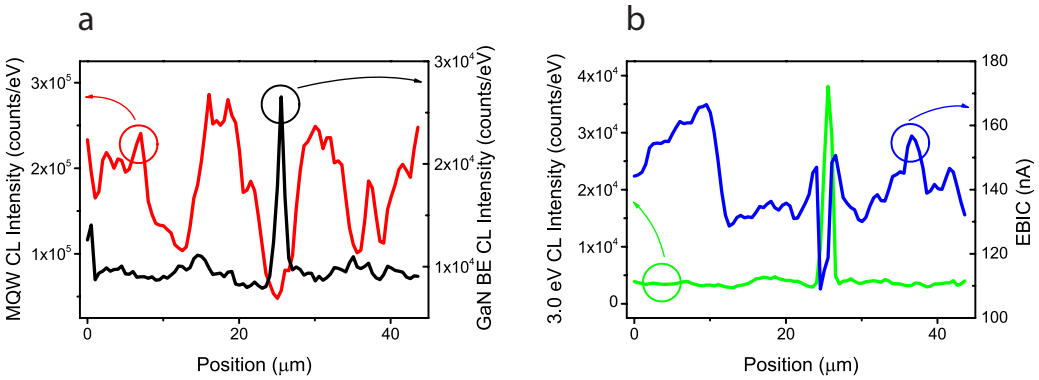

Figure 6.16: *Linescans from the EBIC and various CL bands from the line identified in figure 6.15(e). (a) is the MQW CL and GaN band-edge and (b) is the EBIC and peak centred around 3.0 eV*

MQW luminescence at 2.5 eV drops and a new band, centred at 3.0 eV appears which correlates strongly with the decreased EBIC. Fig 6.15 (c) shows that the GaN band-edge luminescence at 3.4 eV increases along with the 3.0 eV band. The linescans in figure 6.16 reveal the large change in the EBIC, 3.0 eV band and GaN luminescence which occur over less than 1 micron.

The physical origin of the ring structure in the 4.5 nm well device was investigated by transmission electron microscopy (TEM) at the University of Cambridge. Versions of the LED structures without the *p*-GaN layer were studied using TEM and high resolution secondary electron microscopy.

The results of these measurements are shown in figure 6.17, where (a) is the SE image and (b) the TEM. A large pit exists at the centre of the ring which penetrates to the level of the active region and destroys the QW/QB structure. At the centre, AlN is still present - this can be seen as a faint shadow above the QWs in (b). Since there is InN from the quantum wells in this region it suggests that the 3.0 eV peak could be due to AlInN emission. The lack of the quantum wells explains the increased GaN band-edge luminescence, since recombination is more likely in the *n*-GaN since there are no QWs to capture the charge carriers.

The origin of the large reduction in the EBIC signal is also suggested by the TEM. Recall that the EBIC requires the depletion region in order to separate the generated electron/hole pairs. At the centre of the pit the *p*-GaN and *n*-GaN are separated by only a few nanometres of AlGaN, which is itself *p*-doped.

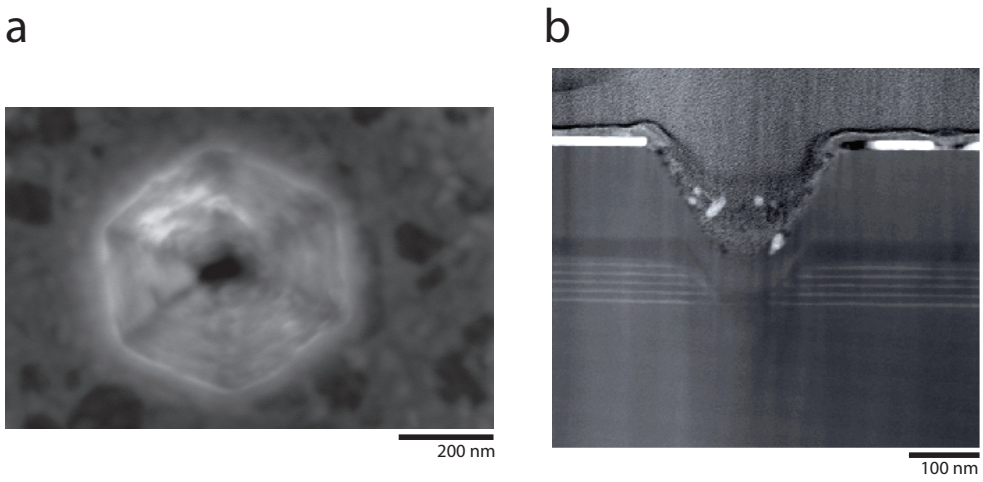

Figure 6.17: *Secondary electron (a) and TEM (b) images of the pit at the centre of the rings in the 4.5 nm devices. The images were produced at the University of Cambridge. The dark shadow above the wells in (b) is the AlGaN EBL which has replaced the QWs at the centre of the pit.*

Therefore, a greatly reduced depletion region exists at the centre and so there is a lower driving force for the EBIC at that point.

Despite the presence of the bright spots, the efficiency of the 3.5 nm QW LED is slightly greater at 50 mA than the 2.5 nm sample which, although having the more uniform emission appears to decrease in intensity with current more quickly.

6.4 Template dislocation density

As seen in previous sections in both this chapter and earlier chapters, the template upon which the LEDs are grown has a strong effect on the emission homogeneity and intensity. As discussed in the experimental chapter the template consists of the sapphire substrate, a nucleation layer and then, in each case, a 2 μm non-intentionally doped GaN layer before the *n*-GaN layer. Ridges coming from the template have already been discussed in respect to their influence on both the luminescence and EBIC. In this section three LED devices with templates with different threading dislocation densities (TDD) were studied to determine the effect of threading dislocations propagating to the active region upon LED performance and uniformity. Each of the devices contains a 22 nm InGaN under-

layer, an AlGaN EBL and a 5 period MQW structure with 3.2 nm thick wells, grown using the 2T method. The TDD of the templates used are 4×10^{9} cm^{-2} (HDD), 8×10^{8} cm^{-2} (MDD) and 4×10^{8} cm^{-2} (LDD).

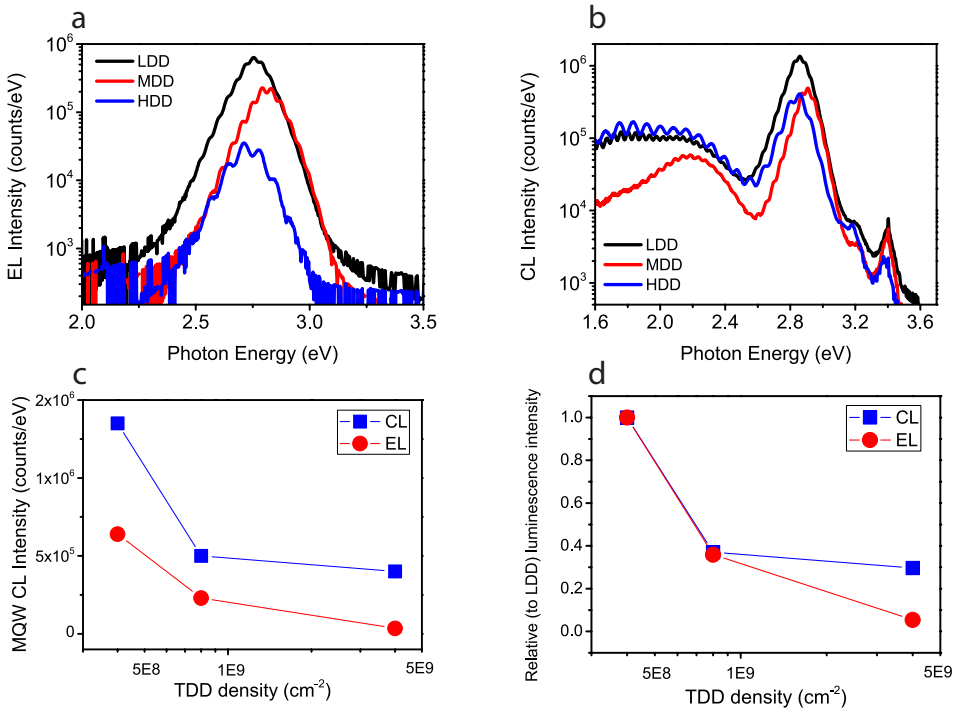

Figure 6.18: *EL (a) and CL (b) spectra from the three TDD samples. These are mean spectra from the datasets display in the next figures. (c) is a plot of the CL MQW and EL peak height vs. TDD in absolute numbers with (d) the same plot where each series has been normalized to the value in the LDD sample*

The electroluminescence and cathodoluminescence spectra from the three devices are shown in figure 6.18 (a) and (b), respectively. The EL was acquired in cw mode at 5 mA and the CL using the standard 10 kV and 1 nA beam conditions. The traces shown are the mean spectra from two sets of 3 hyperspectral datasets, from which maps are shown in figure 6.20. The EL spectra are, as in previous devices, dominated by a single peak at around 2.75 eV with the intensity dropping with a higher dislocation density. The CL spectra are similar to those observed in the underlayer devices in that alongside the MQW emission a shoulder peak associated with the InGaN underlayer is also present at around 3.2 eV. The main MQW peak is shifted by around 10 meV from the peaks in the EL and this is

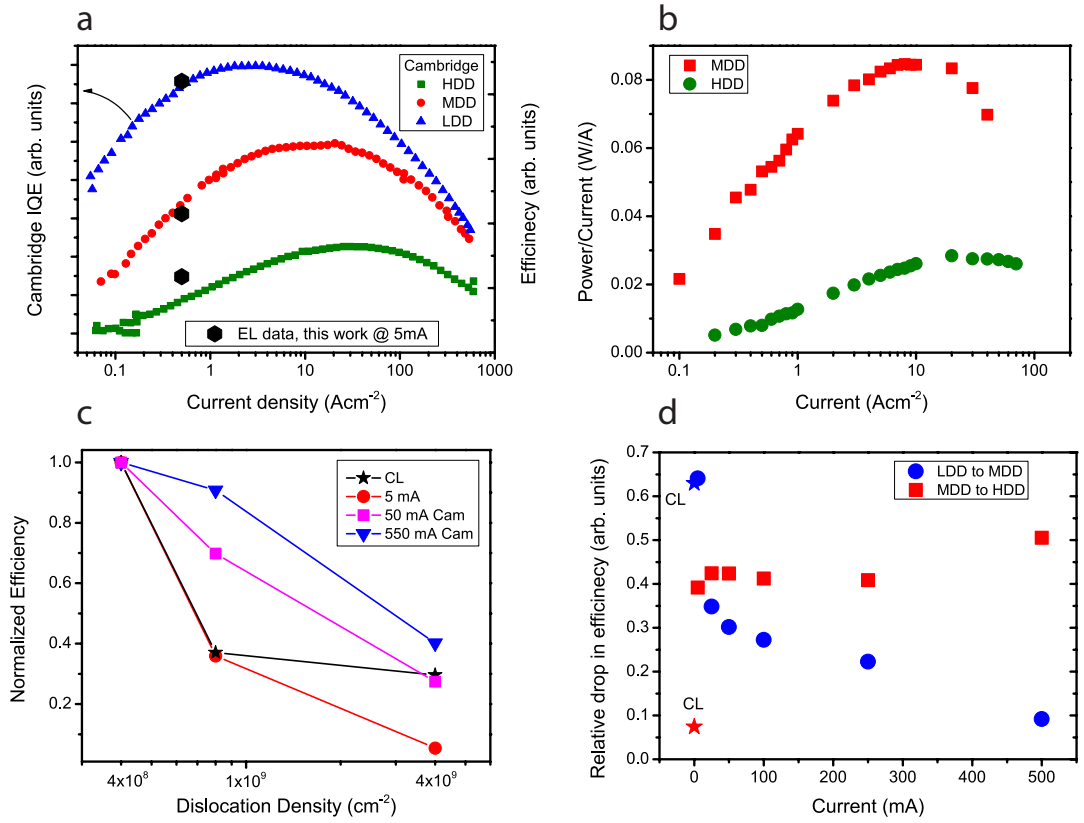

Figure 6.19: *(a) Efficiency curves of the three LED materials with different dislocation densities. These were provided by the University of Cambridge. The large black hexagons are the data, at 5 mA, from the EL data obtained here. The plot in (b) shows the normalized efficiency as a function of dislocation density for several currents and the CL.*

likely due to both that the CL is acquired with the devices held at 0 V whereas the EL is at around 2.8 V where the quantum well occupation is different. The drop in intensity with the increase in TDD is shown in figures 6.18(c) and (d). The graph in (c) plots the absolute values for the CL and EL and shows a sharp decline between 4×10^8 cm^{-2} and 8×10^8 cm^{-2} and then a slower decrease to the highest TDD. A study of the EL efficiency at high currents was performed at the University of Cambridge and a plot of the efficiency curves is shown in figure 6.19. The black hexagons are data points at 5 mA taken from this work, and are approximately in line with the curves. Efficiency curves measured in this work, using the integrating sphere, are shown in (b). It is noticeable that there is no

curve for LDD; the die shorted out before a similar curve could be taken and so only MDD and HDD are presented. Due to this, the Cambridge obtained curves have been used to analyse the effect of defect density on efficiency, along with the 5 mA data point and the CL. The integrating sphere curves are looked at again in the last section of this chapter, where all the LEDs in the thesis are compared in terms of their efficiencies. Fig 6.19 (c) plots the change in efficiency versus defect density at different EL currents, along with the intensity of the CL measured here. Note that the plot at 5 mA is based on the data measured in this work, while those at 50 mA and 550 mA are from data taken at Cambridge. As in fig 6.18 (b) the plots are normalized using the values at 4×10^8 cm^{-2}. As can be seen the dependence changes markedly upon a decrease in drive current. At very high drive currents, a reduction of defect density from 8×10^8 cm^{-2} to 4×10^8 cm^{-2} has relatively little effect on the EL efficiency. This was observed at Cambridge and an explanation was postulated which suggests that the effect of dislocations saturates at high current. This is consistent with reports in the literature by Schubert [172] and Dai [173] where it has been observed that non-radiative recombination is only dominant, for both high and low defect densities, at low currents. At high current losses are more due to carrier leakage and Auger recombination and are not as dependent on defect density. In the results seen here, this is particularly apparent between the LDD and MDD (4×10^8 cm^{-2} to 8×10^8 cm^{-2}). At 5 mA, there is a very large drop (around 60% decrease), whereas at 550 mA the decrease is marginal (just 10%). The effect of the current on the efficiency/intensity loss going from LDD to MDD is plotted in the blue curve in figure 6.19 (d). A clear trend can be observed, whereby as the current increases the effect of increasing the defect density to 8×10^8 cm^{-2} is reduced. However the effect of further increasing the defect density to 4×10^9 cm^{-2} does not have a strong dependence on drive current, as shown by the red squares. To account for this, it is necessary to compare the EL with the CL data. Figure 6.19 (c) also plots the normalized CL intensity vs. defect density and the shape is significantly different to the EL plots. The drop from LDD to MDD is very similar to the 5 mA EL efficiency but, unlike the EL, there is almost no effect observed when increasing the defect density to 4×10^9 cm^{-2} (this is shown by the red star in (d)). To explain this it is necessary to consider the difference between CL and EL. As discussed previously the CL depends mostly on the quantum wells whereas EL depends on every

layer between the contacts due to current injection. The trend seen in the CL is consistent with a model where the effect of dislocations in the active region has started to saturate by the 8×10^8 cm^{-2} value. Any further increase has little effect on the CL intensity. However, there is a large and relatively current-independent decrease in the EL efficiency upon continued dislocation increase. This could be accounted for by the effect on carrier transport from the contacts to the active region, and by increasing threading dislocation density in the *n*-GaN material (although carriers also travel through the *p*-GaN, the *n*-GaN is more important due to dislocation termination the quantum wells).

The effects of the dislocation density on the spatial uniformity of the luminescence and EBIC was studied by CL/EBIC and EL mapping. The results are shown in figure 6.20 which contains maps of the EL intensity, MQW CL peak height and EBIC from the three TDD LEDs. As with the underlayer devices there is a strong correlation between the EL and EBIC maps where large filament type variations are observed with bright contrast in both EBIC and EL. The appearance of the filament structures reduce with increasing dislocation density and this is illustrated by linescans taken across areas including filaments. Linescans approximately 100 μm long were taken from the EBIC and CL maps (roughly along the lines shown in the EBIC maps) and the EL maps, and the results are plotted in figures 6.21. In the LDD device the scans clearly resolve two distinct filaments, with an increase in the EBIC signal correlating closely with a drop in the CL signal. The filaments are spaced by around 50 μm and the relative increase of the EBIC and reduction of the CL is 6 % and 17 %, respectively. In the MDD, the scan is noisier, however three filaments in the EBIC trace can be resolved and are spaced by about 20–30 μm with a 3.7 % variation. In the CL the scan is significantly noisier but anti-correlations with the EBIC can be seen at 25, 40 and 80 μm. In the HDD device both traces are extremely noisy and no structure can be resolved with any confidence in the either map.

The differing uniformity in the LDD, MDD and HDD devices is related to the variations in the associated templates. Figures 6.22 (a), (b) and (c) present Nomarski images of the templates, taken by Dr Menno Kappers at University of Cambridge. As can be seen there is a marked difference in the scale of the inhomogeneities. The LDD template in (a) is similar to the Nomarski image of the template shown in chapter 4; long, roughly parallel, filament structures,

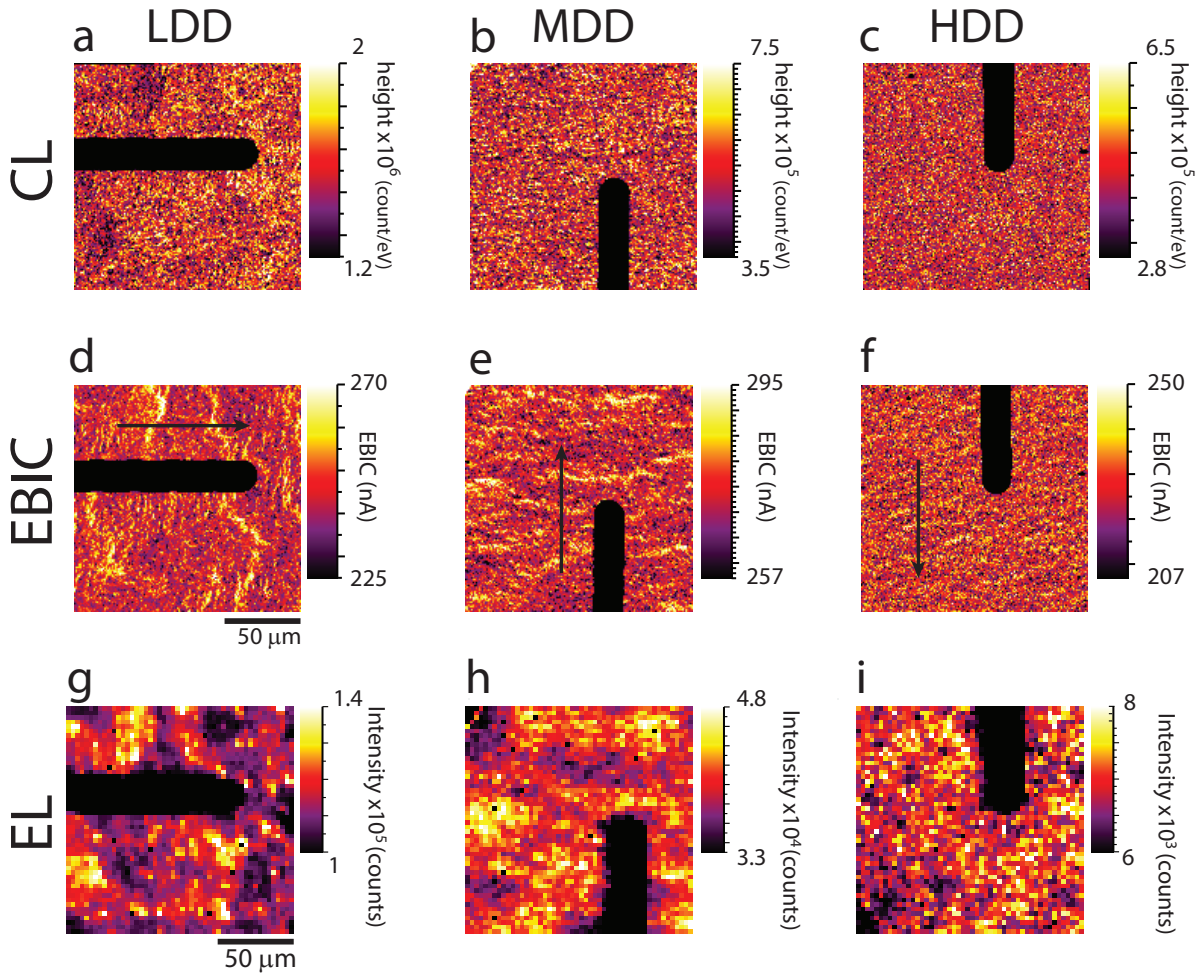

Figure 6.20: *CL (a-c), EBIC (d-f) and EL MQW (g-i) intensity maps from the 3 devices with different defect densities. The black lines in d, e & f indicate the region of the linescans shown in figure 6.21*

approximately 50-100 µm in length dominate the surface. In the template with the highest dislocation density, the surface appear more uniform. The MDD lies somewhere in between, with fewer, smaller filaments. These observations are in line with those seen in the CL/EBIC maps in figure 6.20, and so confirm that the filament related uniformity in the CL/EBIC/EL is related to the template.

The overall uniformity of the maps is found from the coefficient of variation (COV), defined as standard deviation over the mean. The COVs from the CL

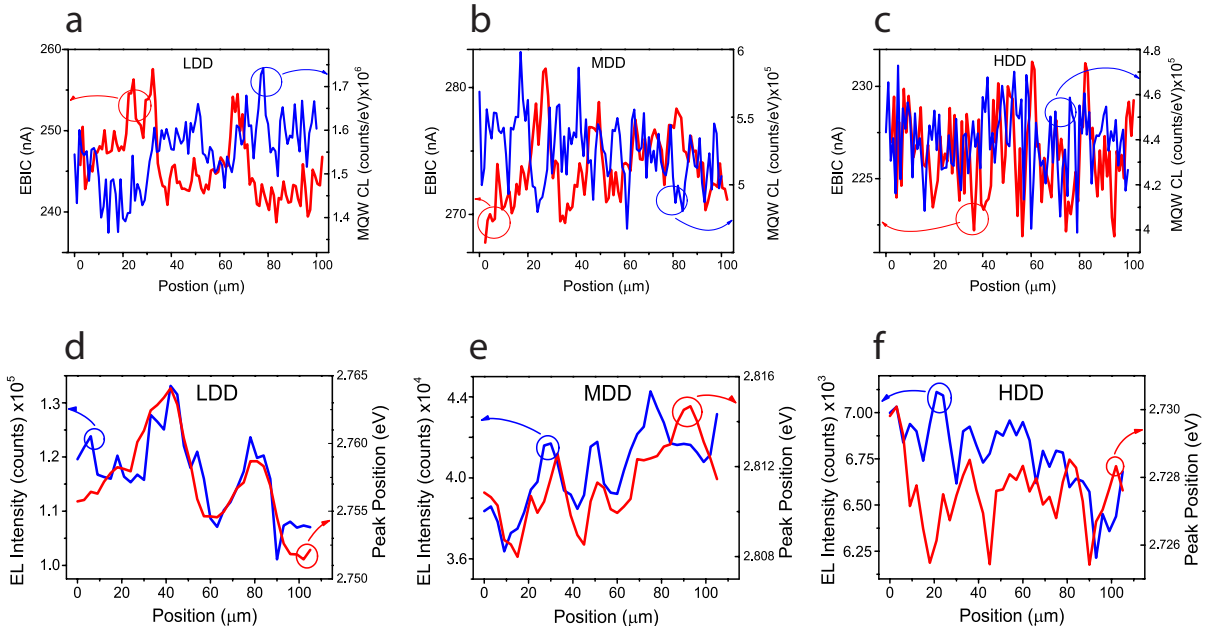

Figure 6.21: *Linescans taken from the CL and EBIC maps of the LDD (a), MDD (b) and HDD (c) samples. (d), (e) & (f) are linescans from the EL intensity maps and EL position maps (not shown). The length of the scans is the same for each to emphasise the different length scales of the non uniformity.*

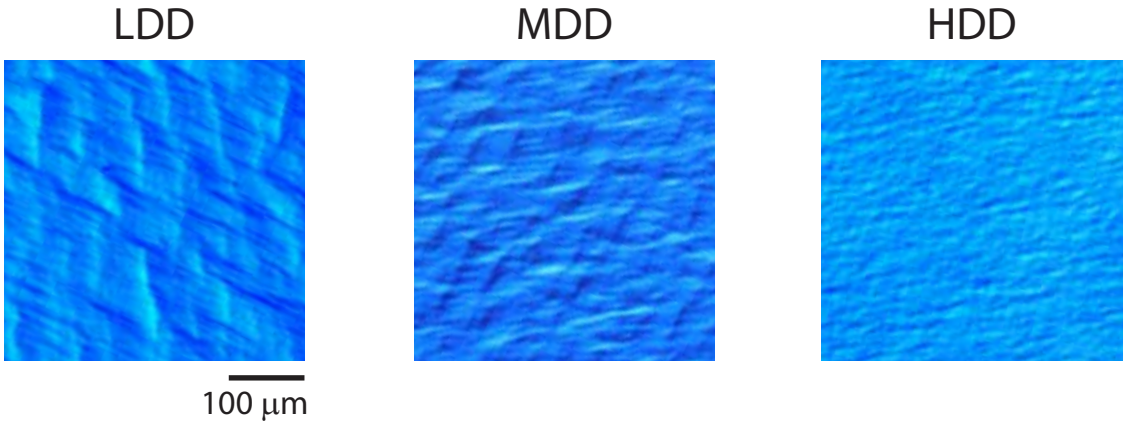

Figure 6.22: *Nomarski image of the template of the LDD (a), MDD (b) and HDD (c) samples. Kindly supplied by Menno Kappers at University of Cambridge*

and EL intensity maps are plotted in figures 6.23 (a) and (b), along with the associated mean intensities. Note that the areas comprising the dark contact

fingers are not included in the calculations. As can be seen, despite the large scale variations being larger in the LDD material, the overall uniformity shows a different trend. In the CL in particular, the COV is inversely proportional to the mean intensity. In the EL the trend is similar, but the uniformity does not as elegantly follow the mean intensity as in the CL. Given the clear anti-correlation in the CL between uniformity and intensity, it is likely that the analysis presented previously for the latter parameter holds here; namely the effects of the threading dislocations in the active region saturates beyond $1\times10^{9}\text{cm}^{-2}$. In the EL, there is little change in the uniformity between $4\times10^{8}\text{cm}^{-2}$ and $8\times10^{8}\text{cm}^{-2}$ and then a much larger increase in COV occurs from MDD to HDD. While this does not mirror the EL intensity variation at 5 mA, it is similar to the trend observed at high currents in the EL and it is conceivable that the uniformity is less dependent on current density than is the mean intensity.

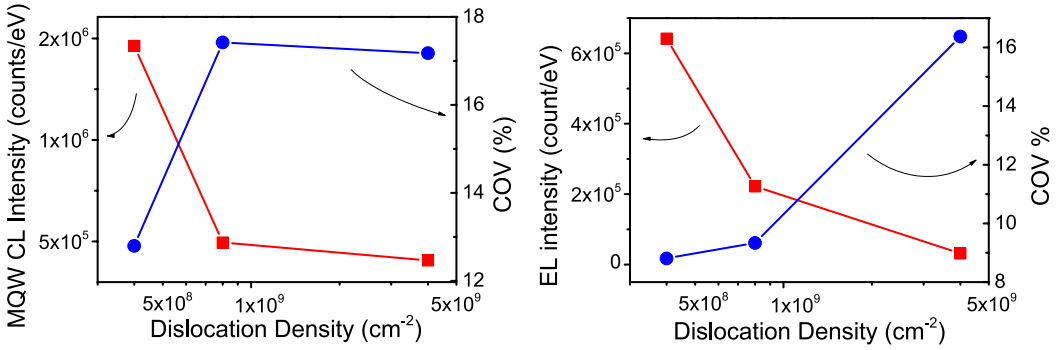

Figure 6.23: *Plots of the mean luminescence intensity and coefficient of variation from the MQW CL (a) and EL (b) maps in figure 6.20*

In summary, it has been shown that at lower dislocation densities (DD) the sensitivity to a continued reduction is strongly dependent on current density. Higher drive currents (500 mA) saturate the effect of the dislocations at medium densities, whereas at low currents (5 mA) a further reduction in DD has a large effect due to the dominance of non-radiative recombination at this current regime. Furthermore it has been shown, by a comparison between EL and CL, that a large part of the efficiency suppression at the highest defect densities, in EL, may be down to the deleterious effect of threading dislocations in the *n*-type GaN on the transport of carriers to the active region. The uniformity of the LED material

is effected in two ways. First, there is a suppression of the large scale template variations (filaments) by a global increase in defect density. Second the coefficient of variation is found to be inversely proportional the mean intensity in the CL and EL, though the effect is weaker in the latter case, possibly due to the uniformity being less sensitive than the intensity to the current density.

6.5 LED efficiency comparison

The final section of this chapter compares several of the different devices that have been studied in both this chapter and in the previous ones. In order to aid clarity, the devices has been reclassified for this section in the following table. The classification is based on 4 growth/material characteristics;

- If the growth of the active region is Q2T or 2T
- If there is an underlayer present
- If there is an electron blocking layer present and
- What the template dislocation density is

The table lists the devices by these parameters and assigns an new label to each. The final column in the table gives the original labelling of the device and the series it belongs to, from earlier in the thesis.

Label	QW growth type	UL	EBL	DD (cm^{-2})	original device reference
"A"	Q2T	no	no	4x10^8	Temp series "Q2T"
"B"	Q2T	no	yes	4x10^8	UL series "no-UL"
"C"	Q2T	yes	yes	4x10^8	UL series "UL"
"D"	2T	no	no	4x10^8	Temp series "2T"
"E"	2T	no	yes	4x10^8	width series "2.5 nm"
"F"	2T	yes	yes	4x10^8	TDD - LDD
"MDD"	2T	yes	yes	8x10^8	TDD - MDD
"HDD"	2T	yes	yes	4x10^9	TDD - HDD

Table 6.1: *Growth and material layers in the LEDs used in the plot in figure 6.24 The underlayer is 23 nm* $In_{0.05}GaN_{0.95}N$ *and the blocking layer is 20 nm thick* $Al_{0.17}Ga_{0.83}N$

The quantitative efficiencies of several devices, measured in the integrating sphere, in W/A, are plotted in figure 6.24.

From the barrier series, the Q2T (A) and 2T (D) devices are shown, from the well width series the 2.5 nm QW device (E), the "no-UL" (B) and the InGaN UL (C) devices from the UL series and the three defect density devices (F, MDD and HDD). As stated in the previous section, due to the relevant die being damaged, it was not possible to obtain an efficiency curve in the integrating sphere for the LDD device. However, data was produced by the University of Cambridge for all three devices and these were plotted on the same x and y scale. The y-scale adjustment was made by computing the approximate ratio of the curves in the Cambridge scale to the two integrating sphere curves taken in this work, i.e. those curves in figure 6.19 (b). The ratio of both the MDD:MDD and the HDD:HDD was approximately 6 and so a multiple of 1/6 was applied to the three Cambridge curves to align them approximately with the efficiency axis used in this work.

Two features in the plot are important; the maximum efficiency and the shape of the curves.

Devices "A" and "D" can be seen as baselines, in that they do not contain underlayer or electron blocking layers. The addition of an EBL for both types of QW/QB structure can be seen going from "A" to "B" for the Q2T grown material and from "D" to "E" for the 2T grown LEDs width device. The shape of the curves are unchanged but the efficiency increase is by a factor of around 2.3× and 1.2×. By comparison, the addition of the InGaN UL ("C" and "F") has a relatively small effect on the intensity, at 50 mA the increase is just 5% in both the 2T grown and Q2T grown devices.

Unsurprisingly the least efficient material is that with the high defect density template (H); at 5 mA the MDD (G) is around 3 × brighter and the LDD material (F) is another factor of 2 brighter still. This is roughly consistent with the data found by using the EL intensity maps, in figure 6.18.

The differences in the shapes of the curves are influenced by the barrier growth type and the defect density. As shown in the previous chapter, the samples with a maximum efficiency at higher currents, are those with more non radiative defects, and a higher A coefficient. This accounts for the shape of the HDD and MDD devices which, despite having 2T grown active regions, are more akin to the Q2T devices.

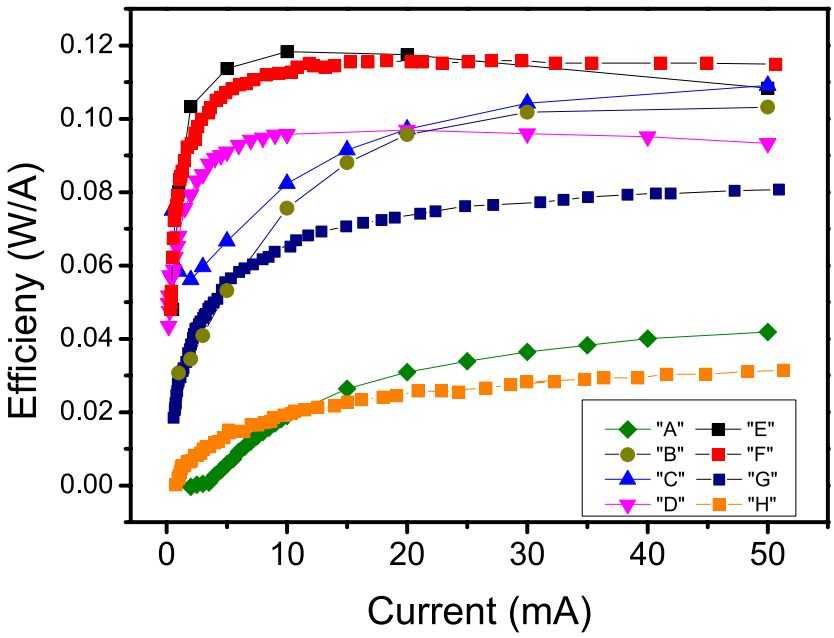

Figure 6.24: *Efficiency curves from the LEDs presented in this chapter, up to 50 mA (this range covers the drive current at which all the EL maps were taken) The LDD, MDD and HDD curves are those obtained at University of Cambridge, and were corrected to fit this scale in the manner described in the text*

The progressive improvement of device efficiency, when adding different layers, is shown in the plots in figure 6.25. The efficiency at 10 mA is plotted in (a) and at 50 mA in (b). In both graphs, two tracks are plotted; red circles for the devices grown with the 2T method and the blue squares for those with Q2T active regions. The x-axis has been designated "development" and is used to reflect the progress of the LED design. Starting with devices with only the active region and *n*-type and *p*-type GaN regions ("A", "D"), the development added an AlGaN EBL ("B", "E") and then by adding an InGaN:Si underlayer ("E", "F"). The MDD and HDD are shown at the end of the 2T tracks to show how detrimental the defect density is on device efficiency. The most striking change is the addition of the electron blocking layer to the Q2T, especially at 50 mA. In general, the Q2T grown devices benefit more from the additions. This is consistent with the observations in the CL mapping where the black spots are greatly diminished by

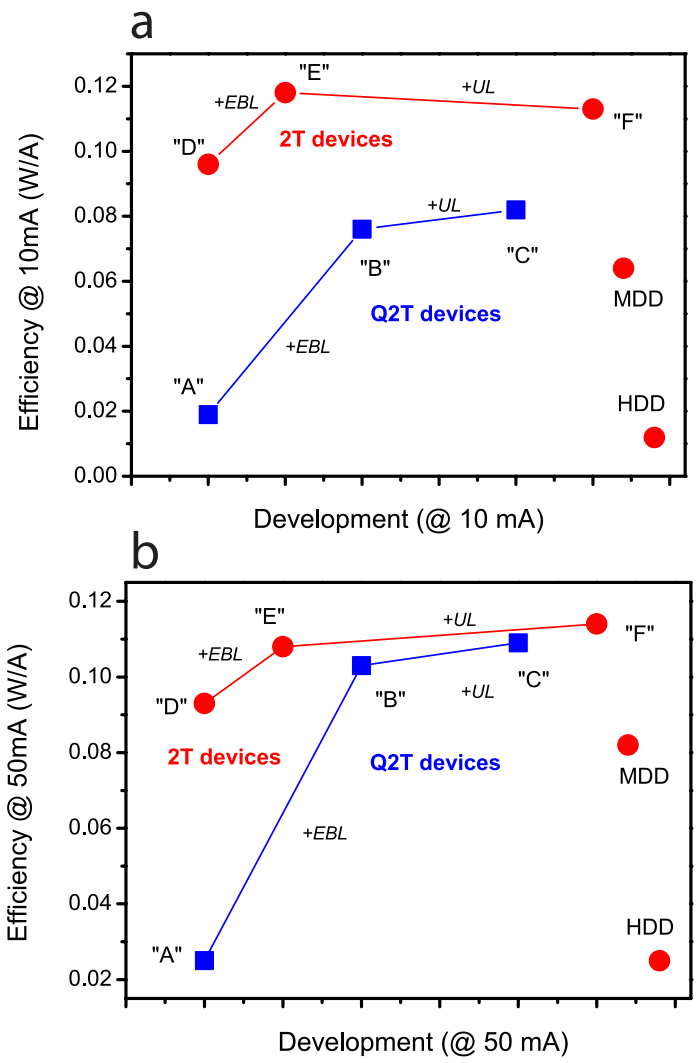

Figure 6.25: *Plots charting the improvement of the LED efficiency via addition of new layers or change in growth. The lines are split into two tracks; for the 2T and Q2T MQW grown devices. (a) is at a current of 10 mA and (b) is at 50 mA.*

the EBL and then entirely removed by the addition of the InGaN underlayer. The benefits to the 2T device is comparatively modest, but at 50 mA it is clear that the most efficient LED is that which is grown with the 2T method, has a low defect density template and contains an AlGaN EBL and a InGaN UL. The difference between the 2T and Q2T grown devices, at the end of the development (with the EBL and UL), is greatly reduced at the higher current, as was seen

with the barrier growth devices in chapter 5. However, this gap is even further reduced with the addition of the EBL and UL and shows that the large difference between the two barrier growth methods is greatly reduced with the addition of the layers which remove the dark spots.

It is important to note that only one die of each type has been used presented here. The devices chosen were those which had a low leakage current and good forward voltage current relationship. Typically at ±3 V the reverse current was no larger that 100 μA and the forward current around 25–50 mA. The spread in device luminescence intensity between the "good" devices was around 5–10% at a given current. Other devices, where there was a larger leakage current (>5μA), possessed a much lower efficiency, around a factor 3-10× less, where the effect was larger with the more efficient devices. Those shown are representative of the average efficiency of those dies considered "good".+

6.6 Summary

In this chapter the varying effects of changing the nature of the LED layers or adding new ones was studied by the combined CL/EBIC and EL methods.

The addition of the underlayer effected the spectral position, intensity and width of the LED MQW emission due to the change in electric field across the quantum wells. The bottom-most well is particularly affected, due to the additional polarization interface between the UL and first barrier. By comparison with modelling, it was possible to show that, at 5 mA in EL mode, carriers do not recombine in the first well to a great degree, whereas in CL, a larger bluehsift is seen due to recombination in that well. An additional peak at 3.24 eV was found, which was shown to be due to direct band to band recombination from the UL itself. The underlayer also removes the dark spots from the Q2T device due to a reduction in non-radiative point defects in the active region, caused by the growth stabilisation of growing a LT-InGaN layer between the high temperature GaN:Si and the quantum wells/barriers. Only spatial variations relating to template inhomogeneities still appear and an anti-correlation between GaN band-edge and yellow band luminescence suggest that, on top of the effect on the MQW parameters, there is a lower instance of defects around the filaments in the GaN.

The addition of an AlGaN blocking layer to the previously studied Q2T devices showed that the growth of the high temperature AlGaN layer on top of the active region reduced the size and strength of the dark spot point defects. Furthermore the EL efficiency was markedly increased by addition of the EBL, consistent with the reduction in the point defects clusters.

The increase of the quantum well width to 3.5 nm showed improved EL efficiency at higher current in comparison with the 2.5 nm and 4.5 nm well devices. The initial growth at 3.5 nm and particularly at 4.5 nm resulted in the creation of large pits in the material where the AlGaN electron blocking layer penetrated into the active region, reducing the MQW CL and EBIC signal. Large spots around these pits, >20 μm across, are brighter in EL and EBIC suggesting increased carrier transport in these areas.

The change in the template quality was studied by both CL and EL and it was found that the sensitivity to a reduction in defect density is strongly dependent on current density. Higher drive currents (500 mA) saturate the effect of the dislocations at medium densities, whereas at low currents (5 mA) a further reduction in DD has a large effect due to the dominance of non-radiative recombination. Suppression of EL intensity at the highest defect densities may be down to the deleterious effect of threading dislocations in the *n*-type GaN on the transport of carriers to the active region. Furthermore, there is a suppression of the large scale template variations (filaments) by a global increase in defect density and the coefficient of variation is found to be inversely proportional to the mean intensity in the CL and EL.

The efficiency, up to 50 mA, of all the devices was compared in the context of the effects of the differences between the layers in the LEDs. The largest benefit was seen with the addition of electron blocking layers; although this was most pronounced in the devices grown with the Q2T method. The addition of the underlayer improved the maximum efficiency modestly but reduces the current dependent efficiency droop.

Chapter 7

Conclusions

This final chapter summarises the main results of the work presented in this thesis, and suggests possible extensions of the work which would develop the results.

This thesis has entailed the study of the optoelectronic properties of light emitting diodes based on InGaN/GaN and their optimisation via the variation of their composition and growth parameters. The introductory chapters summarised the background physics of the materials and devices used, and then the operation and principles of the apparatus and techniques employed.

The first result chapter demonstrated the strong effect of the inbuilt, piezoelectric and applied electric fields upon LED luminescence. The effect was first explored via the observation of die to die variations on a wafer, indicating the importance of appreciating the effects of the e-beam measurement upon the electronic state of the LEDs, as well as a potential check on the uniformity and success of processing. The combined CL-EBIC study of the LED revealed dark spots where non radiative recombination occurs and, via the effects on the peak position revealed through bias dependence, where charge may be trapped. The location of the defects was probed via the bias dependence size and intensity of the CL and EBIC signals from the spots, indicating that they exist not just in the QWs but through the active region. Based on this, the origin of the dark spots were suggested to be due ot clusters of point defects in the active region. Bias and depth dependent CL was used to compare minority carrier transport in the p-type and n-type GaN. At 7 kV and 11 kV, where the spatial distribution of the energy deposition around the active region is very similar, the CL intensity

was found to be larger at 11 kV where generation is weighted to the n-GaN, and this suggests improved carrier transport from that side of the depletion region. Using power dependent PL, the effect of the applied bias was found to be three fold - prevention of majority carrier escape from the active region, reduction in tunnelling through the QWs and greater ease of diffusion based transport to the QWs.

In chapter 5 a simultaneous combination of cathodoluminescence (CL) hyperspectral imaging and electron beam induced current mapping (EBIC) was used to study the variations in luminescence and conductivity of InGaN/GaN LEDs grown with different barrier temperature profiles. Those devices where the quantum wells are uncapped prior to being exposed to a high temperature (2T, T-B) were found to have uniform luminescence intensity and an anti-correlation between CL and EBIC, on a micron scale, due to competition between carrier recombination and escape from the active region. Where the devices are grown with a protective GaN low temperature cap (Q2T, 1T) both the CL and EL are dominated by dark spots 2—10 μm in size despite having uniform quantum well thicknesses on a nanoscale. These dark spots are also found to have a lower EBIC signal, indicating regions of non-radiative recombination and possible carrier trapping. Studies of both unprocessed and incomplete LED structures support the theory that the variation is not caused by either processing or post growth p-GaN annealing steps. The peak electroluminescence efficiency of those samples without the high temperature ramp was shown to be both lower and occur at a higher drive current density than in the 2T/T-B family. The reduction in efficiency in the 1T/Q2T devices is due to the effect of the cluster of point defects in the active region. These defects are annealed out in the 2T/TB devices due to the high temperature ramp immediately after well growth. The mapping of the variation in EL efficiency curves from the non-uniform samples showed that while the bright regions are similar to the high temperature cap devices the dark spots appear to dominate the overall LED efficiency curve and have lower droop. The effect of encapsulation on the more efficient 2T sample was shown to increase the external quantum efficiency by between a factor of around 2.5.

The final results chapter studied the progressive addition and improvement of layers in the LED, including adding an InGaN underlayer, an AlGaN electron blocking layer as well as varying the thickness of the quantum wells and the

quality of the LED template. The effects of the incorporation of a silicon doped InGaN underlayer was investigated. The addition of the underlayer, affected the spectral position, intensity and width of the LED MQW emission due to the change in electric field across the quantum wells. The bottom-most well is particularly affected, due to the additional polarization interface between the UL and first barrier. By comparison with modelling, it was possible to show that, at 5 mA in EL mode, carriers do not recombine in the first well to a great degree, whereas in CL, a larger bluehsift is seen due to recombination in that well. An additional peak at 3.24 eV was found, which was shown to be due to direct band-to-band recombination from the UL itself. The underlayer also removes the dark spots from the Q2T device due to a reduction in non-radiative point defects in the active region, caused by the growth stabilisation of growing a LT-InGaN layer between the high temperature GaN:Si and the quantum wells/barriers. Only spatial variations relating to template thickness variation still appear and an anti-correlation between GaN band-edge and yellow band luminescence suggest that, on top of the effect on the MQW parameters, there is a lower instance of defects around the filaments in the GaN. The addition of an AlGaN blocking layer to the previously studied Q2T devices (without an underlayer) showed that the growth of the high temperature AlGaN layer on top the active region reduced the size and strength of the dark spot point defects. This was borne out in a comparison of the EL efficiency, which showed a significant increase in intensity (3 $\times$, with the addition of the EBL. The increase of the quantum well width to 3.5 nm showed improved EL efficiency at high currents in comparison with the 2.5 nm and 4.5 nm wells where the relatively higher and lower carrier densities resulted in efficiency decrease at high/lower currents respectively. The unfamiliarity of growth at 3.5 nm and especially 4.5 nm resulted in the creation of large pits in the material where the AlGaN electron blocking layer penetrated into the active region, reducing the MQW CL and EBIC signal. Large spots around these pits, >20 μm across, are brighter in EL and EBIC suggesting increased carrier transport in these areas.

The change in the template quality was studied by both CL and EL and it was found that the sensitivity to a reduction in threading dislocation density (TDD) is strongly dependent on current density. Higher drive currents (500 mA) saturate the effect of the dislocations at medium densities, whereas at low currents

(5 mA) a further reduction in TDD has a large effect due to the dominance of non-radiative recombination at low carrier densities. Suppression of EL intensity at the highest defect densities was suggested be down the deleterious effect of threading dislocations in the *n*-type GaN on the transport of carriers to the active region. Furthermore, there is a suppression of the large scale template variations (filaments) by a global increase in defect density and the coefficient of variation is found to be inversely proportional the mean intensity in the CL and EL.

Finally the efficiency, up to 50 mA, of all the devices studied in the work, was compared in the context of the effects of the differences between the layers in the LEDs. The largest benefit was seen with the addition of electron blocking layers; although this was most pronounced in the devices grown with the Q2T method. The addition of the underlayer improved the maximum efficiency modestly but reduces the current dependent efficiency droop.

7.1 Future work

The work performed as part of the thesis could potentially be extended in several ways. These could be categorised into improvements in the techniques used in the study of the devices and improvement or variations in the devices themselves designed to increase their efficiency. The first addition would be to extend the CL/EBIC technique to smaller scales. While the resolution limitation in the EPMA did not hinder study of, for example, the micron scale dark spots in the Q2T type devices, adapting the CL/EBIC mapping to work on high resolution SEMs could be of interest to study smaller scale variation in the LEDs. The presence of the current spreading layer in full devices and the relatively large thickness of the *p*-GaN layer, would impede simultaneous comparison of the CL, EBIC and small scale surface features by SEM/BSE mapping and as such it may prove useful to grow and fabricate "compromise devices", where the *p*-GaN is grown thinner (<50 nm) and only contacts sufficient to drive the devices are deposited. Such a device may allow mapping of smaller features in the within the active region, while still retaining the ability to tune the electric field in the depletion region.

A possible extension of the work on EBIC/EBIV measurements could be to

use it as a probe of acceptor and donor concentrations. As seen earlier, the size of the EBIC or EBIV signal is proportional to the excitation density. The largest induced voltage which can be generated in EBIV mode is the built-in diffusion potential, V_D [116]. By using an electron beam with a very high current, sufficient to saturate the EBIV signal, V_D could, in principle be mapped. The diffusion potential is dependent on the acceptor and donor concentrations and this would, therefore, allow mapping of the local carrier concentrations.

The mapping of the EL efficiency in this work revealed interesting differences between the areas with and without dark spots. By mapping at a large number of currents, it would be possible to effectively create a full efficiency curve for each pixel on a map. Parameters such as the maximum efficiency, the current at the maximum efficiency or percentage size of efficiency droop could be extracted, yielding spatial maps of the efficiency droop.

Continued improvement of the LEDs themselves is partly an issue of growth optimisation and partly down to the engineering of the particular layers. The addition of the doped low temperature underlayers and the AlGaN blocking layers led to significant improvements in LED performance, though this was strongest in those devices which were less efficient to begin with. Of some interest would be the use of large period super-lattices (SL) in addition to the underlayer which have been shown to reduce threading dislocation density [161] as well as increase hole injections [174]. Doping of the quantum barriers with magnesium to make them p-type also would increase hole concentrations in the wells. This is typically difficult as the high temperature anneal to active the acceptors will damage the well. However, in the Q2T material, it appeared as though the high temperature step required to grown the AlGaN EBL actually had a positive effect in the reduction of the dark spots. As such, attempting to anneal a doped active region grown by the Q2T type method may mitigate MQW damage.

Bibliography

[1] *The Nobel Prize in Physics 2014*.

[2] H. P. Maruska and J. J. Tietjen: *The preparation and properties of vapor-deposited single-crystalline GaN*, Applied Physics Letters **15**, 327 (1969).

[3] T. Nagatomo, T. Kuboyama, H. Minamino and O. Omoto: *Properties of $Ga_{1-x}In_xN$ Films Prepared by MOVPE*, Japanese Journal of Applied Physics **28**, L1334 (1989).

[4] N. Yoshimoto, T. Matsuoka, T. Sasaki and A. Katsui: *Photoluminescence of InGaN films grown at high temperature by metalorganic vapor phase epitaxy*, Applied Physics Letters **59**, 2251 (1991).

[5] *U.S. Department of Energy,Office of Basic Energy Sciences basic research needs for solid-state lighting [online]. pp. 167-169.* (2006).

[6] D. J. MacKay: *Sustainable Energy - without the hot air*, UIT, 2009.

[7] J. Swan: *UK patent no. 8* (1880).

[8] T. Edison: *Electric Lamp US patent 223898* (1879).

[9] Zakauskas: *Introduction to Solid State Lighting*, Troy, 2001.

[10] R. D. Dupuis and M. Krames: *History, development, and applications of high-brightness visible light-emitting diodes*, Lightwave Technology, Journal of **26**, 1154 (2008).

[11] N. Holonyak: *Is the light emitting diode (LED) an ultimate lamp?*, American Journal of Physics **68**, 864 (2000).

[12] S. Nakamura and M. Krames: *History of Gallium Nitride-Based Light-Emitting Diodes for Illumination*, Proceedings of the IEEE **101**, 2211 (2013).

[13] H. J. Round: *Carborundum as a wireless telegraph receiver*, Electrical World **Aug. 25** (1906).

[14] H. J. Round: *A note on carborundum*, Electrical World **49**, 309 (1907).

[15] S. Nakamura, M. Senoh, S. ichi Nagahama, N. Iwasa, T. Yamada, T. Matsushita, H. Kiyoku and Y. Sugimoto: *InGaN-Based Multi-Quantum-Well-Structure Laser Diodes*, Japanese Journal of Applied Physics **35**, L74 (1996).

[16] I. Akasaki, S. Sota, H. Sakai, T. Tanaka, M. Koike and H. Amano: *Shortest wavelength semiconductor laser diode*, Electronics Letters **32**, 1105 (1996).

[17] I. Ichimura, F. Maeda, K. Osato, K. Yamamoto and Y. Kasami: *Optical Disk Recording Using a GaN Blue-Violet Laser Diode*, Japanese Journal of Applied Physics **39**, 937 (2000).

[18] N. Teshima, J. Li, K. Toda and P. K. Dasgupta: *Determination of acetone in breath*, Analytica Chimica Acta **535**, 189 (2005).

[19] M. Wurtele, T. Kolbe, M. Lipsz, A. Kulberg, M. Weyers, M. Kneissl and M. Jekel: *Application of GaN-based ultraviolet-c light emitting diodes UV LEDs for water disinfection*, Water Research **45**, 1481 (2011).

[20] J. McKendry, R. Green, A. Kelly, Z. Gong, B. Guilhabert, D. Massoubre, E. Gu and M. Dawson: *High-speed visible light communications using individual pixels in a micro light-emitting diode array*, Photonics Technology Letters, IEEE **22**, 1346 (2010).

[21] T. Honda, T. Kobayashi, S. Egawa, M. Sawada, K. Sugimoto and T. Baba: *Integrated light-emitting diodes grown by MOVPE for flat panel displays*, Journal of Crystal Growth **298**, 736 , thirteenth International Conference on Metal Organic Vapor Phase Epitaxy (ICMOVPE XIII) (2007).

[22] M. H. Crawford: *LEDs for Solid-State Lighting: Performance Challenges and Recent Advances*, Selected Topics in Quantum Electronics, IEEE Journal of **15**, 1028 (2009).

[23] H. Amano, N. Sawaki, I. Akasaki and Y. Toyoda: *Metalorganic vapor phase epitaxial growth of a high quality GaN film using an AlN buffer layer*, Applied Physics Letters **48**, 353 (1986).

[24] H. Amano, I. Akasaki, K. Hiramatsu, N. Koide and N. Sawaki: *Effects of the buffer layer in metalorganic vapour phase epitaxy of GaN on sapphire substrate*, Thin Solid Films **163**, 415 (1988).

[25] I. Akasaki, H. Amano, Y. Koide, K. Hiramatsu and N. Sawaki: *Effects of AlN buffer layer on crystallographic structure and on electrical and optical properties of GaN and* $Ga_{1-x}Al_xN$ *(*$0 < x < 0.4$*) films grown on sapphire substrate by MOVPE*, Journal of Crystal Growth **98**, 209 (1989).

[26] K. Hiramatsu, S. Itoh, H. Amano, I. Akasaki, N. Kuwano, T. Shiraishi and K. Oki: *Growth mechanism of GaN grown on sapphire with AlN buffer layer by MOVPE*, Journal of Crystal Growth **115**, 628 (1991).

[27] H. Amano, M. Kito, K. Hiramatsu and I. Akasaki: *P-Type Conduction in Mg-Doped GaN Treated with Low-Energy Electron Beam Irradiation (LEEBI)*, Japanese Journal of Applied Physics **28**, L2112 (1989).

[28] S. Nakamura, T. Mukai, M. Senoh and N. Iwasa: *Thermal Annealing Effects on P-Type Mg-Doped GaN Films*, Japanese Journal of Applied Physics **31**, L139 (1992).

[29] S. Nakamura, T. Mukai and M. Senoh: *Candela-class high-brightness InGaN/AlGaN double-heterostructure blue-light-emitting diodes*, Applied Physics Letters **64**, 1687 (1994).

[30] J. Christen, M. Grundmann and D. Bimberg: *Scanning cathodoluminescence microscopy: A unique approach to atomic-scale characterization of heterointerfaces and imaging of semiconductor inhomo-*

geneities, Journal of Vacuum Science & Technology B: Microelectronics and Nanometer Structures **9**, 2358 (1991).

[31] E. Yakimov and N. Sobolev: *EBIC study of nonradiative recombination in silicon LEDs with near-band-edge luminescence*, Semiconductors **44**, 1241 (2010).

[32] U. Jahn, S. Dhar, M. Ramsteiner and K. Fujiwara: *Field-dependent nonlinear luminescence response of InGaN/GaN quantum wells*, Phys. Rev. B **69**, 115323 (2004).

[33] H. Masui, J. Sonoda, N. Pfaff, I. Koslow, S. Nakamura and S. P. DenBaars: *Quantum-confined Stark effect on photoluminescence and electroluminescence characteristics of InGaN-based light-emitting diodes*, Journal of Physics D: Applied Physics **41**, 165105 (2008).

[34] W. Shockley and W. T. Read: *Statistics of the recombinations of holes and electrons*, Phys. Rev. **87**, 835 (1952).

[35] R. N. Hall: *Electron-hole recombination in germanium*, Phys. Rev. **87**, 387 (1952).

[36] P. Landsberg and A. Beattie: *Auger effect in semiconductors*, Journal of Physics ans Chemistry of Soilds **8**, 73 (1959).

[37] A. B. Grebene: *Comments on Auger Recombination in Semiconductors*, Journal of Applied Physics **39**, 4866 (1968).

[38] H. Morkoç: *Nitride Semiconductor Devices*, Wiley, 2013.

[39] K. T. Delaney, P. Rinke and C. G. V. de Walle: *Auger recombination rates in nitrides from first principles*, Applied Physics Letters **94**, 191109 (2009).

[40] E. Kioupakis, P. Rinke, K. T. Delaney and C. G. V. de Walle: *Indirect Auger recombination as a cause of efficiency droop in nitride light-emitting diodes*, Applied Physics Letters **98**, 161107 (2011).

[41] Y. C. Shen, G. O. Mueller, S. Watanabe, N. F. Gardner, A. Munkholm and M. R. Krames: *Auger recombination in InGaN measured by photoluminescence*, Applied Physics Letters **91**, 141101 (2007).

[42] A. Laubsch, M. Sabathil, W. Bergbauer, M. Strassburg, H. Lugauer, M. Peter, S. Lutgen, N. Linder, K. Streubel, J. Hader, J. V. Moloney, B. Pasenow and S. W. Koch: *On the origin of IQE-droop in InGaN LEDs*, physica status solidi (c) **6**, S913 (2009).

[43] M. Meneghini, N. Trivellin, G. Meneghesso, E. Zanoni, U. Zehnder and B. Hahn: *A combined electro-optical method for the determination of the recombination parameters in InGaN-based light-emitting diodes*, Journal of Applied Physics **106**, 114508 (2009).

[44] B. Pasenow, S. W. Koch, J. Hader, J. V. Moloney, M. Sabathil, N. Linder and S. Lutgen: *Auger losses in GaN-based quantum wells: Microscopic theory*, physica status solidi (c) **6**, S864 (2009).

[45] W. van Roosbroeck and W. Shockley: *Photon-radiative recombination of electrons and holes in germanium*, Phys. Rev. **94**, 1558 (1954).

[46] M. Meneghini, L. R. Trevisanello, G. Meneghesso and E. Zanoni: *A Review on the Reliability of GaN-Based LEDs*, IEEE Transactions on Device and Materials Reliability **8**, 323 (2008).

[47] M. A. Reshchikov and H. Morkoc: *Luminescence properties of defects in GaN*, Journal of Applied Physics **97**, 061301 (2005).

[48] W. J. Moore, J. A. Freitas, S. K. Lee, S. S. Park and J. Y. Han: *Magneto-optical studies of free-standing hydride-vapor-phase epitaxial GaN*, Phys. Rev. B **65**, 081201 (2002).

[49] S. M. Myers, A. F. Wright, G. A. Petersen, W. R. Wampler, C. H. Seager, M. H. Crawford and J. Han: *Diffusion, release, and uptake of hydrogen in magnesium-doped gallium nitride: Theory and experiment*, Journal of Applied Physics **89**, 3195 (2001).

[50] E. F. Schubert: *Light-Emitting Diodes*, Cambridge University Press, 2006, Second edn..

[51] O. Ambacher: *Growth and applications of Group III-Nitrides*, Journal of Physics D: Applied Physics **31**, 2653 (1998).

[52] B. Gil (ed.): *III-Nitride Semiconductors and their Modern Devices*, Oxford Science Publications, 2013.

[53] J. Wu, W. Walukiewicz, K. M. Yu, J. W. Ager, E. E. Haller, H. Lu and W. J. Schaff: *Small band gap bowing in $In_{1-x}Ga_xN$ alloys*, Applied Physics Letters **80**, 4741 (2002).

[54] N. F. Gardner, G. O. Müller, Y. C. Shen, G. Chen, S. Watanabe, W. Götz and M. R. Krames: *Blue-emitting InGaN–GaN double-heterostructure light-emitting diodes reaching maximum quantum efficiency above 200 A/cm^2*, Applied Physics Letters **91**, 243506 (2007).

[55] W. S. Utsumi, H. Kaneko, H. Watanuki, T. Aoki and O. K Shimomura: *Congruent melting of gallium nitride at 6 GPa and its application to single-crystal growth*, Nature Materials **2**, 735 (2003).

[56] A. Usui, H. Sunakawa, A. Sakai and A. Yamaguchi: *Thick GaN epitaxial growth with low dislocation density by hydride vapor phase epitaxy*, Japanese Journal of Applied Physics **36**, L899 (1997).

[57] P. Vennegues, B. Beaumont, V. Bousquet, M. Vaille and P. Gibart: *Reduction mechanisms for defect densities in GaN using one- or two-step epitaxial lateral overgrowth methods*, Journal of Applied Physics **87**, 4175 (2000).

[58] A. Hangleiter, F. Hitzel, C. Netzel, D. Fuhrmann, U. Rossow, G. Ade and P. Hinze: *Suppression of Nonradiative Recombination by V-Shaped Pits in GaInN/GaN Quantum Wells Produces a Large Increase in the Light Emission Efficiency*, Phys. Rev. Lett. **95**, 127402 (2005).

[59] J. Hader, J. V. Moloney and S. W. Koch: *Density-activated defect recombination as a possible explanation for the efficiency droop in GaN-based diodes*, Applied Physics Letters **96**, 221106 (2010).

[60] O. Ambacher, R. Dimitrov, M. Stutzmann, B. Foutz, M. Murphy, J. Smart, J. Shealy, N. Weimann, K. Chu, M. Chumbes, B. Green, A. Sierakowski, W. Schaff and L. Eastman: *Role of Spontaneous and Piezoelectric Polarization Induced Effects in Group-III Nitride Based Heterostructures and Devices*, physica status solidi (b) **216**, 381 (1999).

[61] B. Bauer, J. Hubmann, M. Lohr, E. Reiger, D. Bougeard and J. Zweck: *Direct detection of spontaneous polarization in wurtzite GaAs nanowires*, Applied Physics Letters **104**, 211902 (2014).

[62] F. Bernardini, V. Fiorentini and D. Vanderbilt: *Spontaneous polarization and piezoelectric constants of III-V nitrides*, Phys. Rev. B **56**, R10024 (1997).

[63] H. Kim, S.-N. Lee and J. Cho: *Electrical and optical characterization of GaN-based light-emitting diodes fabricated with top-emission and flip-chip structures*, Materials Science in Semiconductor Processing **13**, 180 (2010).

[64] T. Takeuchi, C. Wetzel, S. Yamaguchi, H. Sakai, H. Amano, I. Akasaki, Y. Kaneko, S. Nakagawa, Y. Yamaoka and N. Yamada: *Determination of piezoelectric fields in strained GaInN quantum wells using the quantum-confined Stark effect*, Applied Physics Letters **73**, 1691 (1998).

[65] Y. D. Jho, J. S. Yahng, E. Oh and D. S. Kim: *Measurement of piezoelectric field and tunneling times in strongly biased InGaN/GaN quantum wells*, Applied Physics Letters **79**, 1130 (2001).

[66] S.-I. Park, J.-I. Lee, D.-H. Jang, H.-S. Kim, D.-S. Shin, H.-Y. Ryu and J.-I. Shim: *Measurement of Internal Electric Field in GaN-Based Light-Emitting Diodes*, Quantum Electronics, IEEE Journal of **48**, 500 (2012).

[67] Y. D. Jho, J. S. Yahng, E. Oh and D. S. Kim: *Field-dependent carrier decay dynamics in strained $In_{1-x}Ga_xN/GaN$ quantum wells*, Phys. Rev. B **66**, 035334 (2002).

[68] A. Hangleiter, F. Hitzel, S. Lahmann and U. Rossow: *Composition dependence of polarization fields in GaInN/GaN quantum wells*, Applied Physics Letters **83**, 1169 (2003).

[69] J.-H. Ryou, P. Yoder, J. Liu, Z. Lochner, H. Kim, S. Choi, H. J. Kim and R. D. Dupuis: *Control of Quantum-Confined Stark Effect in InGaN-Based Quantum Wells*, Selected Topics in Quantum Electronics, IEEE Journal of **15**, 1080 (2009).

[70] B. Nag: *Physics of Quantum Wells Devices*, Springer Science & Business Media, 2006.

[71] D. A. B. Miller, D. S. Chemla, T. C. Damen, A. C. Gossard, W. Wiegmann, T. H. Wood and C. A. Burrus: *Electric field dependence of optical absorption near the band gap of quantum-well structures*, Phys. Rev. B **32**, 1043 (1985).

[72] M. F. Schubert and E. F. Schubert: *Effect of heterointerface polarization charges and well width upon capture and dwell time for electrons and holes above GaInN/GaN quantum wells*, Applied Physics Letters **96**, 131102 (2010).

[73] K. J. Vampola, M. Iza, S. Keller, S. P. DenBaars and S. Nakamura: *Measurement of electron overflow in 450 nm InGaN light-emitting diode structures*, Applied Physics Letters **94**, 061116 (2009).

[74] M. F. Schubert, J. Xu, Q. Dai, F. W. Mont, J. K. Kim and E. F. Schubert: *On resonant optical excitation and carrier escape in GaInN/GaN quantum wells*, Applied Physics Letters **94**, 081114 (2009).

[75] B. J. Kim, Y. R. Ryu, T. S. Lee and H. W. White: *Output power enhancement of GaN light emitting diodes with p-type ZnO hole injection layer*, Applied Physics Letters **94**, 103506 (2009).

[76] C. H. Wang, C. C. Ke, C. Y. Lee, S. P. Chang, W. T. Chang, J. C. Li, Z. Y. Li, H. C. Yang, H. C. Kuo, T. C. Lu and S. C. Wang: *Hole injection and efficiency droop improvement in InGaN/GaN light-emitting*

diodes by band-engineered electron blocking layer, Applied Physics Letters **97**, 261103 (2010).

[77] S.-H. Han, D.-Y. Lee, S.-J. Lee, C.-Y. Cho, M.-K. Kwon, S. P. Lee, D. Y. Noh, D.-J. Kim, Y. C. Kim and S.-J. Park: *Effect of electron blocking layer on efficiency droop in InGaN/GaN multiple quantum well light-emitting diodes*, Applied Physics Letters **94**, 231123 (2009).

[78] M.-H. Kim, M. F. Schubert, Q. Dai, J. K. Kim, E. F. Schubert, J. Piprek and Y. Park: *Origin of efficiency droop in GaN-based light-emitting diodes*, Applied Physics Letters **91**, 183507 (2007).

[79] M. J. Davies, F. C.-P. Massabuau, P. Dawson, R. A. Oliver, M. J. Kappers and C. J. Humphreys: *Effects of an InGaN prelayer on the properties of InGaN/GaN quantum well structures*, physica status solidi (c) **11**, 710 (2014).

[80] M. J. Davies, P. Dawson, F. C.-P. Massabuau, R. A. Oliver, M. J. Kappers and C. J. Humphreys: *The effects of Si-doped prelayers on the optical properties of InGaN/GaN single quantum well structures*, Applied Physics Letters **105**, 092106 (2014).

[81] M. J. Davies, P. Dawson, F. C.-P. Massabuau, A. L. Fol, R. A. Oliver, M. J. Kappers and C. J. Humphreys: *A study of the inclusion of prelayers in InGaN/GaN single- and multiple-quantum-well structures*, physica status solidi (b) **252**, 866 (2015).

[82] S. P. Chang, C. H. Wang, C. H. Chiu, J. C. Li, Y. S. Lu, Z. Y. Li, H. C. Yang, H. C. Kuo, T. C. Lu and S. C. Wang: *Characteristics of efficiency droop in GaN-based light emitting diodes with an insertion layer between the multiple quantum wells and n-GaN layer*, Applied Physics Letters **97**, 251114 (2010).

[83] A. Laubsch, M. Sabathil, J. Baur, M. Peter and B. Hahn: *High-Power and High-Efficiency InGaN-Based Light Emitters*, Electron Devices, IEEE Transactions on **57**, 79 (2010).

[84] Y. Yang, Y. Ren, Y. Chen, M. Liu, W. Chen, X. Han, X. Lin, Q. Liao, W. Zang, H. Luo, J. Lin, Z. Wu, Y. Liu and B. Zhang: *Light output enhancement of GaN-based light-emitting diodes by maskless surface roughening*, Microelectronic Engineering **139**, 39 (2015).

[85] T. Fujii, Y. Gao, R. Sharma, E. L. Hu, S. P. DenBaars and S. Nakamura: *Increase in the extraction efficiency of GaN-based light-emitting diodes via surface roughening*, Applied Physics Letters **84**, 855 (2004).

[86] C. Huh, K.-S. Lee, E.-J. Kang and S.-J. Park: *Improved light-output and electrical performance of InGaN-based light-emitting diode by microroughening of the p-GaN surface*, Journal of Applied Physics **93**, 9383 (2003).

[87] H.-W. Huang, J. T. Chu, C. C. Kao, T. H. Hseuh, T. C. Lu, H. C. Kuo, S. C. Wang and C. C. Yu: *Enhanced light output of an InGaN/GaN light emitting diode with a nano-roughened p-GaN surface*, Nanotechnology **16**, 1844 (2005).

[88] C. Wiesmann, K. Bergenek, N. Linder and U. Schwarz: *Photonic crystal leds - designing light extraction*, Laser & Photonics Reviews **3**, 262 (2009).

[89] A. D. Jonathan J Wierer and M. M. Megens: *III-nitride photonic-crystal light-emitting diodes with high extraction efficiency*, Nature Photonics **3**, 163 (2009).

[90] C.-E. Lee, C.-F. Lai, Y.-C. Lee, H.-C. Kuo, T.-C. Lu and S.-C. Wang: *Nitride-based thin-film light-emitting diodes with photonic quasi-crystal surface*, Photonics Technology Letters, IEEE **21**, 331 (2009).

[91] P. Shields, M. D. Charlton, T. Lee, M. Zoorob, D. Allsopp and W. N. Wang: *Enhanced Light Extraction by Photonic Quasi-Crystals in GaN Blue LEDs*, Selected Topics in Quantum Electronics, IEEE Journal of **15**, 1269 (2009).

[92] C. Lewins, D. Allsopp, P. Shields, X. Gao, B. Humphreys and W. Wang: *Light Extracting Properties of Buried Photonic Quasi-Crystal Slabs in InGaN/GaN LEDs*, Display Technology, Journal of **9**, 333 (2013).

[93] A. Pavluchenko, I. Rozhansky and D. Zakheim: *Manifestation of the injection mechanism of efficiency droop in the temperature dependence of the external quantum efficiency of AlInGaN-based light-emitting diodes*, Semiconductors **43**, 1351 (2009).

[94] J. Piprek: *Efficiency droop in nitride-based light-emitting diodes*, physica status solidi (a) **207**, 2217 (2010).

[95] Y. Yang, X. A. Cao and C. Yan: *Investigation of the Nonthermal Mechanism of Efficiency Rolloff in InGaN Light-Emitting Diodes*, Electron Devices, IEEE Transactions on **55**, 1771 (2008).

[96] U. Ozgur, H. Liu, X. Li, X. Ni and H. Morkoc: *GaN-based light-emitting diodes: Efficiency at high injection levels*, Proceedings of the IEEE **98**, 1180 (2010).

[97] J. Hader, J. V. Moloney, B. Pasenow, S. W. Koch, M. Sabathil, N. Linder and S. Lutgen: *On the importance of radiative and Auger losses in GaN-based quantum wells*, Applied Physics Letters **92**, 261103 (2008).

[98] J. Iveland, L. Martinelli, J. Peretti, J. S. Speck and C. Weisbuch: *Direct Measurement of Auger Electrons Emitted from a Semiconductor Light-Emitting Diode under Electrical Injection: Identification of the Dominant Mechanism for Efficiency Droop*, Phys. Rev. Lett. **110**, 177406 (2013).

[99] M. Binder, A. Nirschl, R. Zeisel, T. Hager, H.-J. Lugauer, M. Sabathil, D. Bougeard, J. Wagner and B. Galler: *Identification of nnp and npp Auger recombination as significant contributor to the efficiency droop in (GaIn)N quantum wells by visualization of hot carriers in photoluminescence*, Applied Physics Letters **103**, 071108 (2013).

[100] M. F. Schubert, J. Xu, J. K. Kim, E. F. Schubert, M. H. Kim, S. Yoon, S. M. Lee, C. Sone, T. Sakong and Y. Park: *Polarization-matched*

GaInN/AlGaInN multi-quantum-well light-emitting diodes with reduced efficiency droop, Applied Physics Letters **93**, 041102 (2008).

[101] S. N. Hisashi Masui and S. P. DenBaars: *Experimental technique to correlate optical excitation intensities with electrical excitation intensities for semiconductor optoelectronic device characterization*, Semiconductor Science and Technology **23**, 085018 (2008).

[102] S. Hammersley, M. J. Davies, P. Dawson, R. A. Oliver, M. J. Kappers and C. J. Humphreys: *Carrier distributions in InGaN/GaN light-emitting diodes*, physica status solidi (b) **252**, 890 (2015).

[103] B. Roul, S. Mukundan, G. Chandan, L. Mohan and S. B. Krupanidhi: *Barrier height inhomogeneity in electrical transport characteristics of InGaN/GaN heterostructure interfaces*, AIP Advances **5**, 037130 (2015).

[104] H. Schneider and K. v. Klitzing: *Thermionic emission and Gaussian transport of holes in a GaAs/$Al_xGa_{1-x}As$ multiple-quantum-well structure*, Phys. Rev. B **38**, 6160 (1988).

[105] J. R. Lang, N. G. Young, R. M. Farrell, Y.-R. Wu and J. S. Speck: *Carrier escape mechanism dependence on barrier thickness and temperature in InGaN quantum well solar cells*, Applied Physics Letters **101**, 181105 (2012).

[106] I. M. Watson: *Metal organic vapour phase epitaxy of AlN, GaN, InN and their alloys: A key chemical technology for advanced device applications*, Coordination Chemistry Reviews **257**, 2120 , chemistry and Applications of Metal Nitrides (2013).

[107] T. Tanaka, A. Watanabe, H. Amano, Y. Kobayashi, I. Akasaki, S. Yamazaki and M. Koike: *p-type conduction in Mg doped GaN and $Al_{0.08}Ga_{0.92}N$ grown by metalorganic vapor phase epitaxy*, Applied Physics Letters **65**, 593 (1994).

[108] D. J. Kim, D. Y. Ryu, N. A. Bojarczuk, J. Karasinski, S. Guha, S. H. Lee and J. H. Lee: *Thermal activation energies of Mg in GaN:Mg*

measured by the Hall effect and admittance spectroscopy, Journal of Applied Physics **88**, 2564 (2000).

[109] N. Nanhui, W. Huaibing, L. Jianping, L. Naixin, X. Yanhui, H. Jun, D. Jun and S. Guangdi: *Improved quality of InGaN/GaN multiple quantum wells by a strain relief layer*, Journal of Crystal Growth **286**, 209 (2006).

[110] N. Nanhui, W. Huaibing, L. Jianping, L. Naixin, X. Yanhui, H. Jun, D. Jun and S. Guangdi: *Enhanced luminescence of InGaN/GaN multiple quantum wells by strain reduction*, Solid-State Electronics **51**, 860 (2007).

[111] N. Otsuji, K. Fujiwara and J. K. Sheu: *Electroluminescence efficiency of blue InGaN-GaN quantum-well diodes with and without an n-InGaN electron reservoir layer*, Journal of Applied Physics **100**, 113105 (2006).

[112] T. Akasaka, H. Gotoh, Y. Kobayashi, H. Nakano and T. Makimoto: *InGaN quantum wells with small potential fluctuation grown on InGaN underlying layers*, Applied Physics Letters **89**, 101110 (2006).

[113] P. Torma, O. Svensk, M. Ali, S. Suihkonen, M. Sopanen, M. Odnoblyudov and V. Bougrov: *Effect of InGaN underneath layer on MOVPE-grown InGaN/GaN blue LEDs*, Journal of Crystal Growth **310**, 5162 (2008).

[114] H.-S. Kim: *Unusual strategies for using indium galliun nitride grown on silicon (111) for solid-state lighting*, Proceeding of National Academy of Sciences of the USA **108**, 10023 (2011).

[115] E. Rutherford: *The scattering of alpha and beta particles by matter and the structure of the atom*, Philosophical Magazine **21**, 669 (1911).

[116] D. Holt and D. Joy (eds.): *SEM Microcharacterization of Semiconductors*, Academic Press, 1989, First edn..

[117] K. Heinrich: *Interrelationships of sample composition, backscatter coefficient, and target current measurement.*, Adv X-Ray Anal **7**, 325 (1964).

[118] K. Heinrich (ed.): *Theory of Quantitative Electron Probe Microanalysis:Primary Emission, Electron Beam X-Ray Microanalysis.*, Van Nostrand Reinhold, New York, 1981.

[119] T. E. Everhart and P. H. Hoff: *Determination of kilovolt electron energy dissipation vs penetration distance in solid materials*, Journal of Applied Physics **42**, 5837 (1971).

[120] K. Kanaya and S. Okayama: *Penetration and energy-loss theory of electrons in solid targets*, Journal of Physics D: Applied Physics **5**, 43 (1972).

[121] D. Drouin, A. R. Couture, D. Joly, X. Tastet, V. Aimez and R. Gauvin: *Casino v2.42 - a fast and easy-to-use modeling tool for scanning electron microscopy and microanalysis users*, Scanning **29**, 92 (2007).

[122] T. E. Everhart and R. F. M. Thornley: *Wide-band detector for micro-microampere low-energy electron currents*, Journal of Scientific Instruments **37**, 246 (1960).

[123] E. Yakimov, S. Borisov and S. Zaitsev: *EBIC measurements of small diffusion length in semiconductor structures*, Semiconductors **41**, 411 (2007).

[124] J. Bruckbauer, P. R. Edwards, T. Wang and R. W. Martin: *High resolution cathodoluminescence hyperspectral imaging of surface features in InGaN/GaN multiple quantum well structures*, Applied Physics Letters **98**, 141908 (2011).

[125] E. Yakimov, P. Vergeles, A. Govorkov, A. Polyakov, N. Smirnov, I.-H. Lee, C. R. Lee and S. Pearton: *EBIC and CL studies of ELOG GaN films*, Superlattices and Microstructures **45**, 308 (2009).

[126] P. Pellin and A. Broca: *A spectroscope of fixed deviation*, Astrophysical Journal **10**, 337 (1899).

[127] L. A. Whitehead and M. A. Mossman: *Jack o' lanterns and integrating spheres: Halloween physics*, American Journal of Physics **74**, 537 (2006).

[128] M. Avella, E. de la Puente, J. Jimenez, A. Castaldini, A. Cavallini and L. Polenta: *Electron beam induced current, cathodoluminescence and scanning photoluminescence study of GaN layers*, Journal of Crystal Growth **210**, 220 (2000).

[129] A. Boudjani, B. Sieber, F. Cleton and A. Rudra: *CL and EBIC analysis of a p+ InGaAs/n-InGaAs/n-InP/n+ -InP heterostructure*, Materials Science and Engineering: B **42**, 192 (1996).

[130] X. Li, L. Huiyong, X. Nia, U. Ozgur and H. Morkoc: *Effect of carrier spillover and Auger recombination on the efficiency droop in InGaN-based blue LEDs*, Superlattices and Microstructures **47**, 118 (2010).

[131] J. P. Liu, J.-H. Ryou, R. D. Dupuis, J. Han, G. D. Shen and H. B. Wang: *Barrier effect on hole transport and carrier distribution in InGaN/GaN multiple quantum well visible light-emitting diodes*, Applied Physics Letters **93**, 021102 (2008).

[132] O. Ozgur, X. Ni, X. Li, J. Lee, S. Liu, S. Okur, V. Avrutin, A. Matulionis and H. Morkoc: *Ballistic transport in InGaN-based LEDs: Impact on efficiency*, Semiconductor Science and Technology **26**, 014022 (2011).

[133] A. Satake, K. Soejima, H. Aizawa and K. Fujiwara: *Carrier capture and escape processes in In,GaN single-quantum-well diode under forward bias condition by photoluminescence spectroscopy*, physica status solidi (c) **3**, 2203 (2006).

[134] A. Cremades and J. Piqueras: *Study of carrier recombination at structural defects in InGaN films*, Materials Science and Engineering: B **B91-92**, 341 (2002).

[135] M. J. Wallace, P. R. Edwards, M. J. Kappers, M. A. Hopkins, F. Oehler, S. Sivaraya, D. W. E. Allsopp, R. A. Oliver, C. J. Humphreys and R. W. Martin: *Bias dependence and correlation of the cathodoluminescence and electron beam induced current from an InGaN/GaN light emitting diode*, Journal of Applied Physics **116**, 033105 (2014).

[136] A. Mao, J. Cho, Q. Dai, E. F. Schubert, J. K. Son and Y. Park: *Characteristics of dotlike green satellite emission in GaInN light emitting diodes*, Applied Physics Letters **98**, 023503 (2011).

[137] D. Neaman: *Semiconductor physics and devices : basic principles*, New York : McGraw-Hill Higher Education, 2012, Fourth edn..

[138] J. C. Gonzalez, K. L. Bunker and P. E. Russell: *Minority-carrier diffusion length in a GaN-based light-emitting diode*, Applied Physics Letters **79**, 1567 (2001).

[139] K. Kumakura, T. Makimoto, N. Kobayashi, T. Hashizume, T. Fukui and H. Hasegawa: *Minority carrier diffusion lengths in MOVPE-grown n- and p-InGaN and performance of AlGaN/InGaN/GaN double heterojunction bipolar transistors*, Journal of Crystal Growth **298**, 787 , thirteenth International Conference on Metal Organic Vapor Phase Epitaxy (ICMOVPE XIII) (2007).

[140] S. Hafiz, F. Zhang, M. Monavarian, V. Avrutin, H. Morkoc, O. Ozgur, S. Metzner, F. Bertram, J. Christen and B. Gil: *Determination of carrier diffusion length in GaN*, Journal of Applied Physics **117**, 013106 (2015).

[141] Z. Z. Bandic, P. M. Bridger, E. C. Piquette and T. C. McGill: *Minority carrier diffusion length and lifetime in GaN*, Applied Physics Letters **72**, 3166 (1998).

[142] L. Chernyak, A. Osinsky, V. Fuflyigin and E. F. Schubert: *Electron beam-induced increase of electron diffusion length in p-type GaN and AlGaN/GaN superlattices*, Applied Physics Letters **77**, 875 (2000).

[143] J. F. Muth, J. H. Lee, I. K. Shmagin, R. M. Kolbas, H. C. Casey, B. P. Keller, U. K. Mishra and S. P. DenBaars: *Absorption coefficient, energy gap, exciton binding energy, and recombination lifetime of GaN obtained from transmission measurements*, Applied Physics Letters **71**, 2572 (1997).

[144] S. Pendlebury, P. Parbrook, D. Mowbray, D. Wood and K. Lee: *InGaN/GaN quantum wells with low growth temperature GaN cap layers*, Journal of Crystal Growth **307**, 363 (2007).

[145] S. Kret, F. Ivaldi, K. Sobczak, R. Czernecki and M. Leszczyki: *Inhomogeneities of InGaN/GaN MOVPE multi quantum wells grown with a two temperatures process studied by transmission electron microscopy*, physica status solidi (a) **207**, 1101 (2010).

[146] E. Thrush, M. Kappers, P. Dawson, D. Graham, J. Barnard, M. Vickers, L. Considine, J. Mullins and C. Humphreys: *GaN/InGaN quantum well and led structures grown in a Close Coupled Showerhead (CCS) MOCVD reactor*, physica status solidi (a) **192**, 354 (2002).

[147] D. M. Graham, P. Dawson, M. J. Godfrey, M. J. Kappers, P. M. F. J. Costa, M. E. Vickers, R. Datta, C. J. Humphreys and E. J. Thrush: *High quantum efficiency InGaN/GaN structures emitting at 540 nm*, physica status solidi (c) **3**, 1970 (2006).

[148] J.-W. Ju, H.-S. Kim, L.-W. Jang, J. H. Baek, D.-C. Shin and I.-H. Lee: *A well protection layer as a novel pathway to increase indium composition: a route towards green emission from a blue InGaN/GaN multiple quantum well*, Nanotechnology **18**, 295402 (2007).

[149] P. M. F. J. Costa, R. Datta, M. J. Kappers, M. E. Vickers, C. J. Humphreys, D. M. Graham, P. Dawson, M. J. Godfrey, E. J. Thrush and J. T. Mullins: *Misfit dislocations in In-rich InGaN/GaN quantum well structures*, physica status solidi (a) **203**, 1729 (2006).

[150] T. Zhu, H. A. El-Ella, B. Reid, M. J. Holmes, R. A. Taylor, M. J. Kappers and R. A. Oliver: *Growth and optical characterisation of multilayers of InGaN quantum dots*, Journal of Crystal Growth **338**, 262 (2012).

[151] Y.-P. W. Jiunn-Chyi Lee, Ya-Fen Wub and T.-E. Neec: *Temperature and current dependences of electroluminescence from InGaN/GaN multiple quantum wells*, Journal of Crystal Growth **310**, 5143 (2008).

[152] R. A. Oliver, F. C.-P. Massabuau, M. J. Kappers, W. A. Phillips, E. J. Thrush, C. C. Tartan, W. E. Blenkhorn, T. J. Badcock, P. Dawson, M. A. Hopkins, D. W. E. Allsopp and C. J. Humphreys: *The impact of gross well width fluctuations on the efficiency of GaN-based light emitting diodes*, Applied Physics Letters **103**, 141114 (2013).

[153] M. J. Wallace, P. R. Edwards, M. J. Kappers, M. A. Hopkins, F. Oehler, S. Sivaraya, R. A. Oliver, C. J. Humphreys, D. W. E. Allsopp and R. W. Martin: *Effect of the barrier growth mode on the luminescence and conductivity micron scale uniformity of InGaN light emitting diodes*, Journal of Applied Physics **117**, 115705 (2015).

[154] Q. Dai, Q. Shan, J. Wang, S. Chhajed, J. Cho, E. F. Schubert, M. H. Crawford, D. D. Koleske, M.-H. Kim and Y. Park: *Carrier recombination mechanisms and efficiency droop in GaInN/GaN light-emitting diodes*, Applied Physics Letters **97**, 133507 (2010).

[155] F. Zhang, M. Ikeda, K. Zhou, Z. Liu, J. Liu, S. Zhang and H. Yang: *Injection current dependences of electroluminescence transition energy in InGaN/GaN multiple quantum wells light emitting diodes under pulsed current conditions*, Journal of Applied Physics **118**, 033101 (2015).

[156] T. Jeong, H.-J. Park, J.-W. Ju, H. S. Oh, J.-H. Baek, J.-S. Ha, G.-H. Ryu and H.-Y. Ryu: *High efficiency InGaN blue light-emitting diode with > 4 W output power at 3 A*, Photonics Technology Letters, IEEE **26**, 649 (2014).

[157] Y. Narukawa, M. Ichikawa, D. Sanga, M. Sano and T. Mukai: *White light emitting diodes with super-high luminous efficacy*, Journal of Physics D: Applied Physics **43**, 354002 (2010).

[158] E. Matioli, E. Rangel, M. Iza, B. Fleury, N. Pfaff, J. Speck, E. Hu and C. Weisbuch: *High extraction efficiency light-emitting diodes based on embedded air-gap photonic-crystals*, Applied Physics Letters **96**, 031108 (2010).

[159] A. M. Armstrong, B. N. Bryant, M. H. Crawford, D. D. Koleske, S. R. Lee and J. J. Wierer: *Defect-reduction mechanism for improving radiative efficiency in InGaN/GaN light-emitting diodes using InGaN underlayers*, Journal of Applied Physics **117**, 134501 (2015).

[160] J. Cho, E. F. Schubert and J. K. Kim: *Efficiency droop in light-emitting diodes: Challenges and countermeasures*, Laser & Photonics Reviews **7**, 408 (2013).

[161] A. H. Ali, A. S. A. Bakar, T. Egawa and Z. Hassan: *InGaN-based multi-quantum well light-emitting diode structure with the insertion of superlattices under-layer*, Superlattices and Microstructures **60**, 201 (2013).

[162] C.-L. Wang, M.-C. Tsai, J.-R. Gong, W.-T. Liao, P.-Y. Lin, K.-Y. Yen, C.-C. Chang, H.-Y. Lin and S.-K. Hwang: *Influence of AlGaN/GaN superlattice inserted structure on the performance of InGaN/GaN multiple quantum well light emitting diodes*, Materials Science and Engineering: B **138**, 180 , society of Vacuum Coaters 2nd Symposium on Smart Materials (2007).

[163] T. Akasaka, H. Gotoh, T. Saito and T. Makimoto: *High luminescent efficiency of InGaN multiple quantum wells grown on InGaN underlying layers*, Applied Physics Letters **85**, 3089 (2004).

[164] J. Son, S. Lee, T. Sakong, H. Paek, O. Nam, Y. Park, J. Hwang, J. Kim and Y. Cho: *Enhanced optical properties of InGaN MQWs with InGaN underlying layers*, Journal of Crystal Growth **287**, 558 (2006).

[165] G. Orsal, Y. E. Gmili, N. Fressengeas, J. Streque, R. Djerboub, T. Moudakir, S. Sundaram, A. Ougazzaden and J. Salvestrini: *Bandgap energy bowing parameter of strained and relaxed InGaN layers*, Opt. Mater. Express **4**, 1030 (2014).

[166] O. Svensk, P. Torma, S. Suihkonen, M. Ali, H. Lipsanen, M. Sopanen, M. Odnoblyudov and V. Bougrov: *Enhanced electroluminescence in 405 nm InGaN/GaN LEDs by optimized electron blocking layer*, Journal of Crystal Growth **310**, 5154 (2008).

[167] H.-Y. Ryu, J.-I. Shim, C.-H. Kim, J. H. Choi, H. M. Jung, M.-S. Noh, J.-M. Lee and E.-S. Nam: *Efficiency and Electron Leakage Characteristics in GaN-Based Light-Emitting Diodes Without AlGaN Electron-Blocking-Layer Structures*, Photonics Technology Letters, IEEE **23**, 1866 (2011).

[168] H. Sakai, T. Koide, H. Suzuki, M. Yamaguchi, S. Yamasaki, M. Koike, H. Amano and I. Akasaki: *GaN/GaInN/GaN Double Heterostructure Light Emitting Diode Fabricated Using Plasma-Assisted Molecular Beam Epitaxy*, Japanese Journal of Applied Physics **34**, L1429 (1995).

[169] A. David, M. J. Grundmann, J. F. Kaeding, N. F. Gardner, T. G. Mihopoulos and M. R. Krames: *Carrier distribution in (0001)InGaN/GaN multiple quantum well light-emitting diodes*, Applied Physics Letters **92**, 053502 (2008).

[170] M. Kunzer, C.-C. Leancu, M. Maier, K. Kohler, U. Kaufmann and J. Wagner: *Well width dependent luminescence characteristics of UV-violet emitting GaInN QW LED structures*, physica status solidi (c) **5**, 2170 (2008).

[171] C. Ren, B. Rouet-Leduc, J. Griffiths, E. Bohacek, M. Wallace, P. Edwards, M. Hopkins, D. Allsopp, M. Kappers, R. Martin and R. Oliver: *Analysis of Defect-Related Inhomogeneous Electroluminescence in InGaN/GaN QW LEDs*, Superlattices and Microstructures , (2016).

[172] M. F. Schubert, S. Chhajed, J. K. Kim, E. F. Schubert, D. D. Koleske, M. H. Crawford, S. R. Lee, A. J. Fischer, G. Thaler and M. A. Banas: *Effect of dislocation density on efficiency droop in GaInN/GaN light-emitting diodes*, Applied Physics Letters **91**, 231114 (2007).

[173] Q. Dai, M. F. Schubert, M. H. Kim, J. K. Kim, E. F. Schubert, D. D. Koleske, M. H. Crawford, S. R. Lee, A. J. Fischer, G. Thaler and M. A. Banas: *Internal quantum efficiency and nonradiative recombination coefficient of GaInN/GaN multiple quantum wells with different dislocation densities*, Applied Physics Letters **94**, 111109 (2009).

[174] Y. Yan Zhang and Y. An Yin: *Performance enhancement of blue light-emitting diodes with a special designed AlGaN/GaN superlattice electron-blocking layer*, Applied Physics Letters **99**, 221103 (2011).